Magnetic Field Induced Transitions and Exchange Interactions in Columbites

A Thesis Submitted to
Indian Institute of Technology Guwahati
for the degree of

Doctor of Philosophy

By
Maruthi R
Roll. No: 196121018

Department of Physics
Indian Institute of Technology Guwahati
Guwahati-781039, Assam (India)

Dedicated To,

Nikola Tesla

&

My Parents

&

Prof. Mohindar Singh Seehra

INDIAN INSTITUTE OF TECHNOLOGY GUWAHATI

Department of Physics

Guwahati – 781039

Declaration

"*Magnetic Field Induced Transitions and Exchange Interactions in Columbites*" is the result of my own doctoral research work. This work was carried out under the supervisions of Prof. Subhash Thota at the Department of Physics, Indian Institute of Technology Guwahati. To the best of my knowledge, the work presented in this thesis has not been submitted to any other Institute/University for the award of any degree.

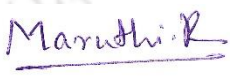

Maruthi R
Research Scholar
Roll No: 196121018
Department of Physics
Indian Institute of Technology Guwahati
Guwahati-781039, India

INDIAN INSTITUTE OF TECHNOLOGY GUWAHATI

Department of Physics

Guwahati – 781039

Certificate

It is certified that the work described in this thesis, entitled "*Magnetic Field Induced Transitions and Exchange Interactions in Columbites*", done by Mr. Maruthi R, a Ph.D. student of Department of Physics, Indian Institute of Technology Guwahati, for the award of degree of Doctor of Philosophy has been carried out under my supervision. This work has not been submitted elsewhere for the award of any degree.

Prof. Subhash Thota
Professor
Department of Physics
Indian Institute of Technology Guwahati
Guwahati-781039, India

List of Publications:

Peer Reviewed Journals:

[1] "Magnetic field-temperature phase diagram, exchange constants and specific heat exponents of the antiferromagnet $MnNb_2O_6$",
Maruthi R, S. Ghosh, M. S. Seehra, D. C. Joshi, M. R. Chowdhury, R. S. Rawat, B. Weise and, S. Thota
Journal of Physics: Condensed Matter **33**, 345801 (2021).

[2] "Determination of the tricritical point, H–T phase diagram and exchange interactions in the antiferromagnet $MnTa_2O_6$",
Maruthi R, M. S. Seehra, S. Ghosh, R. Medwal, R. S. Rawat, B. Weise, E. S. Choi, and S. Thota,
Journal of Physics: Condensed Matter **34**, 155801 (2022).

[3] "Magnetic ground state and exchange interactions in the Ising chain ferromagnet $CoNb_2O_6$",
S. Thota, S. Ghosh, **Maruthi R**, D. C. Joshi, R. Medwal, R. S. Rawat, and M. S. Seehra,
Physical Review B **103**, 064415 (2021).

[4] "Correlated Barrier Charge Hopping and Non-Debye Relaxation in Columbite $MnNb_2O_6$",
Maruthi R, S. K. Deshpande, V. Deshmukh, K. Singh, and S. Thota,
J. Phys. D: Appl. Phys. **56**, 025501 (2022).

[5] "Mapping the Field Induced Transitions On H-T Plane and the Evaluation of Exchange Interactions in Triangular Spin-1 Antiferromagnet $NiNb_2O_6$",
Maruthi R, M. S. Seehra, S. Singh, S. Ghosh, B. Weise and S. Thota,
(*Under Review*).

[6] "Temperature dependent Raman studies on $MnNb_2O_6$ and $MnTa_2O_6$",
Maruthi R, S. Singh, S. Ghosh and S. Thota,
(*Under preparation*).

[7] "Two-Phase Nanocomposites of Antiferromagnet (NiO) and Ceramic (CeO_2)",
Maruthi R and S. Thota,
(Under preparation).

Work presented in international/national conferences and workshops:

[1] "EPR and Magnetic properties of the antiferromagnet $MnNb_2O_6$",
Maruthi R and S. Thota,
Conference on Condensed Matter Physics (CCMP) 2021, Physical Research Laboratory, 16-18 August, 2021.

[2] "Electron Magnetic Resonance of Mangano-Columbite $MnNb_2O_6$",
Maruthi R, R. Medwal, R. Singh and S. Thota,
Third Indian Materials Conclave and the 32ndAnnual General Meeting of MRSI, Materials Conclave, IIT Madras, 20-23 December, 2021, Chennai, India.

[3] "AC- conductivity and Dielectric Relaxation in Columbite $MnNb_2O_6$",
Maruthi R, V. P. Khadse and S. Thota,
International Conference on Emergent Techniques and Functional Materials, 12-14 July, 2022, Indore, India.

Acknowledgements

At this moment, I would like to take the opportunity to look back and express my gratitude and thank all the people who helped me in achieving this highest degree of formal education. Initially, I would like to express my devotion and love to my mother land, India, and to my mother tongue, Kannada, for giving me a good, safe life with all needs and the confidence to live and express myself. Next, I would to thank and express my sincere gratitude to my beloved father Ramachandraiah. B and my mother Muthamma. V for their unconditional love and continuous efforts to secure my education and life.

Now it's a time and my honour to express my sincere respect and gratitude to my thesis supervisor, Prof. Subhash Thota, and I thank him from the bottom of my heart for offering me the opportunity to work under his supervision. I would like to extend my gratitude to my professor for providing his valuable time, motivation, encouragement and continuous support during my Ph.D. career. His quick suggestions and responses, along with his full-time availability at the department, helped me to carry out the research with no time delay. I owe him a great deal for his international collaborations, which greatly increased the breadth of my research experience, and for creating a welcoming learning environment while I was conducting my research at IIT Guwahati. Next, I am extremely thankful to Prof. Mohindar Singh Seehra, Eberly distinguished Professor Emeritus, Department of Physics & Astronomy, West Virginia University, USA for his endless guidance and priceless thoughts. I am really grateful to him for sharing his precious time and knowledge with us, and also for rectifying all my mistakes so patiently. I am very fascinated by the way in which Prof. M. S. Seehra guides the students, especially with handwritten notes that specify a clear understanding, and I myself considered him as a co-supervisor. It was my pleasure to work with Prof. M. S. Seehra, and I can't forget him throughout my life because of his genuine guidance and continuous support, which helped me in understanding the research problems and concepts in my entire Ph.D. career. In this regard, I was very fortunate to have my both supervisors for a fruitful journey, and I finally wish them and also their families the very best in every sense.

I would like to express my sincere thanks to my doctoral committee members, Prof. Kanhaiya Pandey (DC-chairman), Prof. D Pamu and Prof. Arun Tej Mallajosyula for their continual supervision, patience and examine my progress work during seminars in my entire Ph.D. time. Their critical comments and excellent suggestions have significantly improved the quality of my thesis work. I sincerely thank to Prof. Perumal Alagarsamy and Prof. Subhradip Ghosh, present and former Head of the Department of Physics, for allowing me to conduct the research using all of the departmental facilities. My sincere thanks to Prof. Pankaj Kumar Mishra, Prof. Padma K Padmanabhan and Prof. Saurabh Basu for teaching coarse work during first year of my Ph.D.

I would like to acknowledge the financial support from the University Grants Commission (UGC), Ministry of Education (MOE), Government of India for my entire Ph.D. period. Next, I wish to acknowledge the DST FIST-I (XRD and Newton cluster) and DST FIST-II (PPMS-references Nos. SR/FST/PSII-020/2009 and SR/FST/PSII-037/2016) facility in the department of physics, IIT Guwahati, which served in major part of my research work. I also acknowledge the Central Instrument Facility (CIF), IIT Guwahati; North East Centre for Biological Sciences and Healthcare Engineering (NECBH), IIT Guwahati for partial support of my research work. I thank Prof. Vasant Sathe, UGC-DAE, Indore for Raman measurements and I wish to acknowledge the financial support from UGC-DAE CSR through a Collaborative Research Scheme (CRS) Project Number CRS/2021-22/01/383.

I am very thankful to Dr. Bruno Weise, Leibniz-IFW Dresden, Institute for Complex Materials, Germany for helping me with the specific heat measurements. I also express my sincere thanks to Dr. Rohit Medwal and Prof. Rajdeep S. Rawat, Nanyang Technological University Singapore, for their active collaboration. I would like to acknowledge the Ministry of Education (MOE), Singapore through Grant No. MOE2019-T2-1-058 and National Research Foundation (NRF) through Grant No. NRF-CRP21-2018-0003 for the partial support of my research work. My Special thanks to Dr. Eun Sang Choi, National High Magnetic Field

Laboratory, Florida, USA for help me in high magnetic field measurements which helped us to gain good insight into physics. A portion of this work was performed at the National High Magnetic Field Laboratory, which is supported by the National Science Foundation Cooperative Agreement No. DMR-1644779 and the State of Florida. I would to thank Prof. S. K. Deshpande, UGC-DAE Consortium for Scientific Research Mumbai Centre, BARC Campus for measuring the dielectric measurements of our samples. I would like to thank Dr. Sobhit Singh, University of Rochester, USA for fruitful physics discussions.

I am deeply thankful to my dear brother Shivakumar. R for having good discussions and a pleasant brotherhood at every stage of my life. Further, I express my sincere thanks to my friend Subrahmanya L. Hegde for having good friendship, worthful physics discussions and helping me in solving standard physics textbooks which lead to clear very prestigious CSIR-NET-JRF exam to pursue Ph.D.

I am blessed to have senior like Dr. Deep Chandra Joshi, Dr. Prativa Pramanik and Dr. Sayandeep Ghosh who helped me in various ways throughout my research work. I sincerely thank them for their selfless assistance and constant support. I would like to thank my lab mates Suchit, Shaona, Ravi, Dr. Priyanka Tiwari and my juniors Arpita, Harshita and Arijit for their help and pleasant company during my Ph.D. My special thanks to Harshita for checking the grammar and proofreading of my thesis. I acknowledge our lab intern students: Ayush, Shashank, Joya, Atyant, Shalini, Shourya, Rana, Debajyoti, Arjyama, Soham, Srishti, Aryan and Vedanth. I thank them all for the wonderful memories we shared at IITG.

I want to present my special thanks to Prof. B. Eraiah, Department of Physics, Bangalore University for his support and teaching during my M.Sc. Next, I would like to express my sincere gratitude to Prof. R. Hanumantharayappa for teaching a good mathematics during my B.Sc., which is now helping in my physics life. Further, I express my sincere thanks to Prof. Prabhu Kumar and Prof. C. S. Somashekaraiah for teaching physics during my bachelors. I want to express my special thanks to all my teachers during masters, bachelors and schooling, whose teaching at different stages of education helped me in all the means to bring me to this position.

Maruthi R
IIT Guwahati, India
16th March 2023

Contents

List of Figures

Chapter-3

Chapter-5

Chapter-6

Chapter-7

List of Tables

List of Abbreviations and Symbols

XRD – X-ray diffraction
XPS – X-ray Photoelectron spectroscopy
QCP – Quantum critical point
BE – Binding Energy
T_C – Ferromagnetic Curie temperature
T_N – Anti-ferromagnetic Néel temperature
T_{FN} – Ferrimagnetic Néel temperature
E_g – band gap energy
h – hours
ZFC – Zero-Field Cooled
FC – Field Cooled
FM – Ferromagnet
AFM – Anti-ferromagnet
FiM – Ferrimagnet
Å – Angstrom
χ – Magnetic susceptibility
K – Kelvin
M – Magnetization
H – Magnetic field
T – Temperature
μ_B – Bohr magnetron
XPS – X-ray Photoelectron spectroscopy

Chapter 1

Introduction and Importance of Columbites

1.1. Background and Motivation

In 16th century, for the first time, "Columbites" were discovered in Connecticut, USA. Columbites are high-density materials with a metallic lustre and also a key ore of niobium and tantalum. Columbites are at greater importance because of their unique magnetic properties and large commercial demand in the industrial sector. Their physical properties have been used extensively in the field of mobile and satellite communications as dielectric resonators, microstrip antennas, wave guides, including in solid oxide fuel cells, supercapacitors, mechanical filter coatings, and electrochemical gas sensors [1-7]. Moreover, columbites exhibits interesting novel magnetic properties like quantum critical behaviour, field-induced magnetic transitions, and tri-critical behaviour [8-12]. These compounds are the best real examples of some of the ideal theoretical models. In the present era the quest for real systems in condescend matte physics whose measured properties can be readily applied to check the predictions of theoretical-models in solid-state physics and materials science is very much needed these days because such assessments deliver boundless insight into the underlining physics of nano/microscopic world. One such latest Quantum phenomena are the predictions of Quantum critical oscillations/excitations at Quantum-critical-point, which have been successfully observed recently in Ferromagnetic Ising-chain and Heisenberg-chain columbites such as $CoNb_2O_6$ and $NiNb_2O_6$, respectively [8,10].

Among the family of columbites, $CoNb_2O_6$ and $NiNb_2O_6$ are treated as important compounds because they behave as a quantum magnet near absolute zero temperature. This is mainly due to the strong ferromagnetic interactions along their spin-chain axis leading to reduced magnetic dimensions [8,10]. The Quantum spin dynamics near Quantum critical point in the quasi-one-dimensional $CoNb_2O_6$ system predicts the exotic dynamic E_8-spectrum consists of eight particles, which emphasizes the importance of columbites [13,14]. Moreover, these compounds are explored in high temperature thermoelectric applications and also considered as the best suitable dielectric materials for space applications. On the other hand, zinc niobate, $ZnNb_2O_6$ exhibits the highest relative-dielectric permittivity ε_r = 25 with high quality factor $Q \times F$ = 83700 GHz followed by $MnNb_2O_6$ shows ε_r = 20-22 [15,16]. The impedance spectroscopy studies reveal the approximate ionic conductivity of 6.0×10^{-5} ohm^{-1} cm^{-1} in off-stoichiometric $MnNb_2O_{6-\delta}$, however the same material annealed in the presence of hydrogen shows four times higher conductivity compared to pure stoichiometric $MnNb_2O_6$ system [17,18]. Furthermore, the columbites like $NiNb_2O_6$ and $MgNb_2O_6$ shows a good catalytic properties in the water splitting process for the generation of hydrogen gas [16]. Normally, columbites are stable in orthorhombic crystal structure with general chemical formula AB_2O_6 (A = Co, Mn, Ni, Fe, Ca, Zn, Cu, Mg, etc. and B = Nb, Ta) with space group *Pbcn*-D_{2h}^{14}. In the B site tantalum series, $MnTa_2O_6$ is the only system which exhibits columbite structure, and all the other system crystalizes in to rutile structure [19-26]. Here the A site divalent cation is magnetic, but the cation at B-site is non-magnetic with a pentavalent electronic state, both are surrounded by six oxygen atoms forming an AO_6 and BO_6

octahedra [21,23]. These octahedra forms an independent zig-zag chain along the *c*-axis, with a unique alternate arrangement of -A-B-B-A-B-B-A- along the *a*-axis. Further the A site magnetic atoms form an isosceles triangular lattice in *ab*-plane [19,21,23]. In general, a single orthorhombic unit cell consists of four A-site atoms occupying the 4*c* Wyckoff position, with eight B site atoms and 24 oxygen atoms occupying the 8*d* Wyckoff position representing four molecular formulas [20,27,28]. In the present research work we mainly focus on the synthesis, structural characterization, mapping the complete *H-T* phase diagram, estimation of critical exponents and the determination of exchange constants in these columbites. These aspects are precisely explained in this chapter along with some basic fundamental concepts and theoretical models related to above mentioned characteristic features, essentially, different types of exchange interactions acting between the magnetic atoms present in the columbite lattice have been discussed. A brief explanation of the Heisenberg and Ising models, along with necessary mathematical expressions, were provided in this chapter in subsections 1.4.1 and 1.4.2 Furthermore, the complete molecular field theory of both ferromagnetism and antiferromagnetism is included in this chapter. Finally, we end this chapter with a complete description of the research problem undertaken along with the methodology and work plan. Key insights into some of the critical physical phenomena that inspired us to conduct the current research work and the organization of the thesis are given at the end of this chapter.

1.2. Molecular field theory

1.2.1. Molecular field theory of Ferromagnetism

In ferromagnetic materials, the atomic dipole moments align parallelly, even in the absence of an external magnetic field this leads to spontaneous magnetization, which means that there exists a finite net magnetic moment in zero external field (Fig. 1.1). Further, as the thermal energy exceeds a certain critical temperature known as Curie temperature (T_C), the thermal excitations destroy the long-range ordering of dipoles leading to paramagnetic state which results in the loss of spontaneous magnetization. To explain this magnetization Weiss made the first assumption that there is a presence of a strong internal magnetic or molecular field in the specimen which is responsible for the spontaneous magnetization. However, some of the ferromagnetic substances may not show magnetization in the presence of zero external field even though they have spontaneous magnetization property, but produces a large magnetization after the application of a small external field. To explain this phenomenon, Weiss made a second assumption and postulated the Domain theory. According to this theory, the ferromagnetic specimen consists of a large number of spontaneously magnetized small regions called “Domains”. The direction of each domain magnetization is not required to be parallel, but the net magnetization of the entire sample must be the vector sum of the magnetization of each individual domain. The chances of net magnetization may be zero, but a very small external field causes large magnetization because of the reorientation of domains [29].

According to Weiss’s first assumption, the internal magnetic field H_M is directly proportional to magnetization M (popularly known as spontaneous magnetization); hence one can express H_M as [30,31],

$$H_M = C_M M \tag{1.1}$$

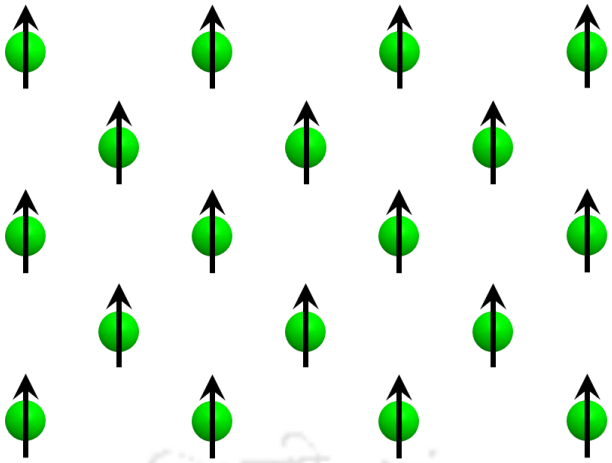

Fig. 1.1. Schematic representation of the Ferromagnetic arrangement of magnetic moments.

In equation (1.1), C_M is termed as Weiss molecular field constant. When an external magnetic field H_{ex} is applied to the system all the magnetic dipole interacts with H_{ex}, then the effective field H_{eff} on the dipole can be expressed as,

$$H_{\text{eff}} = H_{\text{ex}} + C_{\text{M}}M \tag{1.2}$$

Since the atoms in the specimen possess a total angular momentum J, then, the total magnetization of the specimen in the temperature region can be expressed in terms of the Brillouin function as given below.

$$M = ng\mu_{\text{B}}J\, B_J(z) \tag{1.3}$$

$$B_J(z) = \frac{2J+1}{2J}\coth\left(\frac{2J+1}{2J}z\right) - \frac{1}{2J}\coth\left(\frac{Z}{2J}\right) \tag{1.4}$$

$$z = \frac{Jg\mu_{\text{B}}H}{k_{\text{B}}T} \tag{1.5}$$

Here $B_J(z)$ is termed as Brillouin function with number of atoms per unit volume as n. In equation (1.5), H is replaced by H_{eff},

$$z = \frac{Jg\mu_{\text{B}}}{k_{\text{B}}T}(H_{\text{ex}} + C_{\text{M}}M) \tag{1.6}$$

(i) $T < T_C$: To estimate the spontaneous magnetization, let us assume $H_{ex} = 0$ then equation (1.6) reduces to,

$$z = \frac{Jg\mu_{\text{B}}C_{\text{M}}M}{k_{\text{B}}T} \tag{1.7}$$

$$M(T) = \frac{zk_{\text{B}}T}{Jg\mu_{\text{B}}C_{\text{M}}}. \tag{1.8}$$

In the limit of absolute zero, $B_J(z)$ tends to 1 because z tends to infinity. This signifies the saturation magnetization $M_S(0)$ and the equation (1.3) can be simplified as below,

$$M_S(0) = ng\mu_{\text{B}}J \tag{1.9}$$

dividing equation (1.3) by equation (1.9),

$$\frac{M(T)}{M_S(0)} = B_J(z) \tag{1.11}$$

and again, from equation (1.8) and equation (1.9),

$$\frac{M(T)}{M_S(0)} = \frac{k_B T}{n C_M J^2 g^2 {\mu_B}^2} z \tag{1.12}$$

At a specific temperature, the magnitudes of the relative magnetization $\frac{M(T)}{M_S(0)}$ can be estimated graphically through the intersection of two equations (1.11) and (1.12) (as shown in the Fig. 1.2), because both simultaneously satisfy $\frac{M(T)}{M_S(0)}$. The straight lines of equation (1.12) are drawn in the Fig. 1.2 at various temperatures to investigate the nature of the results (magnetic ordering). Moreover, the temperature at which the straight line corresponds to a tangent of the Brillouin function at the origin represents the critical temperature. For relatively less than this temperature there exists the two intersection values one is at origin and the other has a non-zero value of $\frac{M(T)}{M_S(0)}$ (at point Q in Fig. 1.2). This non-zero value signifies the spontaneous magnetization and it is stable below the critical temperature. Above this temperature there will be only one intersection at the origin i.e. $\frac{M(T)}{M_S(0)} = 0$, where the spontaneous magnetization disappears. Thus, this critical temperature is termed as ferromagnetic Curie temperature, T_C. In the limit of z tends to zero the slope of $B_J(z)$ essentially equal to the slope of the straight line of equation (1.12) at $T = T_C$, we obtain the relation between Curie temperature and Weiss molecular field constant as,

$$T_C = \frac{n g^2 {\mu_B}^2 J(J+1)}{3 k_B} C_M \tag{1.13}$$

(*ii*) $T > T_C$: In the paramagnetic region there will be no spontaneous magnetization, but when the magnetic field ($H_{ex} \neq 0$) is applied, the magnetization is produced, and it is given by equation (1.3) with a linear approximation of Brillouin function which is given as below:

$$M = \frac{n g \mu_B (J+1)}{3} z. \tag{1.14}$$

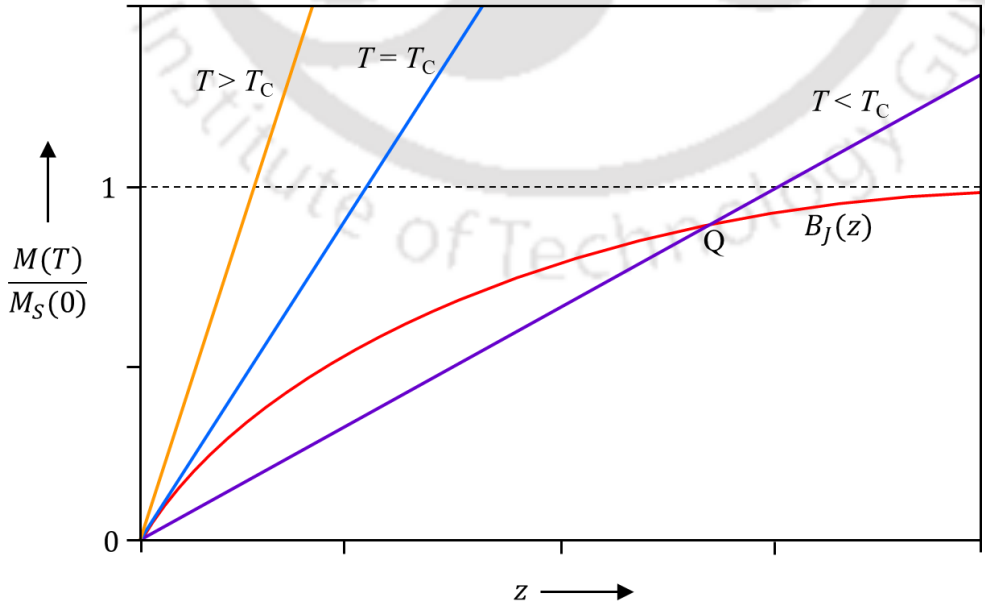

Fig. 1.2. Graphical solution of Eqs. (1.11) and (1.12). The intersection of the two curves give the spontaneous magnetization at temperature $T < T_C$. No solutions are obtained for $T \geq T_C$.

Using equation (1.6) for z and solving for $\chi = M/H$, above equation yields the Curie Weiss law,

$$\chi = \frac{M}{H} = \frac{C}{T - \theta} \tag{1.15}$$

with $C = \frac{ng^2\mu_B{}^2 J(J+1)}{3k_B}$ popularly known as Curie constant and $\theta = \frac{ng^2\mu_B{}^2 J(J+1)}{3k_B} C_M$ is the Curie-Weiss temperature [30].

1.2.2. Molecular field theory of Antiferromagnetism

The atomic dipoles in antiferromagnetic substances are strongly coupled in opposite directions, usually, these systems consist of two sublattices, where the spins of each sublattice are antiparallel to other with an identical magnetic moment. The collective behaviour of these spins shows an exact zero net magnetic moment at absolute zero in the absence of a magnetic field. Further, the magnetization increases gradually with the rise in temperature up to a certain peak temperature, known as Néel temperature (T_N) later it decreases by following the Curie-Weiss law in the disordered paramagnetic region. In 1932 for the first time Louis Néel developed the theory of antiferromagnetism using the concept of the Weiss molecular field approach [30]. Let us consider a simple model of two-dimensional spin arrangements with X and Y interpenetrating sublattices as shown in Fig. 1.3. Here using the same molecular field theory, the internal molecular field ($\boldsymbol{H}_{MX}$) acting on a spin site in X sublattice can be written as [30,32],

$$\boldsymbol{H}_{MX} = -C_{XY}\boldsymbol{M}_Y - C_{XX}\boldsymbol{M}_X \tag{1.16}$$

where C_{XY} and C_{XX} represents the molecular field constants of nearest and next nearest neighbour interactions, respectively. $\boldsymbol{M}_X$ and $\boldsymbol{M}_Y$ are the sublattice magnetizations of X and Y sublattices, respectively. Similar situation is valid for the Y sublattice as well and the internal molecular field $\boldsymbol{H}_{MY}$ can be expressed as below.

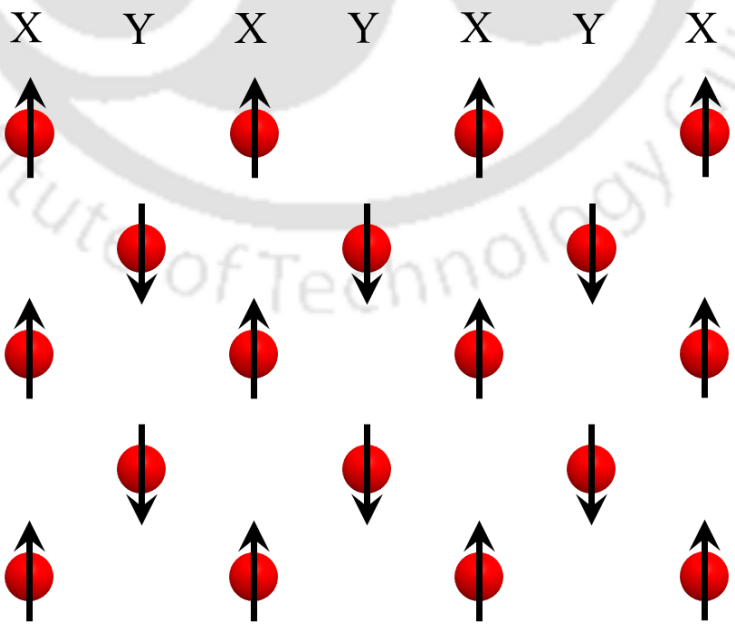

Fig. 1.3. Schematic representation of **a**ntiferromagnetic arrangement of magnetic moments with X and Y interpenetrating sublattices.

$$\boldsymbol{H}_{\mathrm{MY}} = -C_{\mathrm{YX}}\boldsymbol{M}_{\mathrm{X}} - C_{\mathrm{YY}}\boldsymbol{M}_{\mathrm{Y}} \tag{1.17}$$

In the present model we considered the atoms of the same type in both X and Y sublattices, so $C_{\mathrm{XX}} = C_{\mathrm{YY}} = C_{ii}$ and $C_{\mathrm{XY}} = C_{\mathrm{YX}}$ (can be treated as positive in nature). When an external magnetic field $\boldsymbol{H}$ is applied, the total magnetic fields $\boldsymbol{H}_{\mathrm{X}}$ and $\boldsymbol{H}_{\mathrm{Y}}$ acting on acting on X and Y spin-site sublattices can be formulated as formulated as,

$$\boldsymbol{H}_{\mathrm{X}} = \boldsymbol{H} - C_{\mathrm{XY}}\boldsymbol{M}_{\mathrm{Y}} - C_{ii}\boldsymbol{M}_{\mathrm{X}} \tag{1.18}$$

$$\boldsymbol{H}_{\mathrm{Y}} = \boldsymbol{H} - C_{\mathrm{XY}}\boldsymbol{M}_{\mathrm{X}} - C_{ii}\boldsymbol{M}_{\mathrm{Y}} \tag{1.19}$$

(*i*) $T > T_{\mathrm{N}}$: In the presence of an external magnetic field $\boldsymbol{H}$ there will be a small magnetization in the paramagnetic region. By considering the first term of Brillouin function, $B_{\mathrm{S}}(z) = [(S+1)/3S]z$ and by using equation (1.3) the magnetization of the sublattices can be written as,

$$M_{\mathrm{X}} = \frac{ng^2{\mu_{\mathrm{B}}}^2 S(S+1)}{6k_{\mathrm{B}}T} H_{\mathrm{X}} \tag{1.20}$$

$$M_{\mathrm{Y}} = \frac{ng^2{\mu_{\mathrm{B}}}^2 S(S+1)}{6k_{\mathrm{B}}T} H_{\mathrm{Y}} \tag{1.21}$$

and

$$H_{\mathrm{X}} = |\boldsymbol{H}_{\mathrm{X}}|\,; \;\; H_{\mathrm{Y}} = |\boldsymbol{H}_{\mathrm{Y}}|$$

On substituting the values of H_{X} and H_{Y} the equations (1.20) and (1.21) become,

$$M_{\mathrm{X}} = \frac{ng^2{\mu_{\mathrm{B}}}^2 S(S+1)}{6k_{\mathrm{B}}T}(H - C_{\mathrm{XY}}M_{\mathrm{Y}} - C_{ii}M_{\mathrm{X}}) \tag{1.22}$$

$$M_{\mathrm{Y}} = \frac{ng^2{\mu_{\mathrm{B}}}^2 S(S+1)}{6k_{\mathrm{B}}T}(H - C_{\mathrm{XY}}M_{\mathrm{X}} - C_{ii}M_{\mathrm{Y}}) \tag{1.23}$$

Adding the equations (1.22) and (1.23) for net magnetization,

$$M = M_{\mathrm{X}} + M_{\mathrm{Y}} \tag{1.24}$$

$$M = \frac{ng^2{\mu_{\mathrm{B}}}^2 S(S+1)}{6k_{\mathrm{B}}T}[2H - C_{\mathrm{XY}}(M_{\mathrm{X}} + M_{\mathrm{Y}}) - C_{ii}(M_{\mathrm{X}} + M_{\mathrm{Y}})]$$

$$M = \frac{ng^2{\mu_{\mathrm{B}}}^2 S(S+1)}{6k_{\mathrm{B}}T}[2H - (C_{\mathrm{XY}} + C_{ii})M] \tag{1.25}$$

solving for $\chi = M/H$, the above equation yields the Curie Weiss law,

$$\chi = \frac{M}{H} = \frac{C}{T - (-\theta)} \tag{1.26}$$

where, $C = \frac{ng^2{\mu_{\mathrm{B}}}^2 S(S+1)}{3k_{\mathrm{B}}}$ and $\theta = \frac{ng^2{\mu_{\mathrm{B}}}^2 S(S+1)}{6k_{\mathrm{B}}}(C_{\mathrm{XY}} + C_{ii})$.

(*ii*) $T < T_{\mathrm{N}}$: Below T_{N} there exists a magnetic ordering where both the sublattices show spontaneous magnetization in zero field condition. In the vicinity of T_{N} both the equations (1.22) and (1.23) are still effective since the saturation effects do not play a significant role. Thus, using these equations with $H = 0$, the sublattices magnetization can be written as,

$$M_{\mathrm{X}} = \frac{C}{2T}(-C_{\mathrm{XY}}M_{\mathrm{Y}} - C_{ii}M_{\mathrm{X}}) \tag{1.27}$$

$$M_{\mathrm{Y}} = \frac{C}{2T}(-C_{\mathrm{XY}}M_{\mathrm{X}} - C_{ii}M_{\mathrm{Y}}) \tag{1.28}$$

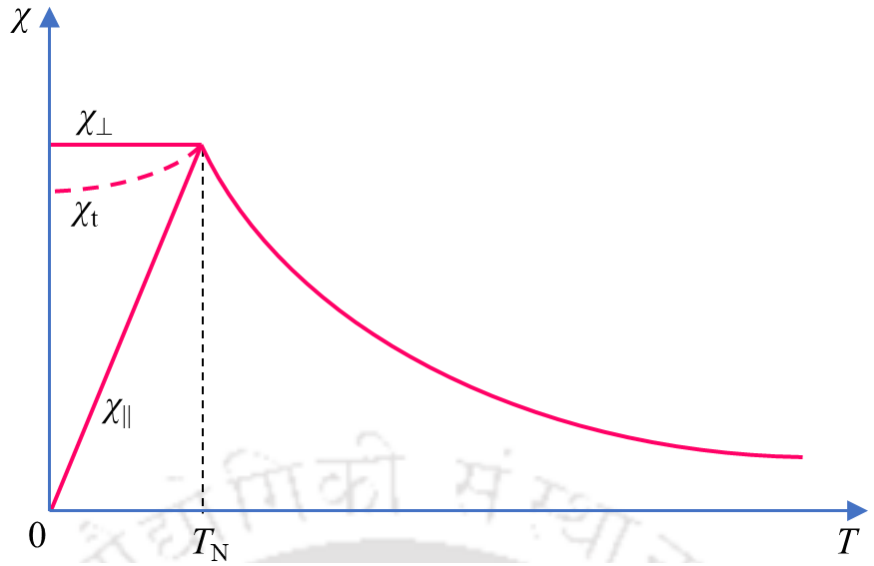

Fig. 1.4. Temperature dependent magnetic susceptibility χ (T) of the antiferromagnetic material. The anomaly in the curve represents the Néel temperature T_N. If the magnetic field is applied parallel to the easy axis, then $\chi_\perp$ and $\chi_{||}$ represents the perpendicular and parallel susceptibility, respectively. The susceptibility χ_t of a polycrystalline antiferromagnet will be a combination of both.

Equating the determinant of the coefficients of M_X and M_Y to zero we get,

$$T_N = \frac{C}{2}(C_{XY} - C_{ii}) \tag{1.29}$$

Substituting C in terms of θ we arrive at the ratio,

$$\frac{T_N}{\theta} = \frac{C_{XY} - C_{ii}}{C_{XY} + C_{ii}} \tag{1.30}$$

If $C_{ii} = 0$ then $T_N = \theta$ and if $C_{ii} > 0$ then $T_N < \theta$. Further, if $C_{ii} >> C_{XY}$, then the two sublattice model becomes unstable. More often, polycrystalline samples are used in magnetic measurements, and usually the easy axes of the crystallites are randomly aligned. If an applied field makes an angle Φ with the easy direction of one

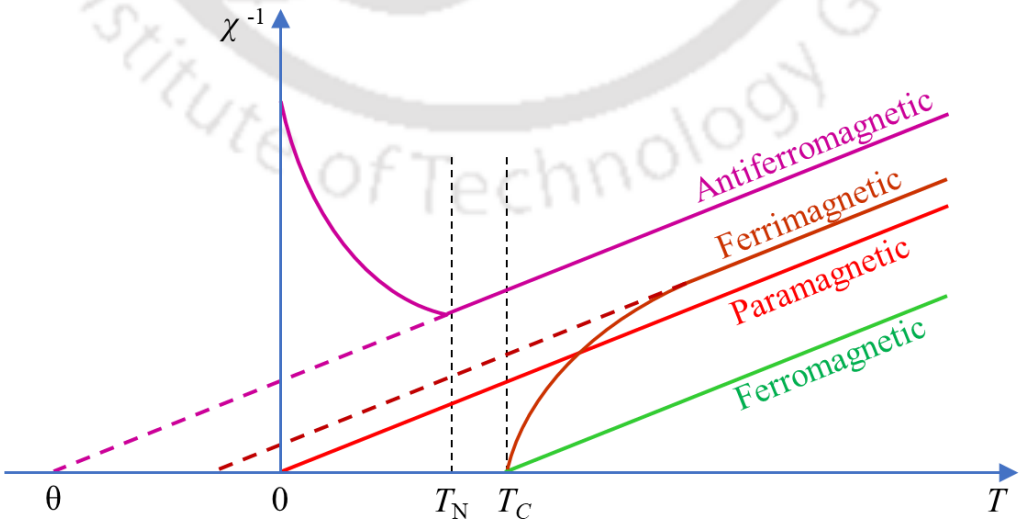

Fig. 1.5. Temperature dependence of inverse susceptibilities (χ^{-1}) of paramagnetic (PM), ferromagnetic (FM), antiferromagnetic (AFM) and ferrimagnetic (FiM) materials.

of the crystallites, then we can separate parallel ($\chi_{||}$) and perpendicular ($\chi_{\perp}$) susceptibilities to the easy axis. As the temperature decreases below T_N, $\chi_{||}$ gradually reduces to zero where as $\chi_{\perp}$ remains constant and it is temperature independent as shown in Fig. 1.4. The total susceptibility χ_t of the polycrystalline sample can be expressed as,

$$\chi_t = \frac{1}{3}\chi_{||} + \frac{2}{3}\chi_{\perp} \tag{1.31}$$

Furthermore, the temperature variation of inverse magnetic susceptibility for all the types of magnetic systems has been graphically depicted in Fig. 1.5 [33].

1.3. Magnetic Exchange interactions

This section deals with the different types of magnetic interactions that occur in magnetic materials. Typically, these interactions allow the magnetic moments to communicate with each other and produce long-range magnetic order. The alignment of moments, either parallel or antiparallel with their neighbours, purely depends on the energetically favourable structure of the magnetic substances. Magnetic interactions mostly fall into two categories; (*i*) Magnetic dipolar interaction and (*ii*) Magnetic Exchange interaction. Usually magnetic dipolar interactions are very weak to explain the magnetic ordering of systems, but they are very important to account for the properties of those having milli Kelvin ordering temperatures. In the majority of magnetic materials exchange interactions describe the complete magnetic ordering, hence we dedicated this section to magnetic exchange interaction. To understand this let us consider a simple model having two electrons in a similar potential field with spatial co-ordinates $\boldsymbol{r}_1$ and $\boldsymbol{r}_2$, respectively. Let $\psi_1(\boldsymbol{r}_1)$ and $\psi_2(\boldsymbol{r}_2)$ be the individual electron's state giving rise to a joint wave function $\psi(\boldsymbol{r}_1, \boldsymbol{r}_2) = \psi_1(\boldsymbol{r}_1)\psi_2(\boldsymbol{r}_2)$. However, it does not represent the total spatial wavefunction of two electrons system because of their indistinguishability and exchange symmetry behaviour. Further, the exchange of two electrons provides the same electron density i.e. $|\psi(\boldsymbol{r}_1, \boldsymbol{r}_2)|^2 = |\psi(\boldsymbol{r}_2, \boldsymbol{r}_1)|^2$ and for fermionic systems $\psi(\boldsymbol{r}_1, \boldsymbol{r}_2) = -\psi(\boldsymbol{r}_2, \boldsymbol{r}_1)$. The total wavefunction $\boldsymbol{\Psi}$ is the product of both spatial and spin wavefunction. Particularly for electrons, the total wavefunction should be antisymmetric, for a two-electron system, there are two possibilities (*a*) For *S* = 0, an antisymmetric singlet spin state (χ_S) with a symmetric spatial state, and (*b*) For *S* = 1, a symmetric triplet spin state (χ_T) with an antisymmetric spatial state. Therefore, the total wavefunction for the singlet ($\boldsymbol{\Psi}_S$) and triplet ($\boldsymbol{\Psi}_T$) states can be written as [31];

$$\boldsymbol{\Psi}_S = \frac{1}{\sqrt{2}}[\psi_1(\boldsymbol{r}_1)\psi_2(\boldsymbol{r}_2) + \psi_1(\boldsymbol{r}_2)\psi_2(\boldsymbol{r}_1)]\chi_S \tag{1.32}$$

$$\boldsymbol{\Psi}_T = \frac{1}{\sqrt{2}}[\psi_1(\boldsymbol{r}_1)\psi_2(\boldsymbol{r}_2) - \psi_1(\boldsymbol{r}_2)\psi_2(\boldsymbol{r}_1)]\chi_T \tag{1.33}$$

If the states $\boldsymbol{\Psi}_S$ and $\boldsymbol{\Psi}_T$ are normalized then the energies of the corresponding states are,

$$E_S = \int \boldsymbol{\Psi}_S^* \hat{H} \boldsymbol{\Psi}_S d\boldsymbol{r}_1 d\boldsymbol{r}_2 \tag{1.34}$$

$$E_{\mathrm{T}} = \int \boldsymbol{\Psi}_{\mathrm{T}}^{*}\, \hat{H} \boldsymbol{\Psi}_{\mathrm{T}} d\boldsymbol{r}_1 d\boldsymbol{r}_2 \tag{1.35}$$

For a singlet state $\boldsymbol{S}_1.\boldsymbol{S}_2 = -\frac{3}{4}$ and for a triplet state $\boldsymbol{S}_1.\boldsymbol{S}_2 = \frac{1}{4}$, then the effective Hamiltonian can be written as,

$$\hat{H} = \frac{1}{4}(E_{\mathrm{S}} + 3E_{\mathrm{T}}) - (E_{\mathrm{S}} - E_{\mathrm{T}})\boldsymbol{S}_1.\boldsymbol{S}_2 \tag{1.36}$$

The exchange constant, J is defined as,

$$J = \frac{E_{\mathrm{S}} - E_{\mathrm{T}}}{2} = \int \psi_1^{*}(\boldsymbol{r}_1)\psi_2^{*}(\boldsymbol{r}_2)\hat{H}\,\psi_1(\boldsymbol{r}_2)\psi_2(\boldsymbol{r}_1) d\boldsymbol{r}_1 d\boldsymbol{r}_2 \tag{1.37}$$

The spin-dependent effective Hamiltonian is

$$\hat{H}_{\mathrm{Spin}} = -2J\, \boldsymbol{S}_1.\boldsymbol{S}_2 \tag{1.38}$$

Here $\boldsymbol{S}_1$ and $\boldsymbol{S}_2$ are the spin operators similar to Pauli spin matrices and J has the dimensions of energy, usually it can be written as J/K_{B} in the units of kelvin (K). If $J > 0$, it implies that $E_{\mathrm{S}} > E_{\mathrm{T}}$ and favours the triplet state ($S = 1$). Particularly, this indicates the ferromagnetic interaction through the parallel alignment of two spins. Similarly, if $J < 0$, $E_{\mathrm{S}} < E_{\mathrm{T}}$ favouring the singlet state ($S = 0$) with antiferromagnetic interaction. The equation (1.38) holds good only for a two-electron system but generalizing it to many body system is more difficult. However, it can be generalised to estimate the nearest neighbour exchange constant in many body system as proposed by Heisenberg Hamiltonian;

$$\hat{H} = -\sum_{ij} J_{ij}\, \boldsymbol{S}_i.\boldsymbol{S}_j \tag{1.39}$$

In equation (1.39), J_{ij} is the exchange constant between the i^{th} and j^{th} spins and the number 2 is omitted because the summation itself double counts each pair of spins. Equation (1.39) can be expressed in another way as,

$$\hat{H} = -2\sum_{i>j} J_{ij}\, \boldsymbol{S}_i.\boldsymbol{S}_j \tag{1.40}$$

where the condition $i > j$ avoids the double-counting and the number 2 returns to the equation. The sign and magnitude of J_{ij} decides the type of magnetic ordering in the materials. The positive sign of J_{ij} signifies the ferromagnetic (FM) state, whereas the negative sign of J_{ij} represents the antiferromagnetic (AFM) state. In case when $J_{ij} = 0$, indicates randomly orientation of the spins with no exchange interactions, corresponds to the paramagnetic (PM) state. The exchange interactions are mainly classified into direct and indirect exchange interactions.

1.3.1. Direct exchange

In the direct exchange interaction, the localized electrons in the neighbouring magnetic ions couple with each other via exchange interaction without any intermediate atoms. This type of exchange interaction usually occurs in 3*d*-transition metals through a direct overlap of extended *d* orbitals as shown in Fig. 1.6. The sign of the direct exchange interaction mainly depends on orbital occupancy and interatomic spacing. Usually, the antiferromagnetic (AFM) exchange interaction is achieved only when the *d* orbitals are half-

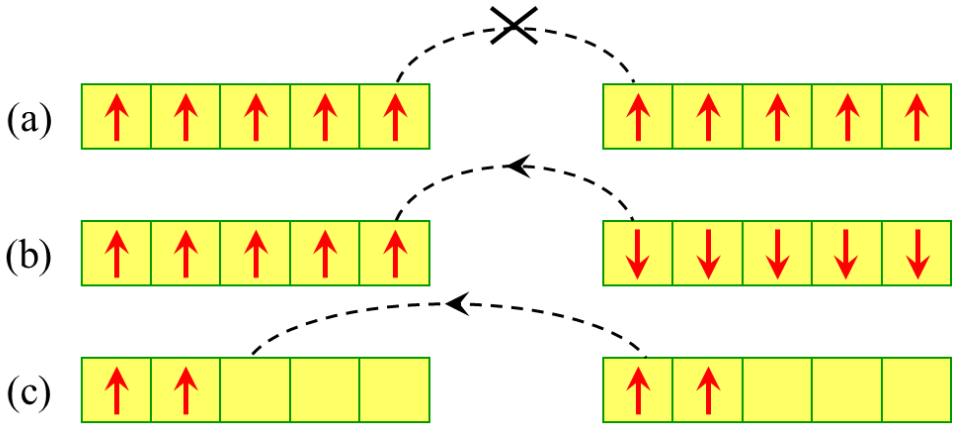

Fig. 1.6. Electron delocalization in *d* orbitals which are (a) and (b) half-filled, (c) nearly filled.

filled with oppositely aligned to the neighbouring *d* orbitals, as shown in Fig. 1.6(b). Whereas, the configuration shown in Fig. 1.6(a) is not permissible because of a violation of Hund's rule. On the other hand, ferromagnetic (FM) exchange interaction takes place in partly filled *d* orbitals because of the hopping of similarly polarized electrons into neighbouring empty states, as shown in Fig. 1.6(c). This provides the explanation for the AFM nature of manganese and chromium and also the FM behaviour of nickel, cobalt and iron [34].

1.3.2. Indirect exchange

Indirect exchange interactions occur via the overlap of electronic wave functions of two magnetic atoms through the wave functions of intermediate atoms. The most relevant indirect exchange interactions are superexchange, RKKY exchange, and double exchange; here we focus only on superexchange since it is related to our thesis work. Superexchange interaction occurs when the non-neighbouring magnetic ions are communicated through a non-magnetic ion that is sandwiched between the magnetic ions. This theory was proposed and developed by Kramers and Anderson, which is illustrated in Fig. 1.7 for AFM interactions by considering two divalent Mn and one O ions. If we consider the four-electron model which consists of one

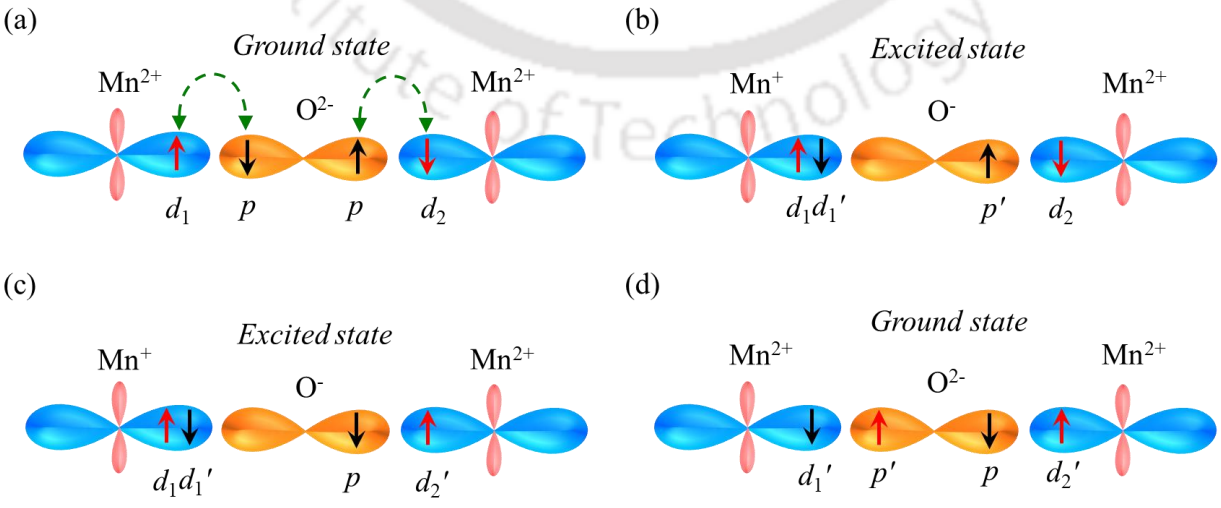

Fig. 1.7. Schematic representation of various steps of AFM Superexchange interaction.

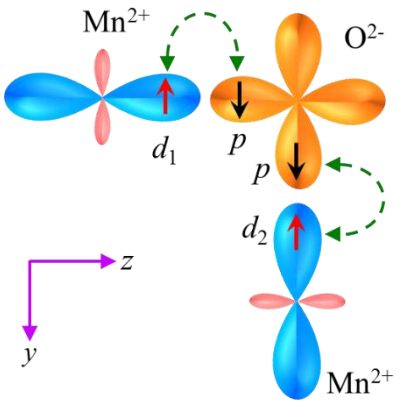

Fig. 1.8. Schematic representation of FM Superexchange interaction.

electron in each ground state (d_1 and d_2) of Mn^{2+} ion and two electrons in p orbitals of O^{2-} ion as shown in Fig. 1.7(a). Due to the overlap of the orbitals there is some probability of transferring of one of the electrons in the oxygen p orbital to either of the Mn^{2+} ions, as represented in Fig. 1.7(b). The electron transfer leads to an excited state, further, the electron coupling takes place between d_1 and d_1' sates in Mn^{2+} ion. Simultaneously, the remaining electrons in the O^{2-} ion couple with the d_2 states of other manganese ion, such complete exchange interaction between the magnetic ions is shown in the Fig. 1.7(c) and Fig. 1.7(d) via electron transfer. Usually, AFM exchange interactions occur when the metal-oxygen-metal (M-O-M) bond makes a 180º angle, and for FM exchange interactions M-O-M should be 90º as illustrated in Fig. 1.8 [30].

1.4. Spin-Chain models

In general, the magnetically isolated one-dimensional spin arrangement is commonly known as a one-dimensional (1D) model, frequently referred to as Spin-Chain system. Mostly, real materials are in three dimensions, but they can be thought of as Quasi-one-dimensional systems if the magnetic interactions are sufficiently strong in one particular direction relative to the other two directions. In an array of spins, if the spin aligns either parallel (||) or antiparallel (⊥) to a specific reference direction, then it is termed as Ising spin-chain. Further, if the spins are fixed in a plane, it gives an XY spin-chain and if the orientation is arbitrary, it is a Heisenberg spin chain. Moreover, the low dimension, along with the low-spin and frustration, causes the quantum fluctuations that result in novel magnetic ground state properties, which opens a new field called Quantum magnetism [35].

1.4.1. Heisenberg model

Werner Heisenberg developed this model, which has been vividly used to explore the magnetic properties mainly in phase transitions and critical point studies [36,37]. This model can be applied to any spin lattice dimension in both quantum and classical regimes. Mathematically, the isotropic Heisenberg Hamiltonian for nearest neighbour interactions can be written as,

$$H = -J \sum_{ij} \boldsymbol{S}_i . \boldsymbol{S}_j \qquad (1.41)$$

If the systems have anisotropy in all the spin dimensions (n =3), then the equation (1.41) can be expressed as below.

$$H_{XYZ} = \sum_{i=1}^{N} [J_x S_i^x S_{i+1}^x + J_y S_i^y S_{i+1}^y + J_z S_i^z S_{i+1}^z] \tag{1.42}$$

In the above expression N represents the total number of spins. Depending on the spin dimensions (n) we can reduce the above Hamiltonian into many special cases. Starting with n = 1 and $J_x \neq 0, J_y = 0, J_z = 0$, we arrive Ising model; for n = 2, and $J_x \neq J_y \neq 0, J_z = 0$, we arrive XY model; for n = 3, and $J_x = J_y = J_z = J$ we arrive isotropic Heisenberg model or XXX model further for $J_x = J_y = J_{xy} \neq 0, J_z \neq 0$ we arrive XXZ model [38].

Usually, when the spins are large enough, the quantum mechanical spin operators are replaced by the classical spin vectors. Henceforth, the classical Heisenberg spin chain can be expressed as [39],

$$H = -2J \sum_{-\infty}^{+\infty} \vec{S}_i \vec{S}_{i+1} = -2JS^2 \sum_{-\infty}^{+\infty} \vec{q}_i \vec{q}_{i+1} \tag{1.43}$$

Here, $\vec{q}_i$ be the unit vector and the above Hamiltonian yields zero-field susceptibility as,

$$\chi = \frac{C}{T} \sum_{m=-\infty}^{m=+\infty} \langle \vec{q}_i \vec{q}_{i+m} \rangle \tag{1.44}$$

where C is the Curie constant and $\langle \vec{q}_i \vec{q}_{i+m} \rangle = \Gamma^m$ is the correlation function between nearest neighbours. The equation (1.44) can be modified as,

$$\chi = \frac{C}{T} \sum_{m=-\infty}^{m=+\infty} \Gamma^m = \frac{C}{T} \left(\frac{1+\Gamma}{1-\Gamma} \right) \tag{1.45}$$

$$\text{and, } \Gamma = \coth\left(\frac{2JS^2}{k_B T}\right) - \left(\frac{2JS^2}{k_B T}\right)^{-1} \tag{1.46}$$

1.4.2. Ising model

Ising model is a simplest mathematical model of magnetic or thermodynamic systems. It provides an overview of phase transitions as well as how thermodynamic quantities behave across phase transitions. The 1D Ising model was exactly solved by Ernst Ising in 1925, and it's a simple model of ferromagnetism that exhibits no phase transition [40]. Later in 1944, Lars Onsager provided the solution for the two-dimensional Ising model and it is a basic model to show magnetic phase transition. Now let us assume that the spins are oriented along the z-axis (easy axis) for the time being. Then the corresponding Hamiltonian for Ising spin chain can be expressed as [39],

$$H = -2J \sum_{-\infty}^{+\infty} S_i^z S_{i+1}^z \tag{1.47}$$

$$H = -2JS^2 \sum_{-\infty}^{+\infty} \sigma_i \sigma_{i+1} = -J' \Sigma_i \sigma_i \sigma_{i+1} \tag{1.48}$$

where $J' = 2JS^2$ and $\sigma_i = \pm 1$. Ising model can also be treated as simplest classical model and the equation (1.44) and (1.45) are still valid when $\vec{q}_i$ is replaced by σ_i. The correlation length for this case is quantified as $\Gamma = \tanh\left(\frac{2JS^2}{k_B T}\right)$, and the equation (1.45) provides the parallel component of the susceptibility in the presence of magnetic field (along the z direction) as follows:

$$\chi_{||} = \frac{C}{T} e^{\left(\frac{4JS^2}{k_B T}\right)} \tag{1.49}$$

In the above expression *C* is the Curie constant. The perpendicular component of susceptibility remains constant and is significantly smaller than the parallel component.

1.5. Gaps-in the literature, motivation and description of the current research problem

The novel and peculiar magnetic properties of columbites, such as quantum phase transitions, quantum critical behaviour and spin flip/flop transitions, excited us to work on this system. These novel aspects mainly arise due to quantum fluctuations, low spin, geometrical frustration and degeneracy in the ground states. Furthermore, some of the columbites are considered as ideal candidates for the quasi 1D system as a result an exotic field called Quantum magnets is emerged recently. Also, wide range of industrial applications compelled us to conduct additional research on this system to explore their applications in field of both energy sector and mobile communications. Although there exists a literature on magnetic studies and the electrical properties of columbites, there are still many unexplored fields in this research domain present in the literature and we aim to fill such gaps with a meticulous study of their magnetic behaviour and dielectric properties so that one can easily understand the exact nature of magnetic behaviour and the link of crystallography on the exchange interaction paths in the columbite system. In this direction we have chosen the family of columbites like $MnNb_2O_6$, $MnTa_2O_6$, $CoNb_2O_6$ and $NiNb_2O_6$. Although we separately studied these systems in depth, special focus has been given to the $CoNb_2O_6$ system because there is close resemblance of Quasi-Ising-Spin-Chain nature of this system with the theoretically predicted Transverse-Field Ising chain (TFIC) model. Hence one can experimentally realize the TFIC model and it is considered as a unique development of direct correlation of theoretical Ising model with a practical system. Despite the fact that many researchers have reported on the ground state magnetic properties of $CoNb_2O_6$, yet we explored a completely new ground state spin configuration of this system using the standard magnetometry and determined the dominant exchange constants using different methods discussed in the forthcoming chapters. In particular, we accomplished such tasks with a detailed magnetic field and temperature dependence of magnetization. Further the magnetic studies on bulk polycrystalline columbites such as $MnNb_2O_6$ and $MnTa_2O_6$ are completely lacking in the literature except a brief study on the single crystals is discussed in the literature. Hence we under took this problem and successfully established a detailed magnetic phase diagram along with the accurate determination of exchange coupling strength in both the systems. The magnetic ground state properties, along with the complete mapping of the field-temperature (*H-T*) phase diagram are established at the end of each chapter which were completely absent in the literature when we started this research work. Moreover, accurate estimation of dominant magnetic interaction present in each system is really challenge task both from experimental and theoretical view point. Such analysis is

really needed to understand the magnetic structure of these compounds. Our high magnetic fields measurements from the National High Magnetic Field Laboratory (NHMFL), Tallahassee, Florida (USA), helped us immensely to determine the exact ground state of the system and unveil the new field-induced transitions in these compounds at T = 1.5 K. On the other hand, recent studies on $NiNb_2O_6$ reveal the rich magnetic behaviour including the existence of Quantum spin fluctuations at finite temperatures ($T \neq 0$) lead to the realization of Quantum critical region. Such unique features have drawn our interest and motivated us to investigate on this $NiNb_2O_6$ system. A meticulous study on the boundaries of different magnetic phases along with critical points provides the complete physical picture of this system. Another completely unexplored scientific talks in the field of colombites is the determination of critical exponents in the vicinity of magnetic ordering temperature and the magnetic entropy change across such spin order-disorder transitions. Such important gaps are filled in this thesis through a detailed temperature and field dependence of heat-capacity study which is the strong point of this Ph.D. thesis. Further, columbites are excellent dielectric materials because of their high commercial demand and wide variety of applications in the field of communication technology. These materials are low-cost, and they possess a high dielectric constant with a low loss factor. Therefore, dielectric studies on columbites are very essential, and there is currently very little literature available on this topic which motivated us to investigate their dielectric behaviour from liquid nitrogen to at high temperatures till (~500 K) in this current work. Such investigations are complemented by a meticulous study on the electronic transport mechanisms and the dielectric relaxation process on all investigated columbites. Such a detailed study was completely lacking in the literature when we initiated the research problem and our work perfectly fulfils such gaps in the literature appropriately. All the above described research objectives are extensively studied and presented in the coming chapters, yet in the below section we provide details of the organization of the current doctoral work.

1.6. Organisation of the thesis

The remaining portions of this thesis are structured as follows:

The chapter 2 provides a detailed explanation of the sample fabrication and characterization techniques.

The chapter 3 deals with the complete mapping of *H-T* phase diagram, exchange constants and specific-heat exponents of the Columbite antiferromagnet $MnNb_2O_6$.

In chapter 4, we mainly focus our studies on dielectric relaxation and the *ac*-electrical charge transport mechanism in the polycrystalline $MnNb_2O_6$ system.

The chapter 5 describes the detailed analysis of magnetic ground state properties along with the determination of the tricritical point and exchange interactions in the antiferromagnet $MnTa_2O_6$.

The chapter 6 deals with the synthesis and magnetic characterization of Ising chain ferromagnet $CoNb_2O_6$, mainly focuses on the exchange interactions and magnetic ground state.

In chapter 7, we primarily give emphasis on the spin-flip transitions, magnetic entropy and the estimation of tri-critical point in the antiferromagnet $NiNb_2O_6$ polycrystals.

Finally, chapter 8 presents the gaps-in the literature, motivation and description of the current research problem.

भारतीय प्रौद्योगिकी संस्थान गुवाहाटी
Indian Institute of Technology Guwahati

Chapter 2

Fabrication and Characterization Techniques

This chapter provides information related to the synthesis and characterization of the system under investigation: columbite niobates and tantalites. A detailed explanation of the experimental techniques employed in this work are clearly illustrated with the help of doodles along with a short summery about the basic theoretical concepts of each characterization technique. Brief working principle has also been discussed in this chapter. These techniques are mainly aimed to understand the crystal and electronic structure, dielectric behaviour and magnetic properties of the columbites.

2.1. Fabrication of Columbites

2.1.1. Solid-state reaction method

In the current doctoral thesis work, all the bulk polycrystalline columbite systems were prepared by the standard solid-state reaction (SSR) method. This SSR method involves mechanically mixing of the constituent binary metal oxides or carbonates followed by repeated grinding and heat treated at high temperatures. It is well known that the SSR method is thermodynamically stable process in which ions diffuses across the solid interface. Characteristic reaction time in SSR technique ranges from few days to few weeks and the heat-treatment involves very high temperatures (>1000°C) to overcome the diffusion barrier. In the present case, all the polycrystalline compounds: $CoNb_2O_6$, $MnNb_2O_6$, $MnTa_2O_6$, and $NiNb_2O_6$ were synthesized using the SSR method involving the following methodology. Stoichiometric amounts of commercially (from Alfa-Aesar GmbH) available high purity binary transition metal oxides have been selected as precursors. For the synthesis of above systems, we used the precursors Co_3O_4, MnO_2, NiO, Nb_2O_5 and Ta_2O_5. Appropriate amounts are weighed and grounded together using an agate mortar with pestle for 5 hours so that the oxides mixture become homogeneous. These mixed powders were pressed into cylindrical pellets of size ~ 13 mm in diameter using a KBr die set as mould and hydraulic press (50 kg/cm^2). These pellets were placed in an alumina boat and sintered at 1200°C for 24 hours in air with heating rate of ~ 5°C/minute and then slowly cooled down to room temperature naturally. High temperature sintering leads to the chemical decomposition and resulting in the uniform grain growth of the desired compounds. In order to achieve perfect homogenization, desired density and single phase of the compounds, we crushed the sintered pellets and re-grinded for 2 h and heat treated again at slightly higher temperatures as compared to the initial sintering temperature in air. After the final heat treatment process, all the compounds are characterized using various non-destructive techniques including the X-ray diffraction method so that one can identify the phase purity and crystal structure.

2.2. Characterization Techniques

In this section we covered the various characterisation methods used in the current thesis. Prior to discussing several other experimental procedures, we first discuss the structural characterization using X-ray diffraction measurements, including the microstructure/morphology using electron microscopy.

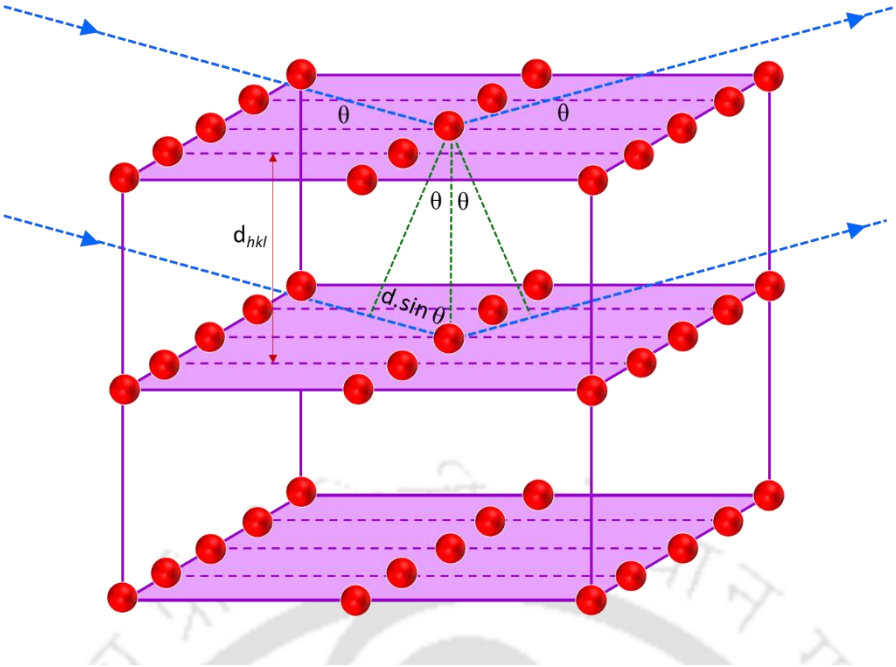

Fig. 2.1. Diagrammatic representation of the Bragg's law of X-ray diffraction.

2.2.1. Crystal Structure and Morphology

To examine the crystal structure of the system under investigation, we used the X-ray diffraction (XRD) technique. This non-destructive technique gives precise information about the unit cell sizes and interaxial angles of the understudied system. This technique also provides useful information about various structural properties of crystalline compounds such as micro-strain, grain-size, phase composition and defect structure. The XRD analysis is based on constructive interference of monochromatic X-rays after being reflected from the crystalline specimen. When an X-ray beam, generated by a cathode ray tube, is allowed to incident upon a crystal, the beam undergoes diffraction from the set of planes (Miller indices (hkl)), as the geometrical condition satisfies the Bragg's law: $2d_{hkl}\sin\theta = n\lambda$ [41]. Here 'd_{hkl}' is the inter-planer spacing between the set of (hkl) planes, θ is the Bragg's angle or Diffraction angle, 'n' is an integer and λ is the wavelength of X-ray radiation. Figure 2.1 shows the geometry of the Bragg's law for the X-ray diffraction from a set of crystallographic planes. The locus of the diffracted beams taken together from the different sets of planes is collectively known as the diffraction pattern of the crystal. In the present work we used a high-resolution X-ray diffractometer from Rigaku (Model: TTRAX-III) (18 kW rotating anode X-ray source) with Cu $K\alpha$ source radiation with λ = 1.5406 Å. In order to extract the detailed crystallographic information from the obtained diffraction pattern we performed the Rietveld refinement using the open source programs FullProf-Suite and Powder-cell [42,43]. On the other hand, to probe the surface morphology and microstructure of the samples investigated in the present work we employed a field emission scanning electron microscope (Gemini 500 FE-SEM) working under secondary-electron (SE) mode. This instrument is also equipped with energy dispersive X-ray spectrometer (EDS/EDAX) which is used to trace the elements present in the samples.

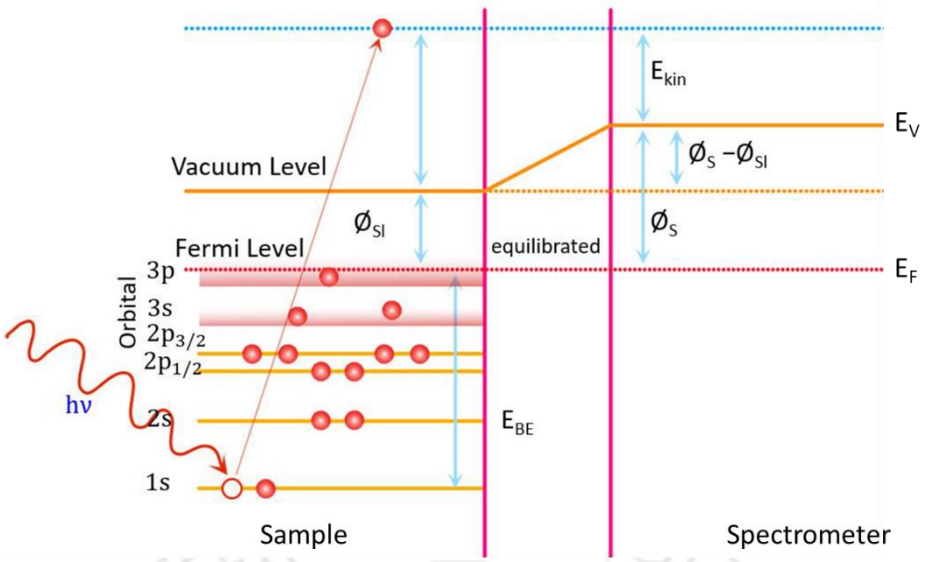

Fig. 2.2. Schematic energy level diagram showing the basic principle of the core-level photoelectron emission.

2.2.2. Electronic structure determination using the X-ray Photoelectron Spectroscopy

In the current thesis, the electronic states of the investigated samples were explored using x-ray photoelectron spectroscopy (XPS). XPS technique is one of the most powerful non-destructive surface sensitive characterization method used to determine the chemical and physical phenomenon occurring at surfaces of wide variety of compounds. XPS technique has gained attention by the scientific community mainly due to the following important reasons: (a) It can provide the quantifications of elemental composition from the solid surface up to a thickness less than ten nanometers, (b) It can also provide an insight to the chemical and atomic environment of the elements, (c) one can obtain the above information with relative ease and minimal sample preparation, (d) one can explore first few atomic layers and assign chemical states to the detected atoms. Since the mean free path of the electrons in any solid is very small, the detected electrons originated from the top few atomic layers provide important information which makes XPS a unique surface-sensitive technique for chemical analysis. In XPS, a monochromatic beam of soft X-rays (Mg Kα (1253.6 eV) and Al Kα (1486.6 eV)) are exposed to the surface of the sample which interact with the core-level electron and transfer its energy to the electron which leads to the emission of core-level electrons (popularly called as photoelectric effect). The recorded spectrum consists of the core-level photoelectron intensity detected per energy interval (on *y*-axis) plotted against their kinetic energy or Binding energy (on *x*-axis). Since each element has a unique characteristic photoelectron spectrum, different set of elements give a spectrum comprising of the intermixture of individual peaks of the constituent elements. The basic principle behind the XPS is Photoelectric effect in which electrically charged particles are released from the core of the material when it absorbs electromagnetic radiation as shown in Fig. 2.2. In the case of XPS, the interaction of soft X-rays with specimen leads to the photoemission process and its energy is analysed by the spectrometer. Generally, the X-rays are capable in knocking out the electrons not only from outer shells but also from the core levels. The emission of an electron from the 1*s* shell of an atom is schematically represented in Fig. 2.2. The kinetic energy of an ejected photoelectron (E_{KE}) is equivalent to the difference between x-ray photon energy ($h\nu$) and the binding energy of the core-level electron (E_{BE}).

Relation between these parameters and the work function of the spectrometer (Φs) is given by the below expression [44-46]:

$$E_{KE} = h\nu - E_{BE} - \Phi_{S1} - (\Phi_S - \Phi_{S1}) \quad (2.1)$$

$$E_{KE} = h\nu - E_{BE} - \Phi_S \quad (2.2)$$

In addition, the work function for the sample (Φ_{S1}) is defined as the difference between the energy of the Fermi level (E_F) and the energy of the vacuum level (E_V). E_V is the zero point of the electron energy scale:

$$\Phi_{S1} = E_F - E_V \quad (2.3)$$

Usually, Φ_S is determined from a detailed calibration for the spectrometer. From equation 2.3 it is clear that only binding energies lower than the excitation radiation (in the present case 1486.6 eV for Al Kα and 1253.6 eV for Mg Kα) can be probed. In addition to the photoelectric process, relaxation of the excited ion may occur by the emission of Auger electrons (Fig. 2.3). The Auger emission is dominated for elements having low atomic numbers (Z < 30). When an electron is emitted from a core level, another electron from a higher level falls to occupy the core level vacancy [44-46]. In order to conserve the total energy of the system, a third electron is emitted during this process which is known as Auger electron (Fig. 2.3 (b)). Auger emission is independent of the photon energy and therefore the *x*-ray source. Another important relaxation process, which can significantly contribute to the XPS spectrum, is the "Shake-up"/"Shake-off" process in which electrons from the valence levels are excited to the bound/unbound states (Fig. 2.3 (c, d)). Moreover, 'Multiplet' splitting of the XPS peaks can also occur when atoms having unpaired electron couple with other unpaired electrons in the atoms giving rise to several possible final state configurations, consequently peaks

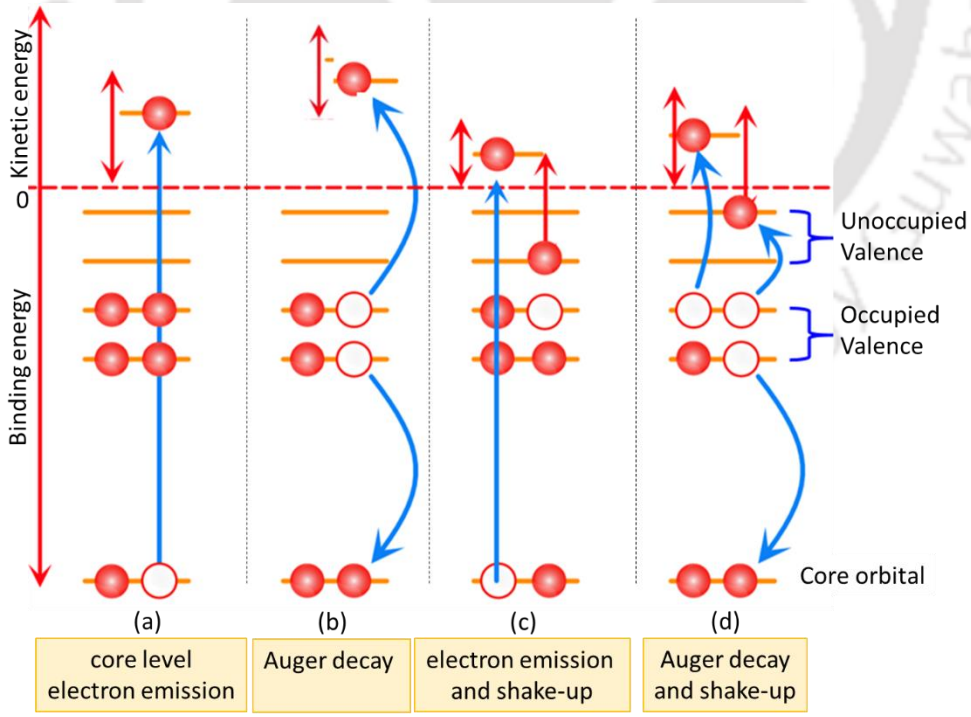

Fig. 2.3. Schematic representation of the energy level diagram showing various emission procedures of photoelectric effect. In particular, the (a) core level electron emission, (b) emission of Auger electron, and (c, d) emission of electron in shake-up/shake-off process.

shift to higher binding energy from the principle peak [44-46]. Some less intense Plasmon peaks also appear at higher binding energies from the principle peak at equal spacing due to specific amounts of energy losses when the photoelectron excites free electrons in a material.

2.2.3. Probing the local atomic environment using Electron Spin Resonance

Electron spin resonance (ESR), often referred to as electron paramagnetic resonance (EPR), is a crucial method for examining the local structure of a molecule. This is one of the key research techniques used to study the behaviour of material which possess unpaired electron, free radicals, and other paramagnetic centres (atom with odd number of electrons). Generally when an electron is subjected to an external magnetic field, the electron spin degeneracy splits down which is governed by the spin Hamiltonian $\hat{H}_S = g\mu_B B\hat{S}_Z$, here g is called the Landé g factor, μ_B is the Bohr magneton and B is the magnetic field strength. The ESR spectrum is obtained in continuous wave by sweeping the magnetic field to obtain the resonance when $h\nu = g\mu B$ [47,48]. Using a simple electromagnet, magnetic field up to 10 kOe are easily obtained, hence, one can use the microwave radiation with frequency (ν < 42 GHz). Within this microwave region, the most common choice is X-band (ν ~ 9-10 GHz) frequency in which the free electron resonance can be found at 3.39 kOe. Figure 2.4 shows the simplified block diagram of typical ESR spectrometer. In general, klystron tube is used for the generation of plane-polarized microwaves and power levels are adjusted by using the attenuator. The microwaves entering from the klystron tube are directed towards the Magnet Cavity by using circulator. These waves are again reflected back from cavity (with reduced power) to Circulator, which are then directed to Diode detector. If any power is reflected back by the detector that will be completely absorbed by the load. The detector converts the plane-polarized microwaves into electrical signal, which is proportional to the microwave power reflected from the cavity. Thus, the absorption of microwaves by the sample could be detected by noting a decrease in current in the micro-ammeter. Under ideal conditions, a commercial X-band spectrometer can detect about 10^{12} spins at room temperature. The

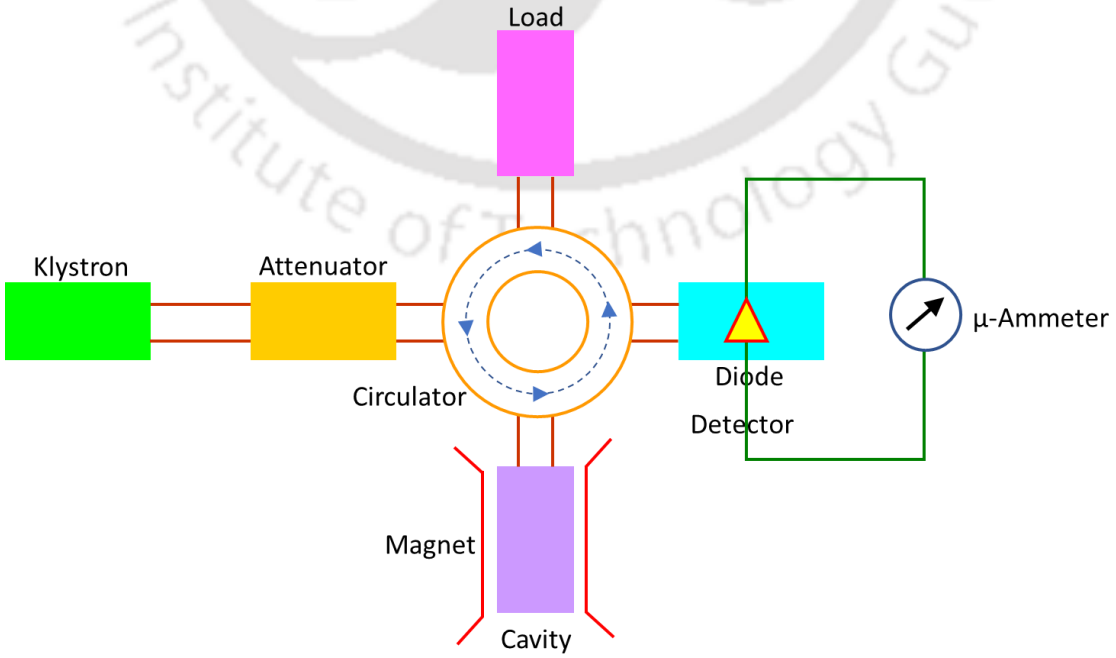

Fig. 2.4. Typical block diagram of electron spin resonance (ESR) spectrometer [47].

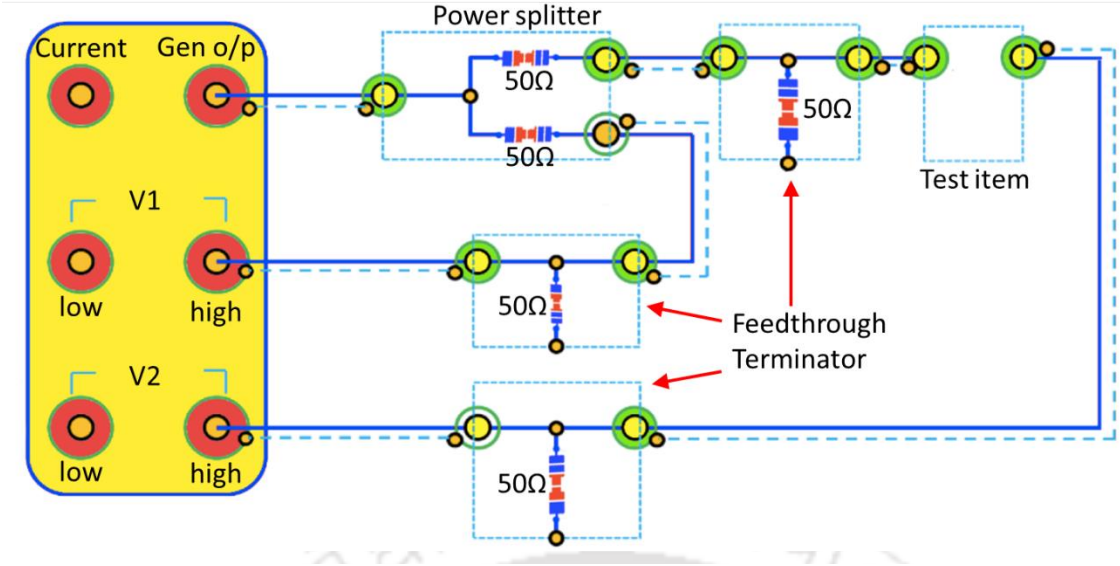

Fig. 2.5. Typical connections for high frequency voltage measurements.

ESR measurements for this thesis were carried out using a JEOL JESFA200 spectrometer which operates in X-band frequency of 9.45 GHz.

2.2.4. Impedance Spectroscopy

We used a highly accurate RF Impedance and Gain Phase analyzer to investigate the *ac*-electrical conductivity and dielectric characteristics of the columbites. This instrument is an important characterization tool used in the field of ferroelectrics and high-κ dielectrics using which one can probe the different relaxation mechanism and transition temperatures [49-51]. The frequency and temperature dependence of *ac*-resistivity and dielectric permittivity of the polycrystalline columbites were measured using the Precision Impedance Analyzers from Wayne-Kerr Electronics Pvt. Ltd. (Model WK-6500B/1J6530B). This

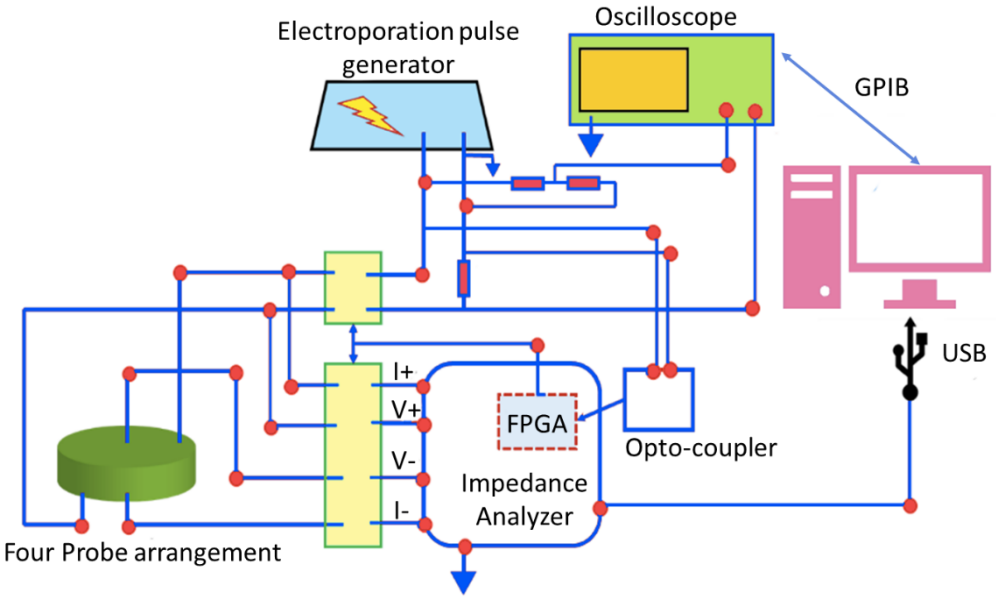

Fig. 2.6. Schematic representation of an Impedance Analyzer block diagram [52].

instrument is equipped with temperature controller (Eurotherm-2204 e) and heater capable of reaching 600°C for the high temperature measurements. However, for the low-temperature (77-300K) measurements we used a liquid nitrogen based cryostat assembled with the Lakeshore temperature controller (Model 325). For these measurements, two sides of the sintered pellets were fashioned like parallel-plate electrode geometry using silver coating. Constant *ac*-peak-to-peak sinusoidal driving potential of 100 mV with varying frequencies between 100 Hz and 20 MHz has been used as input signal. In order to match the input/output impedances of the instrument and investigating sample under high frequency limits, a 50 Ω feedthrough terminator cable was connected at the input and simultaneously a 50 Ω power splitter was used at output terminal as shown in Fig. 2.5. The most common and standard technique to measure impedance is by applying a single-frequency voltage (V) or current (I) to the interface and measuring the phase shift and amplitude (or real and imaginary parts) of the resulting current at that frequency using either analog circuit or fast Fourier transform (FFT) analysis of the response [52,53]. Generally, three different types of electrical stimulations can be used: (*i*) For the transient measurements, a step function of voltage [$V(t) = V_0$ for $t > 0$, $V(t) = 0$ for $t < 0$] may be applied at $t = 0$ to the system and the resulting time-varying current I(t) measured. The ratio $V_0/I(t)$, often called the indicial impedance or the time varying resistance, measures the impedance resulting from the step function voltage perturbation at the electrochemical interface. (*ii*) The second technique is to apply a signal V(t) composed of random noise to the interface and measure the resulting current. Fourier-transformation of the results is required to pass into the frequency domain and obtain definite value of the impedance. This approach offers the advantage of fast data collection because only one signal is applied to the interface for a short time. The technique has the disadvantages of requiring true random noise. (*iii*) The third approach, the most common and standard one, is to measure impedance by applying a single-frequency voltage or current to the interface and measuring the phase shift and amplitude, or real and imaginary parts, of the resulting current. Figure 2.6 shows the general architecture of any commercial Impedance and Gain Phase Analyzer. Figure 2.7 shows the simplest way of connecting the capacitance (C) and resistance (R) network of the measurement. The following are the four specific

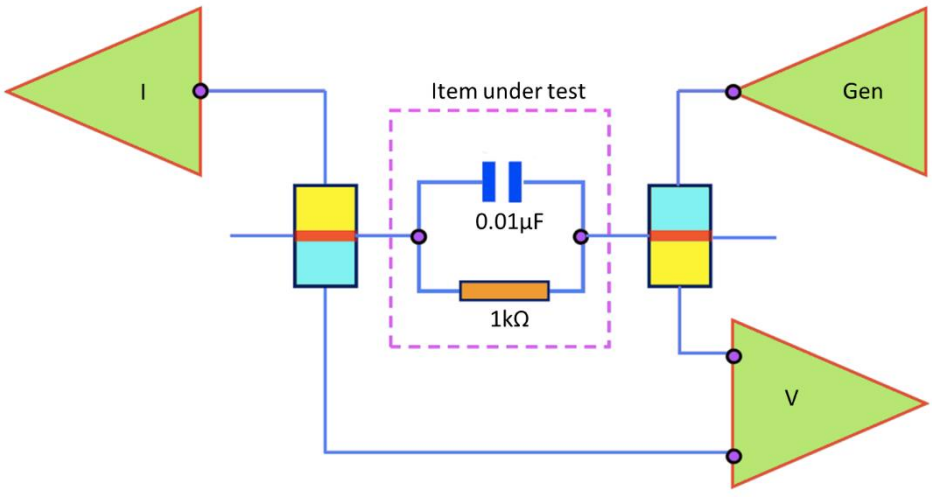

Fig. 2.7. Electrical connection for a simple impedance measurement [52].

components that we extracted to study the dielectric behaviour of columbites: Capacitance (C), Dissipation factor (D=Tan δ) Impedance (Z), and Phase Angle (Φ).

2.2.5. Physical Property Measurement System (PPMS)

The PPMS is an automated low-temperature and magnet system from Quantum Design essentially used to measure the material physical properties such as magnetic, thermo-electric, specific heat, and magneto-transport properties. In the current Ph.D. research work we have extensively used PPMS with VSM (vibrating-sample magnetometer) accessory to measure the magnetic moment of the columbites. It is well known that the VSM section operates on Faraday's Law of Induction in which the change in magnetic field

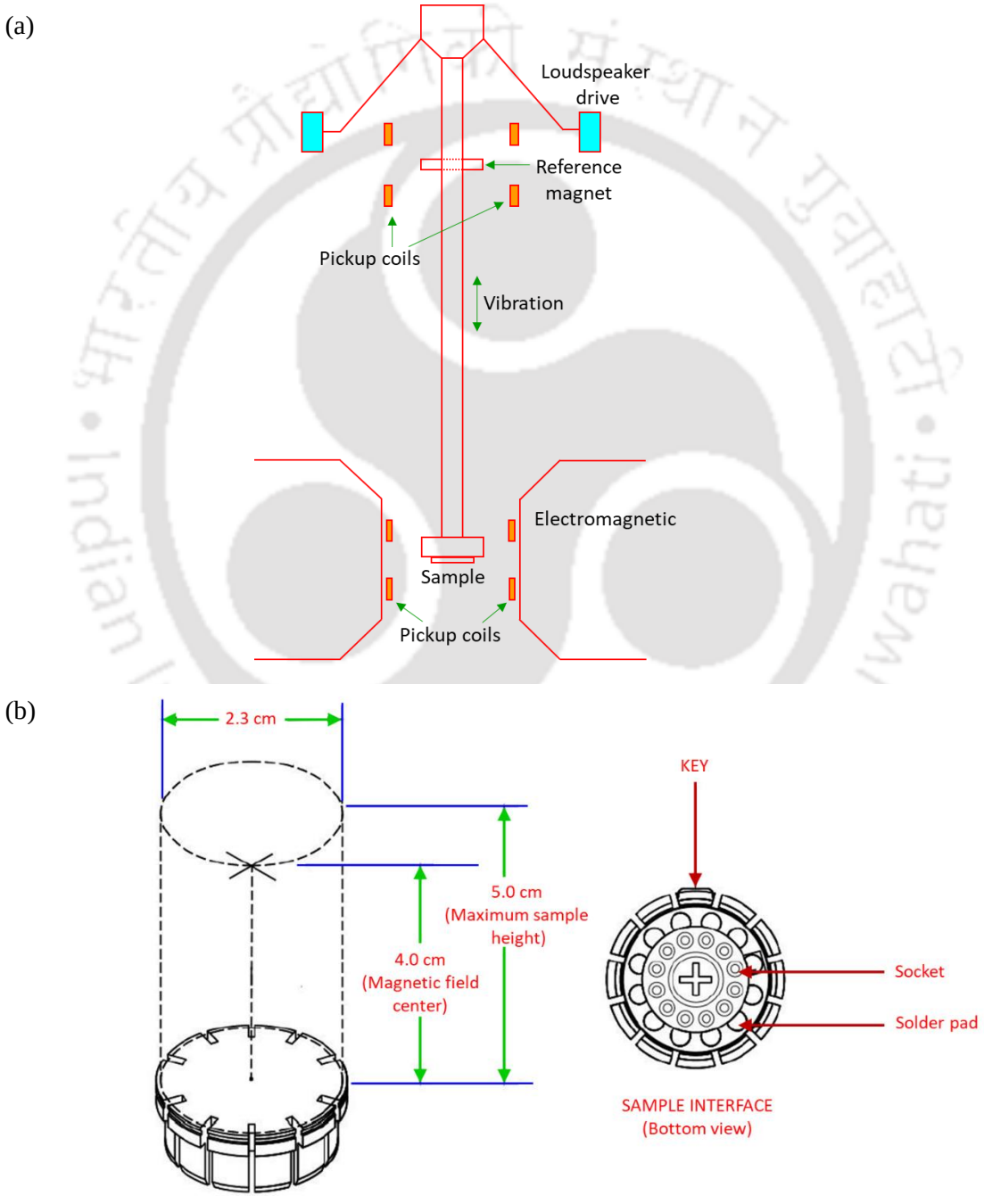

Fig. 2.8. (a) Diagrammatic representation of VSM showing pickup coils and (b) Schematic picture of top and bottom views of a sample puck [29].

Fig. 2.9. Picture of PPMS-DynaCool System from Quantum Design instruments.

will produce an emf which provide information about the changing magnetic moment of the system with respect to the external magnetic field. In VSM mode a sample is first placed in a constant magnetic field, which magnetize the sample by aligning the magnetic domains, or the individual magnetic spins, with the field. The stronger the applied field, the larger the magnetization will be induced within the system. The magnetic dipole moment of the sample will create a magnetic field around the sample, sometimes called the magnetic stray field. As the sample vibrates up and down, this magnetic stray field is changing as a function of time and can be sensed by a set of pick-up coils (as shown in the Fig. 2.8(a)). The alternating magnetic field will develop emf in the pick-up coils according to Faraday's Law of Induction which will be proportional to the magnetization of the sample. The induced emf is amplified and fed to the lock-in amplifier. Various components are hooked up to a computer interface using controlling and monitoring software [29]. In the present case the PPMS-VSM (Model: DynaCool) has been employed for the magnetic measurements which is capable of reaching 1.9 K from 400 K using a cryogen free close-cycle technology. Specifically, its uses a single two-stage Pulse-Tube cooling technology to cool the samples and the superconducting magnet and provides a low vibration environment to the samples. PPMS-DynaCool also offers continuous low temperature control and precise field and temperature sweep modes. Figure 2.9 shows the PPMS-DynaCool System from Quantum Design instruments which is extensively used in the current study.

The DynaCool system employs a minimum amount of condensed liquid Helium for cooling both the sample chamber and superconducting magnet. As a result, the system requires only a small volume of bottled helium gas for its fully automated startup and operation involving a vacuum pump which evacuates the sample space to a pressure of $< 10^{-4}$ Torr. For temperature control, DynaCool uses a novel gas flow regulation system (Fig. 2.10) to increase both cooling power and temperature. This system offers a sophisticated control software; this system provides seamless transitions between 1.9 K to 400 K with minimal cooling power

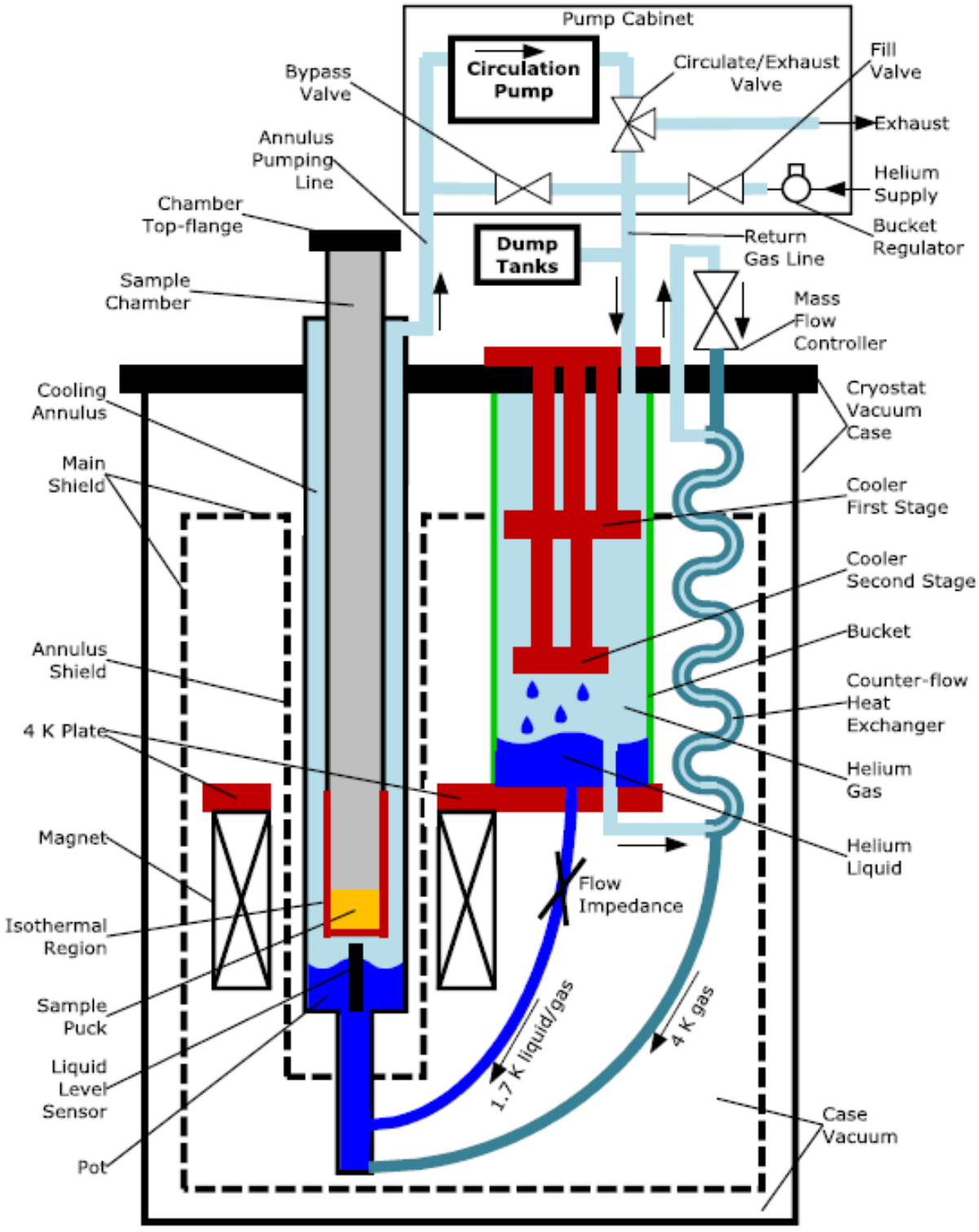

Fig. 2.10. The DynaCool Cryostat showing the components of the Cryostat Control System, Chamber Temperature Control System, and Magnetic Field Control System [54].

including a stable operation near the base temperature (< 1.8 K) with cooling provided by evaporating liquid helium. With such new control system PPMS-DynaCool is capable of cooling a standard PPMS sample puck from 300 K to 1.9 K less than 40 minutes time. The sample chamber design has also been improved for better thermal uniformity at both low and high temperatures while maintaining the robust 12-pin sample

puck (Fig. 2.8(b)) interfaced with the main chamber. Multiple thermometers and heaters manage temperature gradients endorse smooth temperature control throughout the accessible temperature range. The PPMS-DynaCool has a built-in magnetic shield. For a system with a 90 kOe magnet, this shield maintains the 5 gauss line <30 cm the surface of the cryostat cabinet allowing the system to be installed closer to other sensitive accessories. Figure 2.10 displays the schematic diagram of the complex cryostat control system of DynaCool, which is accountable for keeping all the components at the precise temperatures and allows easy operation of the remaining subsystems [54].

2.2.6. Specific heat measurements using PPMS

We employed a separate PPMS (from Quantum Design) machine to measure the temperature dependence of specific heat ($C_P(T)$) with heat capacity accessory in which heat added and removed from a sample by monitoring the resulting change in temperature [55]. In particular, a dual-slope analysis was implemented near the transition temperature to observe the magnetic field effect on phase transition. In this technique, the heat capacity of the sample is measured directly by comparing the heating and cooling rates of the sample temperature without explicit use of the thermal conductance between sample and bath [56]. Usually, heat capacity C is defined as the amount of heat Q required to effect a corresponding change in temperature T at a constant volume; $C = dQ/dT$. At low temperatures, the heat capacity of material can be expressed as the sum of electronic and phonon contribution: $C = \gamma T + AT^3$, where γ and A are the characteristic constants vary from material to material. The contribution from electronic part is linear with T and is dominant at very low temperature. In each measurement cycle, a known amount of heat is supplied to the sample at constant power for a fixed time, then this heating period is followed by a cooling period of the same duration. After each cycle, the software option fits the temperature response of the sample stage to an appropriate mathematical model. It is possible that weak thermal contact between the sample and sample-platform causes thermal relaxation. Hence, the model considers the thermal relaxation of the sample stage to the thermal bath and also the relaxation between the sample-platform and the sample itself which offers the accurate value of C_P of the sample [56]. Figure 2.11 illustrates the schematic of thermal connections to the sample and sample platform in PPMS Heat Capacity accessory. A heater and a thermometer are attached at the bottom of the sample stage. The sample is attached on the stage by thin layer of Apiezon N Grease

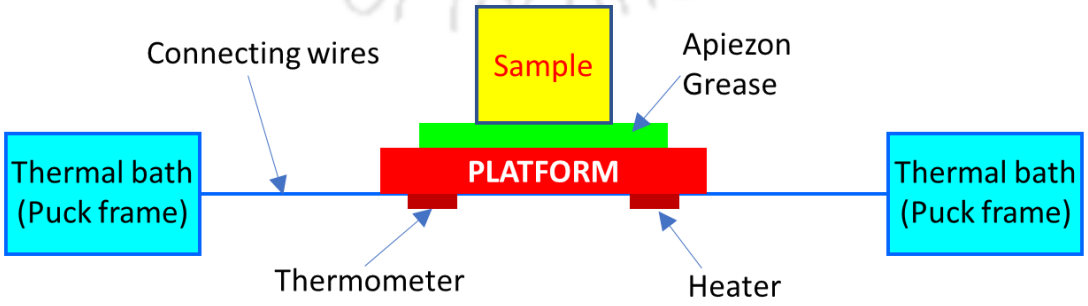

Fig. 2.11. Schematic diagram of the specific heat measurement assembly and connections adopted from Quantum Design PPMS.

which helps to make thermal contact between sample and the sample-platform. Highly sensitive wiring system is connected with the heater and thermometer to provide electrical and thermal connections. Usually, the additional measurements are performed before the $C_P(T)$ measurement of the sample, which consists of measuring the C_P of the sample holder. In the supplementary run, a thin layer of Apiezon N Grease is placed on the sample stage and the measurement is taken. After the completion of additional run, the sample is carefully attached with the grease without disturbing it. The measurement is performed once more and the correct value of the C_P of the sample is determined by subtracting the C_P of the sample holder from the total magnitude. In the present case C_P(T) measurements were performed at both zero-field case as well as in the presence of a constant magnetic field of strength 90 kOe field. These results are discussed in the coming chapters in detailed way.

Chapter 3

H-T Phase Diagram, Specific-Heat Exponents of $MnNb_2O_6$

In this chapter we mainly focus our studies on the synthesis and various magnetic properties of $MnNb_2O_6$. In particular, a complete mapping of *H-T* phase diagram with a triple point, estimation of critical exponents near T_N using specific heat data and the determination of exchange constants using Molecular field theory will be presented. We begin with a brief introduction to the systems under investigation and outline the details of experimental methods employed in line with the chapter 2 and discuss the key results. Final section of this chapter focuses on the summary of important findings.

3.1. Introduction and Literature Review

The four transition metal niobates MNb_2O_6 (M = Mn, Fe, Co, and Ni) crystallize in the columbite structure (space group D_{2h}^{14}–*Pbcn*) with orthorhombic unit cell containing four molecules per unit cell. For $MnNb_2O_6$, the lattice parameters are: a = 14.4204 Å, b = 5.7566 Å and c = 5.078 Å [57–59] and for M = Fe, Co and Ni, the lattice parameters decrease nearly linearly with decreasing ionic size of Fe^{2+}, Co^{2+} and Ni^{2+} ions in that order [19,22,60–67]. This crystal structure has zig-zag like chains of M^{2+} ions along the *c*-axis containing two crystallographically inequivalent M^{2+} ions and isosceles triangular arrangement of M^{2+} ions in the *ab* plane. A schematic diagram of this structure based on available literature [57–67] is shown in Fig. 3.1 Consequently, the Hamiltonian describing the exchange coupling among M^{2+} ions in these systems can be written as [19,22,67,68]:

$$H = -J_0 \sum_i S_i^z S_{i+1}^z - J_1 \sum_{<ij>} \boldsymbol{S}_i . \boldsymbol{S}_j - J_2 \sum_{<ij>} \boldsymbol{S}_i . \boldsymbol{S}_j \qquad (3.1)$$

In equation (3.1), the sum is over nearest-neighbours (nn) along the *c*-axis for J_0, over nn along the *b*-axis for J_1, and over next-nn for J_2 in the *ab* plane (see Fig. 3.1). When independent determination of J_1 and J_2 is not possible, they are replaced by an average $J_\perp$ as the interchain exchange coupling [66].

Despite the similarity of the crystal structure of the four niobates, the nature of magnetic ordering in these systems is sufficiently different. For $FeNb_2O_6$, the reported studies by Yaeger *et al.* [61], Heid *et al.* [19] and Sarvezuk *et al.* [22] reported $T_N \simeq 4.9$ K to 5.5 K with canting angle $\Phi \sim 17^o$ from the easy *a*-axis. For $NiNb_2O_6$, the studies by Yaeger *et al.* [60], Heid *et al.* [19] and Sarvezuk *et al.* [22] reported T_N = 5.7 K with easy direction being closer to *c*-axis. The magnetic properties of $CoNb_2O_6$ are somewhat different in that it is shown to be a good example of an Ising chain ferromagnet along the *c*-axis with effective spin S = 1/2 and exchange constant J_0/k_B = 6.2 K and the interchain antiferromagnetic exchange constants J_1/k_B = –0.42 K and J_2/k_B = –0.67 K [68]. The Co^{2+} moments are aligned close to *c*-axis with canting angle $\Phi = \pm 31^o$. In addition, for $H \parallel b$-axis, T_C = 2.95 K for H = 0 reduces to absolute zero in a critical field H_C = 52.5 kOe. For $H > H_C$, quantum critical fluctuations have been reported well above T = 0 K [8,9,14,69].

The main theme of this chapter is to probe the magnetic properties of $MnNb_2O_6$ on which previous magnetic studies include those of Nielsen *et al.* [57,58] and Holmes *et al.* [59] who reported $T_N \simeq 4.4$ K with moments aligned close to the *a*-axis. The new results reported here include the following: (i) structural characterization of the sample using x-ray photoelectron spectroscopy (XPS) in addition to the Rietveld refinement of the X-ray diffraction (XRD) pattern; (ii) measurements and analysis of specific heat covering the region around T_N ; (iii) complete mapping of the *H*-*T* phase diagram and determining the triple point $T_{TP}(H, T)$ = (18 kOe, 4.06 K) from the *M* vs *H* and *M* vs *T* data; (iv) determination of the exchange constants J_0 and $J_\perp$ from the temperature dependence of magnetic susceptibility; and (v) estimating the anisotropy energies from the spin-flop field. In the following we provide the experimental details pertaining to the specific columbite system $MnNb_2O_6$. These details are in consonance with the content given in chapter 2.

3.2. Experimental details

Polycrystalline bulk samples of $MnNb_2O_6$ were prepared using MnO_2 and Nb_2O_5 as precursors and the standard solid-state reaction method. Stoichiometric amounts of the precursors were first mixed in an agate mortar with pestle for 4-6 h and then pressed into cylindrical pellets using a hydraulic press with pressure of 20 kN m^{-2}. These pellets were then sintered in air at 1150°C for 12 h. The resulting sample was

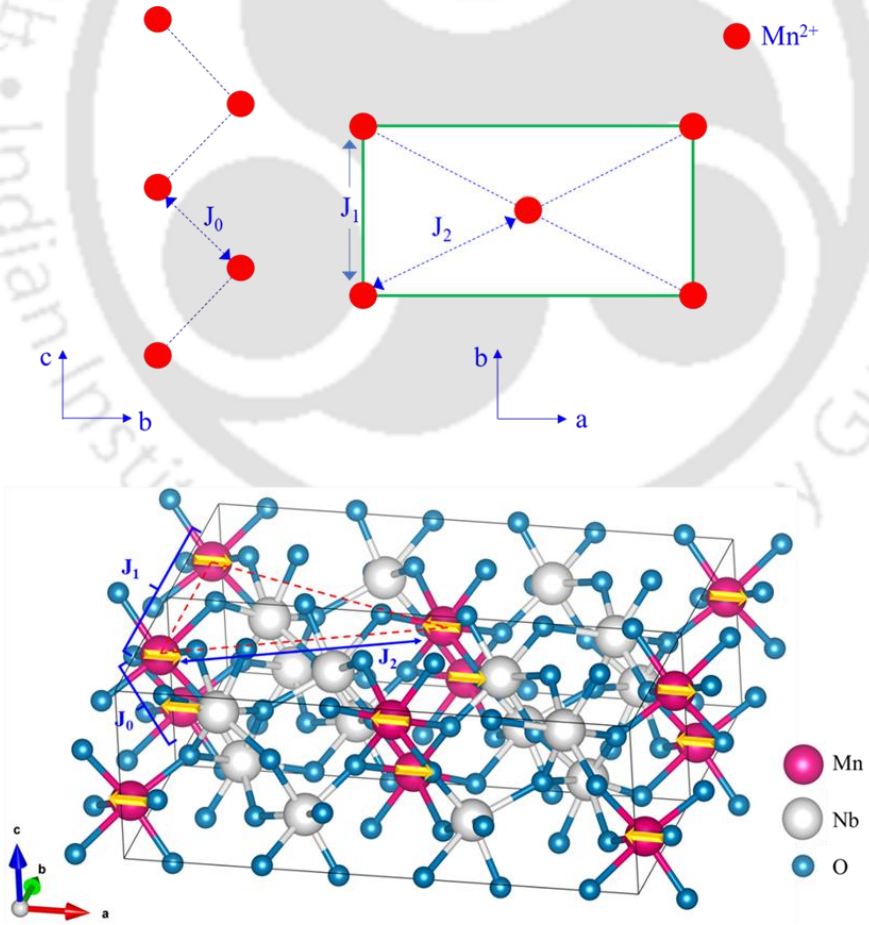

Fig. 3.1. (Top) Schematic diagrams showing the antiferromagnetic intrachain exchange interaction J_0 along the zigzag chains running along the *c*-axis and the interchain interactions J_1 and J_2 in the *a*-*b* plane; (bottom) two-unit cells of $MnNb_2O_6$ showing the exchange interaction paths.

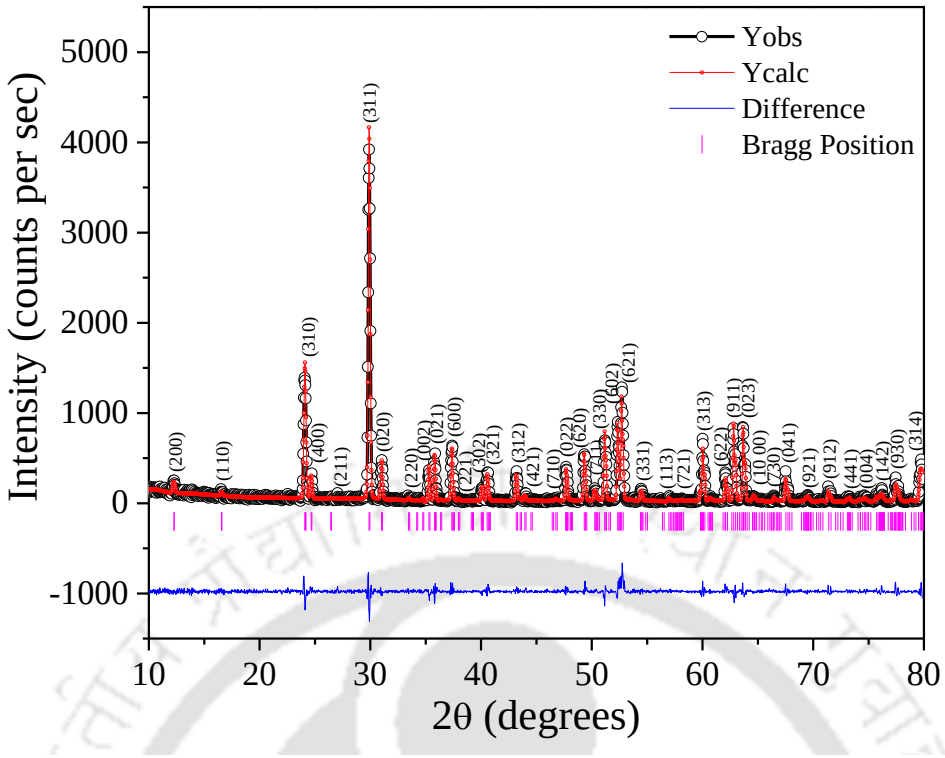

Fig. 3.2. Rietveld refined data of XRD pattern of the $MnNb_2O_6$ sample at room temperature along with the Miller indices of the Bragg lines are listed. The difference between the measured and simulated patterns is indicated by the blue line at the bottom.

re-grinded/pelletized and then finally sintered at 1200°C for 24 h in air. Re-grinding and re-sintering were found to be very important to obtain a bulk grain size ~ 2μm and dense polycrystalline ceramic $MnNb_2O_6$ of ideal stoichiometric columbite structure. The purity and crystal structure of this prepared material was investigated using the XRD technique employing a Rigaku x-ray diffractometer (model-TTRAX III, Cu Kα radiation with wavelength ~ 1.54 Å). The XRD pattern was recorded in the θ–2θ geometry between $2\theta = 10^o$ and 80^o with slow scan rate of 1^o/minute. Fig. 3.2 shows the XRD pattern of the prepared sample plotted along with the Rietveld refinement data performed using the FullProf programme confirming the single-phase nature of the prepared $MnNb_2O_6$ sample having stoichiometric columbite structure with lattice constants a = 14.4327 Å, b = 5.7627 Å and c = 5.0819 Å and absence of any secondary impurity phase within the sensitivity of the XRD technique.

The electronic structure and chemical composition of the pelletized sample were probed using XPS. For this, we used Kratos analytical spectrometer (model: AXIS Supra+) configured with a dual monochromatic x-ray source Al Kα /Ag Lα (2984.2 eV) with spatial resolution less than 1 μm. The electronic spectra for Mn, Nb and Oxygen are shown in Fig. 3.3. The binding energy of carbon C-1*s* orbital (~ 284.8eV) was used for the calibration of all the recorded core-level spectra. The Nb-3*d* core level spectrum (Fig. 3.3(a)) exhibits two sharp peaks centred at 207.25 eV and 210 eV with binding energy separation between these peaks Δ ~ 2.75 eV confirming the pentavalent oxidation state of Nb [70]. The deconvolution of Mn-2*p* core level spectrum (Fig. 3.3(b)) required minimum of five peaks; four main peaks at 640.41 eV (M_1), 642.0 eV (M_2), 652.15 eV (M_3), and 653.48 eV(M_4) and one broad satellite peak at 645.2eV(S_1). For the

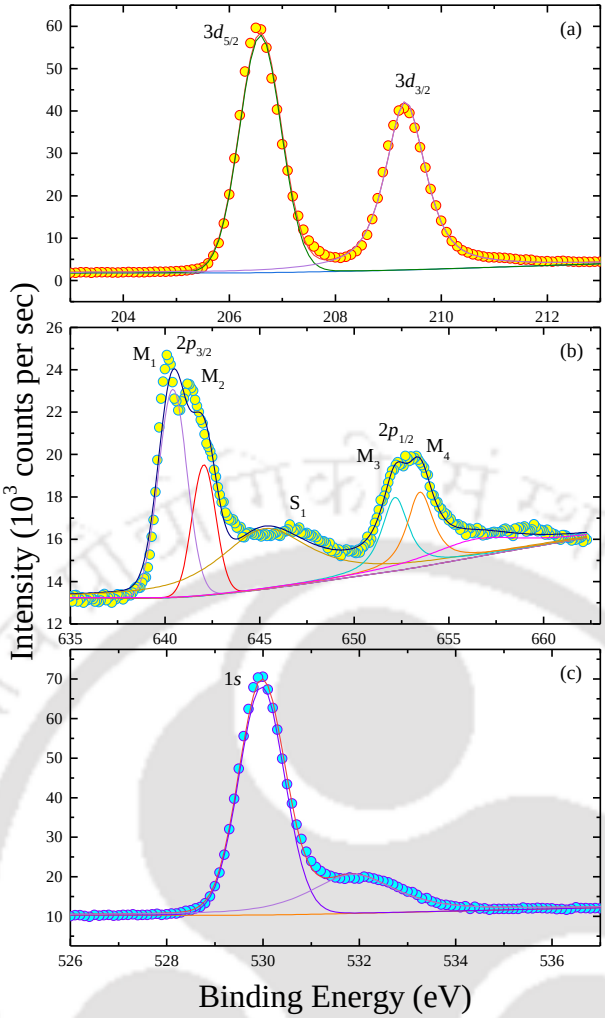

Fig. 3.3. X-ray photoelectron spectra of (a) Nb-3*d*, (b) Mn-2*p* and (c) O-1*s* for the polycrystalline $MnNb_2O_6$ sample.

deconvolution, we applied a fitting constraint on the FWHM of the peak profile i.e. the FWHM should range within 0.2 eV. This constraint is relaxed during the final iteration. The observed values of spin orbit splitting Δ ($M_3 - M_1$) ~ 11.74 eV and Δ ($M_4 - M_2$) ~ 11.4 eV suggests the divalent oxidation state of 'Mn' [71]. Moreover, the O-1*s* spectrum (Fig. 3.3(c)) exhibits a sharp peak centred at 529.8 eV along with a low intensity broad hump at 531.9 eV associated with the metal-oxygen (M-O) bonding and surface oxygen, respectively [72], present in the system. Overall, the XPS analysis confirms the presence of Mn^{2+} and Nb^{5+} ions in the polycrystalline $MnNb_2O_6$ sample. Details of the results of magnetic characterization and electron spin/paramagnetic resonance studies are presented in the following sections.

3.3. Temperature and magnetic field dependence of magnetization

Measurements of magnetization (*M*) of the $MnNb_2O_6$ sample were done using a vibrating sample magnetometer based Physical Property Measurement System (PPMS) from Quantum Design (PPMS DynaCool) capable of magnetic fields up to ±90 kOe in the temperature range of 1.9 to 400 K. For these measurements, the sample was cooled to 1.9 K in zero field, followed by applying a measuring non-zero *H*

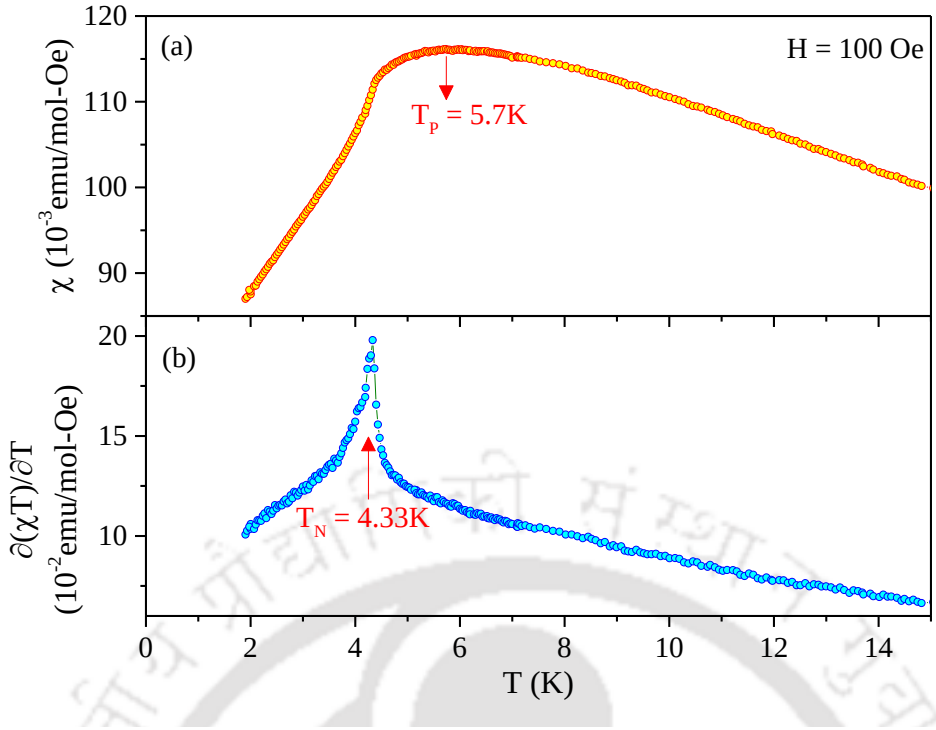

Fig. 3.4. (a) Temperature dependence of the magnetic susceptibility (χ) recorded under zero-field-cooled condition for H = 100 Oe. Figure (b) shows the plot of computed $\partial(\chi T)/\partial T$ vs T between 1.9 K and 15 K. The broad peak at T_P = 5.7 K in (a) and the sharp peak at T_N = 4.33 K in (b) are marked by arrows.

and acquiring the data with increasing T (step size = 0.02 K) after stabilizing the temperature at each T. For isothermal M vs H measurements, the step size was 50 Oe for H < 1500 Oe and 300 Oe for H > 1500 Oe.

3.3.1. Néel temperature and its magnetic field dependence

The temperature dependence of magnetic susceptibility $\chi = M/H$ (H = 100 Oe) of the polycrystalline $MnNb_2O_6$ sample is shown in Fig. 3.4(a) covering the temperature range of 1.9 to 15 K. There is a peak in χ near $T_P \sim 5.7$ K. However as theoretically established by Fisher [73], in antiferromagnets $T_P > T_N$, the Néel temperature. Instead, T_N is accurately given by the peak in $\partial(\chi T)/\partial T$ vs T plots since χT is proportional to magnetic energy. Experimentally, this has been established in several antiferromagnets such as MnF_2 [74] and Er_2O_3 [75]. In Fig. 3.4(b), the plot of computed $\partial(\chi T)/\partial T$ vs T using the χ vs T data yields peak at T_N = 4.33 K, a value in general agreement with T_N = (4.40 ± 0.05) K reported previously by Nielson *et al.* [57, 58] and Holmes *et al.* [59].

The H-dependence of T_N was measured next for H up to 90 kOe following the same procedure of determining the peak in the computed $\partial(\chi T)/\partial T$ vs T plots. This was done to map out the H–T phase boundary analogous to that reported in the uniaxial antiferromagnet MnF_2 with $T_N \simeq 67.3$ K [11,12,74,76]. For lower H, this T_N vs H variation follows the equation:

$$T_N(H) = T_N(0) - D_1H^2 \qquad (3.2)$$

as shown theoretically and experimentally in MnF_2 [11,12]. This plot of $T_N(H)$ vs H^2 is shown in Fig. 3.5 with $D_1 = 0.9 \times 10^{-9}$ K Oe^{-2} determined from the slope and $T_N(0)$ = 4.36 K. These results are compared with

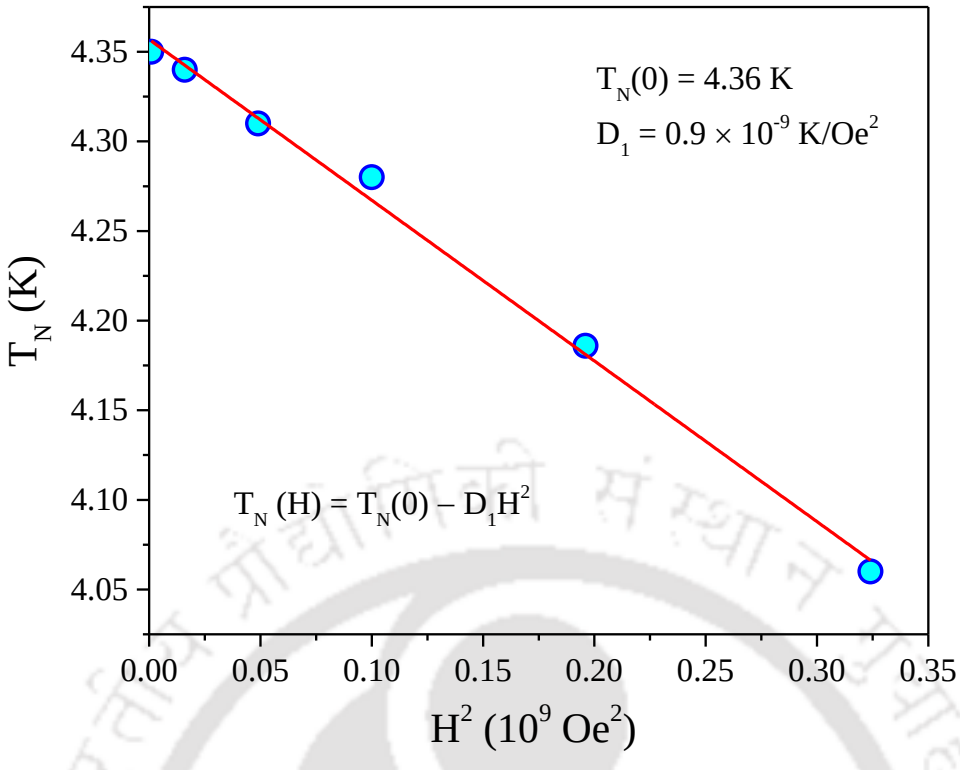

Fig. 3.5. Plot of T_N vs H^2 for smaller H. The solid line is linear fit to the equation: $T_N(H) = T_N(0) - D_1H^2$ yielding $T_N(0) = 4.36$ K and $D_1 = 0.9 \times 10^{-9}$ K Oe^{-2}.

$D_1 = 1.59 \times 10^{-10}$ K Oe^{-2} for MnF_2 [11,12] and $D_1 = 7.3 \times 10^{-9}$ K Oe^{-2} for Er_2O_3 [75]. Theoretically, the molecular field theory (MFT) for H parallel to the easy axis yields [11,12]:

$$D_1 = \frac{g^2\mu_B^2(2S^2 + 2S + 1)}{40k_B^2T_N} \qquad (3.3)$$

Using $g = 2.001$ and $S = 5/2$ for $MnNb_2O_6$ as shown later yields calculated $D_1 = 1.92 \times 10^{-9}$ K Oe^{-2} compared to the experimental $D_1 = 0.9 \times 10^{-9}$ K Oe^{-2}. As in MnF_2 [11,12] and Er_2O_3 [75], the difference in the calculated and measured D_1 is likely related to the inadequacy of the MFT near T_N.

3.3.2. Temperature dependence of specific heat

The temperature dependence of specific heat $C_P(T)$ measurements from 1.9 to 8 K were performed using a PPMS of Quantum Design using the standard heat-pulse calorimetry [56]. Near the phase transition, a dual-slope analysis was applied to precisely study the effect of the magnetic field on the phase transition. In this method, at any temperature the specific heat is estimated by direct comparison of the heating and cooling rates of the sample temperature without explicit use of the thermal conductance between sample and bath [77]. The plots of the C_P vs T data so obtained for $H = 0$ and $H = 90$ kOe are shown in Fig. 3.6 yielding peaks at $T_N = 4.36$ K for $H = 0$, which is in good agreement with $T_N = 4.33$ K obtained earlier from the peak in $\partial(\chi T)/\partial T$ vs T plot of Fig. 3.4(b). For $H = 90$ kOe, the peak shifts to $T_N = 3.52$ K, a result discussed later

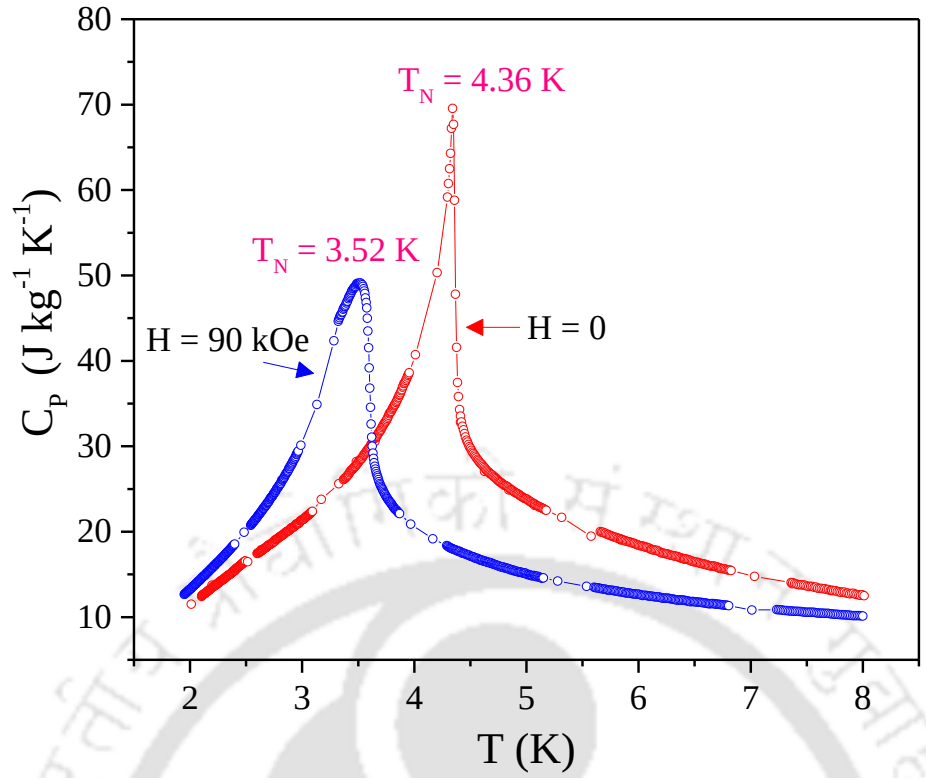

Fig. 3.6. Plots of the C_P vs T data for both H = 0 and H = 90 kOe with the peak positions marked as the Néel temperature T_N.

in connection with the H–T phase diagram. The temperature variation of C_P near a second order phase transition is expected to vary as: $C_p = A(T - T_N)^{-\alpha}$ where α is the critical exponent [78] and A is a constant.

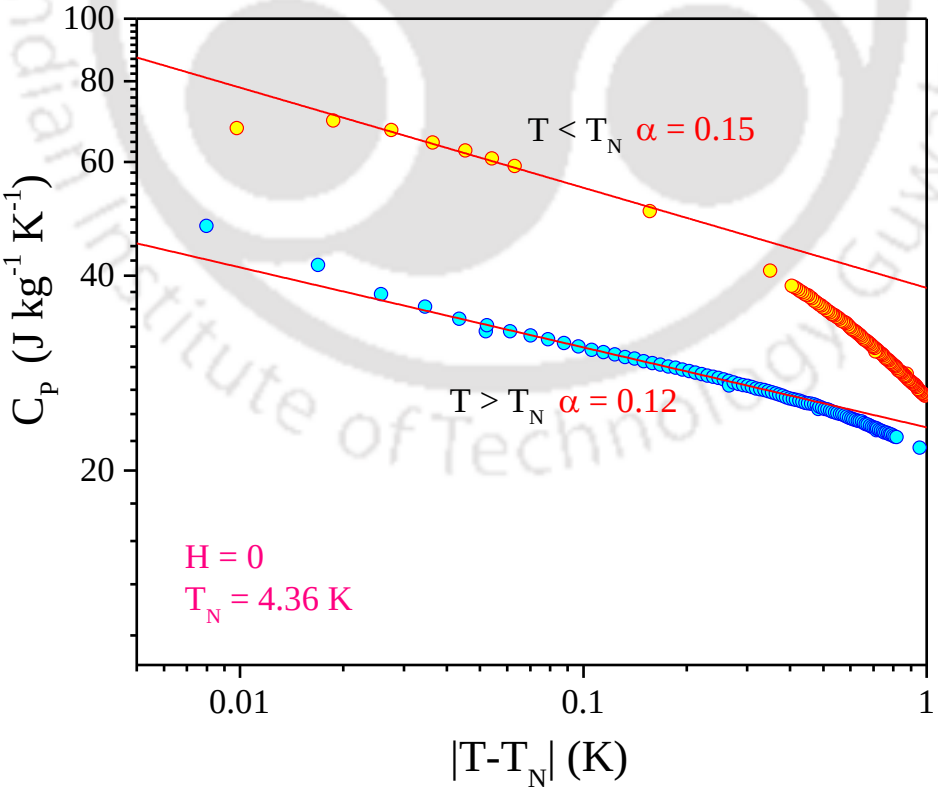

Fig. 3.7. Log-Log plot of the measured C_P in H = 0 vs $|T - T_N|$ to determine the exponent α in the equation $C_p = A\,(T - T_N)^{-\alpha}$ for both above and below T_N.

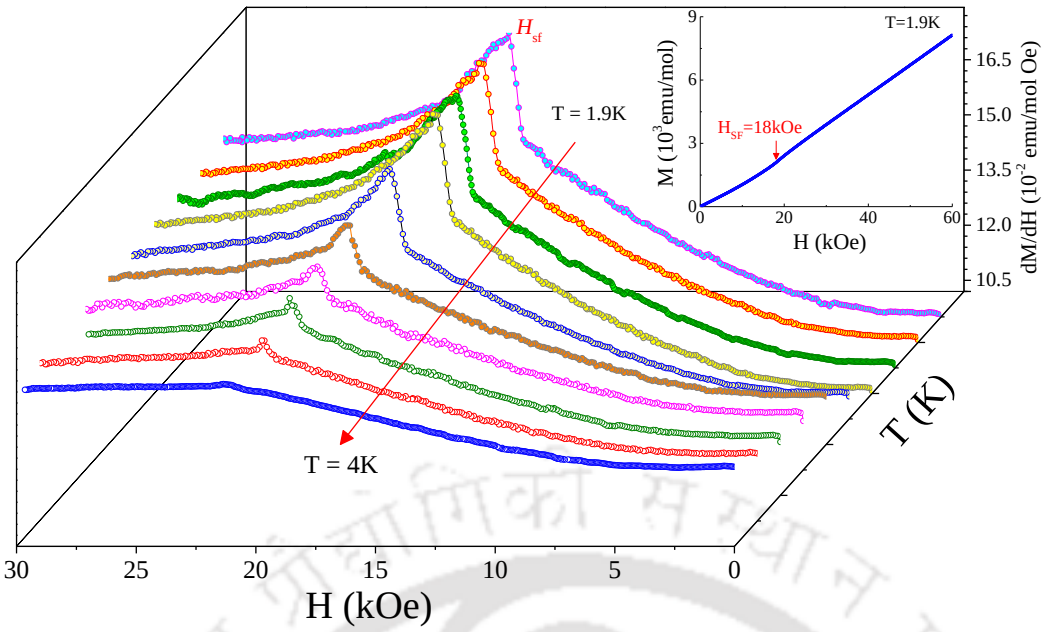

Fig. 3.8. Plots of computed $\partial M/\partial H$ vs H for $MnNb_2O_6$ determined from the magnetization curves (shown in the inset measured at 1.9 K) for T = 1.9 to 4 K. The peak positions denote the spin-flop field H_{sf}.

Using log-log plot, the plots of C_P vs $|T - T_N|$ for temperatures both above and below T_N are shown in Fig. 3.7. As observed in other systems [78], the linear fit is sensitive to the choice of T_N and so we varied T_N between 4.32 K and 4.36 K in 0.01 K steps and determined that T_N = 4.36 K gives the best overall linear fit yielding α = 0.12 (0.15) for $T > T_N$ ($T < T_N$). For comparison, similar magnitudes of α = 0.16 (0.18) for $T > T_N$ ($T < T_N$) have been reported in the uniaxial antiferromagnet MnF_2 with T_N = 67.3 K [78].

3.3.3. Spin-flop field and its temperature dependence

The variation of M vs H in $MnNb_2O_6$ was measured in the temperature range of 1.9 K to T_N with a typical variation shown in the inset of Fig. 3.8. There is a clear change in the slope of the M vs H curve near 18 kOe which becomes distinctly evident in the computed $\partial M/\partial H$ vs H curves shown in Fig. 3.8 for different temperatures. The position of the peak near H = 18 kOe is identical to the results reported by Nielsen *et al.* [57,58] at a few temperatures $T < T_N$ for $H \parallel a$-axis in a single crystal of $MnNb_2O_6$. In a polycrystalline sample, only a fraction of the grains has $H \parallel a$-axis and so the anomaly is understandably weaker than reported by Nielsen *et al.* [57,58] in a single crystal. This peak in $\partial M/\partial H$ vs H is associated with the spin-flop transition since a-axis is the easy axis. The magnitude of H_{sf} increases slightly with increase in T towards T_N hinting at the presence of triple point, like that reported in MnF_2 [11,12,76]. The magnitudes of H_{sf} determined here in the polycrystalline sample of $MnNb_2O_6$ at different $T < T_N$ are in excellent agreement with those reported by Nielsen *et al.* [57,58] at a few temperatures in a single crystal with $H \parallel a$-axis.

3.3.4. H-T phase diagram

The H-T phase diagram determined here from the variation in T_N with H using the peaks in $\partial(\chi T)/\partial T$ vs T and H_{sf} vs T from the peaks in $\partial M/\partial H$ vs H at different T is shown in Fig. 3.9. We have included the

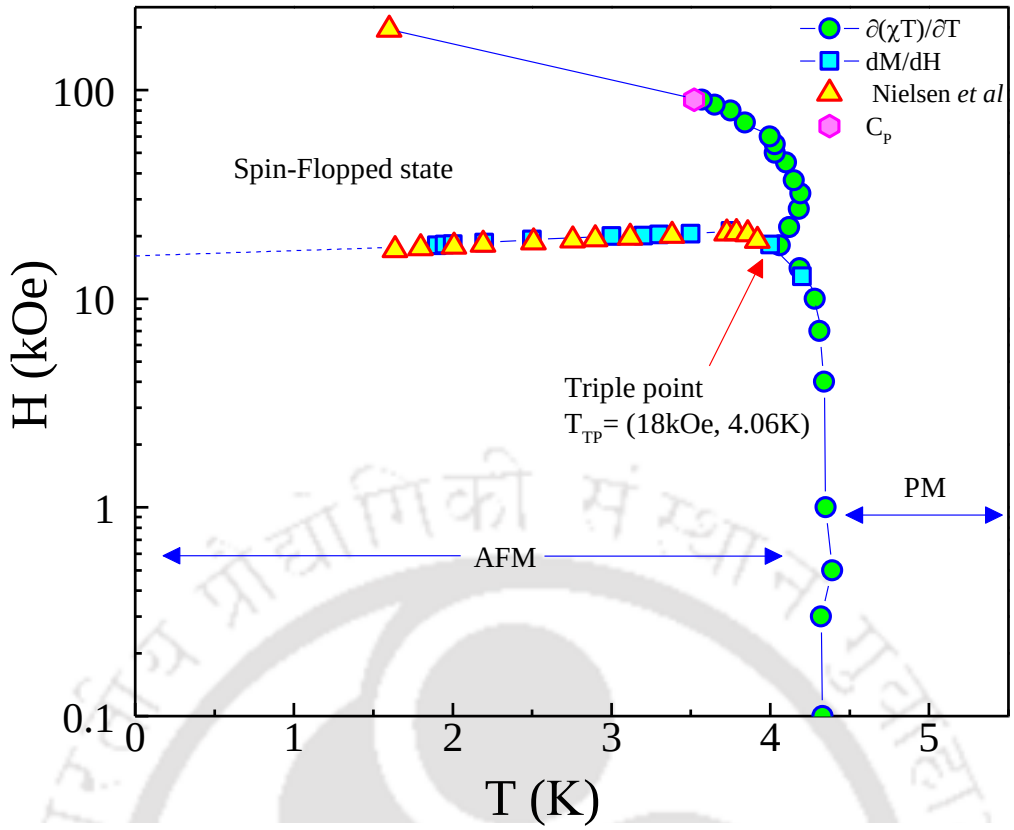

Fig. 3.9. *H-T* phase diagram for the polycrystalline $MnNb_2O_6$ sample determined here from the peaks in $\partial(\chi T)/\partial T$ vs. T at different H, $\partial M/\partial H$ vs H at different temperatures, and the C_P vs T data at 90 kOe. Also included are the data points (triangles) of H_{sf} vs T reported by Nielsen *et al*. [1, 2] in single crystals of $MnNb_2O_6$ for H applied along the easy a-axis. The lines connecting the data points are visual guides. The triple point is represented as $T_{TP}(H, T)$ = (18 kOe, 4.06 K). The magnetic phases marked are: PM = paramagnetic; AFM= antiferromagnetic.

data of H_{sf} vs T reported by Nielsen *et al.* [57,58] who also reported that for $\vec{H} \| \vec{a}$, M saturates for $H > 190$ kOe and this point is also included in the plot. The phase diagram in Fig. 3.9 with triple point $T_{TP}(H, T)$ = (18 kOe, 4.06 K) is qualitatively similar to that reported in the uniaxial antiferromagnet MnF_2 [11,12,76]. This is an important result of this work because of its resemblance to the *H-T* phase diagram in MnF_2 and drastic differences from the *H-T* phase diagram of $CoNb_2O_6$ [68].

For $MnNb_2O_6$, two critical fields are evident in Fig. 3.9: (i) the spin flop field H_{sf} = 18 kOe at 1.9 K and $H_{C2} \sim 200$ kOe at 1.6 K determined by Nielsen *et al.* [57,58] above which the spins are forced to align along the applied field thus overcoming the exchange field H_E and yielding the saturation magnetization $M_S \simeq 27 \times 10^3$ emu mol^{-1}. Using the well-known relation: $M_S = \chi_\perp H_E$ [79] yields $\chi_\perp$ = 0.135 emu mol^{-1} Oe^{-1} as the susceptibility perpendicular to the easy axis which is near equal to the peak value of χ just above T_N near 5.7 K shown in Fig. 3.4(a). This is like the observation in the antiferromagnet MnF_2, for which $\chi_\perp$ below T_N is nearly temperature independent [11] and equal to the peak value of χ just above T_N. For $MnNb_2O_6$, the calculated $M_S = N_A g \mu_B S_Z = 27.9 \times 10^3$ emu mol^{-1} at absolute zero is quite close to $M_S \simeq 27 \times 10^3$ emu mol^{-1} measured at 1.6 K by Nielsen *et al.* [57,58]. Using the equation $H_{sf} = (2H_A H_E)^{1/2}$ [12,75], $H_E \simeq 200$ kOe and H_{sf} = 18 kOe yields H_A = 0.8 kOe as the anisotropy field in $MnNb_2O_6$ between the easy a-axis and the hard

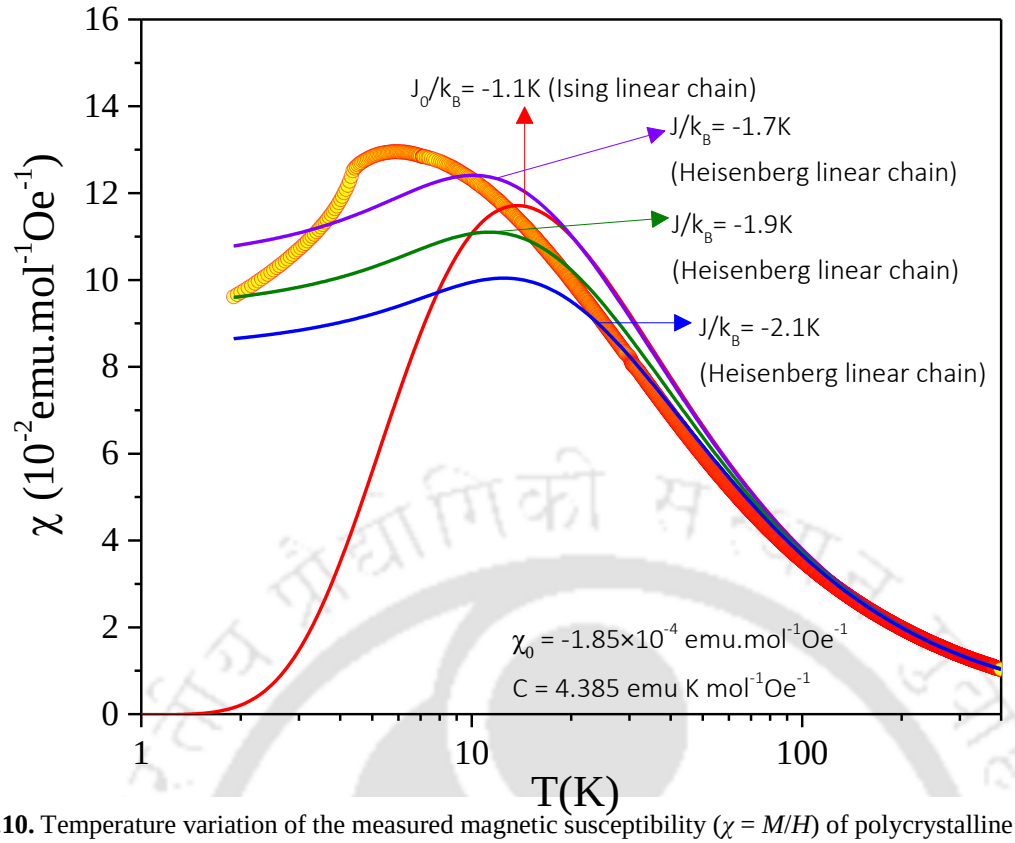

Fig. 3.10. Temperature variation of the measured magnetic susceptibility ($\chi = M/H$) of polycrystalline $MnNb_2O_6$ for H = 300 Oe from T = 1.9 to 400 K (open circles). The solid lines are fits to the ILC (equation (3.10)) and HLC (equation (3.11)) models with different values of the exchange constants J/k_B as marked. Log scale is used for temperature to highlight the variation at lower temperatures.

c-axis. This estimated magnitude of H_A is close to the magnitude of H_A calculated by Nielsen *et al.* [57,58] assuming dipole-dipole interaction as the source of anisotropy.

3.3.5. Temperature dependence of the paramagnetic susceptibility

The temperature dependence of the magnetic susceptibility $\chi = M/H$ (H = 300 Oe) for the temperature range of 1.9 to 400 K is shown in Fig. 3.10. The larger H = 300 Oe (rather than H = 100 Oe) was used for these measurements to improve the accuracy of the data for $T > 300$ K where M with H = 100 Oe is comparatively smaller and noisier. However, since M vs H is linear for $T > T_N$, the paramagnetic susceptibility (χ) is independent of H.

Following the procedure outlined in our analysis of χ vs T data for isostructural $CoNb_2O_6$ [68], we first fitted the data to the modified Curie-Weiss (MCW) law:

$$\chi = \chi_0 + \frac{C}{(T-\theta)} \tag{3.4}$$

Here $\chi_0 = -1.85 \times 10^{-4}$ emu mol^{-1} Oe^{-1} is determined in the limit of $1/T = 0$ from the plot of our data of χ vs $1/T$ with a focus on the high-T data (see inset of Fig. 3.11). This value of χ_0 is in excellent agreement with the theoretical estimate of diamagnetic susceptibility [80] of $MnNb_2O_6$ based on adding the diamagnetic contributions of the constituent atoms. The plot of $(\chi - \chi_0)^{-1}$ vs T for both $\chi_0 = 0$ and $\chi_0 = -1.85 \times 10^{-4}$ emu

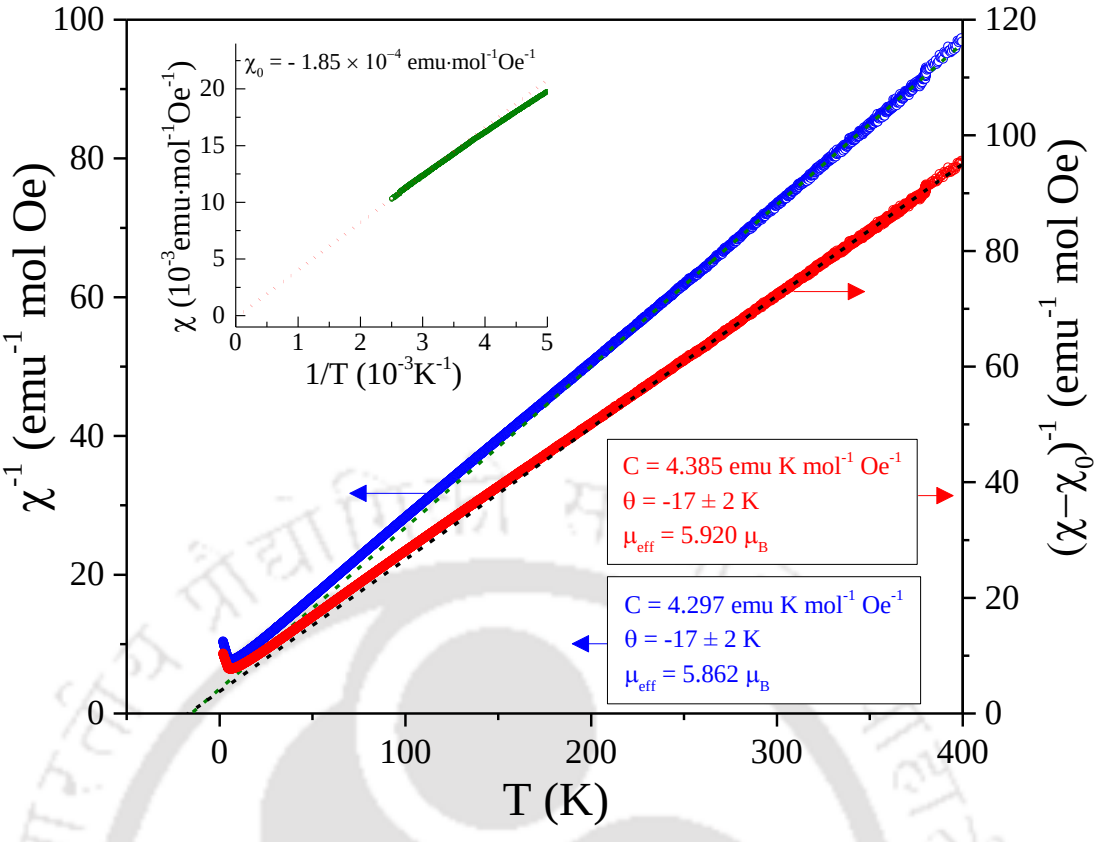

Fig. 3.11. Plots of $(\chi - \chi_0)^{-1}$ vs T for χ_0 = 0 and –0.000185 emu mol^{-1} Oe^{-1} to test the fits to the MCW (equation (3.4)). The linear fits for the higher temperature data (dotted line) are used to obtain C and θ listed in the figure. The χ vs $1/T$ plot shown in the inset is used to determine χ_0 in the limit of $1/T = 0$ by linear extrapolating the high-T data (dotted line).

mol^{-1} Oe^{-1} are shown in Fig. 3.11, both yielding $\theta = (-17 \pm 2)$ K from the linear fit for $T > 100$ K but different magnitudes of C = 4.385 (4.297) emu K mol^{-1} Oe^{-1} for $\chi_0 = -1.85 \times 10^{-4}$ (0) emu mol^{-1} Oe^{-1}. Using $C = N_A\mu^2/3k_B$ (N_A = Avogadro's number, k_B = Boltzmann constant) yields $\mu = 5.920\ \mu_B$ for $\chi_0 = -1.85 \times 10^{-4}$ emu mol^{-1} Oe^{-1} and $\mu = 5.862\ \mu_B$ for $\chi_0 = 0$. Since $\mu^2 = g^2S(S+1)\mu_B^2$, the expected value of μ for S = 5/2 and g = 2 is $\mu = 5.916\ \mu_B$, in good agreement with $\mu = 5.920\ \mu_B$ and g = 2.001 obtained for $\chi_0 = -1.85 \times 10^{-4}$ emu mol^{-1} Oe^{-1}. For $\mu = 5.862\ \mu_B$ obtained for $\chi_0 = 0$ yields g = 1.982 < 2 which is not physical for the S-state of Mn^{2+}. This shows the importance of including the correct non-zero χ_0 in the analysis using the MCW law, as also emphasized for the case of Co_3O_4 [81].

3.3.6. Determination of the exchange constants

The effective spin S = 5/2 of Mn^{2+} in $MnNb_2O_6$ is large enough to be classical like, unlike S = ½ for $CoNb_2O_6$ in which quantum effects were dominant [68]. Therefore, MFT should provide good estimates of the exchange constants in $MnNb_2O_6$. Using the Hamiltonian:

$$H = -\sum_{<ij>} J_{ij} \boldsymbol{S}_i . \boldsymbol{S}_j - g\mu_B H \sum_{<i>} \boldsymbol{S}_i \qquad (3.5)$$

the following equation for θ and T_N using MFT are obtained [79]:

$$3k_B\theta = S(S+1)[J_0Z_0 + (J_1Z_1 + J_2Z_2)] \quad (3.6)$$

$$3k_BT_N = S(S+1)[J_0Z_0 - (J_1Z_1 + J_2Z_2)] \quad (3.7)$$

Following the Hamiltonian defined in equation (3.1), J_0 is the exchange constant between Mn^{2+} ions along the *c*-axis with nearest neighbours $Z_0 = 2$. In addition, J_1 and J_2 are respectively the exchange interaction along the *b*-axis with $Z_1 = 2$ and along the body-diagonal of the *ab* plane with $Z_2 = 4$. Having only two experimental constants θ and T_N, only two exchange constants can be determined. Since there are three exchange constants in equations (3.6) and (3.7), we assume $J_1 = J_2 = J_\perp$ as found to be nearly valid in $CoNb_2O_6$ [68]. These assumptions, and $S = 5/2$ leads to the following equations for J_0 and $J_\perp$:

$$J_0/k_B = 3(\theta + T_N)/35 \quad (3.8)$$

$$J_\perp/k_B = (\theta - T_N)/35 \quad (3.9)$$

Using experimental magnitudes of $\theta = (-17 \pm 2)$ K, and $T_N = 4.36$ K yields $J_0/k_B = (-1.08 \pm 0.17)$ K and $J_\perp = (-0.61 \pm 0.06)$ K. The sum of the three exchange constants $J/k_B = (J_0 + 2J_\perp)/k_B = -2.3$ K. This magnitude of $J/k_B \simeq -2.3$K is further discussed in the next section.

In $CoNb_2O_6$, the variation of the paramagnetic χ vs T was shown to fit nicely with the prediction of Ising linear chain (ILC) using the equation [39,68]:

$$\chi = \chi_0 + \frac{C}{T}\exp\left(\frac{2J_0S^2}{k_BT}\right) \quad (3.10)$$

The fit with $S = ½$ valid for $CoNb_2O_6$ yielded $J_0/k_B = (6.2 \pm 0.2)$ K as the ferromagnetic exchange coupling between Co^{2+} ions along the *c*-axis. For Heisenberg linear chain (HLC), the corresponding expression for the temperature variation of χ is given by [39]:

$$\chi = \chi_0 + \frac{C}{T}\left(\frac{1+\Gamma}{1-\Gamma}\right) \quad (3.11)$$

In equation (3.11), $\Gamma = \coth(y) - (1/y)$ with $y = 2JS^2/k_BT$. We tried fits of the data of χ vs T in $MnNb_2O_6$ to both equation (3.10) for ILC and equation (3.11) for HLC using $S = 5/2$, $C = 4.385$ emu K mol^{-1} Oe^{-1} and $\chi_0 = -1.85 \times 10^{-4}$ emu mol^{-1} Oe^{-1} determined from our analysis based on the MCW law. The fit to equation (3.10) for ILC using positive J_0 is not possible since in this case there is no peak in χ vs T. For negative $J_0/k_B = -1.1$ K, we show the fit to ILC in Fig. 3.10, the fit failing for $T < 100$ K. For HLC, we show the fit for three different values of $J/k_B = -1.7$ K, −1.9K and −2.1 K. For $J/k_B = -2.1$ K, the fit of the data to HLC is very good above 25 K. For $T < 20$ K, the calculated curve falls below the experimental data, the peak position occurring near 15 K compared to about 6 K for the experimental data. This is likely due to neglect of anisotropy in the HLC model. So fits of the data to the HLC model for χ vs T is considered to be semiquantitative only since the position of the peak and magnitude of χ for $T < 20$ K do not match well with the HLC model. However, the magnitude of $J/k_B = -2.1$ K determined from the fit to HLC is close to total $J/k_B \simeq -2.3$ K estimated from the MFT. For these reasons, $J_0/k_B = -1.08$ K and $J_\perp/k_B = -0.61$ K determined

earlier are suggested to be reliable estimates of the intrachain and interchain exchange interactions in $MnNb_2O_6$. There have no other reported estimates of these exchange constants reported in $MnNb_2O_6$ with which to compare these results. For comparison, J_0/k_B = 6.2 K, J_1/k_B = −0.42 K and J_2/k_B = −0.67 K were determined for $CoNb_2O_6$ [68]. Although the signs and magnitude of the interchain exchange constants for $CoNb_2O_6$ and $MnNb_2O_6$ are nearly same, theoretical reasons for J_0/k_B being negative in $MnNb_2O_6$ and positive in $CoNb_2O_6$ still need to be understood.

3.4. Conclusions

The alaysis reported in this chapter on $MnNb_2O_6$ include the following key results: (i) the system orders antiferromagnetically below T_N = 4.36 K, in agreement with previous reports; (ii) a complete *H-T* phase diagram is presented with a triple point T_{TP} *(H, T)* = (18 kOe, 4.06 K), spin flop field $H_{sf} \simeq$ 18 kOe and exchange field $H_E \simeq$ 200 kOe; (iii) MFT and fit to the HLC model yields J_0 = −1.08 K as the intrachain exchange and $J_\perp \simeq$ −0.61 K as the interchain exchange coupling; (iv) the anisotropy field $H_A \simeq$ 0.8 kOe is determined from the magnitude of the spin-flop field, in good agreement with the estimates based on the dipole-dipole interaction; and (v) Analysis of the specific heat data on approach to T_N yields the critical exponent α = 0.12 (0.15) for $T > T_N$ ($T < T_N$). Good theoretical understanding is still needed regarding the differences in the magnetic properties of the four-transition metal niobates MNb_2O_6 (*M* = Mn, Fe, Co and Ni) having the same columbite structure, along the lines of our understanding of the magnetic properties of the transition metal oxides *M*O (*M* = Mn, Fe, Co and Ni) with the NaCl structure [82].

Chapter 4

Correlated-Barrier Hopping and non-Debye Relaxation in $MnNb_2O_6$

This chapter mainly deals with the dielectric properties of columbite $MnNb_2O_6$ system. In the introductory section, we elucidate the importance of columbites and their applications. The gaps in literature related to the dielectric and structural properties of $MnNb_2O_6$ system are also discussed. Later sections deal with brief experimental details and their results together with the systematic analysis followed by summary of important findings.

4.1. Introduction and Literature Background

Columbite compounds are basically transition metal oxides having general chemical formula A $(Nb/Ta)_2O_6$ (A = Mn, Co, Ni, Mg, Ca and Zn) and exhibit the orthorhombic crystal structure with the space group *Pbcn*(60)- D_{2h}^{14} as shown schematically in Fig. 4.1(a) [27,57,60,63,83]. Among the tantalite series (ATa_2O_6) the $MnTa_2O_6$ system is the only compound that exhibits columbite crystal structure with lattice parameters a = 14.4468(8) Å, b = 5.7664(3) Å and c = 5.0924(4) Å and bond angles Mn–O–Mn ≈ 95.4°; Ta–O–Ta ≈ 96.5°; Mn–O–Ta ≈ 127.4° [15,19,24,84,85]. In general, this orthorhombic unit cell consists of 24 oxygen atoms, 8 Nb/Ta atoms and 4 A site transition metals which represents four molecules. Usually, the A site atom is divalent and the Nb/Ta atoms are pentavalent; both the divalent and pentavalent cations are surrounded by six oxygen atoms forming slightly distorted octahedra of AO_6 and NbO_6/TaO_6. These octahedra are stacked in the following series: —A–Nb/Ta–Nb/Ta–A–Nb/Ta–Nb/Ta–A— along the *a*-axis and forms zig–zag chains along the *c*-axis by sharing their edges [19,21,23,27,68,84]. Further, the A site atoms arrange into a perfect isosceles triangular geometry in the *ab*-plane of the crystal which has been reported diagrammatically in our recent work [85, 86]. Since the past two decades, columbites have attracted the interest of the scientific and industrial community due to large commercial demand owing to their interesting physical properties, which have been explored in a wide variety of applications such as in wave guides, solid oxide fuel cells, electrochemical gas sensors, microwave devices, microstrip antennas and supercapacitors [1–3,85]. Due to large requirement and upsurge in the miniaturization of the electronic components in the electrical and mobile/wireless/satellite communication technology there is a need for the materials with high relative-dielectric permittivity (ε_r) and good quality factor (Q). Such requirements can be fulfilled by low cost columbites and their composites, which are treated as novel electronic materials of high ε_r with a low-loss factor useful for ceramic resonators and filters [4,5,7]. The Co-based columbite (Ising-spin chain ferromagnet $CoNb_2O_6$) is quite well-known because it exhibits quantum excitations in the vicinity of the quantum critical point. Field-induced transitions and other unique magnetic and electrical properties and such phenomena can be explored for electro-optical devices and mechanical filter coatings [3,8]. Recent studies on similar systems such as $Mg/NiNb_2O_6$ have been explored in the potential catalytic activity for the generation of hydrogen and related applications in water splitting process [16]. Further, $MnNb_2O_6$ is an excellent ceramic material belonging to the columbite family which possesses good microwave dielectric properties (ε_r = 20–22 with $Q \times F$ = 12 900–34 300 GHz) [15,16]. Interestingly, this system also shows

antiferromagnetic (AFM) ordering at T_N = 4.36 K with an effective magnetic moment of μ_{eff} = 5.96μ_B and further exhibits three distinct magnetic phases with a triple point, $T_{TP}(H, T)$ = (18.0 kOe, 4.06 K), where all the three phases coexist at T_{TP} [86]. Previous studies by Alvarado *et al*. and Orera *et al*. reported the electrical properties of both nominal and off-stoichiometric (δ) $MnNb_2O_{6-\delta}$ and $MnNb_{2-x}Ti_xO_{6-\delta}$ using impedance spectroscopy, these studies reveal higher ionic conductivity of approximately 6.0×10^{-5} ohm^{-1}cm^{-1} [17,18]. However, compounds with oxygen vacancies ($\delta \approx 0.02$ in the presence of 5% H_2 gas) lead to four orders of enhancement in the conductivity as compared to a pure stoichiometric $MnNb_2O_6$ system without any oxygen vacancies [17]. Nevertheless, substitution of Ti at Nb sites ($MnNb_{2-x}Ti_xO_{6-\delta}$ ($x < 0.2$)) results in no change in the crystal structure but a significant change in the ionic conductivities at very high temperature [17]. $MnNb_2O_6$ is also used as the best substituent (≈3 mol%) to enhance the dielectric properties of $Ag(Nb_{0.8}Ta_{0.2})O_3$ which results in enhanced ε_r = 474 and a very low loss-tangent (Tan δ = 0.00307) [87]. Moreover, dielectric studies on its isostructural compound $MnTa_2O_6$ reveals a high quality factor of $Q\times F$ = 16500 GHz with a dielectric constant of $\varepsilon_r \approx 20.3$ which also exhibits three unique magnetic phases which merge at the triple point, $T_{TP}(H, T)$ = (17.0 kOe, 5.69 K) and shows AFM behaviour below the Néel temperature T_N = 6 K [15,85]. Similarly, $ZnNb_2O_6$ ceramic exhibits the highest ε_r (≈25) among all the columbites with $Q\times F$ =83700 GHz in comparison with $MgNb_2O_6$ which shows the highest quality factor of $Q\times F$ = 93800 GHz with a slightly lesser ε_r ≈21 [15]. These two columbites are considered as excellent dielectric materials for microwave technology and they are sintered at relatively low temperatures compared to other ceramics, including perovskites [88]. In the past decade researchers have substituted these columbites with different compounds like TiO_2 and $CaTiO_3$ in order to increase the dielectric constant of these materials. Pullar and his co-workers substituted $ZnNb_2O_6$ with 15%, 22% and 30% of TiO_2 and obtained enhanced ε_r values in the range 29–52 [89]. While the $CaTiO_3$ substitution of 9%, 20% and 25% in $ZnNb_2O_6$ matrix yielded similar ε_r (21–23) values as above. Similar results are noticed in case of the composites $MgNb_2O_6 + xTiO_2$ (x = 7%–13%) and $CaNb_2O_6 + xTiO_2$ (x = 11%–15%) with improved dielectric properties with the magnitude of $\varepsilon_r \approx$ 22–38, 17–25, respectively [89]. On the other hand, substitution of Ta at Nb sites in $MgNb_2O_6$ and $ZnNb_2O_6$ columbites results in a better quality factor but slightly decreased ε_r, both these quantities are quite sensitive to the heat-treatment conditions [90]. All the above discussed results and the technical concepts involved in achieving the improvement of electrical properties strongly motivated us to investigate the electrical properties of $MnNb_2O_6$ over a wide temperature interval and frequencies aiming to understand the type of conductivity mechanism and frequency dependent dipole relaxation mechanism. Until today, there has been a lack in literature on a comprehensive study of the dielectric behaviour of stoichiometric $MnNb_2O_6$. Hence, our current study fulfils this gap by providing a detailed *ac*-conductivity, Nyquist plot analysis comprising the grain/grain-boundary conductivity by circuit analysis and different types of dielectric relaxation mechanism involved with the $MnNb_2O_6$ system by means of modulus spectroscopy.

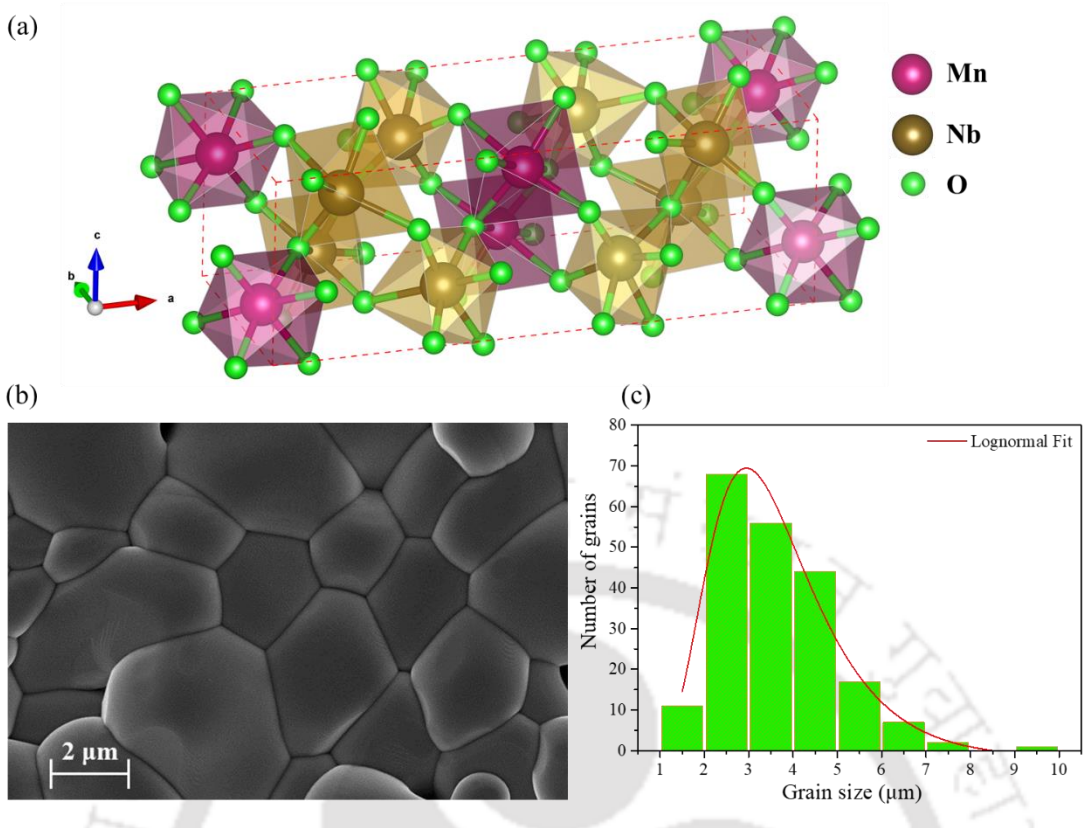

Fig. 4.1. (a) The Orthorhombic Unit cell and (b) the FE-SEM image of re-sintered $MnNb_2O_6$ sample along with (c) the histogram analysis of grain size and the solid red line is lognormal distribution.

4.2. Materials synthesis and morphology

The bulk polycrystalline $MnNb_2O_6$ samples were prepared through standard solid-state reaction method by mixing the stoichiometric proportions of binary oxides MnO and Nb_2O_5 in an agate mortar. The oxide mixture is grinded nearly 5 to 6 h until the homogeneity is attained. This uniformly mixed oxide powder is pressed into cylindrical pellets of 1 mm thickness and 13 mm in diameter with the help of a hydraulic press (50 kg.cm^{-2}). These green pellets were initially heat treated at 1150 ˚C in air for 12 h finally re-grinded and sintered at 1200 ˚C for 24 h in air. The phase evaluation has been done by analysing the crystal structure by means of x-ray diffraction (XRD) technique performed by the Rigaku x-ray diffractometer (model: TTRAX III) with CuKα_1 radiation (λ = 1.5406 Å). The Rietveld refinement of the recorded XRD pattern yields the lattice parameters a = 14.4327(3) Å, b = 5.7627(2) Å and c = 5.0819(2) Å quite close to the standard literature data. For the elemental analysis and electronic structure determination we used an x-ray photoelectron spectrometer (XPS) designed from Kratos analytical (model: AXIS Supra+) configured with a dual monochromatic x-ray source Al Kα/Ag Lα (2984.2 eV) with spatial resolution less than 1 μm. The XPS analysis confirms the pentavalent and divalent configuration of Nb and Mn ions, respectively these details are reported in our previous work [86]. In order to examine the microstructure of the samples we used field emission scanning electron microscope (FE-SEM) in SE mode these images are shown in Fig. 4.1(b) displaying very well grown grains and clear visible grain boundaries. A methodical statistical histogram analysis of grain size distribution along with the lognormal curve fit [$y = y_0 +$

$\frac{A}{xD\sqrt{(2\pi)}} \exp\left[\frac{-\left(ln\frac{x}{x_c}\right)^2}{2D^2}\right]$] shown in the Fig. 4.1(c) yields the median of grain size $x_c \approx 3.4$ μm with standard deviation $D \approx 1.3$ μm and the average grain size is found to be 3.6 μm. A detailed frequency and temperature dependence of broad band dielectric measurements were performed by means of an Alpha-AN impedance analyser equipped with Quatro nitrogen gas cooling/heating system (Novocontrol Technologies, Germany). These dielectric experiments were performed at different frequencies from 50 Hz to 5 MHz with a 0.5 V root mean square ac-voltage in the temperature range 173 K–473 K. For these measurements silver electrodes are deposited on either side of the cylindrical pellet to form a parallel-plate capacitor geometry.

4.3. Dielectric spectroscopy

4.3.1. Dielectric relaxation

Figures 4.2(a) and (b) show the variation of relative dielectric permittivity (ε_r) and the loss tangent (Tan δ), respectively, as a function of temperature, measured for various frequencies (f) between 50 Hz and 5 MHz for the bulk polycrystalline $MnNb_2O_6$ system. We notice relatively higher values of ε_r (≈35) with dielectric loss, Tan $\delta \approx 0.9$ for 1 kHz and for 1 MHz, $\varepsilon_r \approx 28.1$ with very less dielectric loss, Tan $\delta \approx 0.008$ at room temperature. In this case, the magnitude of ε_r increases with increasing temperature for all the

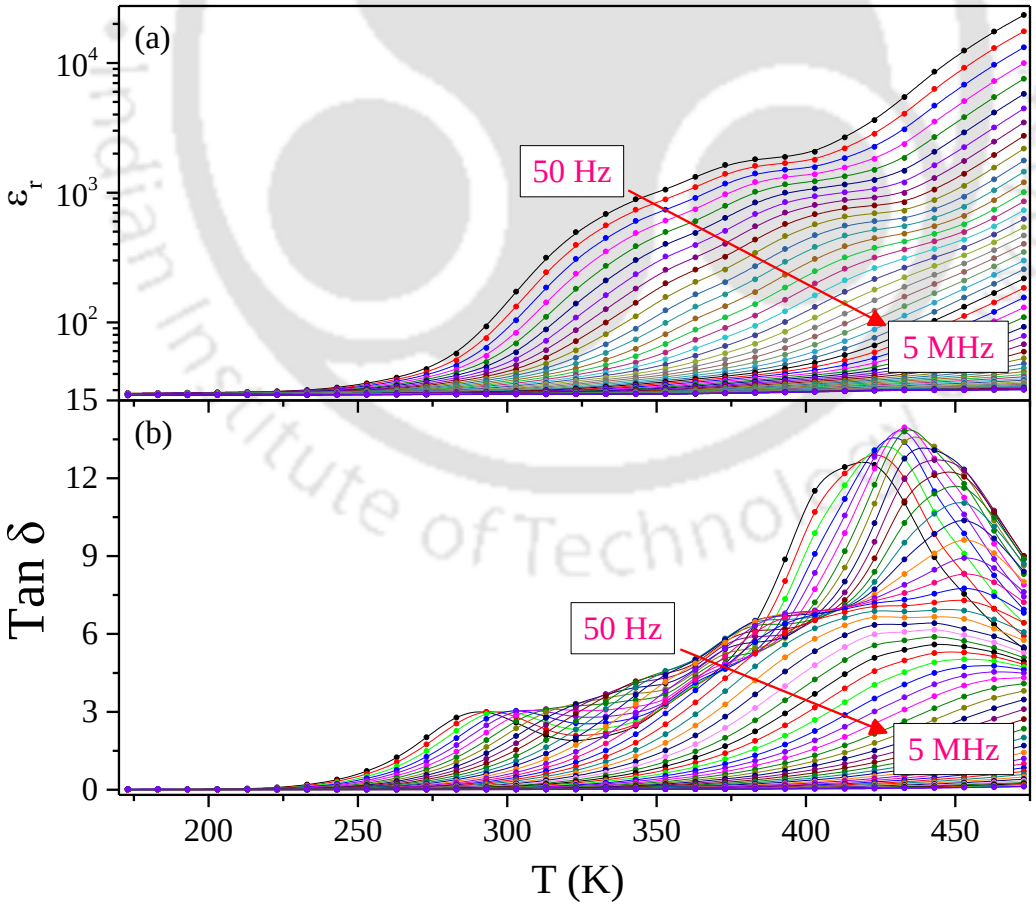

Fig. 4.2. Temperature variation of (a) relative dielectric permittivity, $\varepsilon_r(T)$ and (b) loss tangent, Tan $\delta(T)$ measured at distinct frequencies (50 Hz ⩽ f ⩽ 5 MHz) for the temperature range 173–473 K.

frequencies (Fig. 4.2(a)) due to an increase in thermal energy which facilitates the dipoles in the preferred orientation to attain the highest polarization. However, ε_r is nearly temperature independent below 250 K where the dipoles do not have enough thermal energy to undergo orientation polarization [91,92]. Nevertheless, the variation of ε_r vs T also shows a shoulder around 400 K in the frequency range 50 Hz–1 kHz (Fig. 4.2(a)). Later, this shoulder in ε_r—T disappears as the frequency increases to beyond 1 kHz; we believe that this shoulder appears largely due to space charge polarization at lower frequencies (<1 kHz). This feature is further supported by the temperature dependent loss tangent analysis (Fig. 4.2(b)), where two broad cusps centred across 300 K and 430 K are clearly visible below 1.5 kHz. As the measurement frequency increases above 1.5 kHz both these cusps merge with each other and appear as one single board hump which is associated with the relaxation of permanent dipoles. This large broad hump-like feature is consistent with the disappearance of the shoulder at higher frequencies (till 5 MHz) as noticed in Fig. 4.2(a) [93]. The frequency (f) variation of ε_r and Tan δ at several temperatures from 173 to 473 K is shown in the figures 4.3(a) and (b), respectively. This data reveals a large dispersion in ε_r at lower frequencies and a nearly temperature independent behaviour at higher frequencies. Usually at lower frequencies, due to the slow variation of the *ac*-field, the interaction of the dipoles with the field is high enough to lead to a larger magnitude of ε_r. These higher values of ε_r can also be attributed to the accumulation of residual charges at

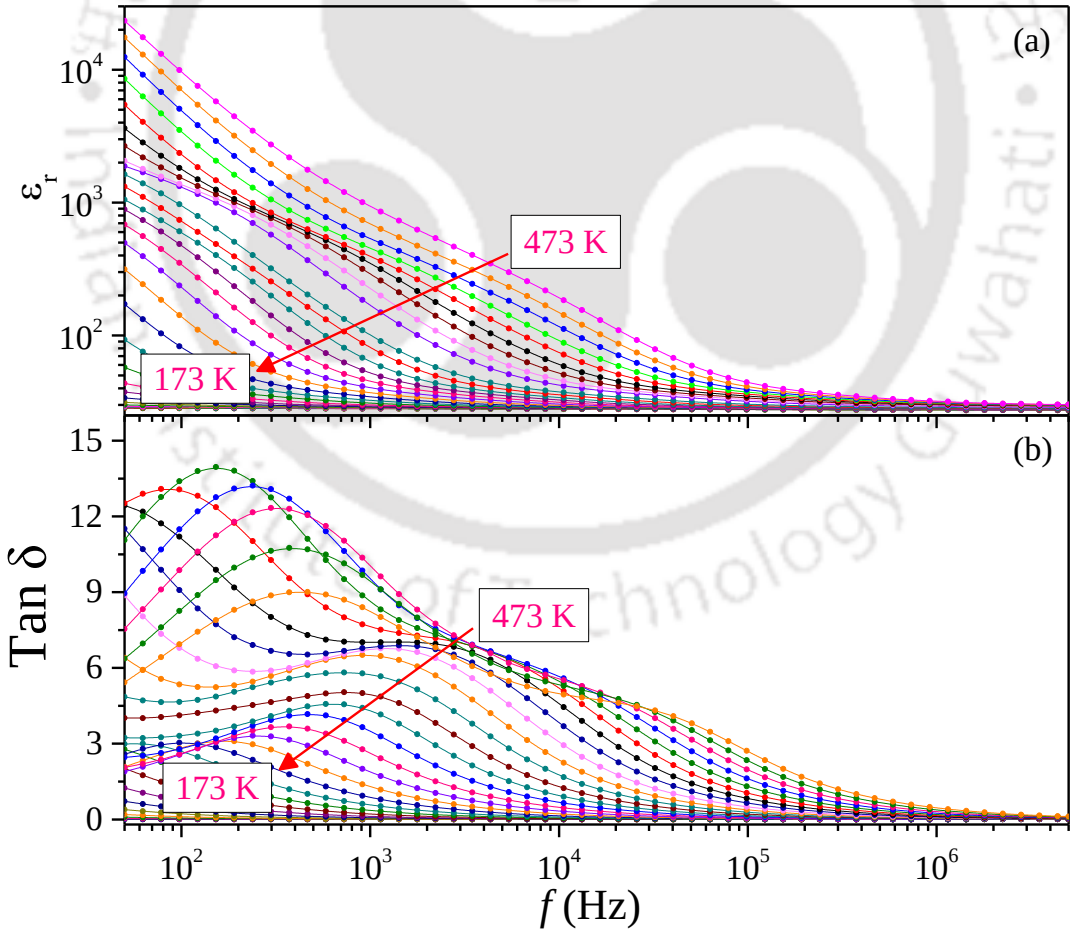

Fig. 4.3. The frequency variation of (a) $\varepsilon_r(f)$ and (b) tan $\delta(f)$ recorded at various temperatures between 173 and 473 K in the frequency range 50 Hz–5 MHz.

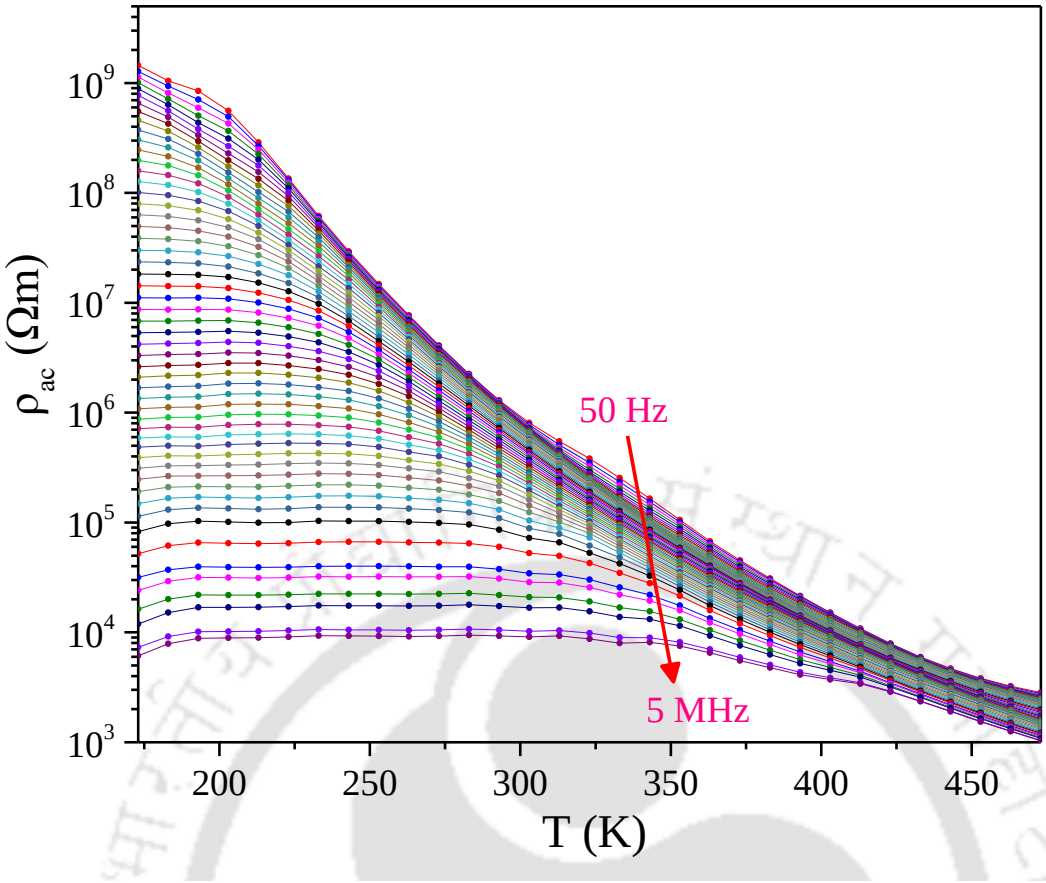

Fig. 4.4. Temperature dependent of *ac*-resistivity, $\rho_{ac}(T)$ for various frequencies between 50 Hz and 5 MHz.

the interfaces across the grain/grain-boundaries of the sample and/or across the boundary of sample-electrode geometry. Whereas, at higher frequencies due to the rapidly changing applied *ac*-field, the dipoles are unable to follow the field yielding to lower values of ε_r [91]. On the other hand, the Tan δ vs f recorded at different temperatures in the range 173–473 K exhibit two dielectric relaxation humps centred at 450 Hz and 32 kHz with a significant loss (tan $\delta \approx 8.9$ and 3.5 respectively) at 473 K. Also, the relaxation frequencies in each case further shifts towards lower frequencies with increasing the measurement temperature. The higher frequency hump is associated with grain boundary relaxation while the lower frequency hump is due to the relaxation of charge carriers in the interface between the sample and the electrode which will be discussed later in detail using the Nyquist plots.

4.3.2. AC conductivity analysis

Next, we discuss the temperature dependence of ac-resistivity ($\rho_{ac}(T)$) which, as shown in the Fig. 4.4, for various frequencies between 50 Hz and 5 MHz. In the present case $MnNb_2O_6$ exhibits the lowest value of $\rho_{ac} \approx 1000$ Ωm and 1200 Ωm for $f \approx 5$ MHz and 1 MHz at 473 K, respectively. The variation of $\rho_{ac}(T)$ from 173 K to 325 K is almost independent of temperature; however, beyond 325 K a continuous decrease of resistivity with rise in temperature is evident till 473 K, signifying the negative temperature coefficient of ρ_{ac} similar to a typical semiconductor. To understand the exact charge transport mechanism in the investigated system we performed an *ac*-conductivity ($\rho_{ac}(T)$) analysis. We initially tested the Arrhenius

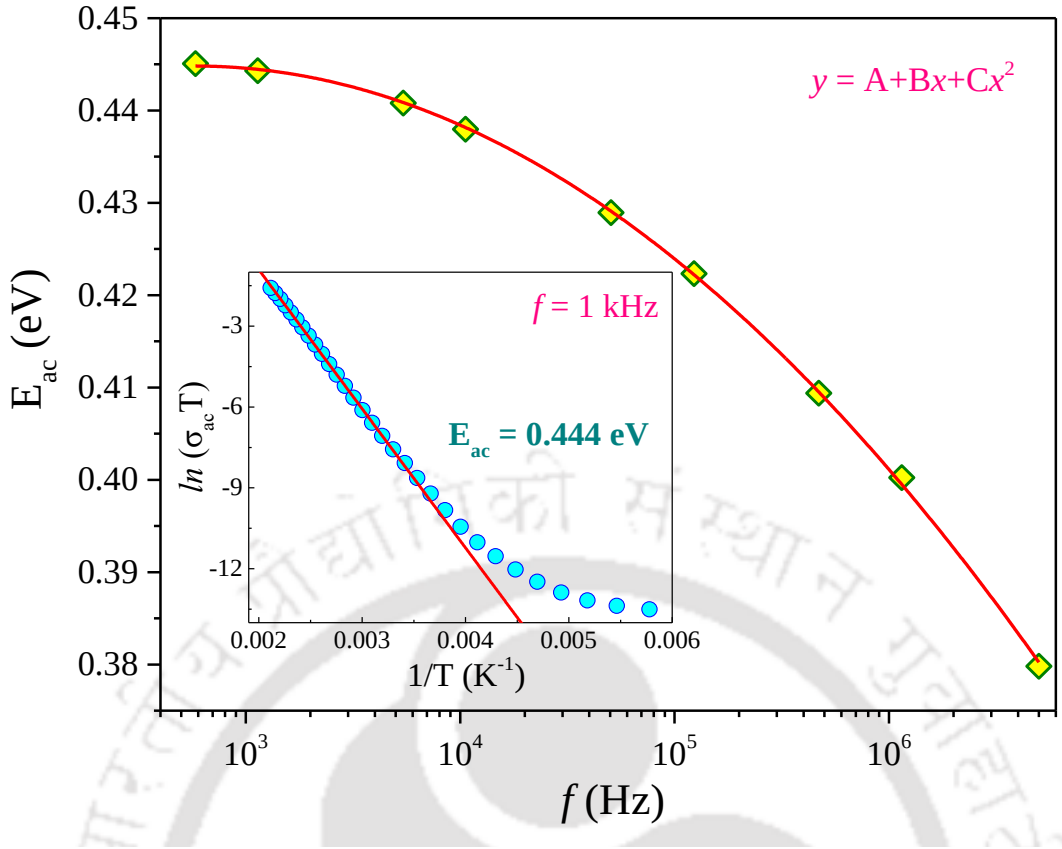

Fig. 4.5. The plot of activation energy (E_{ac}) vs frequency (f) for *ac*-conduction in the frequency range 50 Hz–5 MHz and the inset shows the determination of E_{ac} (0.444 eV) from the Arrhenius equation for the temperatures above 300 K at a particular frequency, f = 1 kHz as an illustration. The solid red curve in the main panel represents the quadratic polynomial fit to the data.

expression given in equation (4.1). Accordingly, the linear fit for the plot between the logarithmic variation of product $\rho_{ac}T$ has been plotted against the inverse of the temperature ($\ln(\rho_{ac}T)$ vs $1/T$) in the inset of Fig. 4.5. The linear variation of $\rho_{ac}T$ supports the Arrhenius behaviour indicating the thermally activated charge transport mechanism prevails in $MnNb_2O_6$ system. Further, the linear fit provides the activation energy, E_{ac} = 0.444 eV for 1 kHz and it starts to deviate for T < 300 K, giving us a signature of different conduction mechanisms at lower temperatures [17,94,95],

$$\sigma_{ac}T = \sigma_0 e^{\left(-\frac{E_{ac}}{kT}\right)} \quad (4.1)$$

The Arrhenius equation holds for all the *ac*-conductivity curves measured at various frequencies (similar to the plot shown in the inset of Fig. 4.5 for f = 1 kHz) for T > 300 K and provides the activation energy E_{ac} of the charge carriers. The estimated magnitudes of E_{ac} for different frequencies are plotted in the main panel of Fig. 4.5. The frequency variation of E_{ac} follows the trend of a quadratic polynomial expression: $y = A + Bx + Cx^2$ with the constants A (0.413 eV), B (0.023 eV Hz^{-1}) and C (−0.004 eV Hz^{-2}). The solid red line represents the mathematical fit corresponding to the above discussed quadratic polynomial while the scattered points represent the magnitude of E_{ac}. The decreasing behaviour E_{ac} with frequency could be attributed to the fact that the applied frequency enhances the jump-frequency of charge carriers between the localized states. This confirms the conduction mechanism is mediated by the hopping process [96–98]. To understand the underlying hopping conduction mechanism at lower temperatures T < 300 K, we analysed

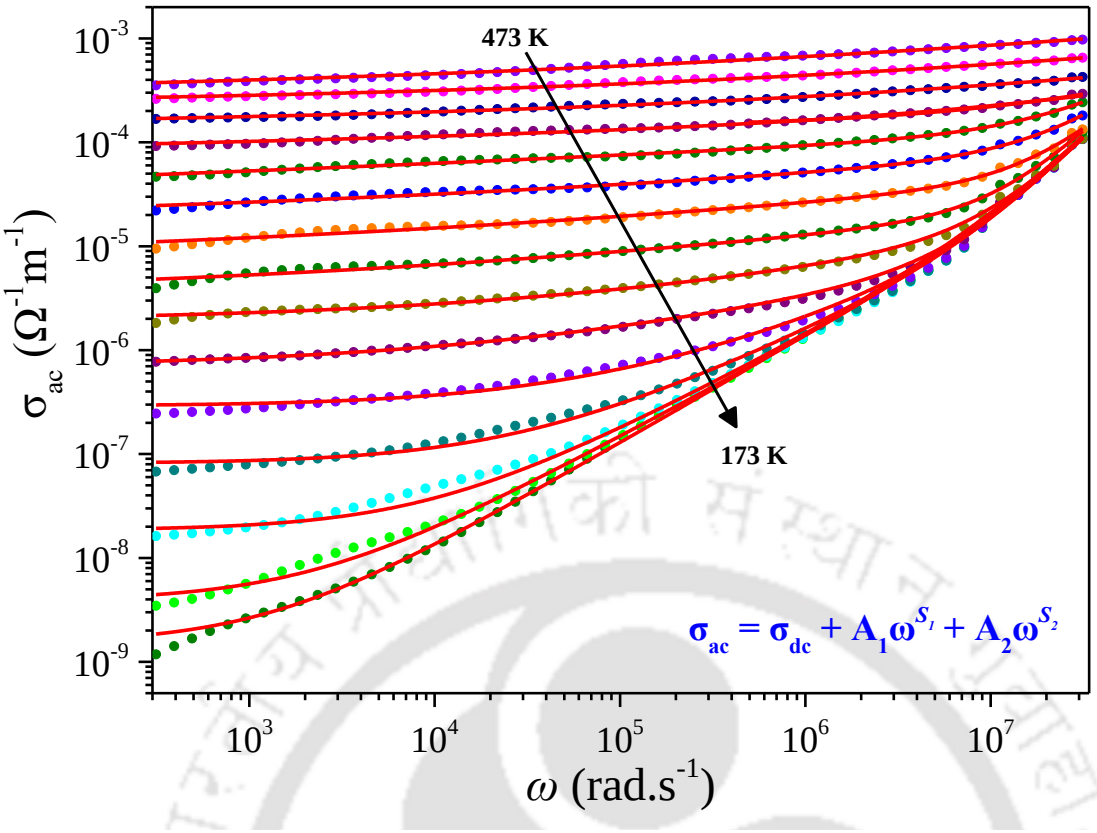

Fig. 4.6. The plot of *ac*-conductivity (σ_{ac}) vs angular frequency ($\omega = 2\pi f$) measured between 50 Hz and 5 MHz at various temperatures (173–473 K). The solid red lines indicate the mathematical curve fitting of Double power law [$\sigma_{ac}(\omega) = \sigma_{dc} + A_1\omega^{s_1} + A_2\omega^{s_2}$].

the frequency dependence of *ac*-conductivity, $\sigma_{ac}(\omega)$ for the frequency range 50 Hz–5 MHz at various measurement temperatures between 173 K and 473 K as depicted in Fig. 4.6. For every temperature plot there exists three different regions in the $MnNb_2O_6$ system. The first region, at lower frequencies corresponds to the *dc*-conduction mechanism as evident by frequency-independent plateaus. Further, as the frequency increases the system shows frequency dependent conductivity (σ_{ac}) which consists of lower (10^3–10^6 rad s^{-1}) and higher frequency (>10^6 rad s^{-1}) dispersive regions corresponding to the second and third region in the conductivity spectra, respectively. This process usually takes place through short-range hopping of charge carriers between localized states (neighbouring vacant sites). Concerning the *dc* counterpart, the hopping process requires a long time period, resulting in long-range translational motion of charge carriers at lower frequencies which is explained by Funke's jump relaxation model [99,100]. Due to the presence of two frequency-dependent conductivity regions in $MnNb_2O_6$ system, we used the Double power law (equation (4.2)) instead of Jonscher power law for the conductivity analysis. Similar type of results with two distinct frequency dispersive conductivity regions and two exponents in the power law has been reported in cerium-based O_6 family of systems such as $CeTiNbO_6$ and $CeTiTaO_6$ [101,102].

$$\sigma_{ac}(\omega) = \sigma_{dc} + A_1\omega^{s_1} + A_2\omega^{s_2} \quad (4.2)$$

where σ_{dc} is the frequency-independent term corresponds to *dc*-conductivity, $\omega(= 2\pi f)$ is the angular frequency, A_1 and A_2 are the temperature-dependent pre-exponent factors and 's_1 and s_2' are the frequency exponents indicating the degree of interaction between the charge carriers and the surrounding environment [103]. The exponent s_1 lies between 0 and 1 which corresponds to the lower frequency dispersive region of

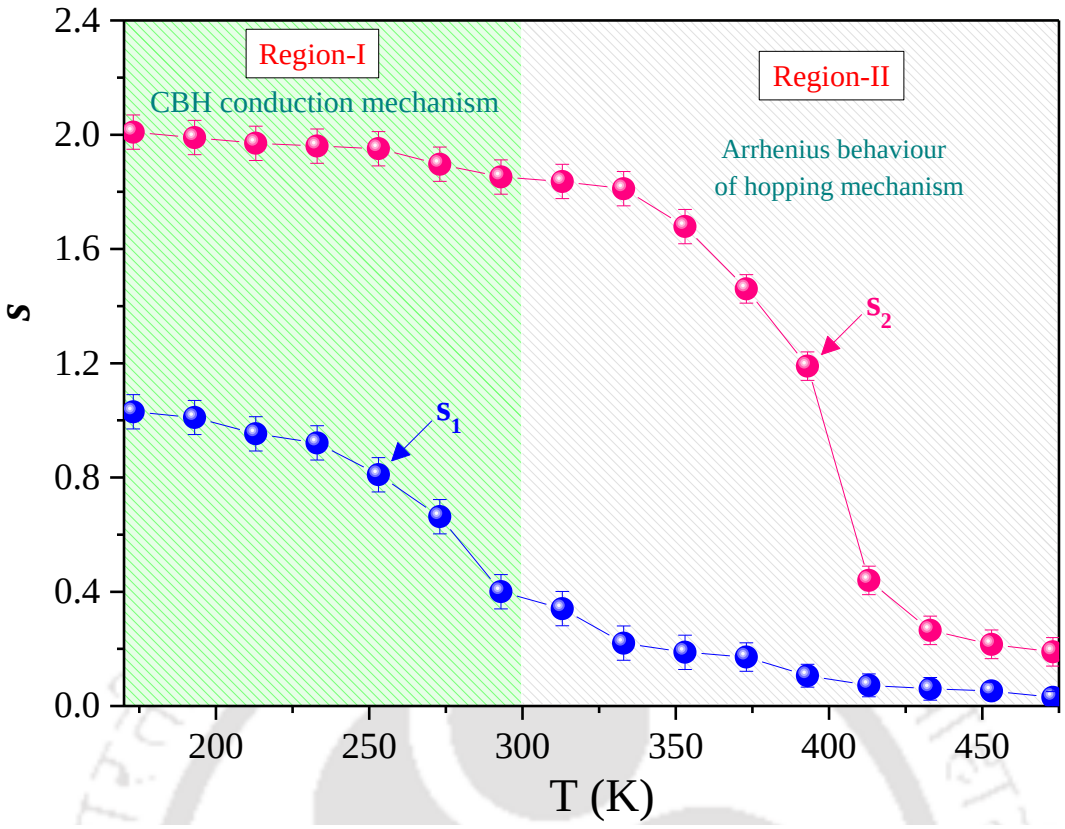

Fig. 4.7. The temperature dependence of the exponents s_1 and s_2 obtained from the Double power law in the temperature range 173–473 K for $MnNb_2O_6$ system.

conductivity (second region) arises due to the grain boundary, whereas the exponent s_2 lies between 0 and 2 which corresponds to the higher frequency dispersive region of conductivity (third region) mainly arises due to grain. Depending on the nature of temperature dependency of 's_1 and s_2' values, the charge transport mechanism can be analysed in any high-*k* dielectric material using different theoretical models such as: quantum mechanical tunnelling model, the correlated barrier hopping (CBH) model, the overlapping large-polaron tunnelling model and the non-overlapping small polaron tunnelling model [104]. In the present system, the Double power law expression given in equation (4.2) [99,100] is fitted systematically to the experimentally obtained data of $\sigma_{ac}(\omega)$ as shown in the Fig. 4.6 where the logarithmic variation of σ_{ac} is plotted as function of ω and the corresponding solid lines represent the best fits of Double power law. These plots yield the magnitude of exponents 's_1 and s_2' and σ_{dc} for various temperatures from 173 K to 473 K. The obtained exponents 's_1 and s_2' are plotted against temperature in Fig. 4.7, from this figure it is clear that the magnitude of exponent s_1 decreases from 1.03 to 0.03 and the exponent s_2 decreases from 2.00 to 0.19 as the temperature increases from 173 K to 473 K, respectively. This behaviour is in-line with those systems which exhibit the CBH conduction mechanism (according to CBH the magnitude of *s* must decrease with temperature) [95,105]. Existence of similar type of CBH conduction mechanism and the decreasing trend of the exponents 's_1' and 's_2' with temperature have been observed in several perovskite and spinel oxides such as $La_{0.9}Sr_{0.1}MnO_3$ [106], $BaZr_{0.1}Ti_{0.9}O_3$ [107] and $MgCr_2O_4$ [108]. Further the temperature dependent of exponent $s(T)$ is divided into two different temperature regions (Region-I: 173–300 K and Region-II: 300–473 K) both the regions show CBH conduction mechanism as estimated by 's_1 and s_2', but for temperatures

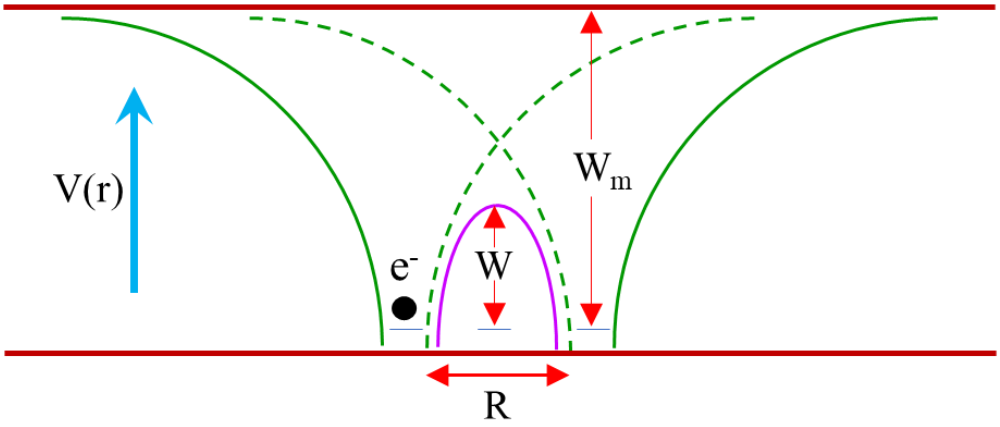

Fig. 4.8. Diagrammatic representation of coulomb wells in the CBH model.

above 300 K (Region-II) the hopping mechanism shows the thermally activated Arrhenius like behaviour as discussed in the first paragraph of this section. However, in Fig. 4.7 the exponent s_1 decreases with the rate $\partial s_1/\partial T = -1.9\times10^{-3}$ K^{-1} and -7.8×10^{-3} K^{-1} for the temperature range 173–233 K and 233–300 K, respectively in Region-I, and $\partial s_1/\partial T = -1.7\times10^{-3}$ K^{-1} in Region-II. Similarly, the exponent s_2 decreases with the rate $\partial s_2/\partial T = -1.3\times10^{-3}$ K^{-1} in Region-I but shows a nonlinear variation in Region-II. The expression for exponent s according to the CBH model is given below [96,109],

$$s = 1 - \frac{6kT}{W_m - kT\ln\left(\frac{1}{\omega\tau}\right)} \tag{4.3}$$

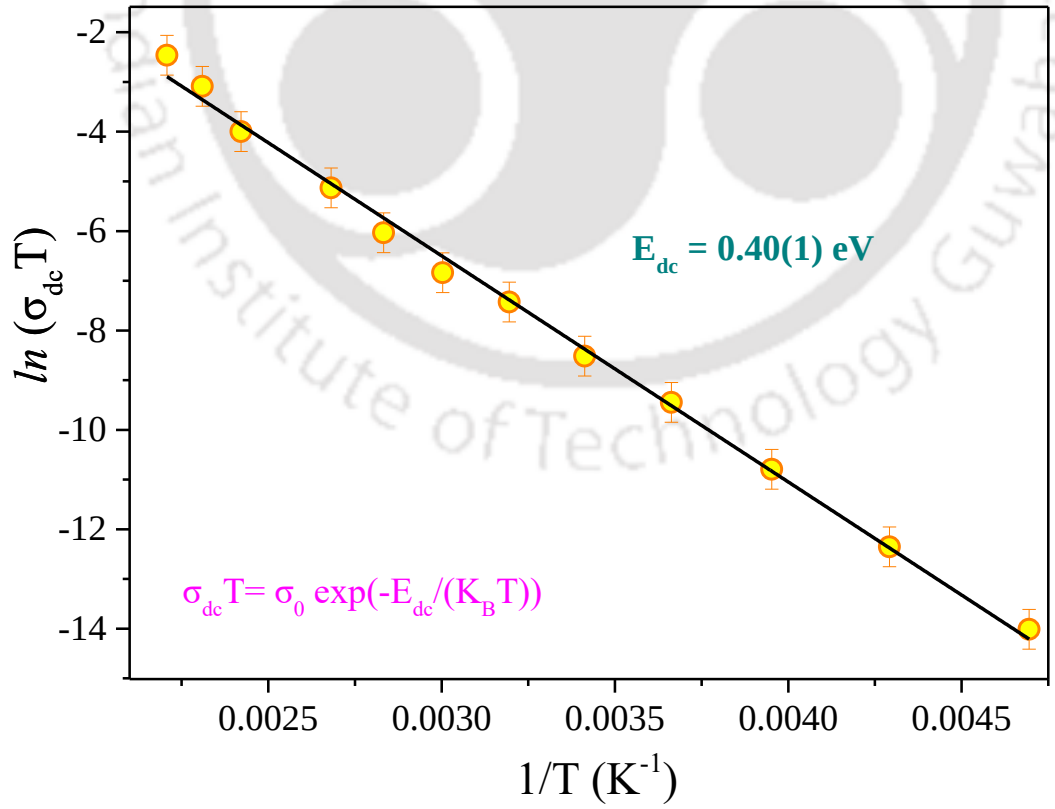

Fig. 4.9. The plot of ln ($\sigma_{dc}T$) vs 1/T for *dc*-conduction obtained from the double power law for lower frequency region and the solid black line is the linear fit of Arrhenius equation.

In the above expression, the quantity τ represents the relaxation time, W_m is the maximum barrier height and k is the Boltzmann's constant (8.617×10^{-5} eV K^{-1}). In the CBH model, the nearest neighbouring Coulombic potential wells overlap, thereby reducing the maximum barrier height W_m to a lower value W (called effective barrier height) as described in equation (4.4). The charge carriers hop over this effective coulombic barrier height W to the neighbouring vacant sites at a hopping length R which is usually termed as 'shortrange translational hopping' mechanism as shown in Fig. 4.8 [96,105],

$$W = W_m - \left(\frac{e^2}{\pi\varepsilon_r\varepsilon_0 R}\right) \tag{4.4}$$

In the low frequency regime, the *dc*-conductivity σ_{dc} (obtained from the Double power law) increases with increasing temperature due to thermally activated charge carriers. For $T > 300$ K the *dc*-conductivity follows the Arrhenius relation given below [95,110];

$$\sigma_{dc}T = \sigma_0 e^{\left(-\frac{E_{dc}}{kT}\right)} \tag{4.5}$$

where σ_0 is the pre-exponential factor, E_{dc} is the activation energy pertaining to the *dc*-conductivity part and k is the Boltzmann constant (8.617×10^{-5} eV K^{-1}). The above Arrhenius equation is fitted linearly to the plot $\ln(\sigma_{dc}T)$ vs $1/T$ as shown in the Fig. 4.9 and the slope of the linear fit provides the activation energy E_{dc} = 0.40 eV for $MnNb_2O_6$.

4.3.3. Complex electric modulus

To extract detailed information about the distribution of the dielectric relaxation times and the actual relaxation mechanism, a complex electric modulus formalism has been employed to verify different polarization mechanisms (such as space charge polarization, electrode polarization and interfacial polarization) [91,111–113]. Initial studies by Macedo *et al*. introduced this Modulus formalism which mainly governs the bulk effects and this idea can be utilized to distinguish the frequency regions of localized short-range and delocalized long-range charge transport. In this representation even, a small capacitance value could play a major role; consequently, the polarization effect from the electrode can be suppressed [113–115]. The reciprocal of the complex dielectric permittivity (ε^*) is termed as complex electric modulus (M^*) as given below [91,115,116],

$$M^*(\omega) = \frac{1}{\varepsilon^*(\omega)} = \frac{1}{\varepsilon' - j\varepsilon''} = \frac{\varepsilon'}{(\varepsilon')^2 + (\varepsilon'')^2} + j\frac{\varepsilon''}{(\varepsilon')^2 + (\varepsilon'')^2} = M'(\omega) + jM''(\omega) \tag{4.6}$$

$$M^*(\omega) = j\omega C_0 Z^*(\omega) = -\omega C_0 Z'' + j\omega C_0 Z' = M'(\omega) + jM''(\omega) \tag{4.7}$$

In the above expressions, C_0 is the vacuum capacitance of the cell and $\omega(=2\pi f)$ is the angular frequency. The real component of the modulus ($M'(\omega) = -\omega C_0 Z''$) and the imaginary component of modulus ($M''(\omega) = \omega C_0 Z'$) are plotted against ω for the temperature range 173–473 K as shown in figures 4.10(a) and (b), respectively. Fig. 4.10(a) shows the continuous frequency dispersion in $M'(\omega)$ with increasing frequency and finally attains a maximum saturated asymptotic value M_∞ ($=1/\varepsilon_\infty$) in the higher frequency region for all temperatures (here ε_∞ is the high-frequency bulk dielectric permittivity). At lower frequencies, $M'(\omega)$

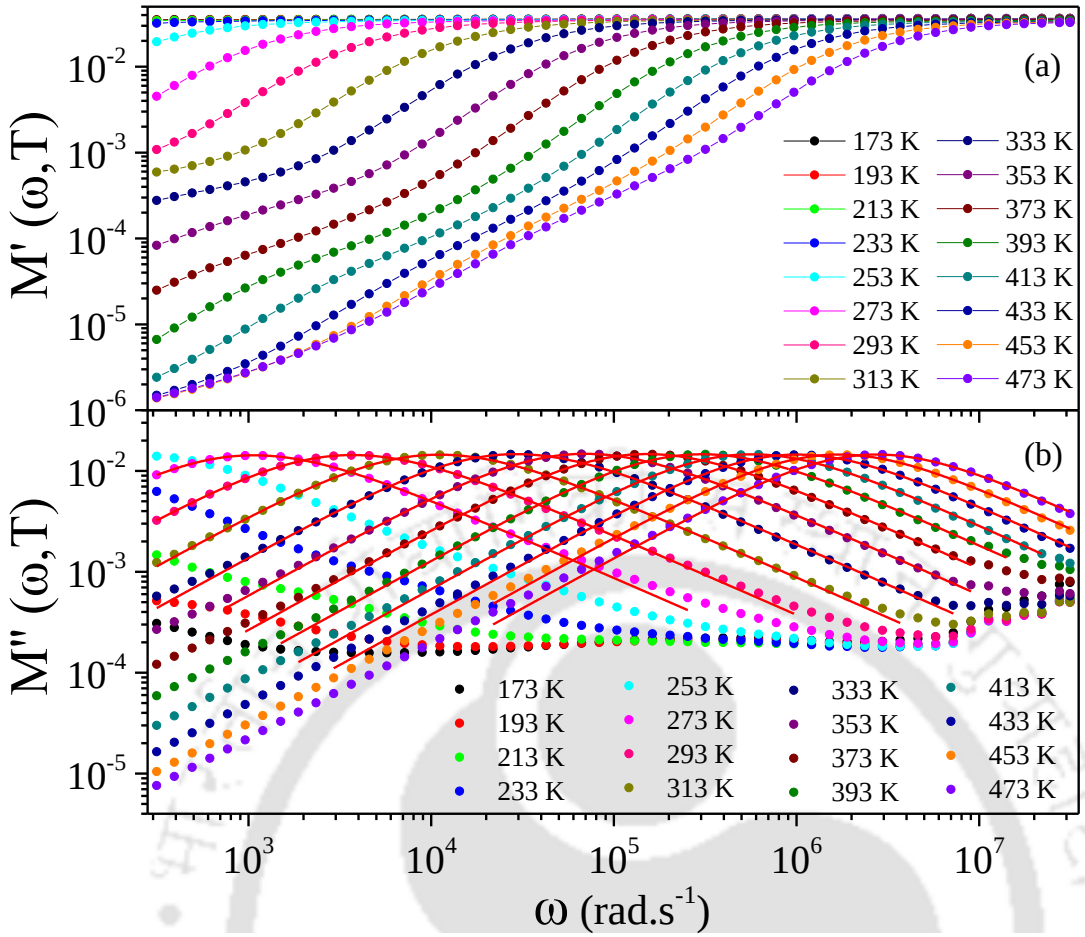

Fig. 4.10. The frequency (ω) variation of (a) real part $M'(\omega)$ and (b) imaginary part $M''(\omega)$ of complex modulus spectra (M^*) at different measured temperatures (173–473 K). The solid red lines are the curve fitting of modified KWW function (equation (4.12)).

gradually approaches a negligibly small value, suggesting that the contribution of electrode polarization is negligible and can be ignored in the complex electric modulus formalism [91,114,115,117]. On the other hand, in Fig. 4.10(b), $M''(\omega)$ curves shows a broad cusp ($M''_{max} \approx 0.0145$) at a particular frequency termed as relaxation frequency (ω_{max}) for all temperatures. These cusps correspond to the dipole relaxation in grains which falls in the bulk region of Nyquist plots. Further, these broad cusps at ω_{max} indicate the transition from *dc* to *ac*-conduction phenomena with increasing frequency. For $\omega < \omega_{max}$, the conduction occurs through long-range translational mobility of charge carriers, whereas the frequency region above ω_{max} the charge carriers are localized and bound to their potential wells. This results in the short-range mobility of carriers [91,114,115,117]. The peak M''_{max} of $M''(\omega = \omega_{max})$ shifts towards the higher frequencies as the temperature increases from 173 to 473 K, suggesting that the relaxation time (τ) decreases with temperature [113]. The condition for relaxation process to occur is $\omega_{max}\tau = 1$, where τ is the relaxation time. In the present system, the relaxation process is of a non-Debye type due to dispersion of relaxation time with respect to temperature which is further supported by β values and Nyquist plots which will be discussed in later section [118]. Macedo *et al*. proposed a model to predict the variation of M' and M'' for both higher and lower frequencies as follows [115,119].

$$\lim_{\omega\tau \gg 1} M' = M_\infty \qquad \lim_{\omega\tau \ll 1} M' = 0 \tag{4.8}$$

$$\lim_{\omega\tau \gg 1} M'' = 0 \qquad \lim_{\omega\tau \ll 1} M'' = 0 \tag{4.9}$$

The experimental data of current $MnNb_2O_6$ system agrees very well with the Macedo criterion of M' and M'' and this model predicts the existence of solid electrolytes in the present system which consists of many RC circuits [57]. The complex electric modulus plots are characterised by stretched exponential decay function $\phi(t)$, which can be expressed in terms of Kohlrausch Williams Watts (KWW) function (equation (4.10)) [91,119],

$$\phi(t) = e^{-\left(\frac{t}{\tau}\right)^{\beta}}; 0 < \beta < 1 \tag{4.10}$$

The relaxation function $\phi(t)$ provides more information on time evolution of electric field within the investigated system. Here the quantities 'τ' is the relaxation time and 'β' is the KWW parameter that lies in the range between 0 and 1 for non-Debye relaxation process. In case of a typical Debye relaxation process, the value of β tends to unity, further if its value is less than unity, that indicates a departure from the linear exponential function [91,95]. The β values increase with decreasing relaxation time (τ) and generally for a practical solid electrolyte, the β values should be less than 1 [115]. Usually, the Laplace transformation of a function $\phi(t)$ relates the complex electric modulus (M^*) as represented below [91,117,119],

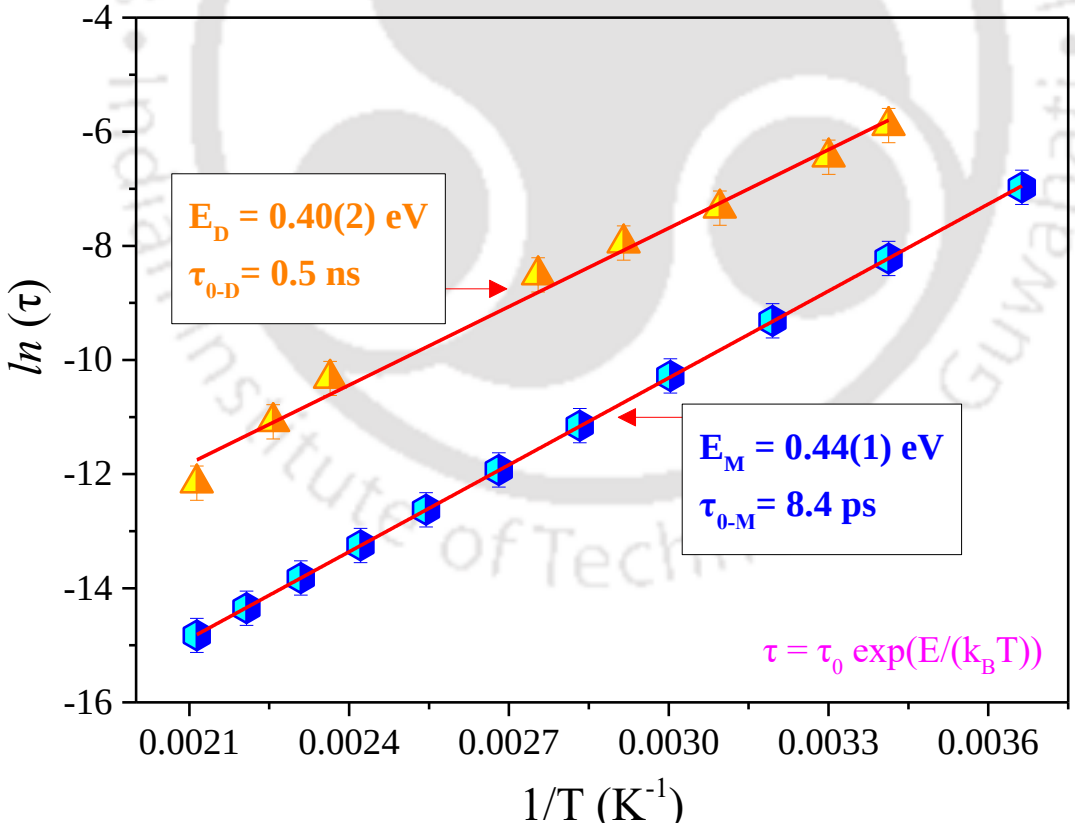

Fig. 4.11. The plot of ln τ vs $1/T$, where τ obtained from $M''(\omega)$ vs ω and tan δ vs f are shown in blue hexagonal data points and orange triangular data points, respectively. The solid red lines are the linear fit of Arrhenius equation.

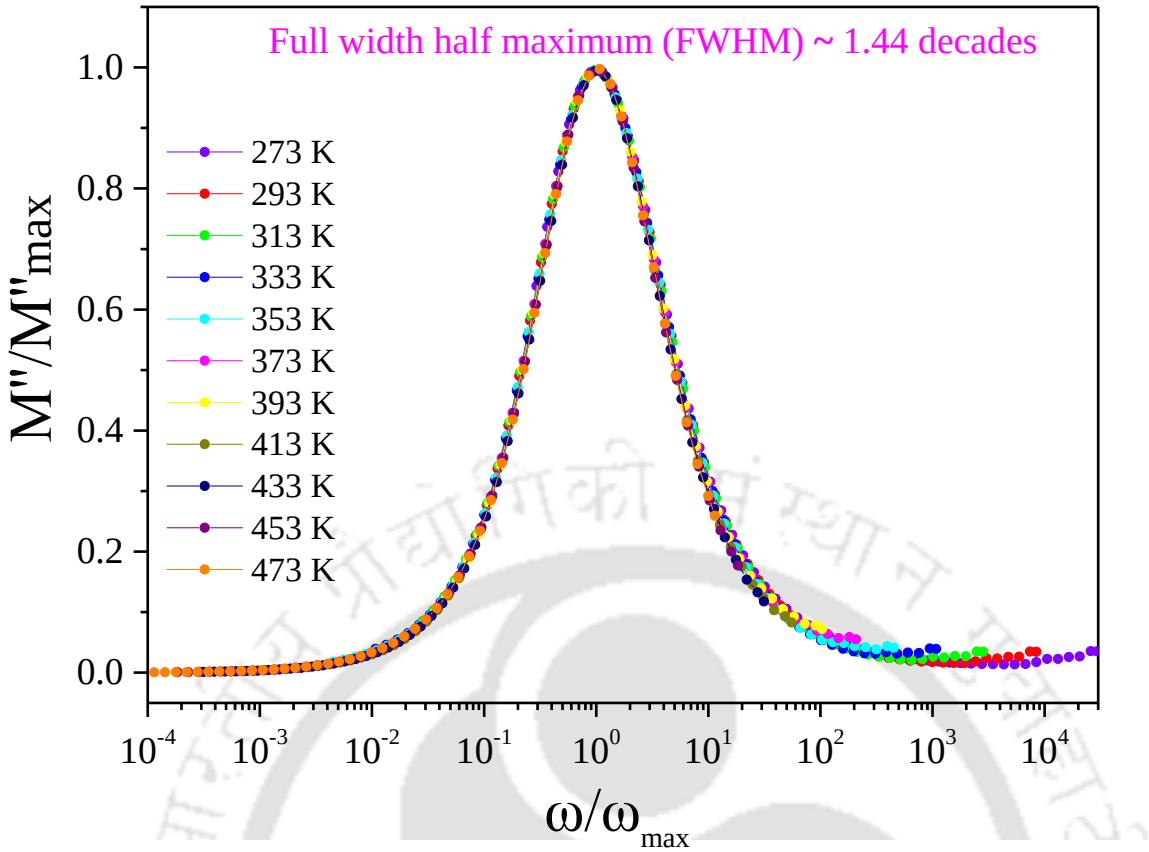

Fig. 4.12. The normalized plot M″/M″$_{max}$ vs ω/ω$_{max}$ at different measured temperatures (273–473 K).

$$M^* = M_\infty \left[1 - \int_0^\infty e^{-j\omega t}\left(-\frac{d\phi}{dt}\right)\right] \tag{4.11}$$

Table 4.1. The list of fitting parameters M''_{max}, ω_{max}, β and τ obtained from mathematical curve fitting of modified KWW function (equation (4.12)) to M'' vs ω data at various temperatures.

Temperature (K)	M''_{max}	ω_{max} (10^4 rad. s^{-1})	β	τ (μs)
273	0.0143	0.107	0.794(9)	936
293	0.0144	0.372	0.796(5)	269
313	0.0145	1.110	0.800(4)	90
333	0.0147	2.913	0.805(6)	34
353	0.0148	6.964	0.809(2)	14
373	0.0147	15.144	0.812(4)	7
393	0.0146	30.425	0.819(7)	3
413	0.0146	56.857	0.833(8)	2
433	0.0145	100	0.837(3)	0.99
453	0.0145	171	0.839(3)	0.58
473	0.0146	275	0.840(7)	0.36

Further, the analysis of $M''(\omega, T)$ is carried by mathematical curve fitting of modified Kohlrausch-Williams-Watts (KWW) function pro

posed by Bergman in the frequency domain which is given as below [91,114,120].

$$M''(\omega) = \frac{M''_{\max}}{(1-\beta) + \left(\frac{\beta}{1+\beta}\right)\left[\beta\left(\frac{\omega_{\max}}{\omega}\right) + \left(\frac{\omega}{\omega_{\max}}\right)^{\beta}\right]} \tag{4.12}$$

The solid red lines in the Fig. 4.10(b) are the curve fits to the modified KWW function of equation (4.12) which provides the magnitudes of fitting parameters M''_{max}, ω_{max} and β (are listed in the table 4.1). The obtained β values lies in the range 0.794–0.840 providing the evidence of non-Debye type relaxation process prevalent in the current system in the temperature range 273–473 K. These results are further supported by depressed semicircles in Nyquist plots (figures 4.14(a) and (b)). Since the β values are less than 1, this proves the existence of solid electrolyte in the present system. The relaxation time (τ) at different temperatures is determined from the value of ω_{max} and the activation energy for relaxation of charge carriers has been estimated from the Arrhenius equation as stated below [91],

$$\tau = \tau_0 e^{\left(\frac{E_M}{kT}\right)} \tag{4.13}$$

In the above expression, τ_0 is the characteristic relaxation time in a very high temperature limit ($\tau \rightarrow \infty$) and E_M is the activation energy of charge carriers ascribed to grain relaxation for the current current $MnNb_2O_6$ system. The linear fit for the plot ln (τ) vs 1/T depicted in Fig. 4.11 (blue coloured hexagonal shaped data points)

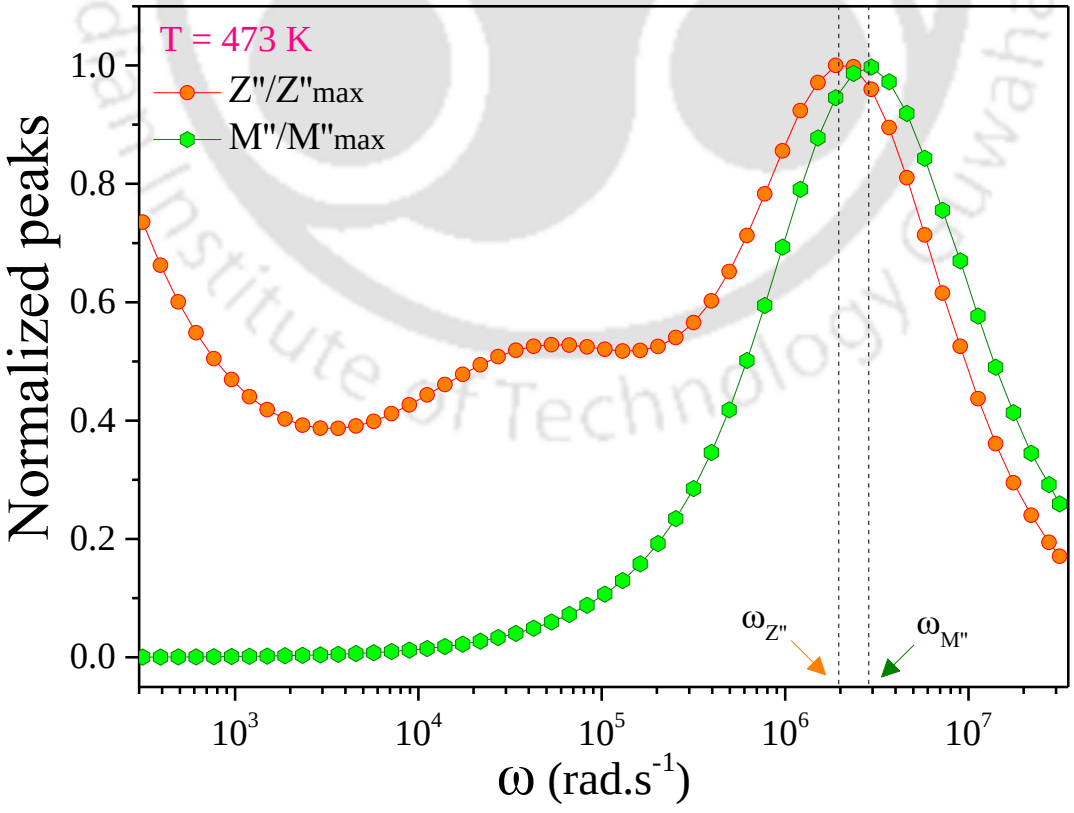

Fig. 4.13. The plot of Z''/Z''_{max} and M''/M''_{max} vs angular frequency (ω) at 473 K. The $\omega_{Z''}$ and $\omega_{M''}$ are the peak frequencies of Z''/Z''_{max} and M''/M''_{max}, respectively.

provides the magnitude of E_M = 0.44(1) eV and τ_0 = 8.04 ps for the current relaxation process. Nevertheless, using the same Arrhenius equation (4.13), we have estimated the activation energy E_D = 0.40(2) eV for the relaxation of charge carriers in electrode-sample geometry as shown in the Fig. 4.11 (orange coloured triangular shaped data points). In this case, the τ at different temperatures is obtained from the maxima of the humps noticed in Fig. 4.3(b). Moreover, the relaxation times obtained from $M''(\omega)$ vs ω and Tan δ vs f are proportional to each other, which is evident by parallel linear fittings in the Fig. 4.11. The plot of M''/M''_{max} vs ω/ω_{max} is depicted in Fig. 4.12 which shows the scaling of electric modulus for various temperatures. Every scaled plot of $M''(\omega)$ shown in Fig. 4.12 superimposes on a single master curve suggesting the occurrence of an identical relaxation mechanism of charge carriers for the whole temperature range 173–473 K [91,114,115]. The master curve provides the full width half maximum (FWHM) ≈1.44 decades which is higher than the 1.14 decades (FWHM for Debye type) indicating the deviation from Ideal Debye type relaxations in the current $MnNb_2O_6$ system [115,121]. Non-Debye type relaxation mechanism has also been reported in $BaFe_{10.5}In_{1.5}O_{19}$ system with FWHM ≈1.343 decades which is in comparison to the present system [121]. Fig. 4.13 displays the normalised plots M''/M''_{max} and Z''/Z''_{max} at 473 K, which are plotted against angular frequency $\omega(= 2\pi f)$. The peak frequency $\omega_{M''}$ of M''/M''_{max} curve is slightly higher than the peak frequency $\omega_{Z''}$ of Z''/Z''_{max} curve in the current case. The superimposing nature of M''/M''_{max} and Z''/Z''_{max} curves provide strong and clear evidence that the charge carriers exhibit long-range translation motion, which indicates the *dc*-conduction mechanism. However, in the present case, the normalised plots exhibit a slight difference between the peak frequencies $\omega_{M''}$ and $\omega_{Z''}$ (Fig. 4.13) indicating the presence of short-range localized conduction instead of long-range conduction at higher temperatures [122,123]. Such incongruity of the normalised plots of M'' and Z'' provides evidence of the non-Debye nature of dipole relaxation in the present columbite $MnNb_2O_6$ system [114]. Nevertheless, the determination of ω_{max} from M''-ω plot (Fig. 4.13) is more reliable method than the maximum obtained from the Z''-ω plots, since M'' suppresses electrode effects [124,125].

4.3.4. Complex impedance spectra in Argand-plane

The dielectric response from various regions of electro ceramic materials can be characterized by the complex impedance ($Z = Z' + iZ''$) spectroscopy technique. In this technique, the impedance data of the material is plotted in the complex/Argand plain (Z'' vs Z') as shown in the figures 4.14 and 4.15 which forms successive semicircles. Each ideal semicircle in the complex impedance plain (Nyquist plot) represents a single parallel resistive and capacitive (RC) element in the circuit. The R and C values are extracted through the fitting approach of Z'' vs Z' impedance plots from various software's [118,126,127]. The Nyquist plot (Cole–Cole plot) in Fig. 4.14(a) at 303 K shows a bigger semicircle in the higher frequency region, this corresponds to grain contribution and a tail at lower frequencies due to the grain-boundary contribution [128]. Fig. 4.14(b) shows the Nyquist plot at 473 K, it consists of two semicircles and a spike, which is consistent with Nyquist plot reported by Lian *et al.* [129]. To estimate the exact frequency range of the dielectric responses arising from grain, grain-boundary and electrode/sample contact, we plotted Z' vs Z''/f

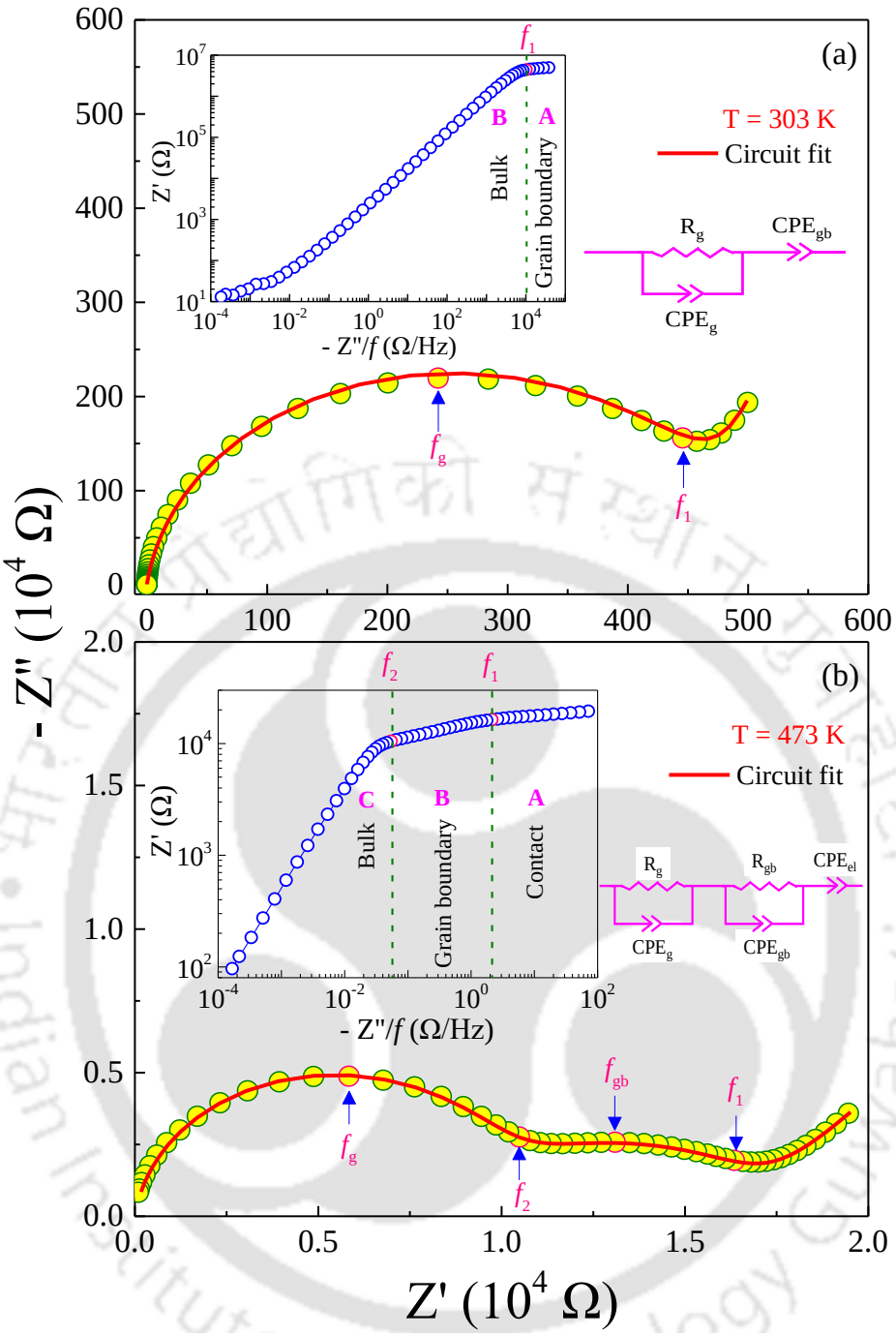

Fig. 4.14. The plot of Z″ vs Z′ (Nyquist plot) for $MnNb_2O_6$ system at (a) 303 K and (b) 473 K with an equivalent circuit in the right inset obtained from the best circuit fit (solid red line) of the main panel (Z″ vs Z′) impedance data. The plot of Z′ vs Z″/*f* in the left inset of the figures (a) and (b) are the different representation of Z″ vs Z′. The frequencies f_1 = 150 Hz and f_g = 700 Hz for 303 K, and f_1 = 900 Hz, f_2 = 50.5 kHz, f_g = 300 kHz and f_{gb} = 8.5 kHz for 473 K.

curve shown in the inset of figures 4.14(a) and (b). The plot of *Z′* vs *Z″/f* in the inset of Fig. 4.14(a) shows two distinct regions marked as A and B separated by a frequency boundary at f_1 = 150 Hz. The region-A corresponds to the dielectric response from grain boundaries ascribed to the tail of Nyquist plot and the region B is assigned to dielectric response from the bulk (grain) counterpart which constitutes the main section of the Nyquist plot. Similarly, in the inset of Fig. 4.14(b), we have provided the *Z′* vs *Z″/f* plot displays three distinct regions assigned as A, B and C separated by two frequency boundaries f_1 = 900 Hz

and f_2 = 50.5 kHz. The region-A corresponds to the dielectric response from the electrode contact ascribed to the tail of Nyquist plot at lower frequencies (f < 900 Hz). The region B represents the dielectric response from grain boundaries attributed to smaller semicircles at middle order frequencies (900 Hz–50.5 kHz) of Nyquist plots. Whereas, the region C indicates the grain contribution assigned to the larger semicircle at higher frequencies (f > 50.5 kHz). The peak frequency f_g = 700 Hz (300 kHz) for 303 K (473 K) represents the bulk relaxation which is in-line with the peak frequency of electric modules plots and f_{gb} = 8.5 kHz is the peak frequency for grain-boundary relaxations as indicated in Fig. 4.14(b) [95,130]. The Nyquist plots can be interpreted on the basis of an equivalent electrical circuit with a suitable combination of lumped parameter networks such as resistor, capacitor, constant phase element (CPE), inductor etc which depends on the best possible fit of the experimental data. In the present case, we have used a CPE instead of a pure capacitor (C) for the circuit fit to establish the Nyquist plots for the columbite system $MnNb_2O_6$, because the centres of all the semicircles lie slightly below the real (abscissa) axis; as a consequence, one can notice the depressed semicircles in figures 4.14(a) and (b). The depressed semicircles in the Nyquist plots further confirms the

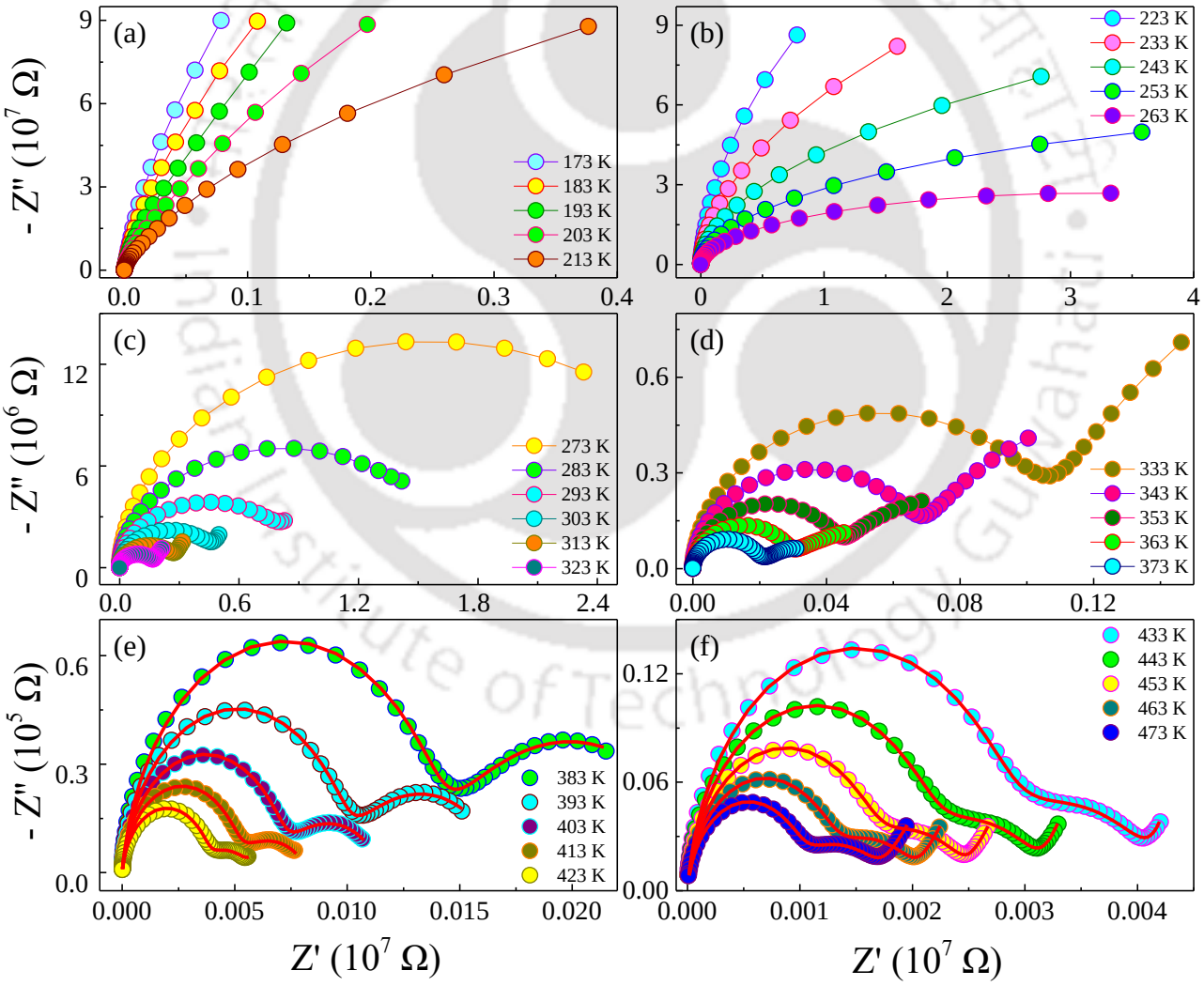

Fig. 4.15. (a) to (f) Z'' vs Z' (Nyquist) plots of $MnNb_2O_6$ system at several temperatures from 173 to 473 K. The solid red lines in the figures (e) and (f) are the best circuit fits.

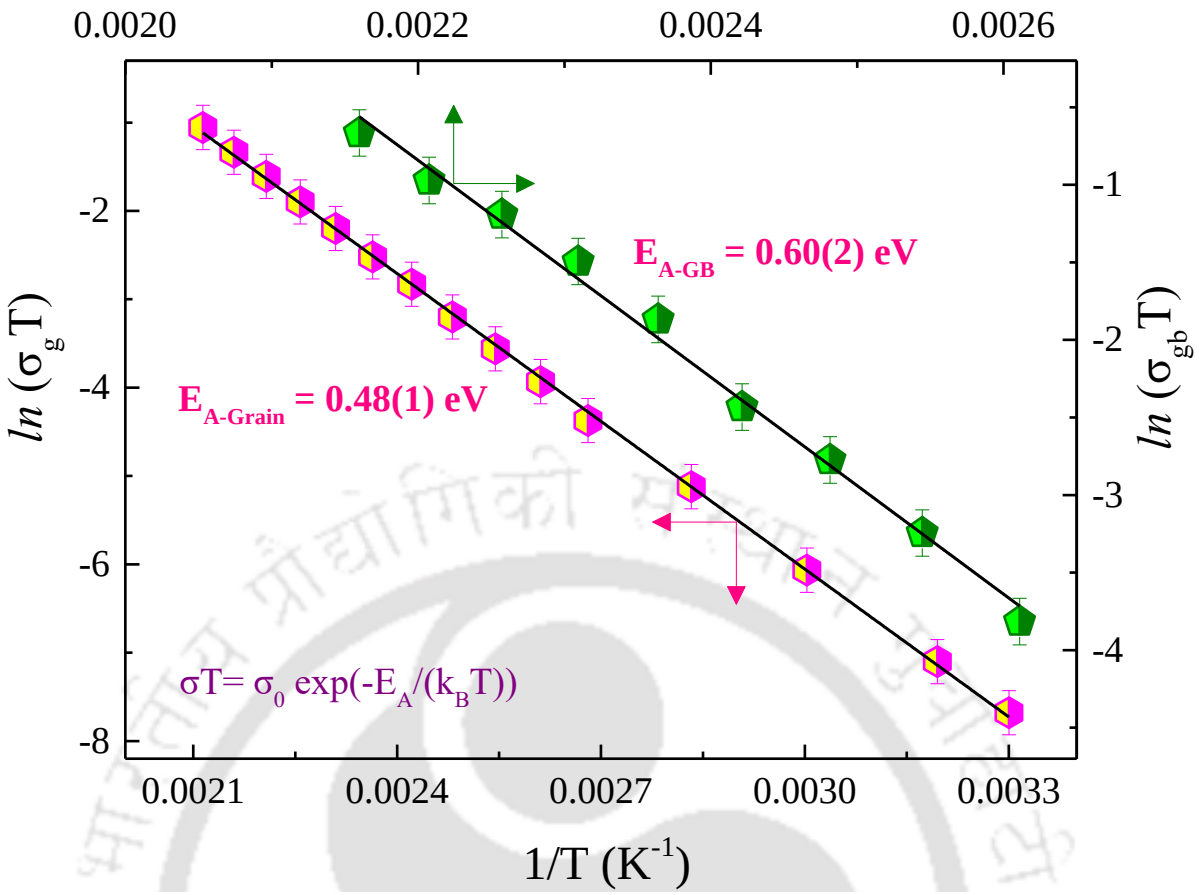

Fig. 4.16. The plot of ln($\sigma_g T$) (left *y*-scale) and ln(σ_{gb}T) (right *y*-scale) vs 1/*T* for grain and grain-boundary conductivity respectively and the solid black lines are the linear fit of Arrhenius equation.

non-Debye type relaxation present in the system [115,128,131]. The impedance (Z_{CPE}) of the imperfect capacitor of CPE is given below [126],

$$Z_{\mathrm{CPE}} = \frac{1}{C_{\mathrm{CPE}}(i\omega)^n} \tag{4.14}$$

Here 'C_{CPE}' is the capacitance value of the imperfect capacitor, 'ω' is the angular frequency and 'n' is the exponent deviation from the pure capacitor (n = 1). The Nyquist plots shown in figures 4.14 and 4.15 are fitted with a n appropriate electrical circuit using an EIS spectrum analyser and the solid red lines are the best circuit fit of the impedance data, (figures 4.15(e) and (f) shows the best circuit fits pertaining to the measurement taken above 383 K). The obtained grain resistance (R_g) and grain-boundary resistance (R_{gb}) from the circuit fit analysis are listed in the table 4.2. The electrical circuit obtained from the software for the Nyquist plot at 303 K is shown in the inset (right side) of Fig. 4.14(a) which provides the magnitudes of components: R_g = 4653.8 kΩ, C_{CPEg} = 2.7×10^{-11} F (n = 0.9) and C_{CPEgb} = 1.75×10^{-9} F (n = 0.8). Similarly, the circuit analysis for the Nyquist plot at slightly higher temperatures 473 K in the Fig. 4.14(b) provides R_g = 9.7 kΩ, C_{CPEg} = 9.4×10^{-11} F (n = 0.9), R_{gb} = 6.3 kΩ, C_{CPEgb} = 1.1×10^{-7} F (n = 0.7) and for the electrode effect C_{CPEel} = 8.7×10^{-6} F (n = 0.6). The last element C_{CPEel} for the spike indicates the formation of a thin layer having effective capacitance across the interface between the electrode and sample [118,126,127,132]. The electrode effect is nil at room temperature (303 K) but its contribution arises above 413 K and is prominent at higher temperatures as shown in the Fig. 4.15. Further the Nyquist plots in Fig. 4.15 indicates

Table 4.2. List of grain (R_g) and grain boundary resistance (R_{gb}) of $MnNb_2O_6$ sample at several temperatures obtained from electrical circuit fitting analysis of Nyquist plots.

Temperature (K)	R_g (kΩ)	R_{gb} (kΩ)
303	4654	-
313	2700	-
333	1020	-
353	420	-
373	210	-
383	139	124
393	98	72
403	70.3	46
413	50	33
423	37	19
433	28	14
443	21	10
453	16	8.5
463	13	6.4
473	10	6.3

that the size of the semicircles decreases with increasing the measurement temperature (from 173 to 473 K). This scenario indicates the fact that the resistance imparted by the grain and grain-boundary to the charge transport diminishes with increasing the measurement temperature, this happens because the resistance of the grain and grain-boundary is proportional to the length of semicircles along the Z' axis in Nyquist plots [95]. Thus, the hopping is completely driven by the thermal activation process. The corresponding grain (σ_g) and grain boundary (σ_{gb}) conductivities are obtained from R_g and R_{gb} values using the relation: $\sigma = L/(R \times A)$, where 'A' and 'L' are the area and thickness of the cylindrical pellets, respectively [104]. Fig. 4.16 shows the linear fit to the plot of $\ln(\sigma_{g/gb}T)$ vs $1/T$ (above 303 K) for both grain and grain-boundary conductivity which results in the activation energies $E_{A-grain}$ = 0.48 eV and E_{A-GB} = 0.60 eV, respectively. Further, these results support the activation energies obtained from the Arrhenius equation (0.445–0.379 eV) [128]. Similar activation energies for grain and grain-boundary conductivity have been reported in $MnNb_2O_{6-\delta}$ ($E_{A-grain}$ = 0.66 eV and E_{A-GB} = 0.84 eV) and $MnNb_{2-x}Ti_xO_{6-\delta}$ ($E_{A-grain}$ = 0.49 eV and E_{A-GB} = 0.60 eV) [95,96]. Thus, there is a clear consistency between the conductivity analysis provided in section 4.3.2 with the Nyquist plot analysis where the grain and grain boundary conductivities follow the Arrhenius expression above 303 K (represented as Region-II in Fig. 4.7). Nevertheless, the smaller values of activation energies (Fig. 4.16) provide the evidence for the hopping conduction mechanism.

4.4. Concluding remarks

In this chapter we present a detailed study of the *ac*-conductivity and dielectric relaxation of the polycrystalline Columbite system $MnNb_2O_6$ over a wide range of temperature and frequencies. Our results

demonstrate that the Arrhenius like behaviour of conductivity is prevalent above room temperature for the frequencies varied from 50 Hz to 5 MHz. The activation energies (0.445–0.379 eV) obtained from the Arrhenius equation decreases quadratically with an increase in frequency ($E_{ac}(f) = A + Bf + Cf^2$ with the constants A (0.413 eV), B (0.023 eV Hz^{-1}) and C (−0.004 eV Hz^{-2})). Moreover, the *ac*-conductivity analysis based on the Double power law ($\sigma_{ac}(\omega) = \sigma_{dc} + A_1\omega^{s_1} + A_2\omega^{s_2}$) reveals the CBH conduction mechanism for all the temperatures from 173 to 473 K. The temperature dependence of the frequency exponent '$s(T)$' reveals two distinct regions with slopes $\partial s_1/\partial T = -1.9\times10^{-3}$ K^{-1} (173–233 K), $\partial s_1/\partial T = -7.8\times10^{-3}$ K^{-1} (233–300 K) and $\partial s_2/\partial T = -1.3\times10^{-3}$ K^{-1} (173–300 K) in Region-I. While in Region-II, the temperature gradient in s_1 is $\approx -1.7\times10^{-3}$ K^{-1} and a complete non-linear variation of the exponent s_2 is evident from Fig. 4.7, yet the CBH mechanism of conduction is intact in both the regions. However, the second region is dominated by the thermally activated Arrhenius like behaviour. The dispersion in relative dielectric permittivity $\varepsilon_r(T, f)$ is clearly evident with both frequency and temperature in the investigated system and these results manifest highest magnitude of $\varepsilon_r \approx 35$ (28.1) for $MnNb_2O_6$ system reported so far measured at frequency 1 kHz (1 MHz) at 303 K. The analysis of complex electric modulus (M^*) identifies both the trends of short-range and long-range conductivity regions in the frequency plane which provides evidence for the distribution of relaxation time ($\tau \approx 935.8-0.36\,\mu s$) with temperature. This study further leads to the estimation of activation energy of charge carriers, E_M = 0.44 eV. The scaling of modulus plots suggests the manifestation of common relaxation mechanism of charge carriers for the entire temperature range under investigation. The mismatch of the normalised plots M''/M''_{max} and Z''/Z''_{max} indicates the presence of shortrange conduction at higher temperatures. Our system exhibits non-Debye relaxation process which is estimated based on the analysis of modified Kohlrausch-Williams-Watts method and its corresponding parameter ($0.794 \leqslant \beta \leqslant 0.840$). This inference of non-Debye relaxation process is further supported by the depressed semicircles in Nyquist plots and also from the higher value of FWHM (≈1.44 decades) of master curve compared to the FWHM (=1.14 decades) of Ideal Debye type in the scaled modulus plots. Complex impedance spectra and its equivalent circuit analysis provides an independent estimation of the activation energies for the charge carriers within the grain and grain boundaries: $E_{A-grain}$ = 0.48 eV and E_{A-GB} = 0.60 eV, respectively which are consistent with those activation energy values obtained from the Double power law (0.40 eV) and the Arrhenius equation (0.445–0.379 eV) in section 4.3.2.

Chapter 5

Tricritical point and Exchange interactions in $MnTa_2O_6$

This chapter deals with the crystal structure along with a detailed analysis on the magnetic ground state of antiferromagnetic manganese tantalite $MnTa_2O_6$. A special emphasis has been given to the study of magnetic field-induced transitions and exchange interactions in this compound. In the introductory section we elucidate the important properties including the literature review of $MnTa_2O_6$ along with the motivation and objectives of the research work. Later sections deal with the brief experimental details, results and discussion followed by summary of important findings.

5.1. Background and literature assessment

The transition metal compounds with general chemical formula AB_2O_6 (A = Mn, Fe, Co, Ni and B = Nb, Ta) crystallize in the orthorhombic crystal structure of columbite ($FeNb_2O_6$) with four molecular formula per unit cell [19–23] except $FeTa_2O_6$, $CoTa_2O_6$ and $NiTa_2O_6$ which crystallize into tetragonal (tri-rutile) crystal structure with two molecular formula per unit cell [15,24–26]. In AB_2O_6 compounds usually A and B sites are occupied by divalent and pentavalent cations respectively, forming octahedra [AO_6 andBO_6] with six oxygen atoms [21,23]. These compounds have potential applications in the field of satellite and mobile communications as dielectric resonators and filters [24,133–135], as electrochemical gas sensors [24,136], and in supercapacitors [24,135].

Like $MnNb_2O_6$, $MnTa_2O_6$ also crystallizes in the columbite orthorhombic crystal structure with four formula units per cell (space group $Pbcn - D_{2h}^{14}$, N 60, oP36) but it has slightly larger unit cell parameters of a = 14.4478 Å, b = 5.7677 Å, and c = 5.0943 Å [24,63] compared to a = 14.4204 Å, b = 5.7566 Å, and c = 5.0784 Å for $MnNb_2O_6$ [57–59,86]. Whereas the magnetic properties of $MnNb_2O_6$ have been reported by several previous investigators [57–59,86] including our own recent work in which we reported complete details of its magnetic field-temperature (H–T) phase diagram below its Neel temperature T_N = 4.36 K and determination of the exchange constants [86], the magnetic properties of $MnTa_2O_6$ are relatively unexplored. Although Gulyaeva *et al* [24] recently reported on the high temperature (300 K to 1203 K) heat capacity and thermal expansion measurements of $MnTa_2O_6$, the only known magnetic studies are those by Weitzel and Klein [63] in $MnTa_2O_6$ and Schraf and Weitzel in $Mn(Nb_{0.5}Ta_{0.5})_2O_6$ [137], both using neutron diffraction only. These studies reported T_N = 5.7 K and 5.2 K for $MnTa_2O_6$ and $Mn(Nb_{0.5}Ta_{0.5})_2O_6$ respectively compared to T_N = 4.4 K for $MnNb_2O_6$ thus showing that T_N increases when Ta replaces Nb in this structure.

Because of the dearth of magnetic studies in $MnTa_2O_6$ using the temperature and magnetic field dependence of magnetization, we undertook such studies in a polycrystalline sample of $MnTa_2O_6$ and our results are reported here. The polycrystalline sample of $MnTa_2O_6$ synthesized using the solid-state reaction method was structurally characterized with x-ray diffraction combined with Rietveld refinement and oxidation states of Mn^{2+}, Ta^{5+} and O^{2-} ions were determined by x-ray photoelectron spectroscopy (XPS) measurements. Heat capacity measurements were used to determine the characteristics of the singularity near the Neel temperature T_N = 5.98 ± 0.02 K and electron spin resonance yielded the g-value of 2.0155

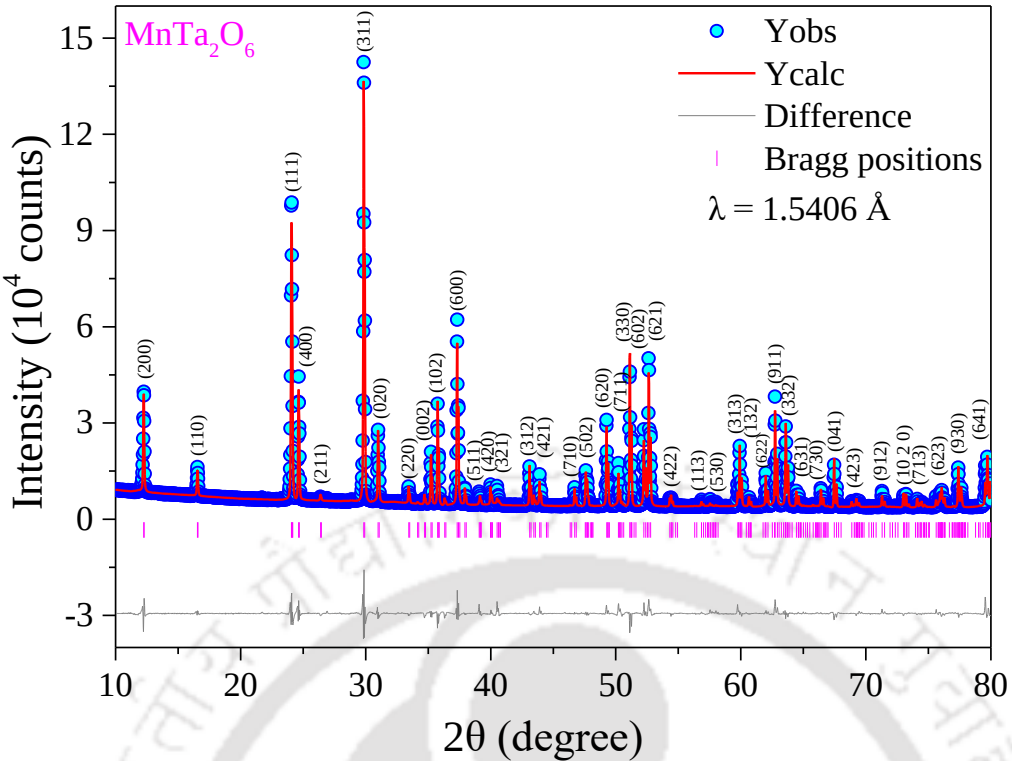

Fig. 5.1. X-ray diffraction pattern (intensity vs Bragg angle (2θ)) of $MnTa_2O_6$ along with the Rietveld refined data and marked positions of Bragg lines. The grey line at the bottom signifies the difference between experimentally measured data and the pattern developed by a software.

characteristic of Mn^{2+} ions with S = 5/2 ground state. Analysis of the detailed data of the temperature and magnetic field dependence of magnetization (M) covering the temperature range of 1.5 K to 400 K in magnetic fields up to 250 kOe is used to map out the H–T phase diagram involving the spin-flop field and the magnetic tricritical or triple point T_{TP} (H, T) and this phase diagram is compared with that of $MnNb_2O_6$ reported recently [86]. Finally, the temperature dependence of the paramagnetic susceptibility for $T > T_N$ is used to determine the exchange constants of the system. These results, their discussion, and analysis are presented below.

5.2. Synthesis and structural characterization

Bulk sample of polycrystalline $MnTa_2O_6$ was prepared using a standard solid-state reaction method starting with stoichiometric proportions of MnO_2 and Ta_2O_5 and grounding the mixture in an agate mortar with pestle for about 6 h. The grounded homogeneous mixture was pressed into cylindrical pellets of 12 mm diameter and thickness of one mm with the help of hydraulic press. The pressed pellets were fired at 1200°C for 24 h as first sintering in air. Again, the first sintered pellets were re-grounded, pelletized, and re-sintered at 1250°C for 36 h.

The phase purity and crystal structure of this bulk samples were investigated using the Rigaku x-ray diffractometer (model: TTRAX III) with Cu Kα (λ = 1.5406 Å) radiation. The x-ray diffraction pattern was recorded from 2θ = 10° to 80° with step size = 0.02° and scan rate 2° per minute. The Rietveld refinement of pure phase room temperature XRD pattern is shown in Fig. 5.1. The refinement is carried out with the help of FullProf programme confirms the absence of secondary phases in the compound and yielded the refined

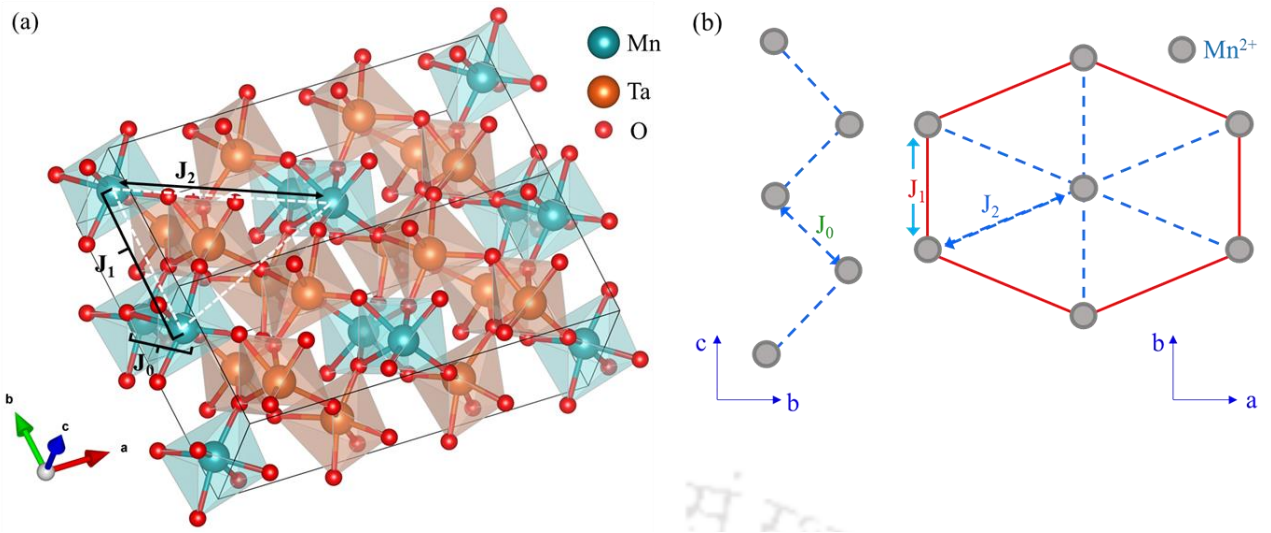

Fig. 5.2. (a) Schematic of the two-unit cells of $MnTa_2O_6$ and the arrows in black colour represent the locus of exchange interaction paths within the given unit cell. (b) The bottom vector diagram demonstrates the intra-chain exchange interaction J_0 pointing along the *c*-axis in zig-zag path and the inter-chain exchange interactions J_1 and J_2 are shown in the *ab*-plane of orthorhombic unit cell.

lattice parameters a = 14.4468(8) Å, b = 5.7664(3) Å and c = 5.0924(4) Å close to the magnitudes of a = 14.4478 Å, b = 5.7677 Å and c = 5.0943 Å reported in the recent paper by Gulyaeva *et al* [24]. From our analysis, the bond lengths and bond angles are found to be Mn–O ∼2.205 Å; Ta–O ∼2.038 Å and Mn–O–Mn ∼95.4°; Ta–O–Ta ∼96.5°; Mn–O–Ta ∼127.4° respectively. This structure has zig-zag chains of Mn^{2+} ions along the *c*-axis and forming –Mn–Ta–Ta–Mn–Ta–Ta–Mn– chains along the *a*-axis. In the *a*–*b* plane Mn^{2+} ions are arranged in isosceles triangular geometry with exchange interactions between them [16,19,68] as shown in Fig. 5.2. The exchange interactions among Mn^{2+} ions in $MnTa_2O_6$ are interpreted by using the Hamiltonian [19,67,68,83],

$$H = -J_0 \sum_i S_i^z S_{i+1}^z - J_1 \sum_{<ij>} \boldsymbol{S}_i . \boldsymbol{S}_j - J_2 \sum_{<ij>} \boldsymbol{S}_i . \boldsymbol{S}_j \qquad (5.1)$$

Here J_0 and J_1 are the intrachain and interchain nearest neighbour exchange interactions along the *c*-axis and *b*-axis respectively, where J_2 is the next nearest exchange interaction in the *a*–*b* plane.

The electronic structure and chemical composition of the sample were probed using an x-ray photoelectron spectrometer (XPS) from Kratos Analytical (model: AXIS Supra+) configured with a dual monochromatic x-ray source Al Kα/Ag Lα (2984.2 eV) with spatial resolution less than 1 μm. The core level electronic spectra of Mn, Ta and oxygen in $MnTa_2O_6$ are calibrated by considering the binding energy of carbon C-1*s* orbital (∼285 eV) as reference shown in the Fig. 5.3. The Mn-2*p* core-level spectrum is deconvoluted into six peaks out of four are main peaks at 640.94 eV (M_1), 642.51 eV (M_2), 652.91 eV (M_3), and 654.4 eV (M_4), the other two are broad satellite peaks at 644.64 eV (S_1) and 656.88 eV (S_2) shown in the Fig. 5.3(a). The spin–orbit splitting between the main peaks of Mn-2$p_{1/2}$ and Mn-2$p_{3/2}$ i.e. ΔE (M_3–M_1) ∼ 11.97 eV and ΔE (M_4–M_2) ∼ 11.89 eV predicts the divalent oxidation state of Mn [71]. The electronic spectra of O-1*s* orbital is deconvoluted into two Gaussian–Lorentzian peaks, one with higher intensity peaked at 530.3 eV due to metal-lattice oxygen (Mn–O and Ta–O) bonding and the other at 531.69 eV as a satellite peak arises due to surface-absorbed oxygen shown in the Fig. 5.3(b) [138]. The deconvolution of

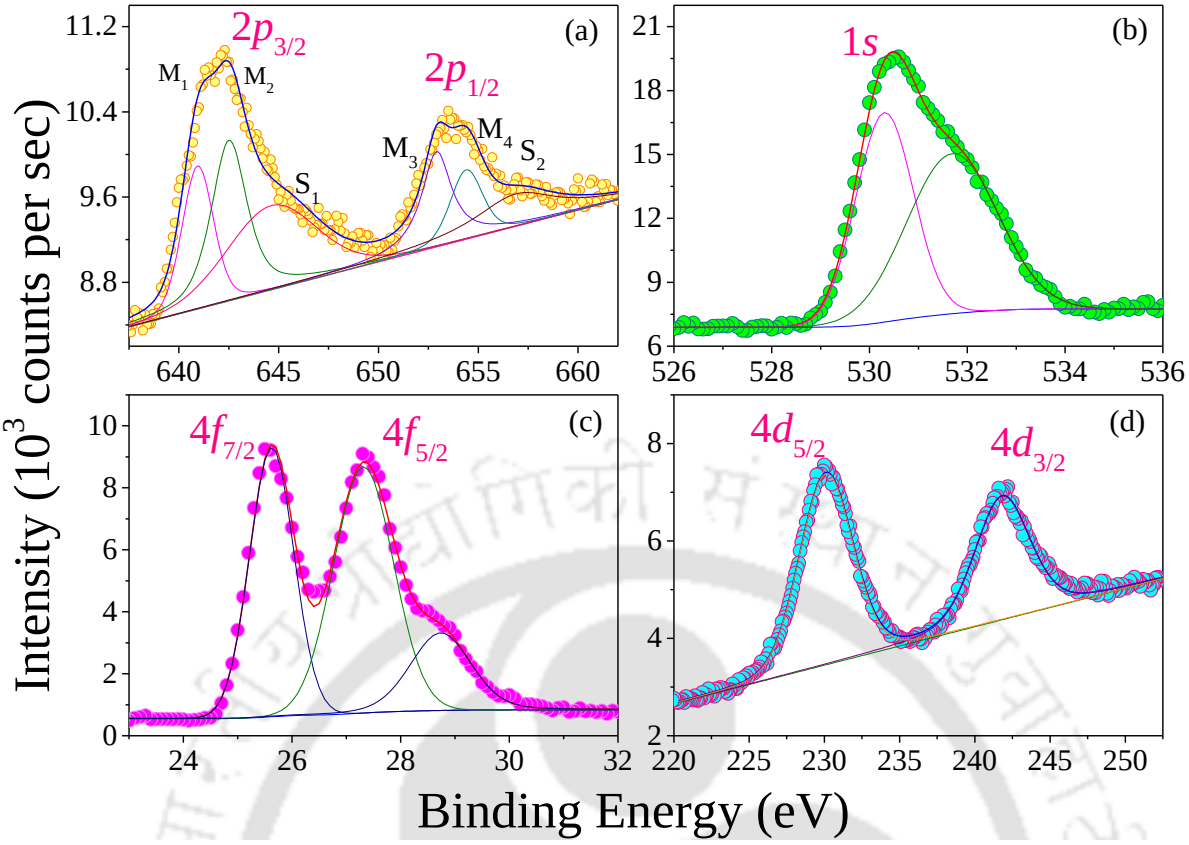

Fig. 5.3. X-ray photoelectron spectra plotted in terms of photoelectron intensity versus binding energy (eV) of core-level (a) Mn-2*p*, (b) O-1*s* (c) Ta-4*f* and (d) Ta-4*d* ions in the polycrystalline $MnTa_2O_6$.

Ta-4 *f* core-level spectrum leads to two main peaks at 25.62 eV (Ta-4 $f_{7/2}$) and 27.32 eV (Ta-4 $f_{5/2}$) with a broad satellite peak at 28.73 eV shown in the Fig. 5.3(c). The binding energy separation (spin–orbit splitting) between two main peaks of Ta-4 *f* orbital $\Delta E \sim 1.7$ eV suggest the pentavalent oxidation state of Ta, further it is confirmed by the electronic spectrum of Ta-4*d* (Fig. 5.3(d)) orbital which exhibits two peaks at 230.11 eV (Ta-4$d_{5/2}$) and 241.82 eV (Ta-4$d_{3/2}$) with a binding energy separation (spin–orbit splitting) $\Delta E \sim 11.71$ eV [138] which matches with the values reported in literature.

5.3. Temperature variation of heat capacity near Neel temperature

The heat capacity $C_P(T)$ measurements of the $MnTa_2O_6$ sample were recorded from 1.9 K to 12 K by using the standard heat-pulse calorimetry [56] in physical property measurement system (PPMS) of Quantum Design. A dual-slope analysis was implemented near the transition temperature to observe the magnetic field effect on phase transition. In this technique, the heat capacity of the sample is measured directly by comparing the heating and cooling rates of the sample temperature without explicit use of the thermal conductance between sample and bath [77]. The temperature dependence of heat capacity $C_P(T)$ curves for $H = 0$ and $H = 90$ kOe are plotted in the Fig. 5.4 indicating a clear distinct peak for both the fields. The C_P curve for $H = 0$ shows transition at $T_N = 6.00 \pm 0.02$ K which is in excellent agreement with $T_N = 5.97 \pm 0.06$ K determined from $\partial(\chi T)/\partial T$ vs T plot for $H = 500$ Oe as shown later. Similarly, the transition temperature at $T_N = 5.47 \pm 0.02$ K obtained from C_P vs T plots for $H = 90$ kOe is also in line with $T_N = 5.53 \pm 0.06$ K obtained from $\partial(\chi T)/\partial T$ vs T plot which are shown later in the H–T diagram. For a second-order

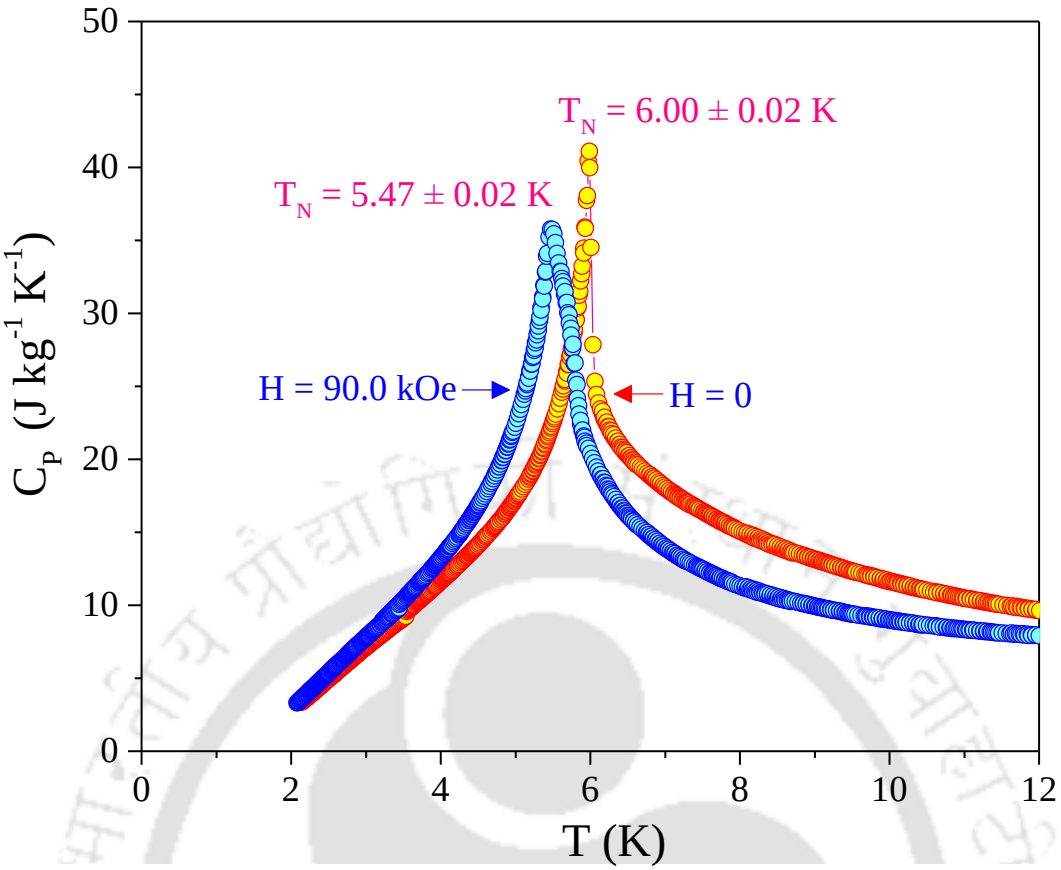

Fig. 5.4. Thermal variation of specific heat C_P (T) data measured for H = 0 and H = 90 kOe showing the antiferromagnetic to paramagnetic phase transition at T_N = 6.00 ± 0.02 K and T_N = 5.47 ± 0.02 K, respectively.

phase transition, the temperature dependence of heat capacity $C_P(T)$ near transition temperature is usually fit to the equation: $C_P = A(T - T_N)^{-\alpha}$ where A is a constant and α is the critical exponent [78]. The slope of linear fit to the log–log plots of C_P vs $|T - T_N|$ gives the value of α for both $T > T_N$ and $T < T_N$ as shown in the Fig. 5.5. Since the linear fit is very sensitive to the selection of transition temperature T_N, we varied T_N from 5.96 K to 6.00 K in steps of 0.01 K to get the best linear fit for the determination of better α values. From the log–log plots of C_P vs $|T - T_N|$ for T_N = 6.00 K (see Fig. 5.5), linear fits are obtained yielding α = 0.13(1) for $T < T_N$ valid in the range of $0.025 < |T - T_N| < 0.15$ and α = 0.106(2) valid for somewhat larger range of $0.04 < |T - T_N| < 0.5$ for $T > T_N$. Similar magnitudes of α have been reported in antiferromagnets MnF_2 [78] with α = 0.18(0.16) for $T < T_N (T > T_N)$ and in $MnNb_2O_6$ [86] with α = 0.15(0.12) for $T < T_N (T > T_N)$.

5.4. Electron spin resonance spectroscopy

The electron spin resonance (ESR) measurements of the sample were carried out at room temperature using an X-band spectrometer of model: JES-FA200 (JEOL) at IIT Guwahati, India. The spectrum obtained for $MnTa_2O_6$ using frequency f = 9.4 GHz is shown in Fig. 5.6, along with its fit to the Lorentzian line-shape expected for exchange narrowed linewidths in insulators. An excellent fit is obtained to the Lorentzian line-shape with peak-to-peak linewidth ΔH_{PP} = 936(1) Oe, and resonance field H_r = 3332.3(1) Oe. Using the standard resonance equation $h.f = g.\mu_B.H_r$ (h = Planck's constant, μ_B = Bohr

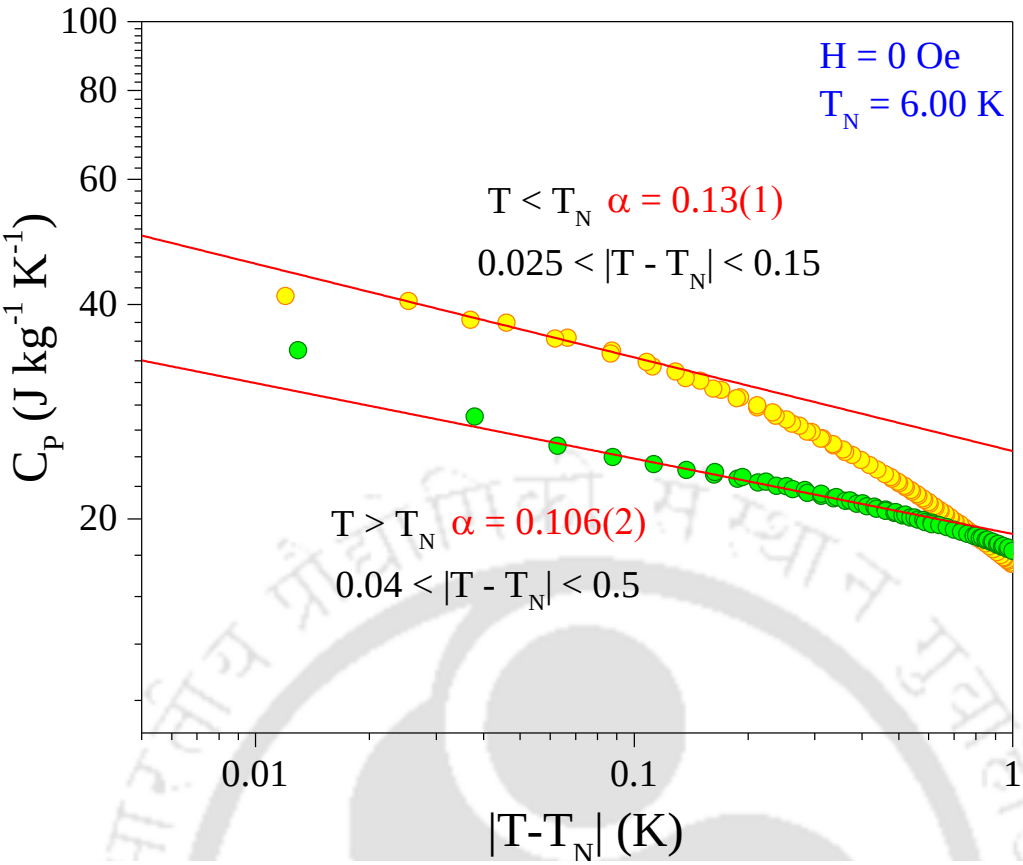

Fig. 5.5. The temperature dependence of C_P near T_N is fit to the equation: $C_P = A|T - T_N|^{-\alpha}$ using log–log plot of C_P vs $|T - T_N|$ with the linear fits shown in the figure yielding the exponent α for both $T > T_N$ and $T < T_N$. The ranges for the validity of α are also listed in the figure.

magneton) [139], g = 2.0155(2) is obtained as the g-value for Mn^{2+} which is characteristic of the $^6S_{5/2}$ ground state of Mn^{2+}. This g-value is also in excellent agreement with g = 2.015(5) obtained from the analysis of the temperature dependence of the magnetic susceptibility above T_N as shown later. Temperature dependence of the ESR spectra could not be done because of lack of appropriate experimental facilities.

5.5. Temperature and magnetic field dependence of magnetization

Magnetic measurements of $MnTa_2O_6$ were carried out using a vibrating sample magnetometer (VSM) mode-based physical property measurement system (PPMS) from Quantum Design (PPMS DynaCool), which has the capacity of magnetic fields (DC) ranging from −90 kOe to 90 kOe and the temperature variation between 1.9 K to 400 K. For the magnetization (M) versus temperature (T) measurements, the sample was cooled to 1.9 K from room temperature in the presence of zero magnetic field. After cooling, a non-zero magnetic field is applied, and the magnetic moments are recorded with increasing temperature in small temperature steps of ΔT = 0.06 K. The step size in magnetic field (H) used for isothermal M vs H measurements was 50 Oe up to ±90 kOe. Additional measurements of magnetization in H up to 250 kOe at 1.5 K were done at National High Magnetic Field Laboratory (NHMFL) located at the Florida State University in Tallahassee (Florida), USA.

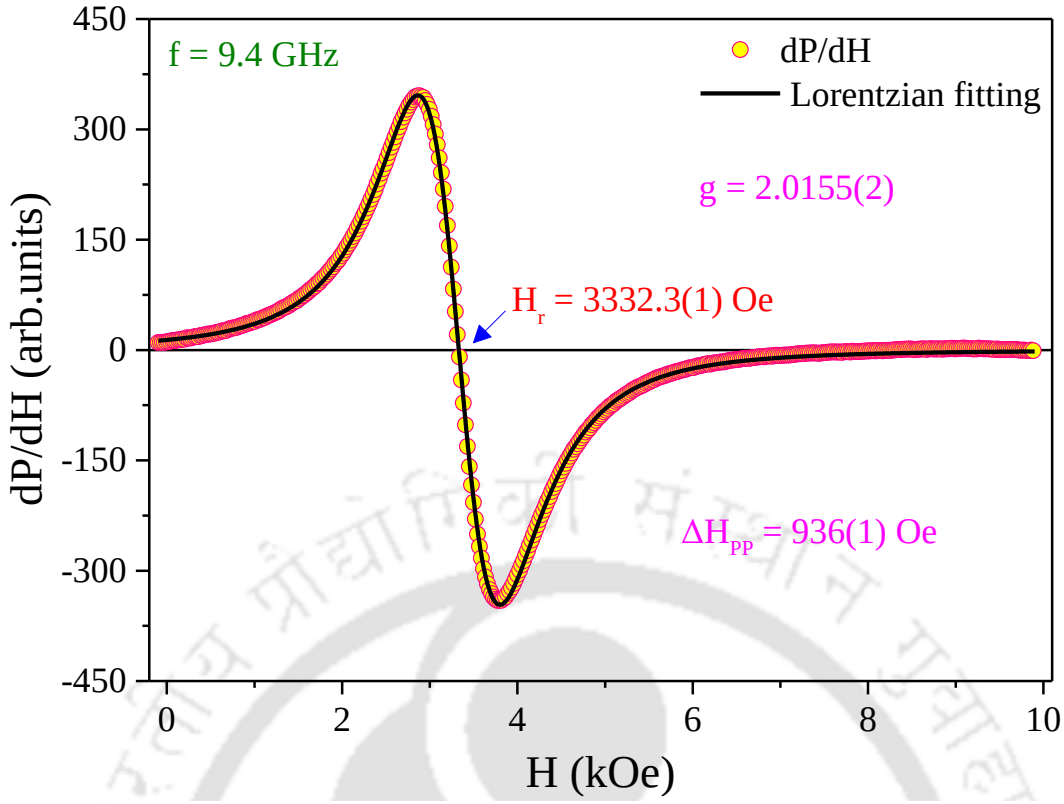

Fig. 5.6. The room temperature electron spin resonance (ESR) spectra of $MnTa_2O_6$ plotted as first derivative of absorption intensity (P) versus magnetic field (H). The solid line is fit to Lorentzian line-shape given by: $\frac{dP}{dH} = -\frac{2P_M(H-H_r)(\Delta H)^2}{[(H-H_r)^2+(\Delta H)^2]^2}$, with $\Delta H = \frac{(\sqrt{3})\,\Delta H_{PP}}{2}$.

5.5.1. Magnetic field dependence of the Néel temperature

The temperature variation of magnetic susceptibility $\chi = M/H$ at the magnetic field H = 500 Oe in the temperature range from 1.9 K to 8 K covering the temperature around T_N is shown in Fig. 5.7(a). The plot indicates a clear change in the slope near 6 K marked by arrow which indicated onset of magnetic ordering from the paramagnetic (PM) to antiferromagnetic (AFM) state. However, the position of the Néel temperature T_N is accurately determined by $\partial(\chi T)/\partial T$ vs T plots because χT represent the magnetic energy and so peaks in both $\partial(\chi T)/\partial T$ vs T and C_P vs T plots have the same physical meaning [86,73–75,140]. In AFM systems, the position of the maximum in the magnetic susceptibility (peak T_P in the χ vs T plot) usually occurs above T_N [73], which in this case occurs at $T_P \sim 10.5$ K as evident in inset of Fig. 5.7(a). The plot of the computed $\partial(\chi T)/\partial T$ vs T shown in Fig. 5.7(b) yields the peak at $T_N = 5.97 \pm 0.06$ K, in close agreement with $T_N = 6.00 \pm 0.02$ K determined from the temperature dependence of the specific heat in figures 5.4 and 5.5. This value is slightly larger than T_N = 5.7 K reported by Scharf *et al.* [137] in 1976. Similar analysis of determining T_N from the computed $\partial(\chi T)/\partial T$ vs T plots was carried out to determine the H dependence of T_N up to H = 90 kOe and this T_N vs H variation is used in complete mapping of H–T phase diagram, following our recent measurements in $MnNb_2O_6$ [86] and earlier measurements reported in AFM MnF_2 [11,12]. Further discussion on the H–T phase diagram is presented later.

For lower H values, T_N is expected to decrease linearly with increase in H according to the following equation based on the molecular field theory (MFT) [11,12,72,75]:

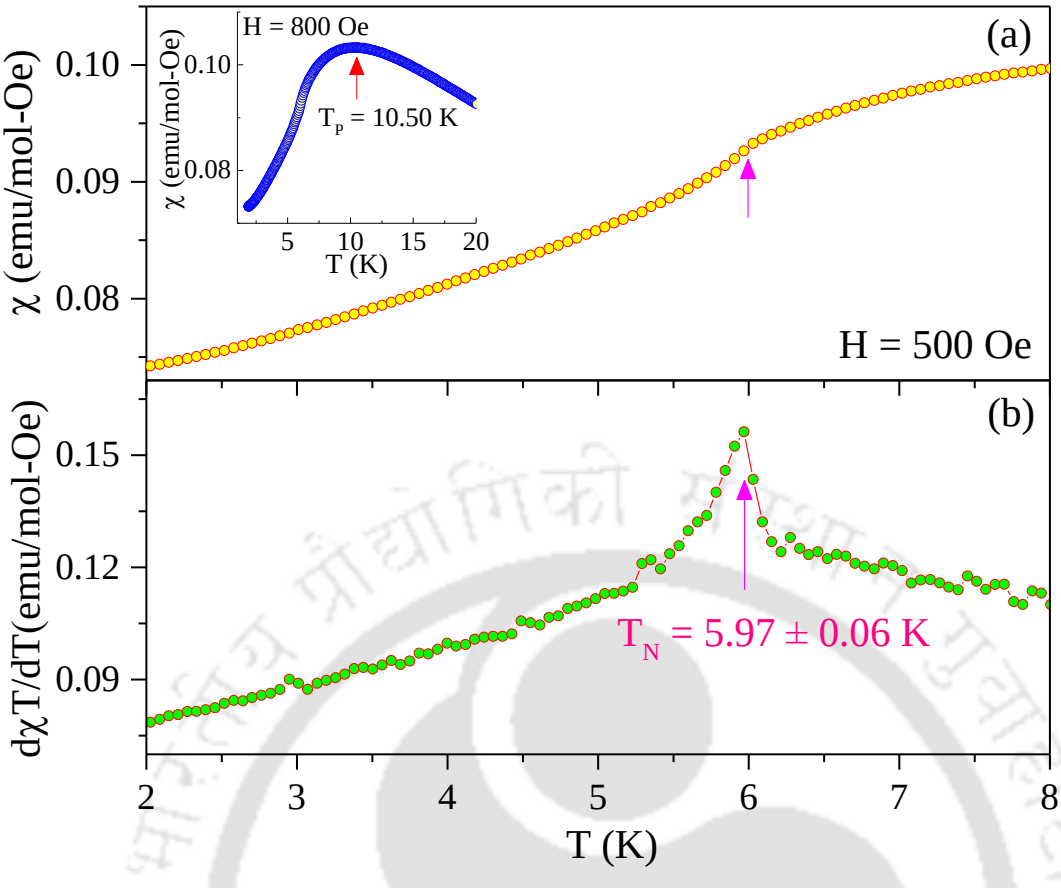

Fig. 5.7. (a) Temperature variation of the dc-susceptibility $\chi(T)$ measured under zero-field-cooled (ZFC) condition at H = 500 Oe. (b) Computed plot of $\partial(\chi T)/\partial T$ versus T showing a peak corresponding to T_N = 5.97 K. The inset of figure (a) shows $\chi_{ZFC}(T)$ vs T measured at H = 800 Oe with broad peak at T_P = 10.50 K marked by arrow.

$$T_N(H) = T_N(0) - D_1H^2 \tag{5.2}$$

$$D_1 = \frac{g^2\mu_B^2(2S^2 + 2S + 1)}{40k_B^2T_N} \tag{5.3}$$

For $MnTa_2O_6$, the plot of T_N determined from the peaks in $\partial(\chi T)/\partial T$ vs T data for different H vs H^2 is shown in Fig. 5.8. From the slope and intercept of linear fit to the equation (5.2) as shown in Fig. 5.8, D_1 = 0.326(5) × 10^{-9} K/Oe^2 and $T_N(0)$ = 5.97 K are obtained. Similar analysis for some other antiferromagnets has been previously reported yielding D_1 = 7.3 × 10^{-9} K/Oe^2 for Er_2O_3 [75], D_1 = 0.159 × 10^{-9} K/Oe^2 for MnF_2 [11,12], D_1 = 0.66 × 10^{-9} K/Oe^2 for $GeCo_2O_4$ [72] and D_1 = 0.9 × 10^{-9} K/Oe^2 for $MnNb_2O_6$ [86]. Using equation (5.3) with g = 2.0155 and S = 5/2 for $MnTa_2O_6$ yields calculated D_1 = 1.41 × 10^{-9} K/Oe^2 which is in fair agreement with the experimental value D_1 = 0.326(5)× 10^{-9} K/Oe^2 determined above. In all the above noted cases, the calculated D_1 using equation (5.3) is somewhat larger than the experimental value. This difference has been assigned to the inadequacy of molecular field theory near T_N, since long-range spin correlations which develop on approach to T_N are not properly taken into account in MFT.

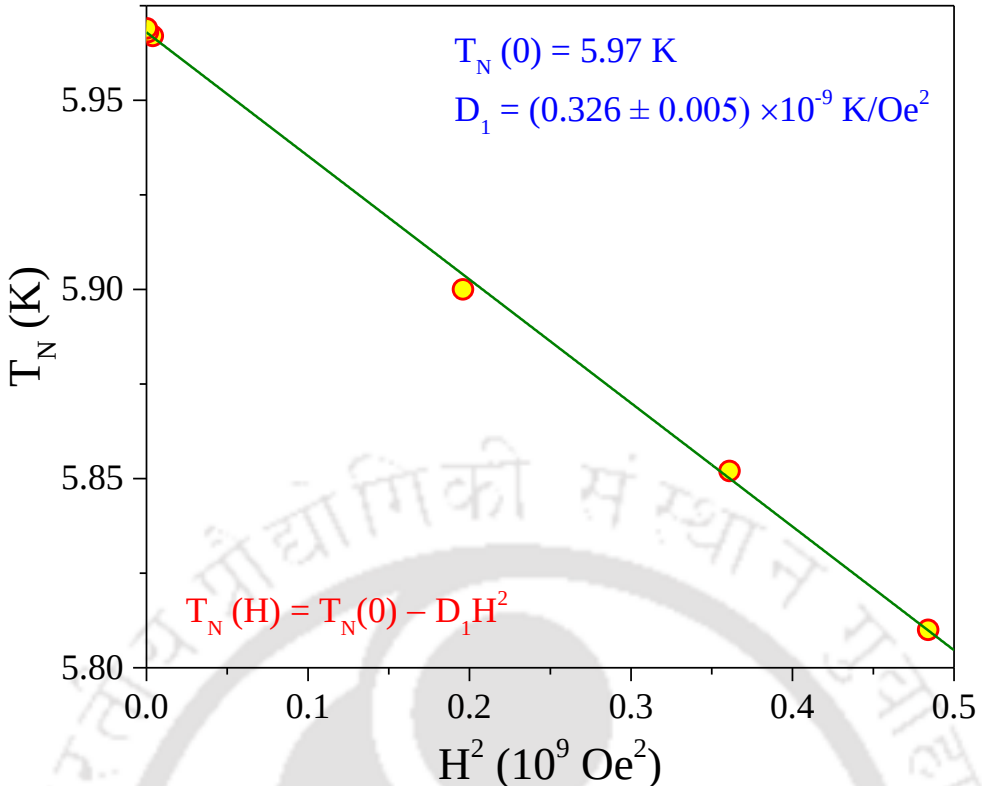

Fig. 5.8. The plot of T_N vs H^2. The solid green line represents the linear fit of the experimental data to the equation $T_N(H) = T_N(0) - D_1H^2$ with magnitudes of evaluated parameters listed.

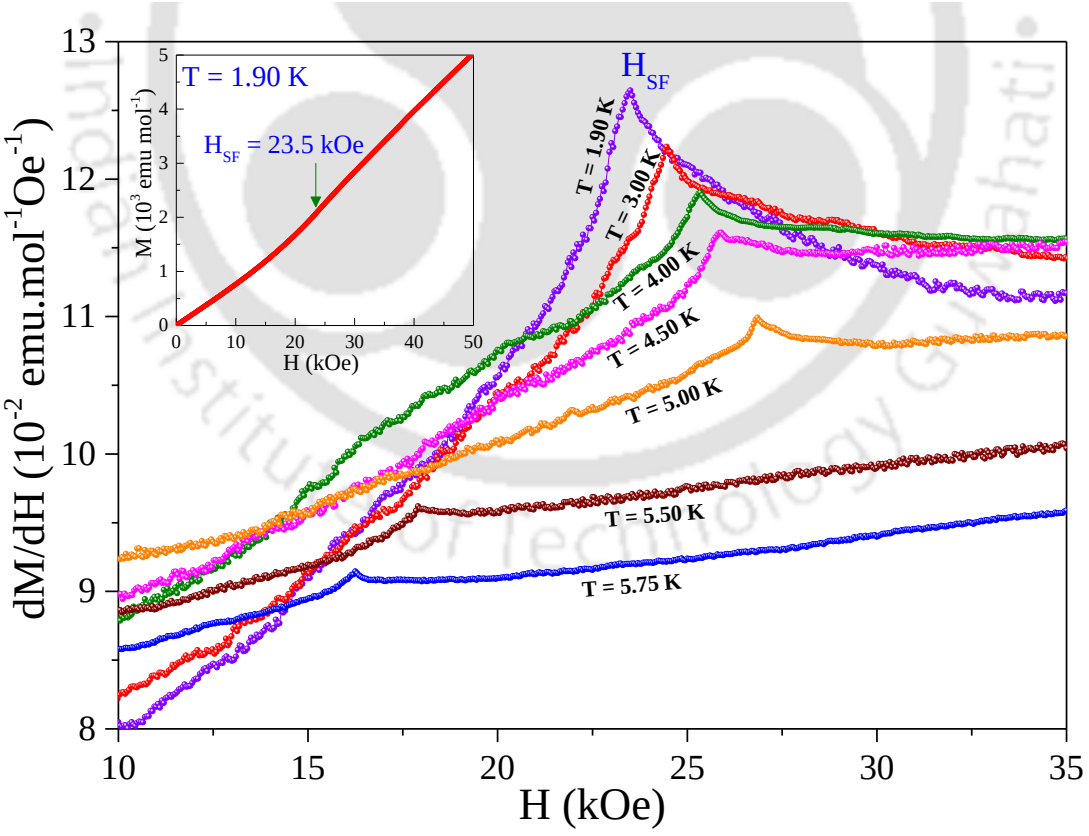

Fig. 5.9. The plots of computed ($\partial M/\partial H$) vs H using the data of the isothermal M vs H variations for different temperatures between 1.9 K and 5.75 K (the inset shows data at 1.9 K). The peaks correspond to the spin-flop field, H_{SF}.

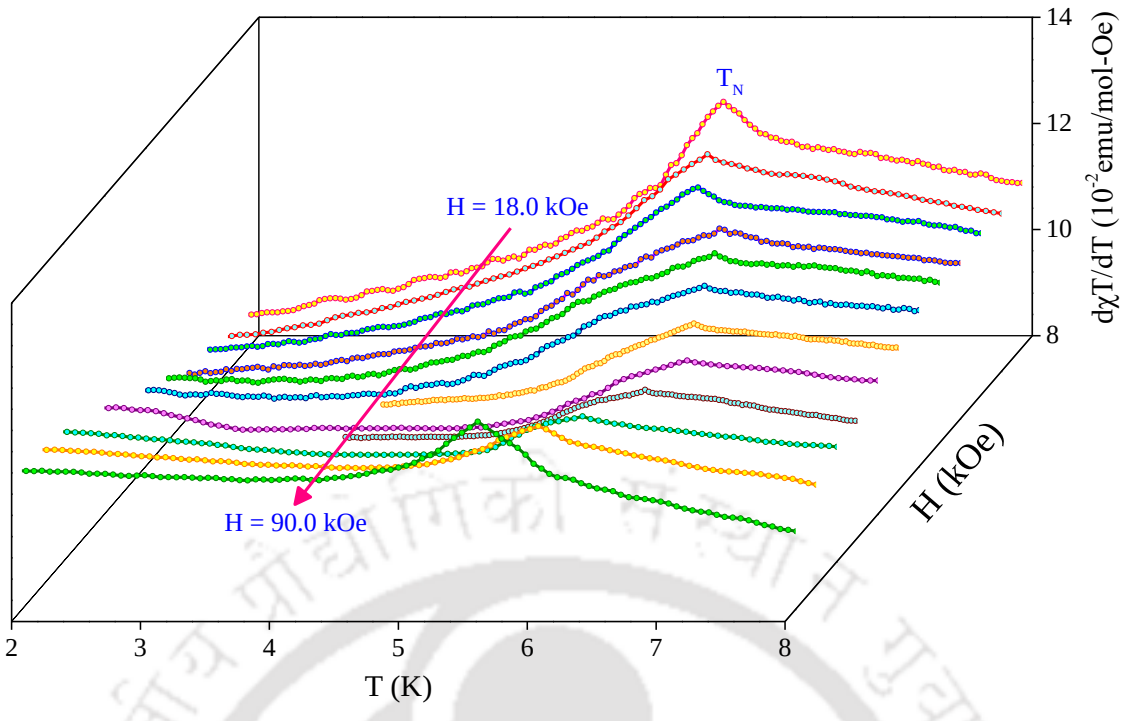

Fig. 5.10. Temperature dependence of the computed curves of $\partial(\chi T)/\partial T$ vs temperature using the measured M vs T plots at $H > H_{TP}$ (17.0 kOe). The plots shown are for H (kOe) = 18, 20, 22, 24, 26, 28, 35, 40, 50, 60, 70 and 90, with the peak representing T_N.

5.5.2. Spin-flop field and its temperature dependence

The magnetic field dependence of magnetization $M(H)$ up to 50 kOe at 1.9 K is shown in the inset of Fig. 5.9, with similar measurements have been done for different temperatures below T_N. The M–H isotherm in the inset of Fig. 5.9 shows clear variation of slope near 23.5 kOe, which is evident in the peak of the computed $\partial M/\partial H$ vs H curve showing a peak at H_{SF} = 23.5 kOe. For $H > H_{SF}$ applied along the easy direction, the spins flop to a direction perpendicular to the applied H, although the overall ordering of the spins is still antiferromagnetic. For a polycrystalline sample, the peak in $\partial M/\partial H$ at H_{SF} is weaker than that in a single crystal since only a fraction of the grains have their easy direction oriented parallel to the applied field. The $\partial M/\partial H$ vs H curves for different $T < T_N$ are plotted in the Fig. 5.9 and the field corresponding to the peaks in these curves are indicated as spin-flop field (H_{SF}). The magnitude of H_{SF} shows a weak temperature dependence as temperature approached T_N, a trend like that observed in antiferromagnets like MnF_2 [11,12] and $MnNb_2O_6$ [18]. The plot of this temperature dependence is given in the next section.

5.5.3. H–T phase diagram

The computed plots of the $\partial(\chi T)/\partial T$ vs T for H > 17 kOe are shown in Fig. 5.10, the peaks in these plots signifying the variation of T_N with H > 17 kOe. Using the H_{SF} vs T and T_N vs H variations obtained from the peaks in $\partial M/\partial H$ vs H and $\partial(\chi T)/\partial T$ vs T plots respectively, the obtained H–T phase diagram of $MnTa_2O_6$ is shown in the Fig. 5.11. This plot shows the triple point $T_{TP}(H, T)$ = (17.0 kOe, 5.69 K) for $MnTa_2O_6$ where the three phases namely AFM, spin-flop and PM coexist. In this plot we have included the data point of T_N = 5.47 K measured at H = 90 kOe using the specific heat measurements (see Fig. 5.4) and M vs H data up to H = 250 kOe and T = 1.5 K measured at the NHMFL (Fig. 5.12). Qualitatively, the H–T

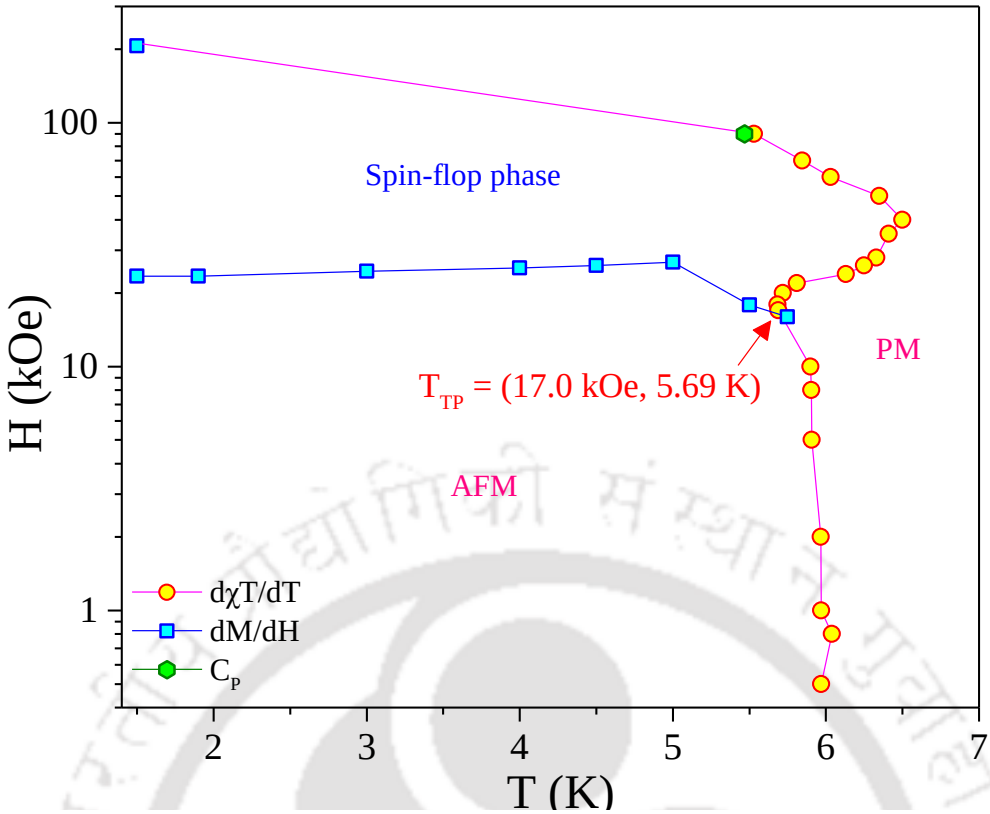

Fig. 5.11. *H–T* phase diagram of polycrystalline $MnTa_2O_6$ sample yielding triple point, $T_{TP}(H, T)$ = (17.0 kOe, 5.69 K) with the source of the data points marked in the legend. Lines connecting the data points are visual guides and PM = paramagnetic and AFM = antiferromagnetic.

phase diagram of Fig. 5.11 for $MnTa_2O_6$ is like that reported recently in $MnNb_2O_6$ with the $T_{TP}(H,T)$ = (18.0

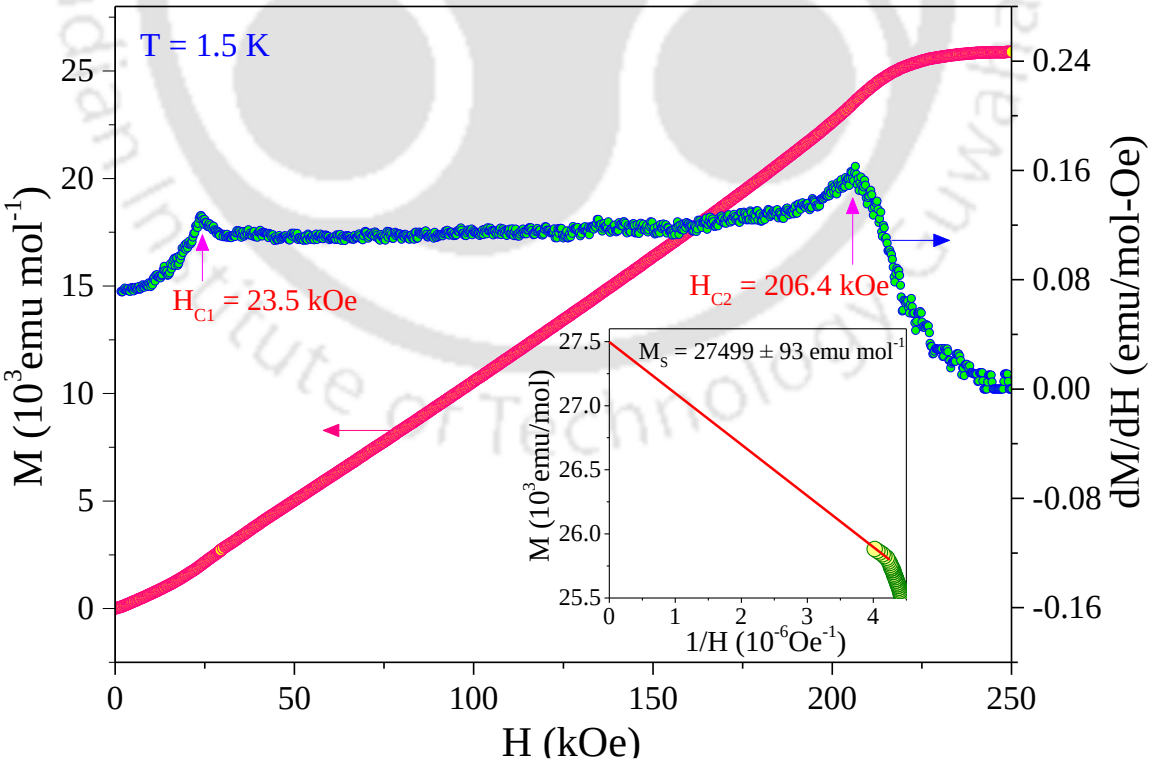

Fig. 5.12. Isothermal (T = 1.5 K) M vs H plot recorded at the NHMFL and the computed plot of dM/dH versus H yielding the two critical fields at H_{C1} = 23.5 kOe and H_{C2} = 206.4 kOe. Inset shows the plot of M vs 1/H at T = 1.5 K for H > 220 kOe to estimate the saturation magnetization M_S in the limit of 1/H →0.

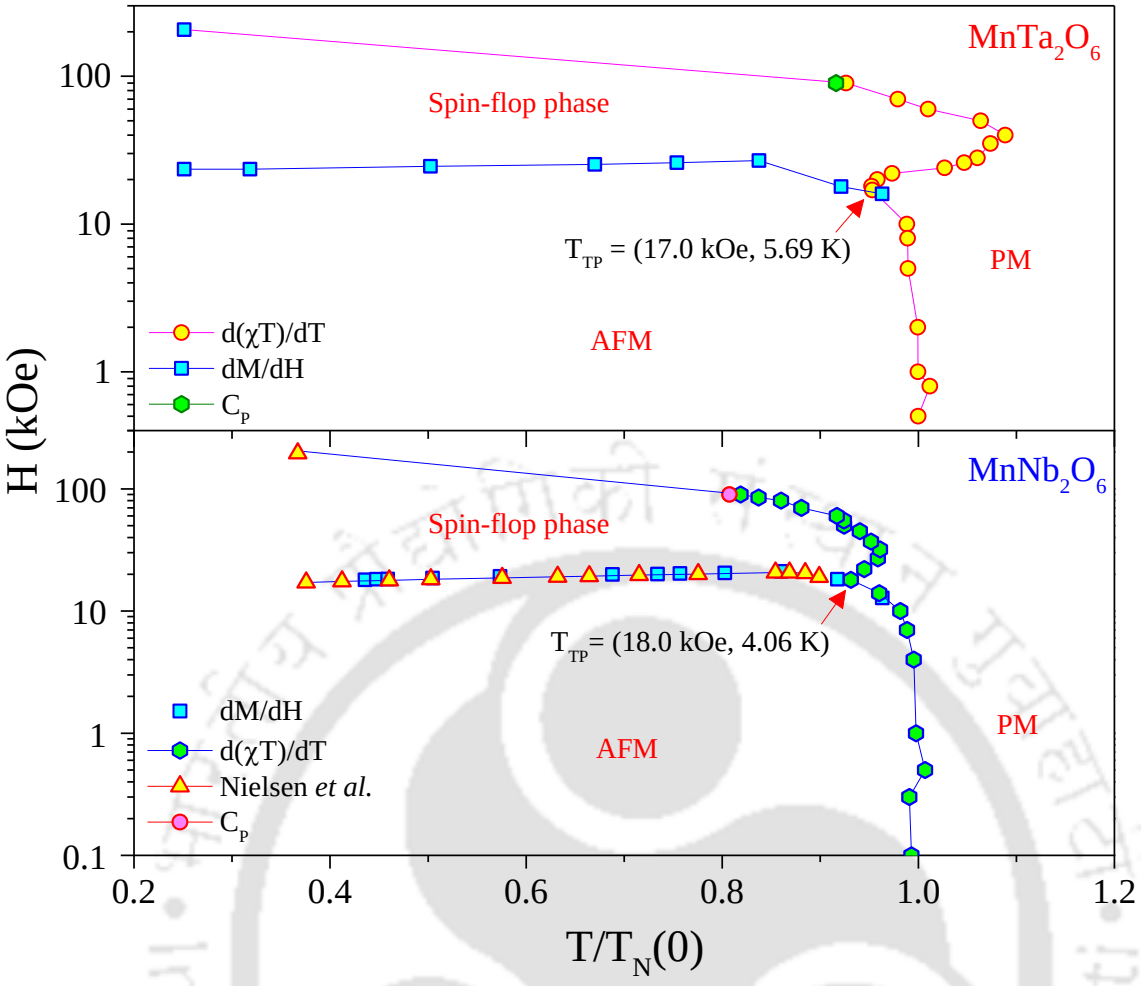

Fig. 5.13. The *H*–*T* phase diagrams of $MnTa_2O_6$ determined in this work (top) is compared with that of isostructural $MnNb_2O_6$ (bottom) reported recently in reference [18] by Maruthi *et al*. The reduced temperature scale of $T/T_N(0)$ with $T_N(0)$ = 6.00 K and 4.36 K for H = 0 Oe for $MnTa_2O_6$ and $MnNb_2O_6$ respectively is used and parameters of the triple point are listed in the figures. See text for discussion.

kOe, 4.06K) and $T_N(0)$ = 4.36 K except that in $MnTa_2O_6$, the increase in T_N for $H > T_{TP}(H,T)$ is more pronounced than that observed in $MnNb_2O_6$ [86] and even in MnF_2 [11,12]. This point is evident in the comparative comparison of the *H*–*T* phase diagrams of $MnTa_2O_6$ and $MnNb_2O_6$ when plotted in the reduced temperature scale of $T/T_N(0)$ as done in Fig. 5.13. The determination of this *H*–*T* phase diagram for $MnTa_2O_6$ is an important result of this work.

5.5.4. Temperature variation of the paramagnetic susceptibility

For applied H = 800 Oe, the temperature variation of magnetic susceptibility $\chi = M/H$ of $MnTa_2O_6$ between 1.9 K and 400 K is shown in Fig. 5.14. The analysis of χ vs T for $T > T_N$ was done based on the modified Curie–Weiss (CW) law [86]:

$$\chi = \chi_0 + \frac{C}{(T-\theta)} \tag{5.4}$$

Here θ and C are the Curie–Weiss temperature and Curie constant respectively and $\chi_0 = \chi_{vv} + \chi_d$ [72, 141] has contributions from both Van-Vleck susceptibility (χ_{vv}) and diamagnetic susceptibility (χ_d). Van-Vleck susceptibility (positive sign) arises when the systems have non-zero orbital angular momentum ($L \neq 0$) i.e.

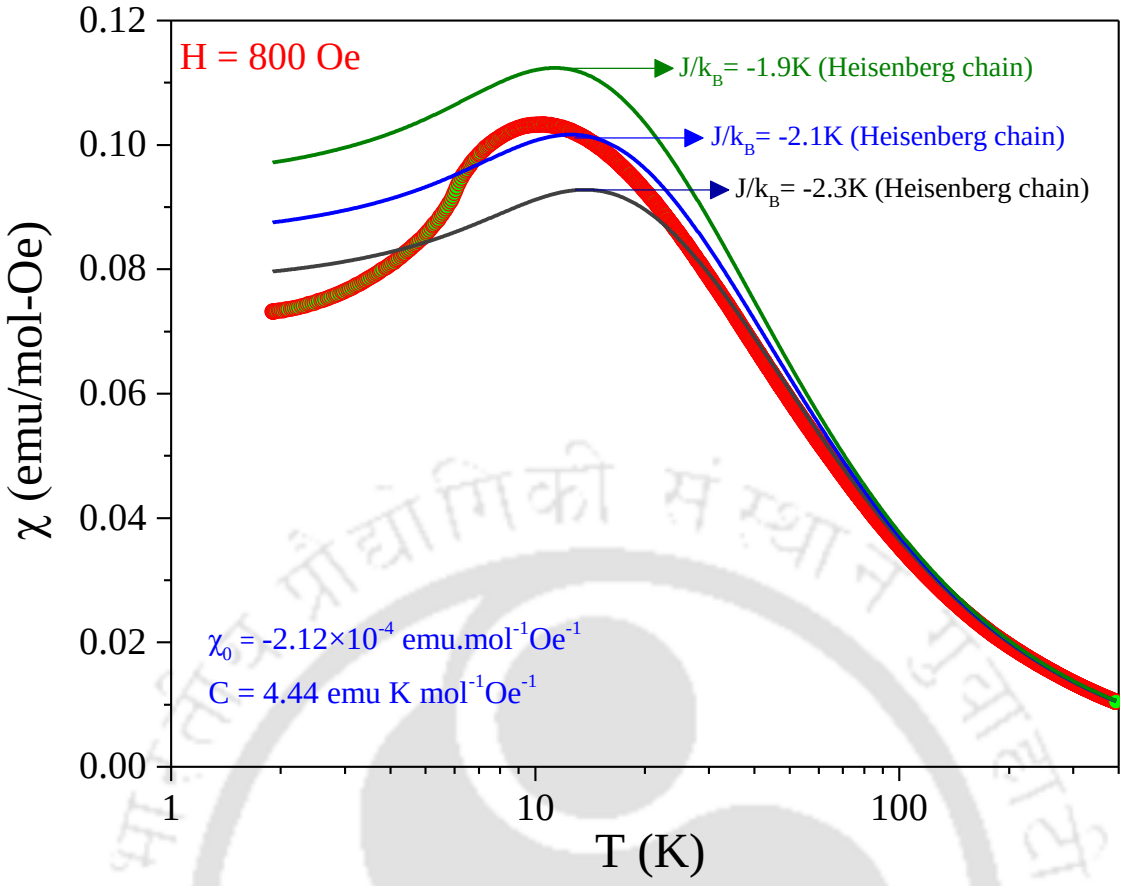

Fig. 5.14. Temperature dependence of magnetic susceptibility $\chi(T)$ recorded under ZFC mode at H = 800 Oe covering the maximum temperature range from 1.9 K to 400 K (red circles). The three solid lines are the fits to Heisenberg linear chain model given by equation (5.9) for different J/k_B values.

due to spin–orbit coupling whereas all systems have a (negative) diamagnetic susceptibility. In $MnTa_2O_6$ only Mn^{2+} contributes to the magnetic properties whereas Ta^{5+} is non-magnetic. The electronic configuration of Mn^{2+} is given as [Ar] $3d^5$ and the corresponding ground state spectral term is $^6S_{5/2}$ (L = 0) [142]. Therefore, spin–orbit coupling does not contribute to the magnetic moment to first order as also confirmed by the g = 2.0155 observed in the ESR experiments (Fig. 5.6). Hence it is expected that in $MnTa_2O_6$, $\chi_{vv} = 0$. The value of $\chi_0 = \chi_d = -2.1262 \times 10^{-4}$ emu mol^{-1} Oe^{-1} is estimated theoretically by adding the diamagnetic contribution of each atom [80]. Experimental determination of χ_0 is done by linear extrapolation of χ to χ_0 in the limit of $1/T = 0$ in the χ vs $1/T$ plot focussing on high temperature regime as shown in the inset of Fig. 5.15. This yields experimental $\chi_0 = -2.12 \times 10^{-4}$ emu mol^{-1} Oe^{-1} value, in agreement with the theoretical value. The CW linear fit for the plots of $(\chi - \chi_0)^{-1}$ vs T in the paramagnetic region for both $\chi_0 = -2.12 \times 10^{-4}$ emu mol^{-1} Oe^{-1} and $\chi_0 = 0$ are shown in the Fig. 5.15, with the intercept yielding θ and the slope yielding C. For $T > 25$ K, the linear fit for $\chi_0 = -2.12 \times 10^{-4}$ emu mol^{-1} Oe^{-1} yields $\theta = -24.0 \pm 2.0$ K, and $C = 4.44 \pm 0.02$ emu K mol^{-1} Oe^{-1} and for $\chi_0 = 0$, $\theta = -21.0 \pm 2.0$ K and $C = 4.33 \pm 0.02$ emu K mol^{-1} Oe^{-1} are obtained. The effective magnetic moment μ_{eff} is determined from the equation $C = N_A\mu^2/3k_B$ (k_B = Boltzmann constant, N_A = Avogadro's number) [86] yielding $\mu_{eff} = 5.89 \pm 0.02\ \mu_B$ per formula unit (f.u.) for $\chi_0 = 0$ and $\mu_{eff} = 5.96 \pm 0.02\ \mu_B$/(f.u.) for $\chi_0 = -2.12 \times 10^{-4}$ emu mol^{-1} Oe^{-1}. The latter is in excellent

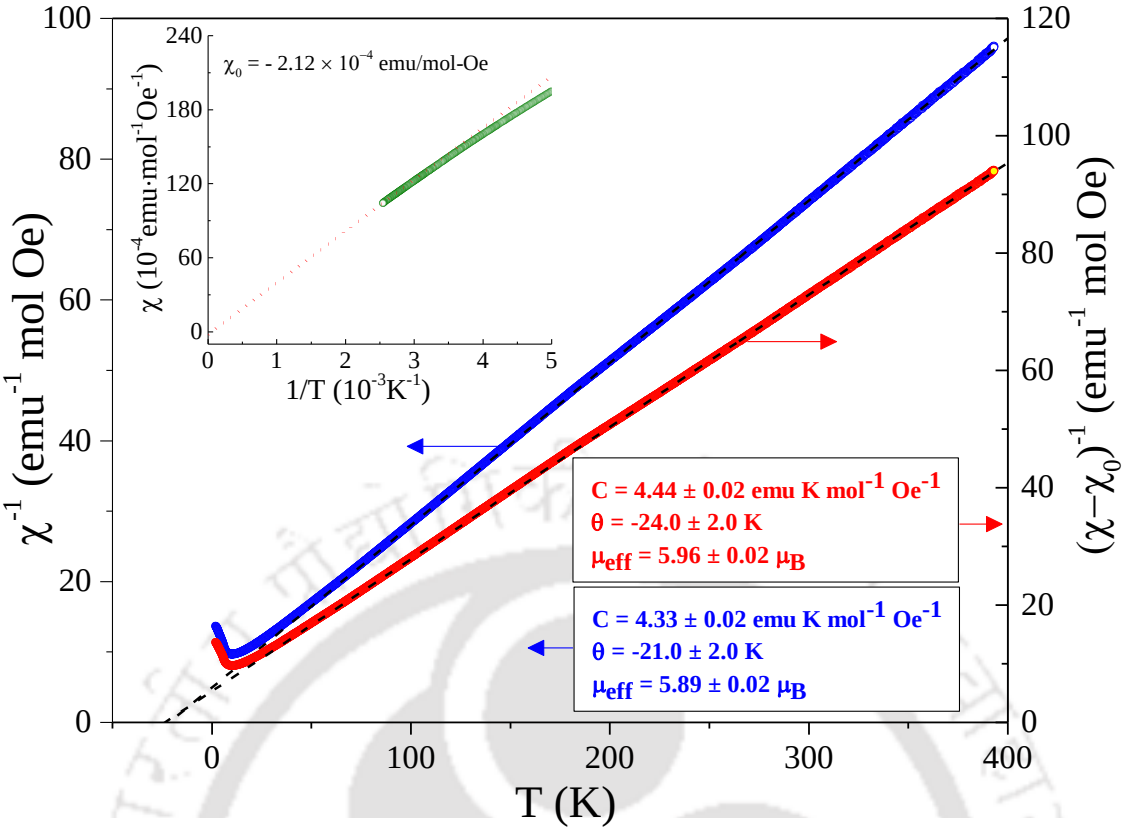

Fig. 5.15. Plots of the temperature variation of inverse magnetic susceptibility $(\chi - \chi_0)^{-1}$ for χ_0 = 0 and −0.000 212 emu mol^{-1}Oe^{-1}. Dotted lines represent the linear fits to modified CW law, equation (5.4), for T above ~25 K yielding the magnitude of C and θ listed in the figure. Note that different y-scales for the two cases are used to separate the two plots. The inset shows linear extrapolation of χ in the limit $1/T \rightarrow 0$ using the high-T points to determine χ_0.

agreement with μ_{eff} = 5.962 μ_B calculated from the equation $\mu^2 = g^2S(S+1)\mu_B^2$ using S = 5/2 for Mn^{2+} and the g = 2.0155 obtained here from ESR measurements, providing additional confidence in this analysis. Hence including the effect of χ_0 leads to the more accurate determination of θ, C and μ_{eff} values.

5.5.5. Saturation magnetization and anisotropy field

From the M vs H variation of Fig. 5.12 for H up to 250 kOe at temperature 1.5 K, the computed $\partial M/\partial H$ vs H plot yields two critical fields: the spin-flop field H_{SF} or H_{C1} = 23.5 kOe and H_{C2} = 206.4 kOe. As already described in section 5.5.2, H_{SF} is not a spin-flip transition which occurs from an antiferromagnetic (AFM) to ferromagnetic state resulting in considerably larger change in magnetization [39] than what is observed in $MnTa_2O_6$. Instead, in $MnTa_2O_6$, H_{SF} is a spin-flop transition to another AFM state, and only for $H > H_{C2}$, all the spins are forced to orient in the magnetic field direction thus overcoming the exchange coupling field H_E leading to forced ferromagnetism and saturation magnetization. The linear extrapolation of magnetization (M) in the M vs $1/H$ plot yields saturation magnetization M_S = 27499 ± 93 emu mol^{-1} in the limit of $1/H$ = 0 and so $H_E = H_{C2}$ = 206.4 kOe. The equation $M_S = \chi_\perp H_E$ [39] yields perpendicular susceptibility $\chi_\perp$ = 0.133 emu mol^{-1}Oe^{-1} which is approximately equal to the peak value of χ at 10.5 K just above the transition temperature shown in the inset of Fig. 5.7(a). This is corroborated by the reported data in single crystal of antiferromagnetic MnF_2 in which the susceptibility ($\chi_\perp$) perpendicular to easy axis is

found to be nearly temperature independent below T_N and so it is nearly equal to the peak value of χ just above T_N. Using $H_E = H_{C2}$ = 206.4 kOe and H_{SF} = 23.5 kOe, the anisotropy field H_A = 1.34 kOe is estimated for $MnTa_2O_6$ from the relation $H_{SF} = (2H_AH_E)^{1/2}$ [12,75,86]. At T = 0 K, the calculated saturation magnetization $M_S = N_A.g.\mu_B.S$ for complete alignment of the spins for $H > H_E$, using g = 2.0155 and S = 5/2, M_S = 28141 emu mol^{-1} is obtained which is only 2.3(3)% larger the measured M_S = 27499 ± 93 emu mol^{-1} at 1.5 K. This small difference is likely due to the temperature dependence of M_S which is expected to decrease with increase in temperature. This good agreement between the measured and calculated M_S leads us to conclude that in $MnTa_2O_6$, the ground state of Mn^{2+} has effective spin S = 5/2 with g = 2.0155, like in $MnNb_2O_6$ [86].

5.5.6. Determination of exchange constants

In $MnTa_2O_6$, as in $MnNb_2O_6$, Mn^{2+} ion has high spin S = 5/2 state. Therefore, molecular field theory (MFT) which becomes more appropriate for classical (large) spins can be applied for the estimation of exchange constants in this compound. Using the exchange Hamiltonian given in equation (5.1), the following expressions for θ and T_N using molecular field theory are obtained [30,79,86,]:

$$3k_B\theta = S(S + 1)[J_0Z_0 + (J_1Z_1 + J_2Z_2)] \quad (5.5)$$

$$3k_BT_N = S(S + 1)[J_0Z_0 - (J_1Z_1 + J_2Z_2)] \quad (5.6)$$

Here J_0 is the nearest neighbour exchange interaction among Mn^{2+} ions along the c-axis with nearest neighbours Z_0 = 2 where as J_1 and J_2 are the interchain exchange interactions among Mn^{2+} ions along the b-axis with nearest neighbours Z_1 = 2 and along the body-diagonal in the ab-plane with next nearest neighbours Z_2 = 4 respectively. Equations (5.5) and (5.6) have three exchange constants J_0, J_1 and J_2 and known values of θ and T_N are available from the Curie Weiss fit. Hence at best only two exchange constants can be determined. Therefore, to reduce the number of variables from 3 to 2, we make the approximation $J_1 = J_2 = J_\perp$ since as shown in Fig. 5.2, J_1 and J_2 are in the ab plane perpendicular to c-axis and have somewhat similar environment. This approximation was also made in isostructural $CoNb_2O_6$ [68] and $MnNb_2O_6$ [86]. Using S = 5/2, $J_1 = J_2 = J_\perp$, $Z_0 = Z_1$ = 2, and Z_2 = 4, equations (5.5) and (5.6) yield the following relations for J_0/k_B and $J_\perp/k_B$:

$$J_0/k_B = 3(\theta + T_N)/35 \quad (5.7)$$

$$J_\perp/k_B = (\theta - T_N)/35 \quad (5.8)$$

Substituting the experimentally determined θ = −24.0 ± 2.0 K and T_N = 6.00 K for $MnTa_2O_6$ in equations (5.7) and (5.8) yields J_0/k_B = −1.5 ± 0.2 K and $J_\perp/k_B$ = −0.85 ± 0.05 K. For $MnNb_2O_6$ with lower T_N = 4.36 K yielded J_0/k_B = −1.08 K and $J_\perp/k_B$ = −0.61 K [86]. This comparison shows that the ratio of $J_0/J_\perp$ is nearly identical in the two cases although the magnitudes of J_0/k_B and $J_\perp/k_B$ are comparatively smaller in $MnNb_2O_6$ because of its comparatively smaller magnitudes of θ = −17 K and T_N = 4.36 K [86]. Following our analysis of χ vs T data of $MnNb_2O_6$ in terms of the Heisenberg linear chain (HLC), a similar analysis is attempted for the data in $MnTa_2O_6$ using the theoretical expression [39,86]:

$$\chi = \chi_0 + \frac{C}{T}\left(\frac{1 + \Gamma}{1 - \Gamma}\right) \tag{5.9}$$

Here $\Gamma = \coth(y) - (1/y)$ with $y = 2JS^2/k_BT$. In this model, only a single exchange constant along the chain axis (*c*-axis) is considered. We fitted the experimental paramagnetic susceptibility χ vs T of $MnTa_2O_6$ with equation (5.9) valid for HLC and using $S = 5/2$, $\chi_0 = -2.12 \times 10^{-4}$ emu $mol^{-1}Oe^{-1}$ and $C = 4.44$ emu K $mol^{-1}Oe^{-1}$ obtained from the linear fits of modified CW law. The Fig. 5.14 shows the fit of susceptibility data to HLC model for different values of $J/k_B = -1.9$ K, -2.1 K and -2.3 K. The fit of the data for $J/k_B = -2.3$ K looks better compared to other J/k_B values and the fitting is very good for $T > 20$ K but for $T < 20$ K the theoretical curve with peak value near 14 K does not match with the experimental curve having peak at about 10 K for $J/k_B = -2.3$ K. From Fig. 5.14, it is evident that the HLC model gives at best a semiquantitative fit for $J/k_B = -2.3$ K. For comparison, $J_0/k_B = -1.5 \pm 0.2$ K and $J_\perp/k_B = -0.85 \pm 0.05$ K were determined earlier using molecular field theory. Since there are no other reported estimates of exchange constants in literature for $MnTa_2O_6$, the above magnitudes are the best estimates available to date in this system. Additional theoretical studies are therefore warranted for determining the exchange constants and to explain the reasons for higher T_N of $MnTa_2O_6$ vis-à-vis $MnNb_2O_6$.

5.6. Concluding remarks

The important results on the magnetic properties of $MnTa_2O_6$ presented here are as follows: (i) transition from the paramagnetic (PM) to antiferromagnetic (AFM) state occurs at $T_N = 6.00$ K; (ii) a complete *H*–*T* phase diagram is presented defined by the tricritical/triple point T_{TP} (*H*, *T*) = (17.0 kOe, 5.69 K), with a spin flop field $H_{SF} \simeq 23.5$ kOe and exchange field $H_E \simeq 206.4$ kOe at 1.5 K and calculated anisotropy field $H_A \simeq 1.34$ kOe; (iii) for $T > 25$ K, the χ vs T data fit well with the modified CW law yielding $\theta = -24.0 \pm 2.0$ K, and $C = 4.44 \pm 0.02$ emu K $mol^{-1}Oe^{-1}$, the latter yielding $\mu_{eff} = 5.96 \pm 0.02\ \mu_B$ and $g = 2.015$ per Mn^{2+}, consistent with the ESR measurements and the $S = 5/2$ ground state of the Mn^{2+} ions with negligible contribution for the spin–orbit coupling; (iv) molecular field theory and magnitudes of θ and T_N are used to determine the exchange constants $J_0/k_B = -1.5 \pm 0.2$ K along the *c*-axis and $J_\perp/k_B = -0.85 \pm 0.05$ K perpendicular to the *c*-axis; and (v) analysis of the specific heat data near T_N yields the critical exponent $\alpha = 0.106$ (0.13) for $T > T_N$($T < T_N$). At appropriate places in this chapter, comparison of these results in $MnTa_2O_6$ is made with those reported recently in isostructural compound $MnNb_2O_6$ with $T_N = 4.36$ K including the *H*–*T* phase diagram. This comparison shows two important differences. First, although the lattice constants of $MnTa_2O_6$ are somewhat larger those of $MnNb_2O_6$ as noted in the introduction, why the T_N and hence the exchange constants in $MnTa_2O_6$ are larger vis-à-vis those in $MnNb_2O_6$ is not understood. Second, there is a noticeable difference in the phase diagram of the two systems above T_{TP} (*H*, *T*) as noted in our results. Further investigations on understanding these differences are warranted.

Chapter 6

Ground-State Spin Configuration of Ising Ferromagnet $CoNb_2O_6$

In this chapter, we focus on the electronic structure and magnetic characterization of cobalt niobate $CoNb_2O_6$ system with a special focus on the ground state spin configuration. A detailed analysis on the magnetic exchange interactions of $CoNb_2O_6$ is presented and compare to the previous results. In the introductory section we present the key results which are already available and gaps in the literature. The following sections present the experimental details focusing on the growth, formation mechanism, microstructure and various other characterization methods employed in this study. In the later sections we discuss the results and summarize the important findings.

6.1. Literature survey

There has always been a great need to find real systems whose measured properties can be used to test the predictions of theoretically solvable models since such comparisons provide great insight into underlining physics. One such recent case is the predictions of excitations near a quantum critical point (QCP), which have been recently tested in the Ising ferromagnet $CoNb_2O_6$ when a critical field H_C = 52.5 kOe is applied transverse to the Ising axis [8,9,14,143]. Prior to these recent observations of quantum fluctuations well above T = 0 K in $CoNb_2O_6$ [8,9,14,69], magnetic properties of this highly anisotropic system have been reported by a number of groups since 1973 using magnetometry, neutron diffraction, and ^{93}Nb nuclear magnetic resonance, both in powder and single-crystal samples [63–67,144–150].

The first reports on the structural and magnetic properties of $CoNb_2O_6$ during the 1970s [63–65] showed that it crystallized in the columbite structure (space group *Pbcn*) with an orthorhombic unit cell of dimensions a = 14.167 Å, b = 5.714 Å, and c = 5.048 Å. In this structure, CoO_6 octahedra form chains along the *c*-axis with isosceles triangular geometry in the *ab*-plane. Magnetically, the Co^{2+} moments lie in the *ac*-plane with angle $\alpha \sim 31°$ from the *c*-axis in a zigzag fashion due to the two crystallographically inequivalent sites. The *ac* magnetic susceptibility (χ_{ac}) studies of Scharf *et al.* [65] in single crystals showed a peak in χ_{ac} near T = 3 K along the *a*-axis and near 2 K along the *c*-axis with no anomaly along the *b*-axis. These results were confirmed later by Hanawa *et al.* [144], who also measured the temperature dependence of the specific heat. The magnetic field dependence of the magnetization (M) at 1.4 K measured by Maartense *et al.* [64] for H parallel to the *c*-axis showed jumps in M near $H_{C1} \sim 300$ Oe and $H_{C2} \sim 3$ kOe leading to saturation magnetization $M_S \sim 14\,000$ emu mol^{-1} for $H > H_{C2}$. Magnetic and neutron diffraction measurements for H parallel to the *c*-axis reported by Heid *et al.* [66] showed that for $H < H_{C1}$, the magnetic phase transition from the paramagnetic (PM) phase to sinusoidally amplitude-modulated incommensurate (IC) magnetic ordering occurs at T_C = 2.95K followed by antiferromagnetic (AFM) ordering below T_N = 1.97K. The IC magnetic phase is characterized by the propagation vector $Q = (0, qy, 0)$ with temperature-dependent q lying in the range of $1/3 < q < 1/2$. Because of the isosceles triangular geometry in the *ab*-plane, the AFM phase below T_N has degeneracy with phases of propagation vector Q = (0, 0.5, 0) and (0.5, ±0.5, 0) that was identified using neutron diffraction [67,146,148,150].

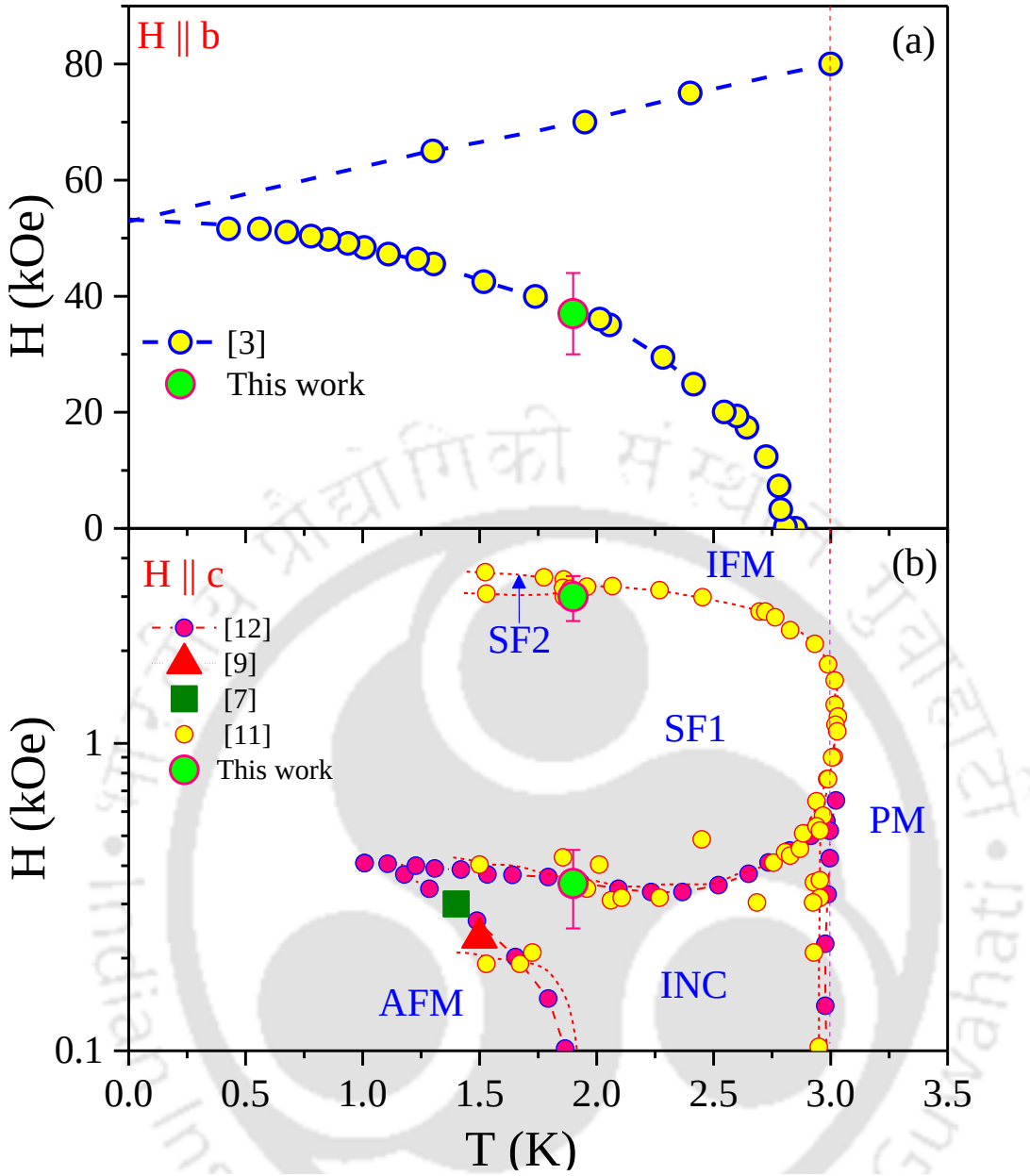

Fig. 6.1. *H-T* phase diagram for $CoNb_2O_6$ for *H* parallel to the *b*-axis in (a) and *H* parallel to the *c*-axis in (b). Lines connecting the data points are visual guides, and references to sources of the data points are listed in the figure. Green solid circles with error bars are data points from this work based on the peaks in *dM/dH* vs *H* shown in Fig. 6.7(b). The acronyms used for the magnetic phases are as follows: PM, paramagnetic; INC, incommensurate; AFM, antiferromagnetic; SF, spin-flip; and IFM, induced ferromagnetic.

The rich details of the *H-T* phase diagram of $CoNb_2O_6$ for *H* along different axes have been investigated by a number of groups. Following up on the earlier studies in Refs. [64-66,144,145] mentioned above, the phase diagram for *H* parallel to the *c*-axis was later confirmed in more detail by Kobayashi *et al.* [67,146,147]. Kobayashi *et al.* [148] also presented the *H-T* phase diagram for *H* along the *a*-axis, whereas Liang *et al.* [8] have reported the phase diagram for *H* parallel to the *b*-axis using specific-heat measurements, which yielded T_C = 2.85 K for H = 0. These results on the *H-T* phase diagrams for *H* along the *c*- and *b*-axis are summarized in Fig. 6.1, a discussion of our results will be presented later. For *H* along the *b*-axis, T_C decreases with an increase in *H*, reaching QCP with T_C = 0 K for H_C = 52.5 kOe [Fig. 6.1(a)].

For $H > H_C$, effects of quantum spin fluctuations have been reported recently even at nonzero temperatures [9,8,14]. With an increase in H applied along the c-axis in the IC phase, a spin-flip phase (SF1) is observed for $H_{C1} < H < H_{C2}$, and for $H > H_{C2}$ an induced ferromagnetic (IFM) phase is observed [Fig. 6.1(b)]. This anisotropic Ising-like linear-chain behaviour also became evident from the specific heat data, which showed the presence of significant magnetic entropy well above T_C up to about 25 K [8,144] and broadening and shifting of the peak to higher temperature with an increase in H.

To understand this rich yet complex magnetic phase diagram, good knowledge of the important exchange interactions and anisotropy energies is required. Recent publications by Kobayashi *et al.* [67,146,147] and Sarvezuk *et al.* [149] have noted that the important exchange interactions among Co^{2+} ions are the intrachain ferromagnetic (FM) exchange constant J_o along the c-axis and interchain AFM exchange constants J_1 and J_2 in the ab-plane using the Hamiltonian

$$H = -J_0 \sum_i S_i^z S_{i+1}^z - J_1 \sum_{<ij>} \boldsymbol{S}_i . \boldsymbol{S}_j - J_2 \sum_{<ij>} \boldsymbol{S}_i . \boldsymbol{S}_j \qquad (6.1)$$

where the sums are over nearest neighbours along the c-axis for J_0 and nearest neighbours and next-nearest neighbours of Co^{2+} ions, respectively, for J_1 and J_2 in the ab-plane. Assuming $S = 3/2$ as the ground state for Co^{2+} ions in $CoNb_2O_6$ based on Hund's rules, and using the above-listed magnitudes of H_{C1} and H_{C2} and molecular field theory for T_C, Kobayashi *et al.* [67,146,147] reported that the intrachain ferromagnetic exchange constant $J_0/k_B = 0.6016$ K and it is an order of magnitude larger than the interchain AFM exchange constants $J_1/k_B = -0.0508$ K and $J_2/k_B = -0.0812$K. Heid *et al.* [66] reported $J_1/k_B = -0.051$ K and $J_2/k_B = -0.029$ K, whereas Sarvezuk *et al.* [149,150] reported $J_0/k_B = 1.18$ K and $J_1/k_B = -0.104$ K.

The focus of this chapter is on two issues: (i) The magnitude of effective spin "S" of the ground state of Co^{2+} ions in $CoNb_2O_6$, $S = 3/2$ as determined by Hund's rules and used in earlier publications [66,67,146–150] or $S = 1/2$ as implied or reported in recent papers on $CoNb_2O_6$ [8,9,14,69]; and (ii) redeterminations of the exchange constants since it is argued here that the ground state of Co^{2+} in $CoNb_2O_6$ has effective $S = 1/2$. Both the effective spin for the ground state of Co^{2+} and accurate values of the intrachain and interchain exchange interactions are important for a proper understanding of the properties of $CoNb_2O_6$. The analysis and discussion of the experimental results on the temperature and magnetic field dependence of the magnetization (M) of $CoNb_2O_6$ presented here show that only $S = 1/2$ (and not $S = 3/2$) can consistently explain the M versus T and M versus H data both above and below T_C. As a result, the new magnitudes of the exchange constants J_0, J_1, and J_2 are presented. As discussed in great detail recently in other Co^{2+} containing systems such as β-$Co(OH)_2$ [151], $GeCo_2O_4$ [72], and $CoCl_2$ [152], the effective $S = 1/2$ in these systems results from combined effects of noncubic crystalline crystal field and spin-orbit interaction. Details of these results in $CoNb_2O_6$ along with their discussion and analysis are presented below.

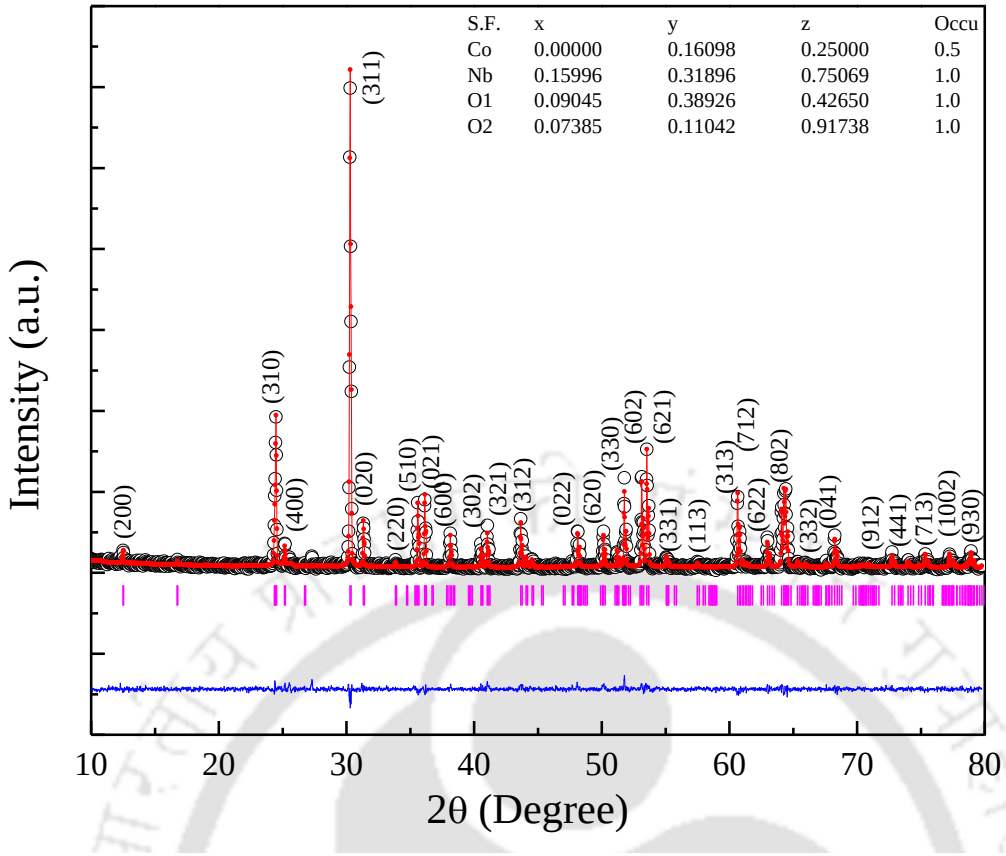

Fig. 6.2. Room-temperature XRD pattern of the $CoNb_2O_6$ sample together with the Rietveld refined data and the Miller indices of the Bragg lines listed. The blue line at the bottom represents the difference between the measured and simulated patterns. The inset shows the position of the atoms.

6.2. Material synthesis and structural characterization

Bulk polycrystalline samples of $CoNb_2O_6$ were prepared using the solid-state reaction method starting with stoichiometric proportions of Co_3O_4 and Nb_2O_5 by thoroughly grinding them in an agate mortar/pestle for 5 h, followed by pressing the homogenized powder into pellets of size 15 mm in diameter using a hydraulic press. The pellets were sintered at 1200 °C in air for 8 h. The crystal structure and phase purity of this sintered material were examined using the Rigaku x-ray diffractometer (model: TTRAX III) with Cu Kα (λ = 1.5406 Å) radiation. The room-temperature x-ray diffraction (XRD) pattern shown in Fig. 6.2 and refined by the Rietveld technique using the FULLPROF Suite showed that the sample is $CoNb_2O_6$ without any secondary phases exhibiting an orthorhombic crystal structure [space group $Pbcn$-D_{2h}^{14} (No.60)] with lattice parameters a = 14.167 Å, b = 5.714 Å, and c = 5.046 Å; average bond lengths of 2.025 Å (Co-O) and 1.960 Å (Nb-O); and average bond angles of 106.0° (Nb-O-Nb), 127.8° (Co-O-Nb), and 100.9° (Co-O-Co). The field emission scanning electron micrograph (FESEM) images of $CoNb_2O_6$ (not shown here) revealed the average size of the grains was ~1.7 to 2 μm. The electronic structure and chemical composition of the sample were probed using an x-ray photoelectron spectrometer (XPS) from Kratos Analytical (model: AXIS Supra+) configured with a dual monochromatic x-ray source Al Kα /Ag Lα (2984.2 eV) with spatial resolution less than 1 μm. These XPS spectra (Fig. 6.3) were calibrated by selecting the binding energy of carbon C 1s orbital (located at E_C = 284.8 eV) as an internal reference. The O1s spectrum is resolved into two Gaussian-Lorentzian peaks centered at 528.17 and 529.98 eV. The origin of the most intense peak at

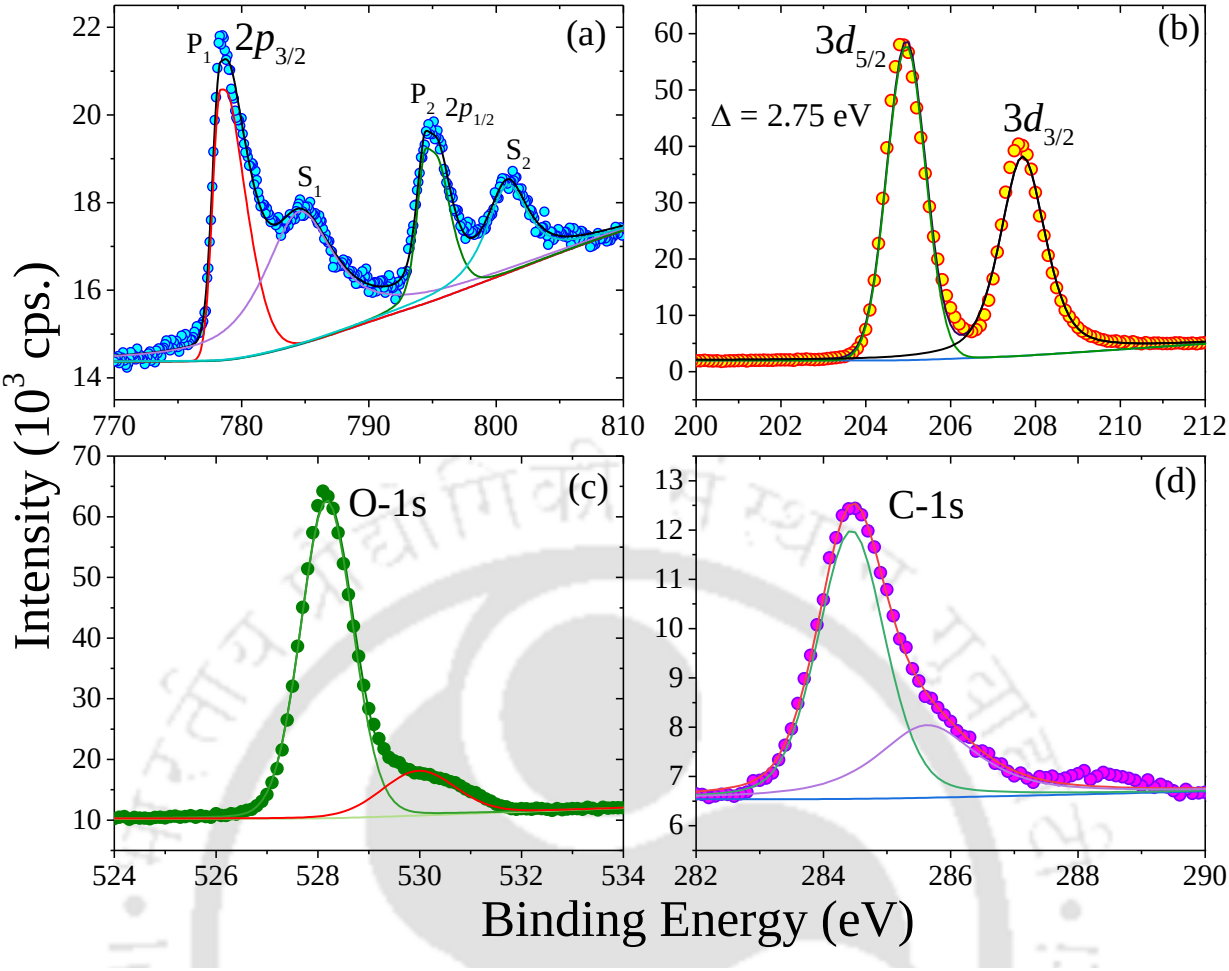

Fig. 6.3. X-ray photoelectron spectra of (a) Co 2*p*, (b) Nb 3*d*, (c) O 1*s*, and (d) C 1*s* for the polycrystalline $CoNb_2O_6$ sample. The solid lines are fits to Gaussian-Lorentzian line shapes.

528.17 eV is associated with the bonding between metal and lattice oxygen, whereas the second peak at 529.98 eV is associated with the surface absorbed oxygen [71,153,154]. The Nb 3*d* core level spectrum exhibits two sharp peaks at 204.95 and 207.70 eV with a binding energy separation between these peaks of $\Delta \sim 2.75$ eV, which is close to the standard value $\Delta = 2.72$ eV, confirming the pentavalent oxidation state of Nb [70]. On the other hand, the deconvolution of the Co 2*p* core level spectrum consists of four peaks, of which two main peaks (P_1 and P_2) are located at 778.34 and 794.48 eV, respectively, ($2p_{3/2}$ and $2p_{1/2}$). The two broad satellite peaks S_1 and S_2 are centered at 784.51 and 800.87 eV, respectively. The binding energy separation (ΔE) between the doublets P_1 and P_2 (spin-orbit splitting ΔE (P_2-P_1)) is approximately 16.14 eV, which confirms the divalent oxidation state of Co [72]. The conclusion from the analysis of the XPS data (Fig. 6.3) shows Co^{2+} and Nb^{5+} as the electronic states in the $CoNb_2O_6$ sample.

6.3. Magnetic properties

6.3.1. Temperature and magnetic field dependence of magnetization

The magnetization (M) of the polycrystalline $CoNb_2O_6$ bulk sample reported here was measured using the vibrating sample magnetometer (VSM) based physical property measurement system (PPMS-

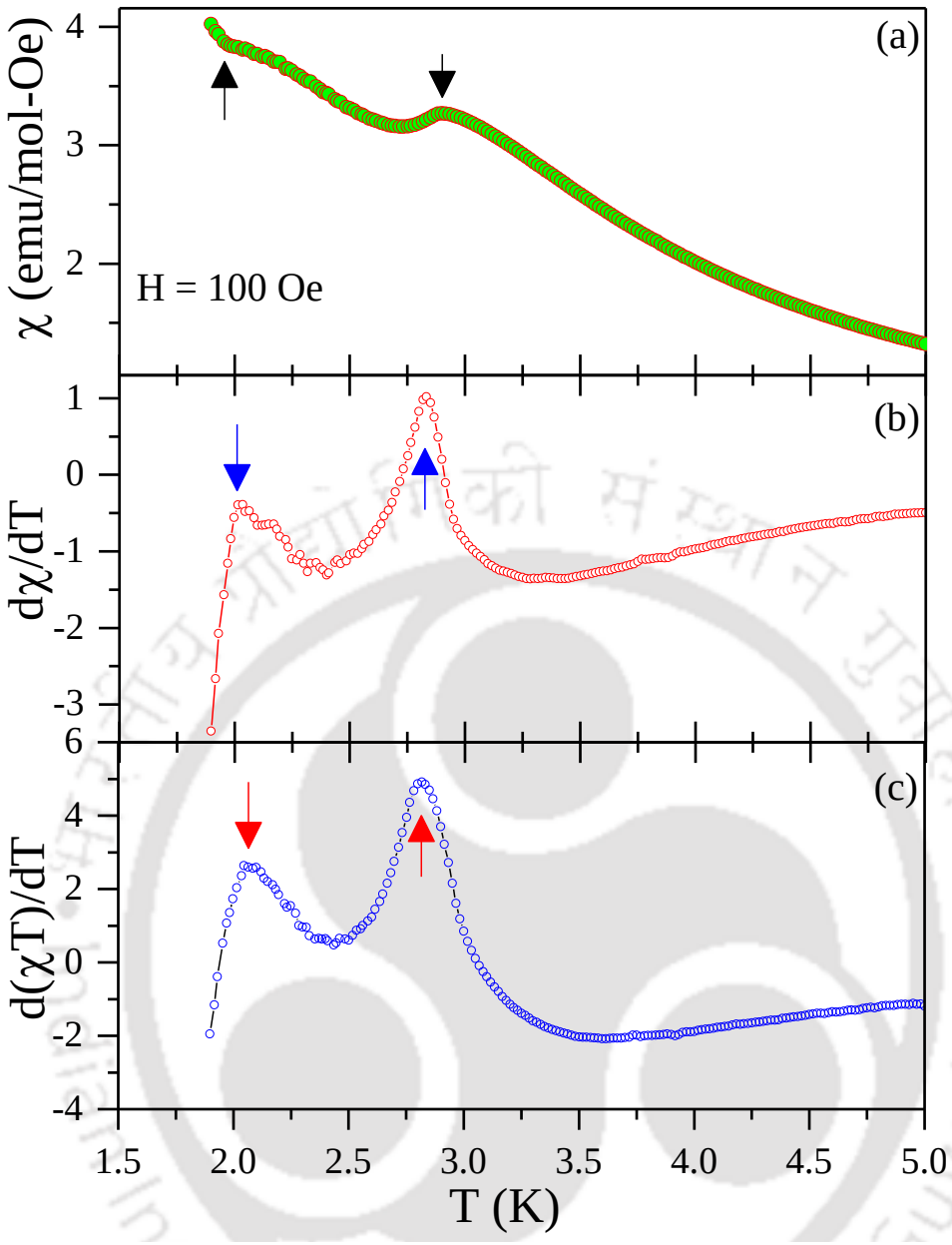

Fig. 6.4. Plots of $\chi = M/H$ (H = 100 Oe) and the computed $d\chi/dT$ and $d(\chi T)/dT$ vs T for the 1.9–5 K range are shown in (a), (b), and (c) respectively. The peaks representing transition points T_C = 2.0 ± 0.1 K and T_N = 2.8 ± 0.1 K are marked by arrows.

VSM) from Quantum Design (Model: Dynacool) with temperature capabilities from T = 1.9 to 400 K in *dc*-magnetic fields (H) up to ±90 kOe. To measure M versus T, the sample was cooled to 1.9 K in H = 0, and a nonzero H was then applied followed by acquiring the data with increasing T after stabilizing the temperature at each T. For M-T measurements, the step size ΔT is 0.02 K, and for M-H measurements the data are recorded at interval ΔH = 50 and 300 Oe for H < 1500 Oe and H > 1500 Oe, respectively. The temperature dependence of the magnetic susceptibility $\chi = M/H$ for H = 100 Oe between T = 1.9 and 5 K is shown in Fig. 6.4(a) with the computed $d\chi/dT$ and $d(\chi T)/dT$ versus T shown in figures 6.4(b) and 6.4(c), respectively. Usually, a peak in $d\chi/dT$ marks the transition from the PM to the FM state since M versus T data in such cases have an inflection point at T_C [155]. In the PM to AFM transitions at the Néel temperature T_N, it has been shown both theoretically [73] and experimentally [74] that T_N is accurately determined by the peak in

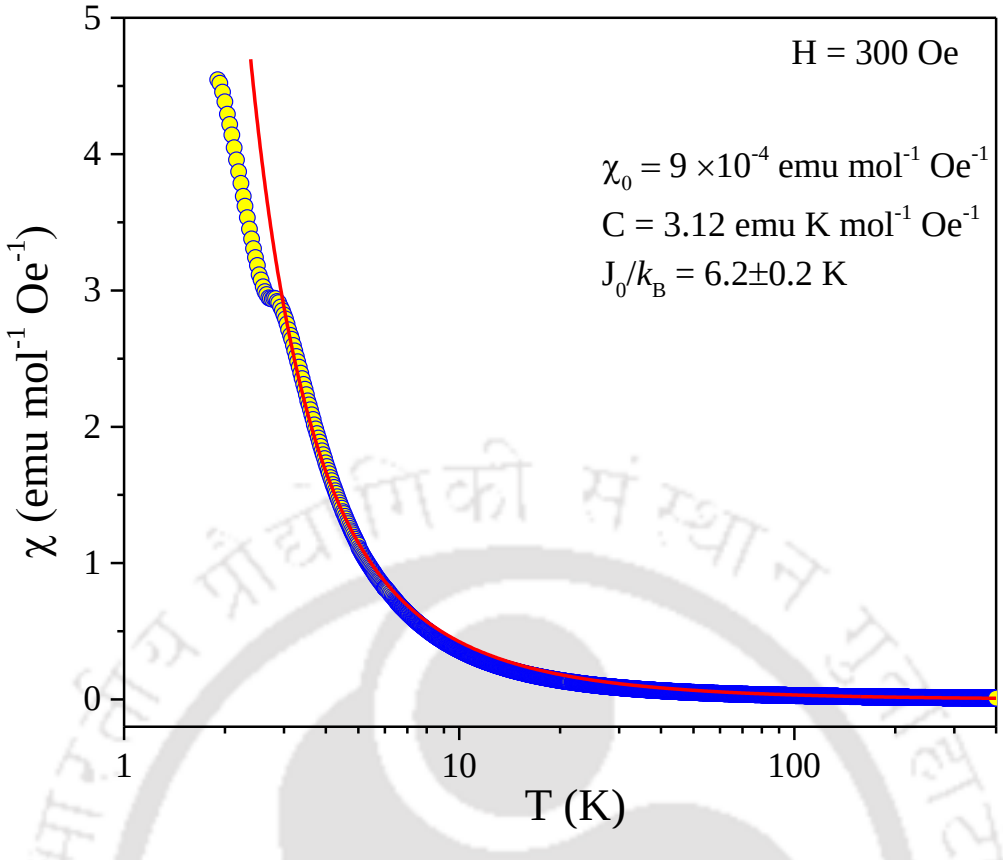

Fig. 6.5. Temperature dependence of the measured $\chi = M/H$ (H = 300 Oe) from 1.9 to 400 K. The solid line is fit to $\chi = \chi_0 + (C/T)\exp(J_o/2k_BT)$ representing the Ising linear chain model with the fitting parameters listed in the figure.

$d(\chi T)/dT$ since χT is proportional to magnetic energy near T_N in an antiferromagnet and so the peak in $d(\chi T)/dT$ corresponds to the peak in the specific heat. In the present case, within the resolution of our experiments, peaks in $d\chi/dT$ and $d(\chi T)/dT$ occur at the same temperature, i.e., T_C = 2.8 ± 0.1K for the PM to the IC state and T_N = 2.0 ± 0.1 K for the IC to the AFM state. These values are close to the magnitude T_C = 2.85–2.95 K and T_N = 1.97 K for $CoNb_2O_6$ reported by others as mentioned in the Introduction. Since our sample is polycrystalline in nature, our data illustrate all the key features of the reported results for H along all three principal directions, although the peaks near T_C and T_N are understandably not as sharp as those observed in single crystals. The measured data of χ versus T with H = 300 Oe and covering the temperature range from 1.9 to 400 K are shown in Fig. 6.5 with the solid line being a theoretical fit discussed later. We chose H = 300 Oe for these measurements up to 400 K since in H = 100 Oe, the data for T > 300 K became noisier due to smaller magnitudes of M at the smaller H. Following the procedures used in the recent papers on several other Co^{2+} containing systems viz. $GeCo_2O_4$ [72] and Co_2RuO_4 [141], the temperature dependence of paramagnetic susceptibility χ of $CoNb_2O_6$ for $T > T_C$ was fit to the modified Curie-Weiss (MCW) law given by $\chi = \chi_0 + C/(T-\theta)$. Here $\chi_0 = \chi_d + \chi_{vv}$ contains contribution from the (negative) diamagnetic susceptibility χ_d and the (positive) Van Vleck susceptibility χ_{vv}, both of which have only a very weak temperature dependence [80,156,157]. All the systems have nonzero χ_d although it may be comparatively negligible [80], whereas χ_{vv} is present in systems with spin-orbit coupling [156,157]. Since χ_d and χ_{vv} are of opposite signs, $\chi_0 = \chi_d + \chi_{vv}$ is often difficult to calculate accurately. Experimentally, χ_0 is determined

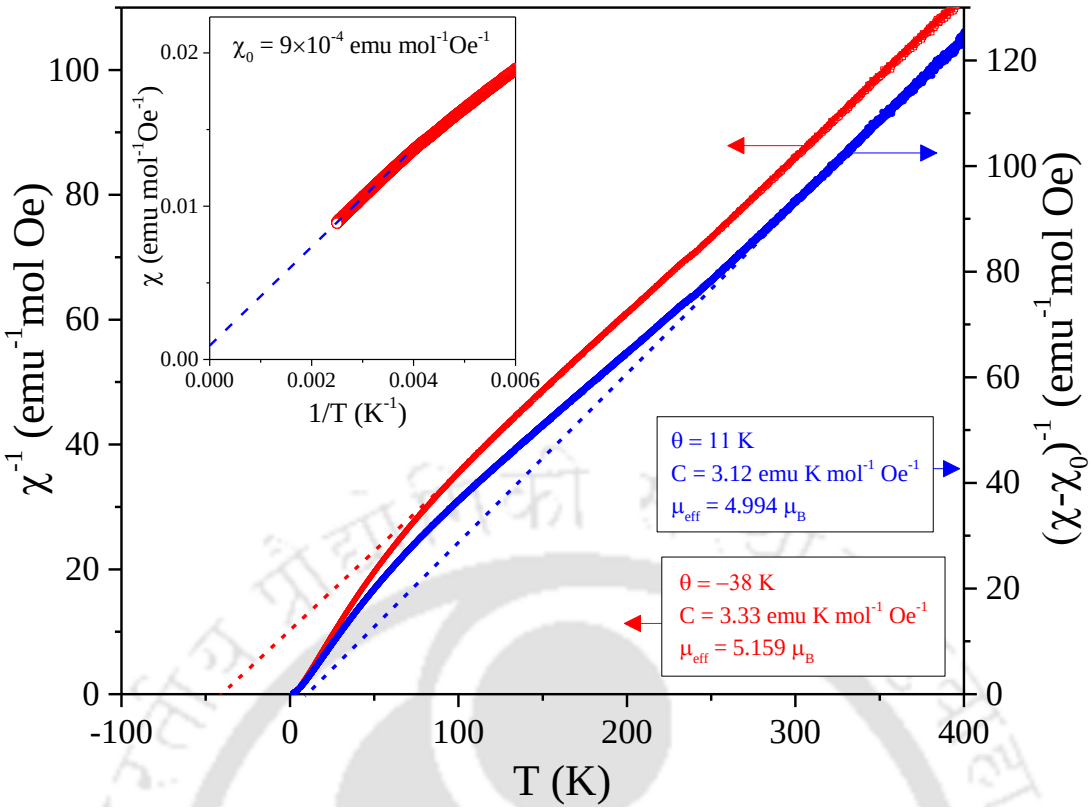

Fig. 6.6. Plots of $(\chi-\chi_0)^{-1}$ vs T for $\chi_0 = 0$ and 0.0009 emu mol^{-1}Oe^{-1} with the straight line fits for the high-temperature data to determine C and θ with the numbers given inside the figure and Table 6.1. The inset shows the plot of χ vs $1/T$ to determine χ_0 by linear extrapolation of the high-T data in the limit of $1/T = 0$.

from the plot of χ versus $1/T$ in the limit of $1/T \rightarrow 0$ with a focus on the high-T data where the contribution from the paramagnetic term $C/(T-\theta)$ becomes neglible. As shown in Refs. [72,141], the χ_0 term can have a significant effect on the magnitudes of the Curie constant C and Curie-Weiss temperature θ, the latter expected to be negative (positive) for antiferromagnetic (ferromagnetic) interaction. The fits of the χ versus T data to the CW ($\chi_0 = 0$) and MCW ($\chi_0 = 9.0 \times 10^{-4}$ emu mol^{-1}Oe^{-1}) laws, as plots of $(\chi-\chi_0)^{-1}$ versus T, are shown in Fig. 6.6, where χ_0 was determined from the plot of χ versus $1/T$ in the limit of $1/T \rightarrow 0$ as shown in the inset of Fig. 6.6. The slope of the linear fits at the higher T yields $1/C$ and intercepts θ. For $\chi_0 = 0$, the linear fit gives $\theta = -38$ K, $C = 3.33$ emu K mol^{-1}Oe^{-1}, whereas for $\chi_0 = 9 \times 10^{-4}$ emu mol^{-1}Oe^{-1}, the linear fit yields positive $\theta = 11$ K and $C = 3.12$ emu K mol^{-1}Oe^{-1}. The negative $\theta = -38$ K for $\chi_0 = 0$ is not realistic in this case since the dominant exchange interaction is ferromagnetic as noted in earlier publications [8,9,14,63–67,69,144–150] and determined accurately here later. Generally, a negative sign of θ implies that the dominant exchange interaction is antiferromagnetic, whereas in the present case the dominant exchange interaction J_0 between Co^{2+} ions is ferromagnetic, as discussed later. The magnetic moment μ determined from $C = N_A\mu^2/3k_B$ (N_A = Avogadro's constant and k_B = Boltzmann's constant) is $\mu = 5.159\mu_B$ ($4.994\mu_B$) for $\chi_0 = 0$ ($\chi_0 = 9 \times 10^{-4}$ emu mol^{-1}Oe^{-1}). Since $\mu^2 = g^2S(S+1)\mu_B^2$, these magnitudes of μ are used to calculate g for $S = 1/2$ and $3/2$ and these numbers are given in Table 6.1. It is noted that $g \sim 6$ for Co^{2+} ions in systems with an $S = 1/2$ ground state is quite common [72,151,152]. The plot of the M versus H data measured at 1.9 K is shown in Fig. 6.7(a) and that of computed dM/dH versus H is shown in Fig. 6.7(b) using the log scale

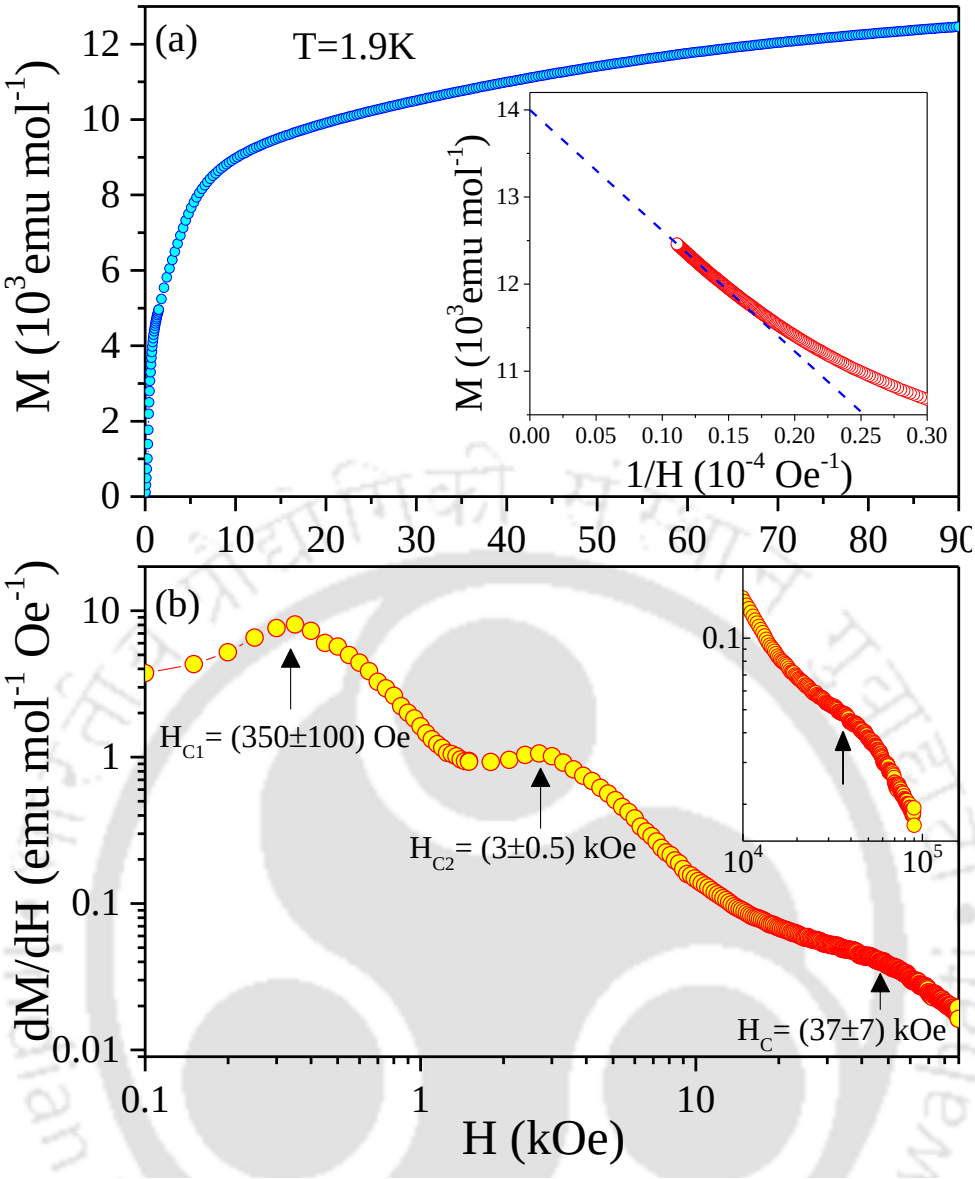

Fig. 6.7. (a) Plot of the measured magnetization (M) vs applied field H in kOe at 1.9 K. The inset shows a plot of M vs $1/H$ to determine the saturation magnetization M_S by linear extrapolation of the high-H data to $1/H = 0$ shown by the dotted line; (b) plot of computed dM/dH vs H using the data of M vs H in (a). Log scale is used for H to show resolved peaks at low H with the inset showing the broad anomaly centered at 37 kOe. These peak positions marked by arrows are plotted in the H-T phase diagram of Fig. 6.1.

for H to highlight the variations for lower H. The peaks in dM/dH versus H are observed at H_{C1} = 350 Oe, H_{C2} = 3.0 kOe, and a broad peak near H_C = (37 ± 7) kOe. These critical fields, plotted in Fig. 6.1 with error bars, are in good agreement with earlier measurements performed on single crystals for H parallel to the c and b-axis, although peaks in our measurements reported here on the polycrystalline sample are understandably diffused. Usually, in the polycrystalline sample, the grains are oriented in different directions, leading to some fraction of grains with their principal axis (a, b, and c) along the applied field. So, in general, one can still expect to observe anomalies such as spin-flip and spin-flop transitions [72], although changes in magnetization associated with the anomalies are expected to be weaker in a polycrystalline sample as compared to those observed in a single crystal in which magnetic field can be

oriented along a particular axis. The results plotted in Fig. 6.1 derived from the peaks in *dM/dH* versus *H* shown in Fig. 6.7(b) are in good agreement with results obtained in single crystals

6.3.2. Effective spin of the magnetic ground state

To distinguish between the S = 3/2 and 1/2 cases as possible ground states for Co^{2+}, the magnitude of the saturation magnetization M_S and magnetic moment μ_Z for $T < T_C$ is determined for the two cases and compared with the experimental results, similar to the procedures described in the recent papers on β-$Co(OH)_2$ [151], $GeCo_2O_4$ [72], and Co_2RuO_4 [141]. Theoretically, $M_S = N_A\, gS\, \mu_B$ in the limit of T = 0 K when all the moments are aligned parallel. Since the magnetic moment of spin S is $gS\,\mu_B$, this leads to $M_S = N_A\, gS\, \mu_B$ per mole when all the moments are aligned parallel yielding the saturation magnetization M_S. Using the magnitudes of g estimated from μ based on the MCW fits for both S = 1/2 and 3/2, the calculated M_S = 16101 emu mol^{-1} (by considering S = 1/2 and g = 5.767) and M_S = 21608 emu mol^{-1} (by considering S = 3/2 and associated g = 2.664) for the case of $\chi_0 = 9 \times 10^{-4}$ emu $mol^{-1}Oe^{-1}$. Similar numbers are obtained for χ_0 = 0, which are listed in Table 6.1. Measurements of M_S at 1.8 K for H parallel to the c-axis by Nandi *et al.* [32] yielded $M_S \sim$ 17 000 emu mol^{-1}, which is understandably larger than our experimentally determined $M_S \sim$ 14000 emu mol^{-1} at 1.9 K estimated in the inset of Fig. 6.7(a) since our data are on a polycrystalline sample of $CoNb_2O_6$. The important point is that the experimental M_S is closer to the calculated value for the case assuming S = 1/2 as the ground state. This is similar to the reported cases of some other Co^{2+} containing systems viz. β-$Co(OH)_2$ [151], $GeCo_2O_4$ [72], and $CoCl_2$ [152]. Using neutron diffraction experiments near 1.5 K, Maartense *et al.* [64] and Heid *et al.* [66] reported $\mu/Co^{2+} = 3.05\mu_B$ and 3.2 μ_B, respectively. Using the above magnitudes of g and S, we have calculated $\mu_z = gS\mu_B = 2.883\mu_B$ for S = 1/2 and $3.869\mu_B$ for S = 3/2 for $\chi_0 = 9 \times 10^{-4}$ emu $mol^{-1}Oe^{-1}$, with similar numbers for the χ_0 = 0 case (listed in Table 6.1). This shows again that the experimental results for the measured magnetic moments for $T > T_C$ and $T < T_C$ can be explained

Table 6.1. Evaluated and calculated parameters for $CoNb_2O_6$ using fits to: $\chi = \chi_0 + C/(T-\theta)$ for χ_0= 0 and χ_0= 0.0009 (emu $mol^{-1}Oe^{-1}$).

Parameters	χ_0= 0.0009	χ_0= 0
C (emu K $mol^{-1}Oe^{-1}$)	3.12	3.33
μ (CW fit)	4.994 μ_B	5.159 μ_B
θ	+11 K	-38 K
g (S=3/2)	2.579	2.664
g (S=1/2)	5.767	5.957
μ_z (S=3/2)	3.869μ_B	3.996 μ_B
μ_z (S=1/2)	2.883 μ_B	2.979 μ_B
Calculated M_S (emu mol^{-1})		
(S=1/2)	16101	16637
(S=3/2)	21608	22,317

only if the ground state of Co^{2+} in $CoNb_2O_6$ has effective spin S = 1/2 and not 3/2. Interestingly, the agreement between the measured μ_z and M_S for $T < T_C$ and their corresponding calculated values for S = 1/2 is somewhat better for the case of $\chi_0 = 0$ than that for $\chi_0 = 9 \times 10^{-4}$ emu $mol^{-1}Oe^{-1}$ (see Table 6.1). This may be due to the fact that the effect of nonzero χ_0 is only observable for T > 150 K. The important point is that this reconciliation of the high-temperature and low-temperature magnetic data in $CoNb_2O_6$ is only possible if the effective spin S = 1/2 for the ground state of Co^{2+}. As explained in great detail in [152] with follow-up discussion in [72,151], this effective spin-1/2 state for Co^{2+} results from the combined effects of spin orbit coupling and noncubic crystalline field. The presence of substantial spin-charge-lattice coupling in $CoNb_2O_6$ has also been inferred by Nandi *et al.* [158] from their magnetostriction and dielectric constant measurements in $CoNb_2O_6$.

6.3.3. Exchange constants

Having established S = 1/2 as the effective spin for the ground state in $CoNb_2O_6$, evaluations of the exchange constants J_0, J_1, and J_2 of equation (6.1) are considered next as previous investigators used S = 3/2 and g = 2.1 in the calculations of J_0, J_1, and J_2 [66,146,147,149] as noted earlier. We first checked and verified the calculations of J_0, J_1, and J_2 reported in Ref. [146] using S = 3/2 and g = 2.1 and then used the same procedure except S = 1/2 and g = 5.767 were used. For calculation of J_1 and J_2, the critical fields H_{C1} = 315 Oe and H_{C2} = 3150 Oe [see Fig. 6.1(b)] are used along with the tilt angle $\alpha = 31^\circ$. Solving the equations given in [146], the following equations are derived for J_1 and J_2:

$$J_1 = -\, g\, \mu_B \cos\alpha\, (2H_{C1}+H_{C2}) / (6S) \qquad (6.2)$$

$$J_2 = -\, g\, \mu_B \cos\alpha\, (H_{C2} - H_{C1}) / (6S \cos 2\alpha) \qquad (6.3)$$

These calculations using equations (6.2) and (6.3) yield $J_1/k_B = -0.0508$ K and $J_2/k_B = -0.0812$ K obtained for S = 3/2 and g = 2.1 and reported in Ref. [146]. However, for S = ½ and g = 5.767, $J_1/k_B = -0.42$ K and $J_2/k_B = -0.67$ K are obtained, which are about an order of magnitude larger than values obtained for S = 3/2 and the corresponding g = 2.1. Similarly, J_0/k_B = 5.47 K is obtained using S = 1/2 and associated g = 5.767 to be compared with J_0/k_B = 0.6016 K obtained in Ref. [146] assuming S = 3/2 and g = 2.1 and the molecular field approximation (MFA) for T_C. These results show that the exchange constants differ by an order of magnitude for the two cases of S = 1/2 and 3/2 along with respective g-values, and so the effective spin S = 1/2 established here is also important for an accurate determination of the exchange constants. Using the standard equation for $T_C = J_0 Z S(S+1)/3k_B$ based on MFA with Z = 2 as the number of nearest neighbours for a linear chain and S = 1/2 and T_C = 2.95 K yields J_0/k_B = 5.9 K, close to J_0/k_B = 5.47 K obtained above.

For a linear ferromagnetic chain with spin S = 1/2 and Hamiltonian $H = -J_0 \sum_i S_i^z S_{i+1}^z$, an exact expression for the temperature dependence of magnetic susceptibility χ is available [39], and it is given by

$$\chi = \chi_0 + \frac{C}{T} \exp\left(\frac{J_0}{2k_B T}\right) \qquad (6.4)$$

In the above equation, we use χ_0 = 0.0009 emu $mol^{-1}Oe^{-1}$ and C = 3.12 emu K $mol^{-1}Oe^{-1}$ obtained earlier from the fit to MCW law. The best fit of the χ versus T data to equation (6.4), plotted in Fig. 6.5, shows

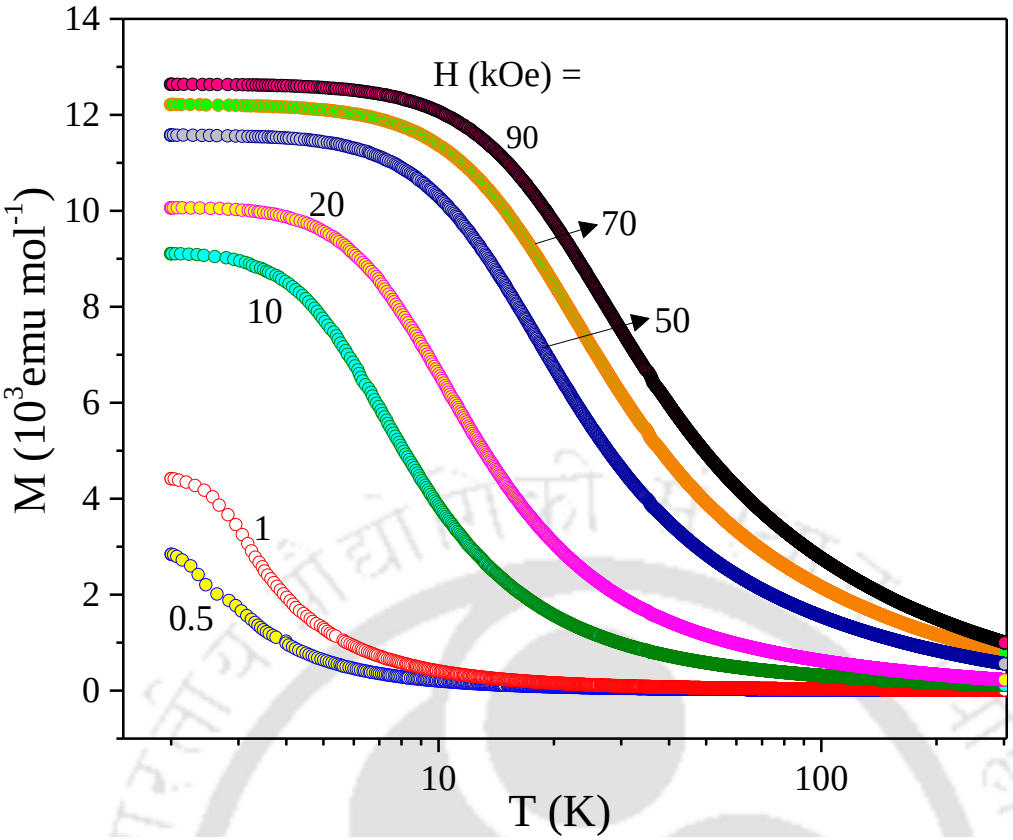

Fig. 6.8. Temperature dependence of magnetization (M) of $CoNb_2O_6$ measured in applied H(kOe) = 0.5, 1, 10, 20, 50, 70, and 90. Log-scale is used for temperature to highlight the variations at lower T.

excellent agreement of the experimental data down to $T_C \sim 3$ K with $J_0/k_B = 6.2 \pm 0.2$ K. This magnitude of J_0/k_B, based on the exact expression [equation (6.4)], is only slightly larger than $J_0/k_B = 5.7$–5.9 K determined earlier based on the MFA.

6.3.4. Short-range ordering above T_C

Using a Maxwell equation, the change in the entropy $\Delta S_M = S_M(H) - S_M(0)$ of a material under an applied field H is written as [141],

$$\Delta S_M = \int_0^H \left(\frac{\partial M}{\partial T}\right)_H dH' \qquad (6.5)$$

In the recent paper on the analysis of M versus T at different H and M versus H at different T in Co_2RuO_4, the proportionality of $\partial M/\partial T$ to ΔS_M in terms of their temperature variations was demonstrated [141]. In Co_2NbO_6, we have used this proportionality to determine ΔS_M from the M versus T data at different H. The plots of M versus T in the presence of different external fields up to 90 kOe are shown in Fig. 6.8 and the computed $(-\partial M/\partial T)$ versus T for different H are shown in Fig. 6.9. Since the applied magnetic field in PM and FM systems improves magnetic ordering and hence lowers the entropy, ΔS_M and hence $\partial M/\partial T$ are negative. For the lowest $H = 0.5$ kOe, $(-\partial M/\partial T)$ versus H shows two peaks, one at $T_N = 2.0$ K and the second near $T_C = 3.0$ K. For $H = 1$ kOe, only a single peak near $T_C = 3.0$ K is observed, which, with an increase in H, becomes broader and shifts to higher T; this shift quantified in the plot is shown in the inset of Fig. 6.9. This H-dependence of the peak is very similar to the observation of the H-dependence of the peak in the

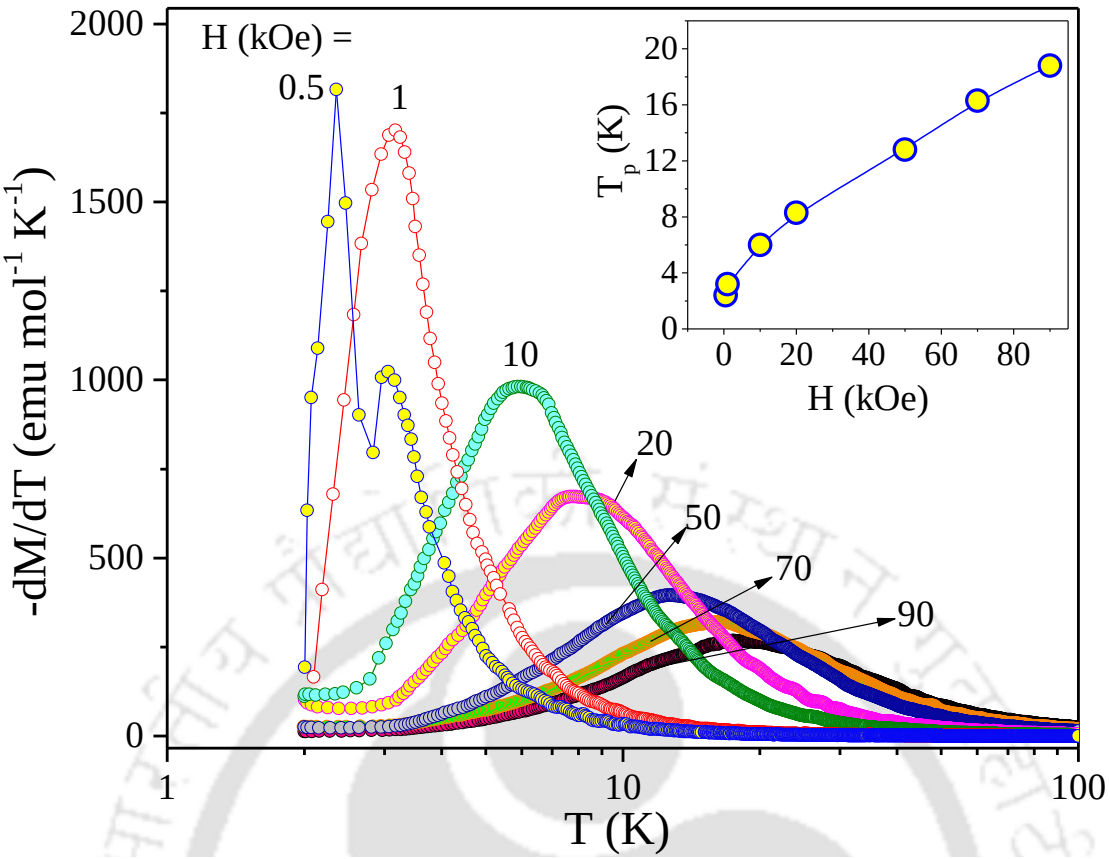

Fig. 6.9. Plots of the computed ($-\partial M/\partial T$) vs temperature for different H (marked by arrows) using the data of M vs T of Fig. 6.8. The very weak oscillations in some curves are artefacts of the numerical computation of $\partial M/\partial T$ from the M vs T data, whereas the magnetic field dependence of the broader peak position T_P of ($-\partial M/\partial T$) vs H is shown in the inset, with the line connecting the data points as a visual guide.

specific heat versus temperature data reported for $CoNb_2O_6$ in [8,144], thus providing a semiquantitative correlation between the specific heat and magnetization data. These observations point to a significant amount of short-range magnetic ordering well above T_C in this pseudo-one-dimensional Ising system, which is enhanced by the applied field. This effective increase of T_C with an increase in magnetic field in a ferromagnet has been explained in a recent report [155] in terms of the coupling and enhancement of the order parameter (magnetization) of a ferromagnet with applied field.

6.4. Concluding remarks

Analysis of the magnetization data in $CoNb_2O_6$ analysed in this chapter leads to the conclusion that the effective spin for the ground state of Co^{2+} is $S = 1/2$ and not $S = 3/2$ usually expected from Hund's rules and assumed in some earlier publications. The effective spin $S = 1/2$ of the ground state in $CoNb_2O_6$ results from the combined effects of a noncubic crystalline field, and spin-orbit coupling is also reported in some other Co^{2+} containing systems [72,151,152]. Using $S = 1/2$ and the associated $g = 5.767$ for the ground state in $CoNb_2O_6$, the exchange constants $J_0/k_B = 6.2$ K, $J_1/k_B = -0.42$ K, and $J_2/k_B = -0.67$ K are determined where the intrachain J_0 is ferromagnetic in nature and it is an order of magnitude larger than the interchain antiferromagnetic exchange constants J_1 and J_2. The excellent fit of the temperature dependence of paramagnetic susceptibility of $CoNb_2O_6$ to the Ising linear chain model with $J_0/k_B = 6.2$ K in Fig. 6.5 shows that magnetic anisotropy along the chain c-axis is much larger than the magnetic anisotropy in the ab-plane.

The critical field H_C = 52.5 kOe applied along the *b*-axis for which T_C is forced to 0 K (Fig. 6.1) is effectively equal to J_0/k_B = 6.2 K in temperature units (1 K ~ 10 kOe) and it provides a measure of the Ising anisotropy of the system. However, a theoretical interpretation of the experimental variation of T_C versus H for H along the *b*-axis (shown in Fig. 6.1) has not yet been reported. Also, the accurate magnitude of the weaker anisotropy in the *ab*-plane needs to be determined. Therefore, additional experimental and theoretical investigations of these issues in this interesting system are warranted.

Chapter 7

Spin-Flip States and Exchange Interactions in Spin-1 $NiNb_2O_6$

In this chapter we primarily give emphasis on the spin-flip transitions and the estimation of tri-critical point in the antiferromagnet $NiNb_2O_6$ polycrystals. Specific importance has been given to the estimation of magnetic exchange interactions, magnetic entropy changes, and critical exponents using specific-heat data. The first section of this chapter summarizes the important magnetic properties of this compound and the results of previously reported magnetic data on this system. The subsequent sections deal with the experimental results and their analysis followed by the conclusions.

7.1. Introductory background

Quantum aspects like quantum criticality, quantum phase transition, and quantum fluctuations are the emerging trends in the field of condensed matter physics. Consequently, there has been need for finding real materials that exhibit these quantum aspects. One such class of material is niobate columbites ($CoNb_2O_6$ and $NiNb_2O_6$) because of their novel quantum magnetic critical characteristics and applications. The quantum phase transition near quantum critical point (QCP) has been experimentally reported in the niobate columbite $CoNb_2O_6$ (Ising magnet with effective spin S = ½) in the presence of a transverse magnetic field and is the closest realization of the transverse-field Ising chain (TFIC) model [8,9]. Very recently, in 2021, quantum critical excitations near QCP have also been reported in $NiNb_2O_6$ (effective spin S =1) in specific heat and thermal conductivity measurements when the critical field H_{QCP} ~ 35 kOe is applied perpendicular to the easy axis [10]. Analogous to $CoNb_2O_6$ [8,9], $NiNb_2O_6$ in a transverse magnetic field is the closest real system for the transverse-field Heisenberg chain Hamiltonian with effective spin S =1ground state [10].

The focus of this chapter being complete mapping of the magnetic field-temperature (H-T) phase diagram of $NiNb_2O_6$ below its Néel temperature and determination of the associated exchange constants, it is important to first describe its crystal structure and summarize results from previous magnetic studies. In the niobate columbites ANb_2O_6 (A = Ca, Mn, Fe, Co, Ni, Cu, Zn, Mg [62,144,159-161]), Nb^{5+} is non-magnetic with A site being the only magnetic divalent cation. These niobate columbites crystallize in an orthorhombic crystal structure (Fig. 7.1(a)) with space group $Pbcn$-D^{14}_{2h}, with an A site cation occupying 4*c* Wyckoff position possessing strong single-ion anisotropy and Nb^{+5} ion occupying 8*d* Wyckoff position in the unit cell [20,27,28]. The lattice parameters of the orthorhombic $NiNb_2O_6$ unit cell are a = 14.0229 Å, b = 5.6769 Å and c = 5.0184 Å [162]. In this orthorhombic-columbite crystal structure, both the NiO_6 and NbO_6 octahedra form an edge-sharing independent zigzag chains along the c-axis (Fig. 7.1(b)), where the magnetic Ni^{+2} ions are arranged ferromagnetically in NiO_6 zigzag chains with super-exchange interaction mediated by oxygen ions (Ni-O-Ni). Further a unique alternate arrangement -Ni-Nb-Nb-Ni-Nb-Nb-Ni- of NiO_6 and NbO_6 octahedra is present along a-axis. The nearest and next-nearest Ni^{+2} zigzag chains couple antiferromagnetically, which leads to the formation of an isosceles triangular arrangement of Ni^{+2} ions in the ab-plane (Fig. 7.1(b)). The non-collinear magnetic moments of Ni^{+2} ions are canted with an angle of 31° to

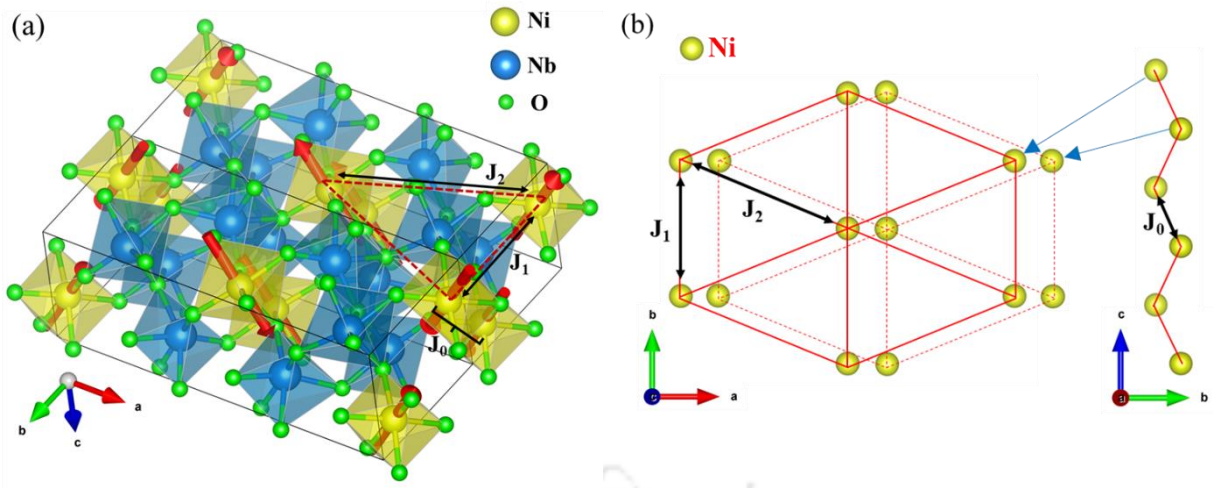

Fig. 7.1. (a) The two-unit cells of $NiNb_2O_6$ represents the exchange interaction paths (black colour arrows) and isosceles triangle lattice (dashed red colour lines) with magnetic moments orientation in red colour vectors. (b) The diagram representation of isosceles triangular lattices in *ab*-plane with inter-chain exchange interactions J_1 and J_2 and next the intra-chain exchange interaction J_0 in zig-zag path along the *c*-axis.

the *c*-axis in the *ac*-plane [19,21,23,68,86,162]. Furthermore, the spin orientation follows the alignment of NiO_6 oxygen octahedra as shown in Fig. 7.1(a) [19].

The first studies of the magnetic properties of $NiNb_2O_6$ were reported by Yaeger *et al.* [60] in 1977. From the susceptibility measurements on single crystals, they reported T_N = 6.0 ± 0.3 K. Further, assuming the two-sublattice model in the mean-field approximation for Ni^{+2} ions, Yaeger *et al.* theoretically estimated the anisotropy constant K = 7.9 ± 0.7 K/spin and the anisotropy field H_K = (98.0 ± 12.7) kOe at T =0 K. Also, the critical fields H_a = 32.8 ± 5.6 kOe, H_b = 45.4 ± 6.4 kOe and H_c = 15.1 ± 10.5 kOe along the *a*-, *b*- and *c*-axis were reported. The net dipolar and exchange field, H_{eff} (= H_{dip} + H_E) = 46.3 ± 10.5 kOe and g = 2.4 ± 0.1 were theoretically estimated, but the mean-field approximation yielded T_N = 6.5 K which is slighter greater than the experimental value, T_N = 6.0 K. The intrachain ferromagnetic interaction is more prominent compared to interchain antiferromagnetic interaction in $NiNb_2O_6$ and this system shows uniaxial magneto-crystalline anisotropy [60].

The temperature dependent neutron diffraction studies on $NiNb_2O_6$ by Heid *et al.* [19] in 1996 reported the existence of antiferromagnetic ordering below T_N = 5.7 K and showed the existence of two distinct magnetic structures corresponding to the two propagation vectors (0 ½ 0) and (½ ½ 0). In addition to this, at T = 2 K, the magnetization measurements on $NiNb_2O_6$ single crystal yielded critical fields H_c = 10.5 kOe and H_a = 27.8 kOe along *c*- and *a*-axis respectively. Using mean-field approximation, they determined the intrachain ferromagnetic exchange term J_0 = 9.86 K (along *c*-axis) and interchain antiferromagnetic exchange terms J_1 = -0.43 K (along *ab*-plane) and J_2 = -1.07 K (along *b*-axis). Since the magnitudes of J_1 and J_2 are very small compared to J_0, this leads to the low-dimensional magnetic behaviour in $NiNb_2O_6$ but not too low as in $CoNb_2O_6$. However, their mean-field calculations considerably overestimated the Néel temperature T_N =15.6 K compared to the experimental value of T_N = 5.7 K. The *g*-factor along the three crystallographic axis g^{xx} = 2.33, g^{yy} = 2.35 and g^{zz} = 2.36 shows weaker anisotropy in $NiNb_2O_6$ compared to other columbites like $FeNb_2O_6$ and $CoNb_2O_6$ [19]. The 2021 studies by Pena *et*

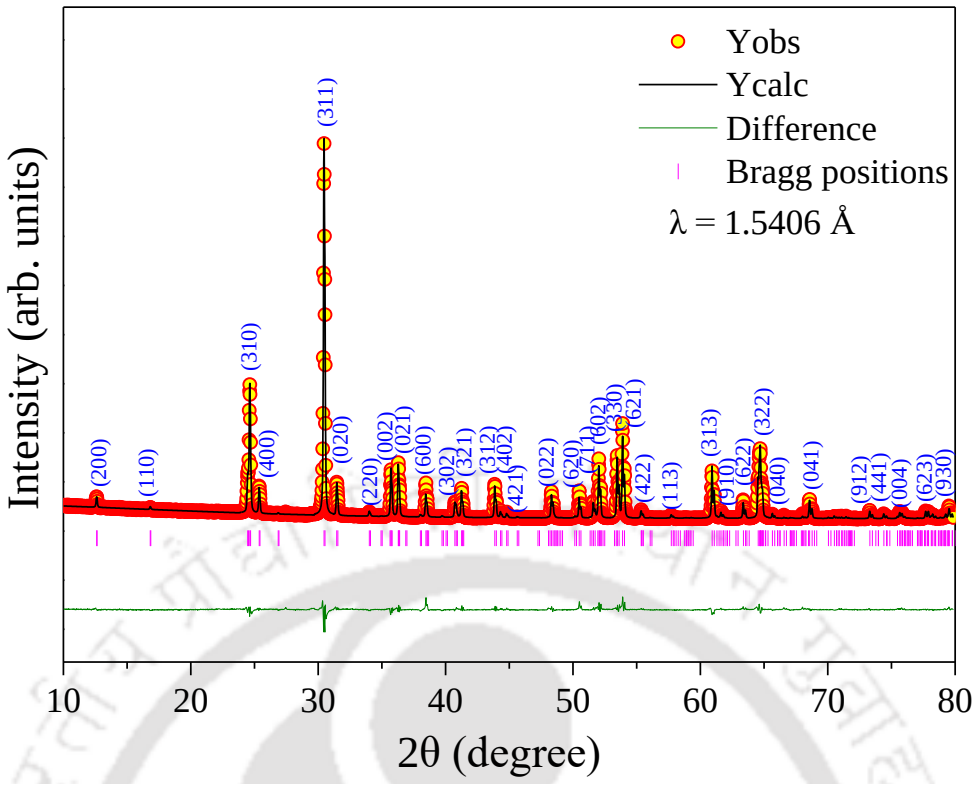

Fig. 7.2. The Rietveld refined data of room temperature x-ray diffraction pattern of $NiNb_2O_6$ sample along with the marked Bragg positions. The bottom green line indicates the difference between the experimental and the simulated XRD pattern.

al.[162] reported T_N = 5.7 K for $NiNb_2O_6$ and their fit of the magnetic susceptibility to the Curie Weiss law for $T > T_N$ yielded Θ_{CW} =12.5 K, C = 1.33 emu K/mol.Oe and μ_{eff} = 3.29 μ_B per Ni^{2+}. In addition, Pena *et al.* reported the intrachain interaction term J_0 = 7.12 K and interchain interaction term $J_\perp$ = -0.29 K from the one-dimensional Ising model approximation and mean-field approximation, respectively [162].

In this chapter, we report results from our detailed investigations of the magnetic properties of $NiNb_2O_6$ using magnetization measurements covering the temperature range of 1.8 K to 300 K in magnetic fields up to 90 kOe. Results from the analysis of these measurements are used for the complete mapping of *H-T* phase diagram along with the determination of triple point, and determination of intrachain (J_0) and interchain exchange (J_1 and J_2) constants. In addition, we also report measurements of the temperature dependence of heat capacity of $NiNb_2O_6$ from 2 K to 35 K and determination of its critical exponents on approach to the Néel temperature T_N = 5.59 K. Appropriate discussion on the comparison of the exchange constants determined here vis-à-vis those reported in previous publications is also presented. Details of these results and their analysis are presented in the following pages.

7.2. Synthesis, experimental methods and electronic structure of $NiNb_2O_6$

The Polycrystalline niobate $NiNb_2O_6$ was synthesised in bulk form by employing the standard solid-state reaction method with the help of a FRITSH ball milling machine. Initially, the stoichiometric proportion of transition metal oxides NiO and Nb_2O_5 were weighed accurately and transferred into a tungsten-carbide jar. Next, the 1:5 weight ratio of weighed powder to the tungsten-carbide balls (10 mm diameter) was

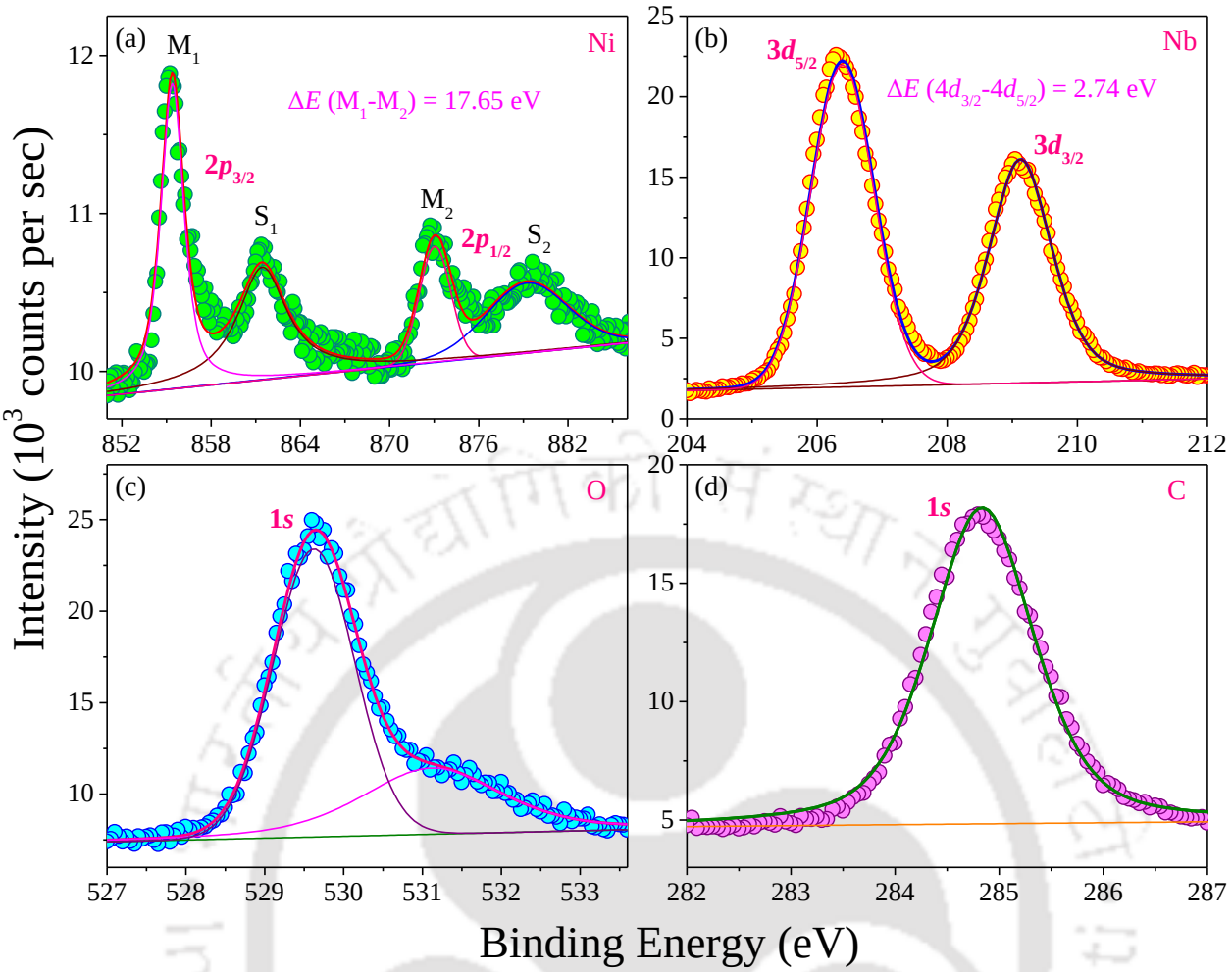

Fig. 7.3. The x-ray photoelectron intensity versus binding energy (eV) of core-level (a) Ni-2*p*, (b) Nb-3*d* (c) O-1*s* and (d) C-1*s* ions in the polycrystalline $NiNb_2O_6$ sample.

maintained in the jar, and a sufficient quantity of ethanol was used as a milling medium to reduce the friction while milling. Finally, these metal oxide powders were milled homogeneously in a ball milling machine at a speed of 120 rpm for 12 hours. The milled aqueous solution was dried in an oven for 24 hours before being pressed into cylindrical pellets with a hydraulic press at a pressure of 50 $kg.cm^{-2}$. The cylindrical pellets were sintered at 1200ºC for 36 hrs in air. To increase the crystallinity, the first sintered pellets were re-milled and re-sintered at 1250ºC for 48 hrs in air.

The crystal structure and phase purity of this bulk polycrystalline $NiNb_2O_6$ sample were investigated using a Bruker x-ray diffractometer (model: D8 ADVANCE ECO) with a Cu-Kα (λ = 1.5406 Å) source. The recorded x-ray diffraction pattern of $NiNb_2O_6$ at room temperature was refined by using Rietveld FULLPROF suite software (see the Fig. 7.2), which yields the lattice parameters a = 14.0380(1) Å, b = 5.6841(6) Å and c = 5.0247(5) Å and moreover confirms the columbite crystal structure of space group *Pbcn*-D^{14}_{2h} with the absence of secondary phases. The chemical composition and electronic structure of the sample were probed using an x-ray photoelectron spectrometer (XPS) from ULVAC-PHI, Inc. (model: PHI 5000 VersaProbe III) configured with a monochromatic Ag x-ray source with a 20 µm x-ray beam size of 4.5 watts. The DC magnetic measurements of the sample were carried out using a Physical Property

Measurement System (PPMS-DynaCool) in vibrating sample magnetometer (VSM) mode from Quantum Design, which has a magnetic field strength up to ± 9 T and a temperature range of 1.9 - 400 K. On the other hand, *M-H* at 1.8 K was measured in a PPMS (CFMS system) from Cryogenic Limited, which has a ± 14 T magnet and can operate in the temperature range of 1.8 - 400 K. The heat capacity measurements of the sample were recorded from 2.5 K to 35 K by using the standard heat-pulse calorimetry in the Physical Property Measurement System (PPMS) of Quantum Design. A dual-slope analysis was implemented near the transition temperature to observe the magnetic field effect on phase transition.

The XPS spectra of Ni, Nb, and oxygen in $NiNb_2O_6$ are calibrated by fixing the binding energy of carbon C-1*s* orbital at 284.8 eV as shown in Fig. 7.3(d). The core-level spectrum of Ni-2*p* displays two main sharp peaks at 855.39 eV (M_1) and 873.04 eV (M_2) with binding energy separation ΔE (M_2 - M_1) ~ 17.65 eV, it includes two broad satellite peaks (861.43 eV (S_1), 879.22 eV (S_2)). The peak positions and binding energy separation confirm the +2 oxidation state of Ni (Fig. 7.3(a)) [163-165]. The Nb-3*d* core-level spectrum in Fig. 7.3(b) consists of two prominent peaks at 206.40 eV (Nb-3$d_{5/2}$) and 209.14 eV (Nb-3$d_{3/2}$) with spin-orbit splitting ΔE ~ 2.74 eV proves the +5 oxidation state in Nb [166,167]. The O-1*s* electronic

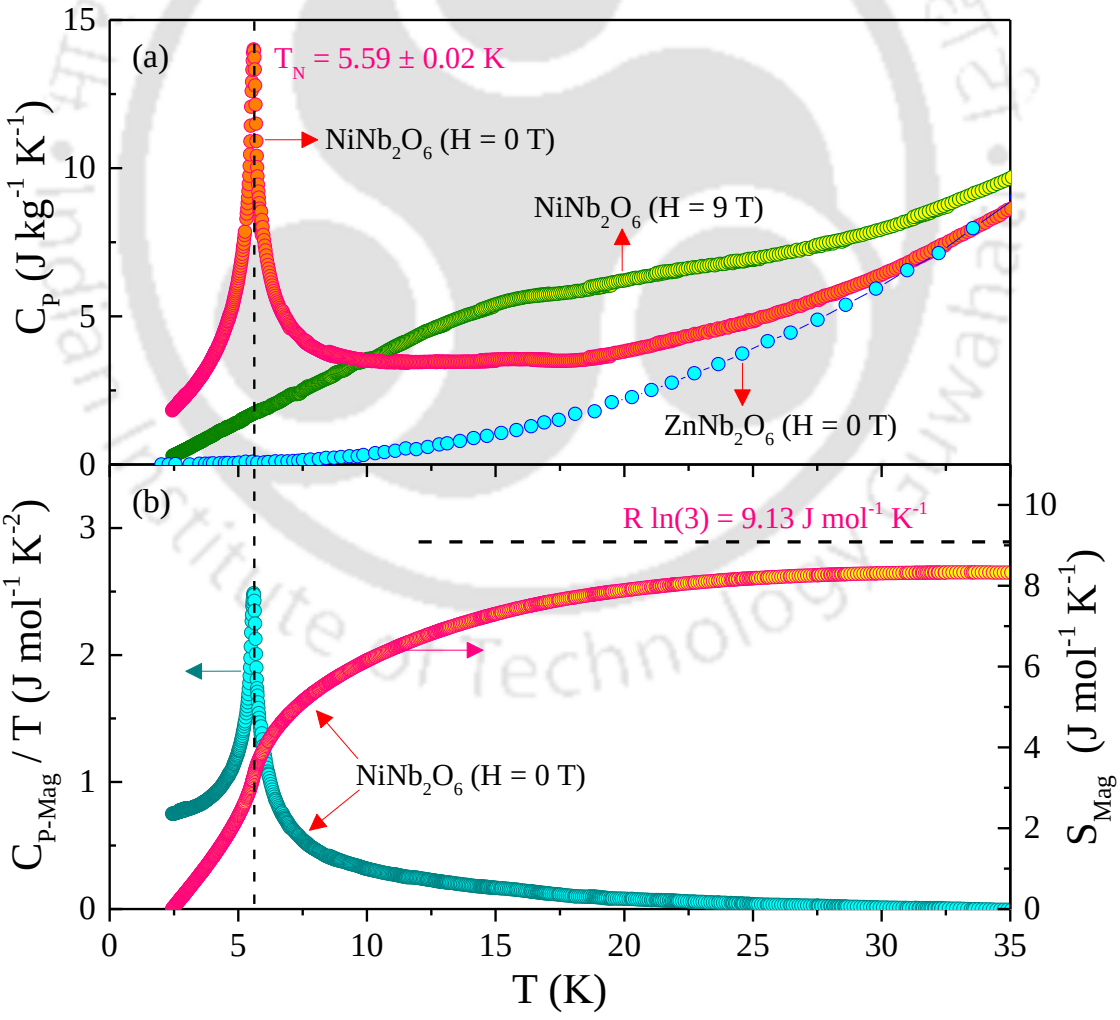

Fig. 7.4. (a) The temperature dependence of heat capacity C_P (T) data measured at H = 0 and H = 90 kOe for $NiNb_2O_6$ sample along with the specific heat data of $ZnNb_2O_6$ from ref [26]. (b) Plot of $C_{P\text{-}Mag}/T$ versus T shows the ordering temperature at T_N = 5.59 ± 0.02 K and the plot of S_{Mag} versus T in the right-y scale.

spectra is deconvoluted into two peaks as shown in Fig. 7.3(c). Out of two, one is peaked at 529.62 eV as a main sharp peak with higher intensity, due to metal-lattice oxygen (Ni-O and Nb-O) bonding. Moreover, the other broad hump at 531.12 eV arises due to absorbed oxygen at the surface [154,168]. Thus, the XPS spectra witnesses the evidence of Ni^{+2} and Nb^{+5} in the polycrystalline $NiNb_2O_6$ sample.

7.3. Thermal variation of Specific heat and critical exponents near Néel temperature

The thermal dependence of specific heat $C_P(T)$ measurements were carried out in the temperature range 2.5-35 K for $H = 0$ and $H = 90$ kOe as shown in Fig. 7.4(a). The zero-field C_P curve indicates a clear λ-type anomaly across the transition temperature, $T_N = 5.59 \pm 0.02$ K which is in close agreement with $T_N = 5.85 \pm 0.07$ K obtained from $\partial(\chi T)/\partial T$ vs. T plot at $H = 500$ Oe (Fig. 7.6(b)). Moreover, the C_P curve at $H = 90$ kOe doesn't show any peak, instead it increases gradually with temperature up to 35 K. The no peak situation, indicates the system in an induced saturated ferromagnetic state, as the magnetic saturation attains approximately above 40 kOe in M-H curves for $T < T_N$. In antiferromagnets, the magnetic contribution of specific heat is in the order of T^3, which is the same as the lattice contribution at lower temperatures. The same temperature dependence leads to difficulty in the separation of magnetic and lattice specific heats. For this purpose, we utilised the C_P(T) measurements of nonmagnetic $ZnNb_2O_6$ columbite system [169]. In Fig. 7.4(b), the magnetic specific heat is plotted as $C_{P\text{-}Mag}/T$ vs. T for $H = 0$, the sharp λ-type anomaly indicates the long-range magnetic ordering below $T_N = 5.59$ K. The magnetic entropy, S_{Mag} of magnons in spin waves is calculated by numerical integration of $C_{P\text{-}Mag}/T$ by using the equation 7.1 [170], which is shown in the right y-scale of Fig. 7.4(b) for the temperature range of 2.5-35 K at $H = 0$. Beyond $T = 33$ K, the total S_{Mag}

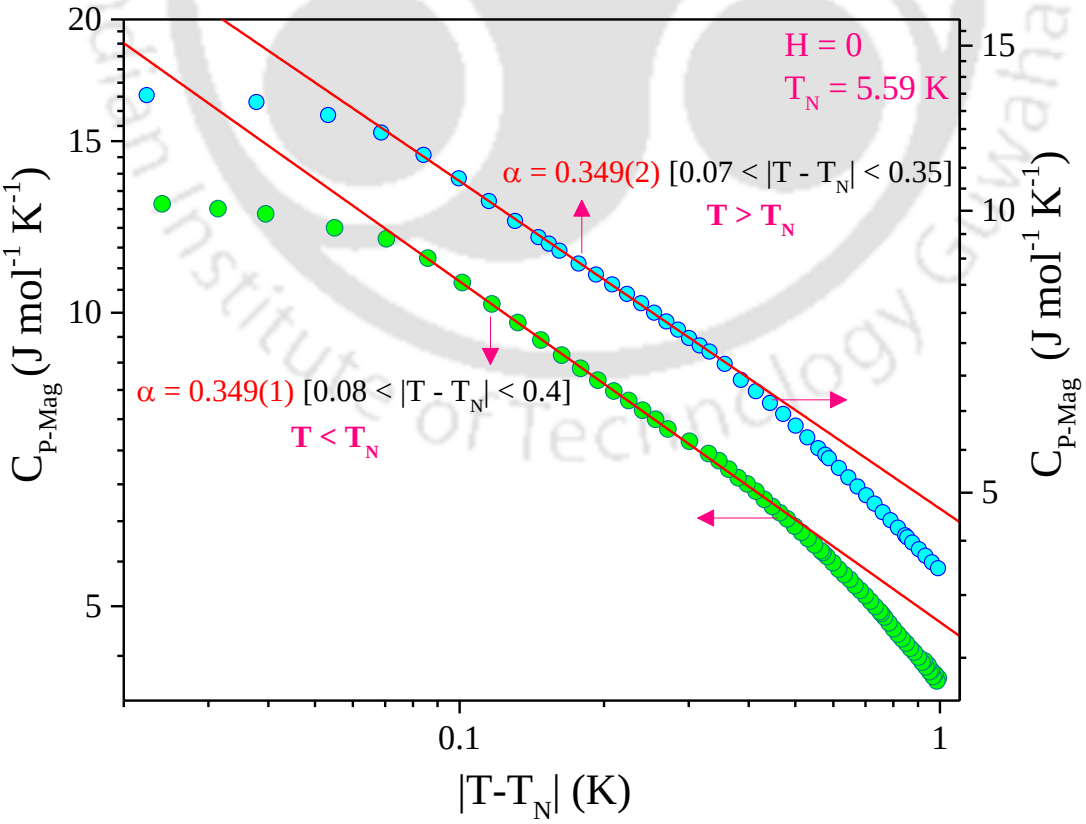

Fig. 7.5. Thermal variation of $C_{P\text{-}Mag}$ in the vicinity of T_N is fitted to the equation: $C_P = A|T - T_N|^{-\alpha}$ using log-log plot of $C_{P\text{-}Mag}$ vs. $|T - T_N|$ with the linear fits yielding an exponent α for both $T < T_N$ and $T > T_N$.

saturates at 8.33 J mol^{-1}K^{-1} for zero field. Moreover, the S_{Mag} saturation indicates the domination of phonon contribution at T > 33 K. The theoretical estimate of $S_{Mag} = R\ ln(2S+1)$ for S = 1 [170], which possesses three degenerate magnetic ground states, produces the limiting value of S_{Mag} = 9.13 J mol^{-1}K^{-1}, which is in close agreement with the experimental estimate of S_{Mag} = 8.33 J mol^{-1}K^{-1} (~91%) at T = 33 K for H = 0. Using this experimental S_{Mag} value and R = 8.314 J mol^{-1}K^{-1}, we determined the spin, S = 0.86 ≈ 1 for $NiNb_2O_6$ system.

$$S_{mag}(T) = \int_0^T \frac{C_{mag}}{T}\, dT \tag{7.1}$$

The specific heat data in Fig. 7.4(a) displays a clear second-order magnetic phase transition at T_N = 5.59 K with no latent heat for H = 0. Further, to estimate the behaviour of C_P in the vicinity of T_N both in the ordered and disordered phase, we employed a critical exponent analysis using an equation: $C_p = A(T-T_N)^{-\alpha}$, where α is the critical exponent and A is a constant [78]. The exponent α is determined for both critical regions, $T > T_N$ and $T < T_N$ by using the linear fit of the C_p vs. $|T-T_N|$ plot represented in log scale as shown in the Fig. 7.5. The ordering temperature T_N is varied in steps of 0.01 K from 5.58 to 5.61 K for the best linear fit and the corresponding better α values. We found an excellent fit for T_N = 5.59 K with α = 0.349(1)

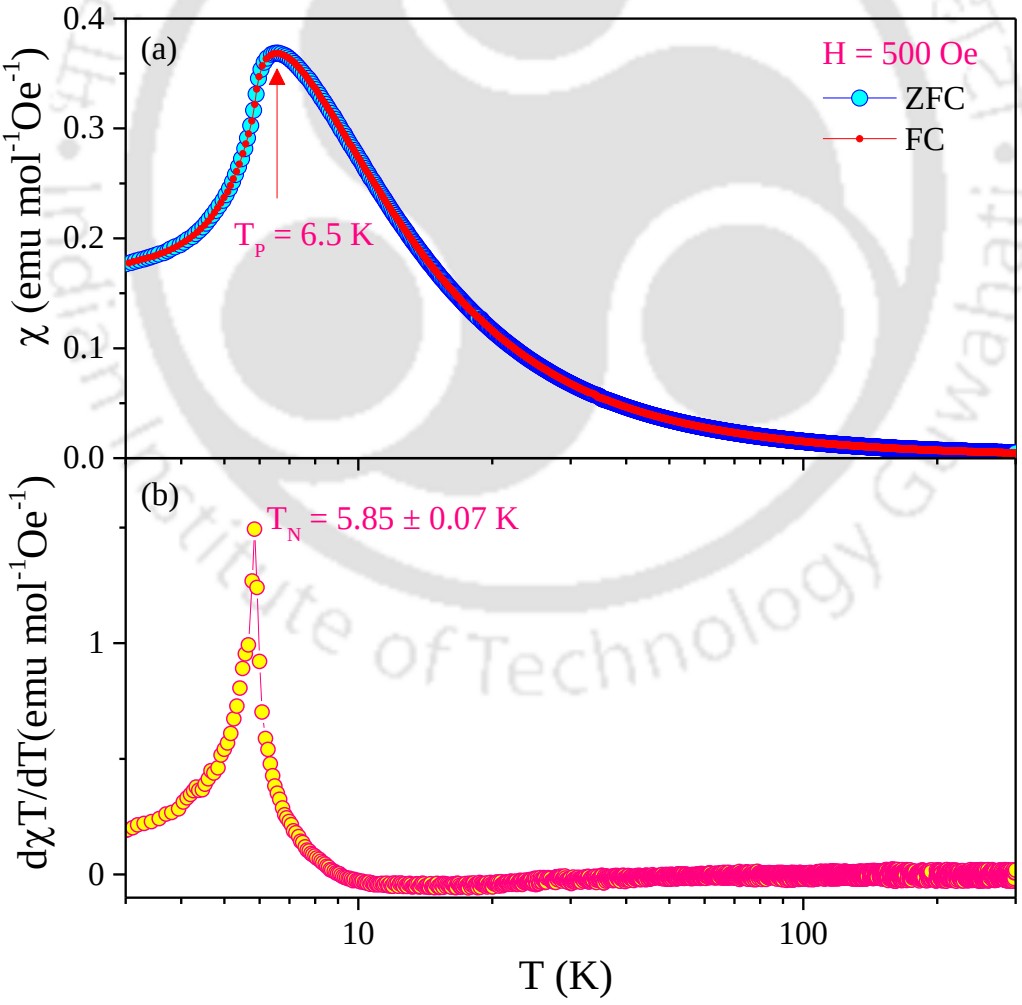

Fig. 7.6. (a) The temperature dependence of *dc*-susceptibility $\chi(T)$ measured at H = 500 Oe showing a broad peak at T_P = 6.50 K in both ZFC and FC condition; (b) Computed plot of $d(\chi T)/dT$ versus T showing a sharp peak corresponding to the AFM to PM phase transition at T_N = 5.85 ± 0.07 K.

for $T < T_N$ valid in the critical region $0.08 < |T\text{-}T_N| < 0.40$ and $\alpha = 0.349(2)$ for $T > T_N$ valid in the critical region $0.07 < |T\text{-}T_N| < 0.35$ for $NiNb_2O_6$ system using the least-square linear fit analysis. Similar estimation of critical exponents has been done for several antiferromagnets like MnF_2 [171], $RbMnF_3$ [172] and $CoCs_3Cl_5$ [173].

7.4. Magnetization results and discussion

7.4.1. Magnetic ordering temperature and its magnetic field dependence

The temperature (3-300 K) dependence of dc-magnetic susceptibility, $\chi(=M/H)$ at H = 500 Oe in both zero field cooled (ZFC) and field cooled (FC) conditions is shown in the Fig. 7.6(a) for $NiNb_2O_6$ sample. Initially, the sample was cooled from 300 to 3 K in the presence of H = 0 Oe (H = 500 Oe) for ZFC (FC) protocol, and the magnetic measurements were recorded during warming of the sample up to 300 K. The

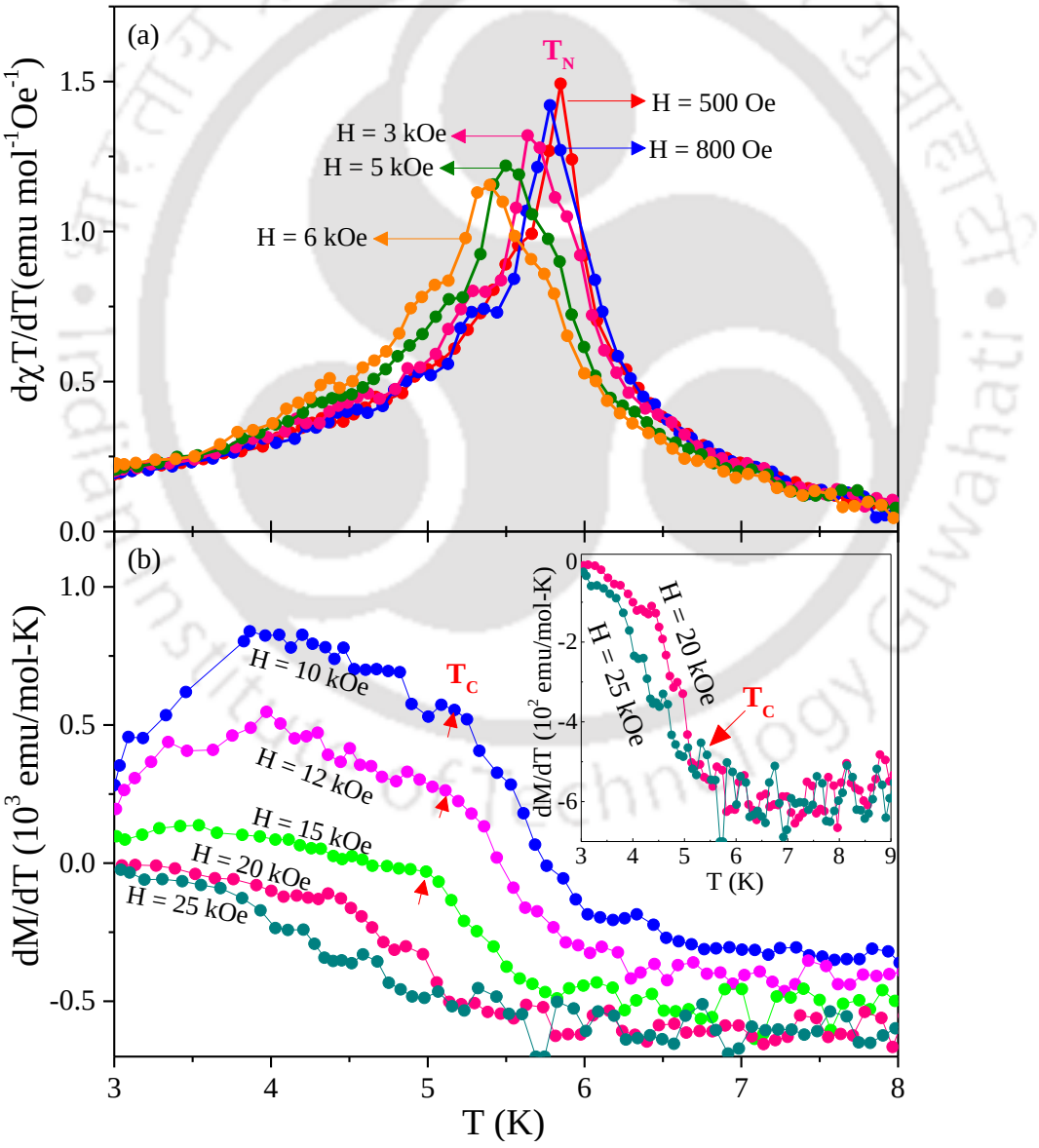

Fig. 7.7. The plots of (a) $d(\chi T)/dT$ vs. T and (b) dM/dT vs. T using the measured M vs. T plots for H < 10 kOe and H > 10 kOe, respectively. Inset in figure (b) shows the clear estimation of T_C for H = 20 kOe and 25 kOe.

χ_{FC} exactly overlaps on χ_{ZFC} for the entire temperature range as shown in Fig. 7.6(a), both the susceptibilities decrease as temperature falls below T_P = 6.5 K (temperature corresponds to the peak in *dc*-susceptibility). This suggests the presence of long-range antiferromagnetic ordering in $NiNb_2O_6$ system and it is confirmed by the sharp peak in specific heat data. The Néel temperature, T_N is accurately determined by $\partial(\chi T)/\partial T$ vs. T plot, because χT represents the magnetic energy and its derivative is equivalent to the heat capacity. Thus, the peak in $\partial(\chi T)/\partial T$ vs. T plot resembles the λ-type anomaly across the transition temperature in specific heat data [73-75,85,140]. The computed $\partial(\chi T)/\partial T$ vs. T plot in Fig. 7.6(b) yields a peak at T_N = 5.85 ± 0.07 K for H = 500 Oe, which is consistent with T_N = 5.59 ± 0.02 K determined from heat capacity analysis at H = 0 (Fig. 7.4(a)) and generally this value should be less than T_P = 6.5 K for antiferromagnetic (AFM) systems [73,174]. Further, these ordering temperatures are in excellent agreement with T_N = 5.7 K reported by Heid *et al.* [19] and Pena *et al.* [162]. The $\partial(\chi T)/\partial T$ analysis is valid only for H < 10 kOe (Fig. 7.7(a)), since the transition is from a low temperature AFM state to high temperature paramagnetic (PM) state. This method fails for $H \geq$ 10 kOe because the peaks are broad and the transition is from spin flip phase to PM phase. The Spin flip phase has some AFM component combined with more FM component and the corresponding ordering temperature T_C is determined from the inflection points (marked by arrows) in *dM/dT* vs. *T* curves up to 15 kOe as shown in the Fig. 7.7(b). Above 15 kOe, since the FM component is more dominant in the Spin flip phase, the minimum in the *dM/dT* vs. *T* curves is considered as T_C which is clearly shown in the inset of Fig. 7.7(b). From overall observation, the ordering temperatures (T_N or T_C) reduces from 5.85 K to 5 K as the magnetic field increases from H = 500 Oe to 25 kOe, beyond H = 25 kOe the system tends to saturate near T = 5 K as noticeable in the latter *H-T* phase diagram.

7.4.2. Temperature dependence of dc-magnetic susceptibility

The thermal dependence of paramagnetic susceptibility, χ for $T > T_N$, has been analysed through mathematical curve fitting approach of modified Curie-Weiss (MCW) law [141]:

$$\chi = \chi_0 + \frac{C}{(T-\theta)} \tag{7.2}$$

Here, the magnitude of χ_0 is very negligible and it is a temperature independent term which arises due to the diamagnetic contribution of materials and also from Van-Vleck susceptibility. The experimental estimate of χ_0 is very challenging due to its negligible value, for this we plotted χ vs. $1/T$ as shown in the inset of Fig. 7.8. The linear extrapolation of χ in the limit of $1/T \rightarrow 0$ (i.e., the paramagnetic term $C/(T-\theta)$ in equation 7.2 vanishes) yields $\chi = \chi_0$ = -2.28 × 10^{-4} emu.mol^{-1}Oe^{-1}. Using χ_0 = -2.28 × 10^{-4} emu.mol^{-1}Oe^{-1} and $\chi_0 = 0$, we have plotted $(\chi - \chi_0)^{-1}$ vs. T as shown in the right and left *y*-scale of Fig. 7.8, respectively. The linear fit to the plot $(\chi - \chi_0)^{-1}$ vs. T in the higher temperature region (T > 30 K) yields C = 1.36 ± 0.02 emu K mol^{-1}Oe^{-1} and θ = 10.5 K for χ_0 = -2.28 × 10^{-4} emu.mol^{-1}Oe^{-1}, further yields C = 1.30 ± 0.02 emu K mol^{-1}Oe^{-1} and θ = 13.2 K for χ_0 = 0. The positive value of θ suggests the dominant exchange interaction is ferromagnetic in $NiNb_2O_6$ and the corresponding exchange interaction term is determined accurately in the later section. The equation $C = N_A \mu_{eff}^2/3k_B$ (N_A = Avogadro's number, k_B = Boltzmann constant) yields the effective magnetic moment μ_{eff} = 3.30(2) μ_B /Ni^{2+} for χ_0 = -2.28 × 10^{-4} emu.mol^{-1}Oe^{-1} and μ_{eff} = 3.22(2) μ_B /Ni^{2+} for χ_0 =

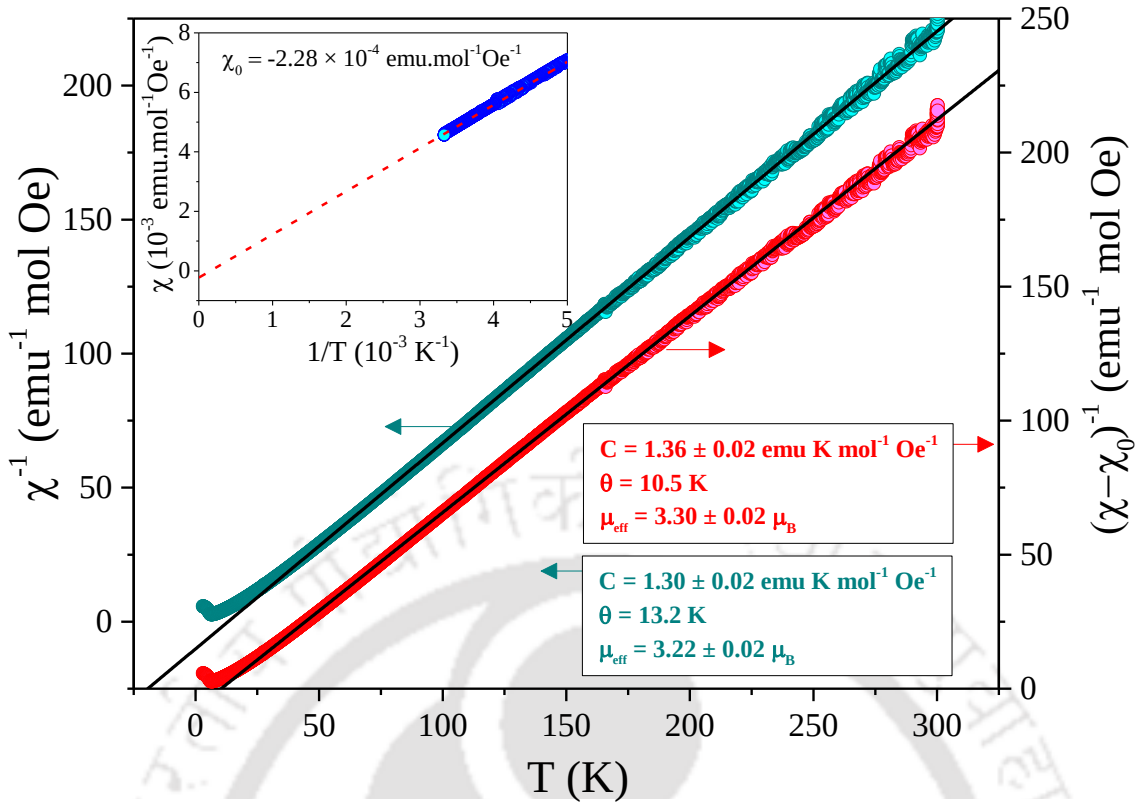

Fig. 7.8. The temperature dependence of inverse magnetic susceptibility $(\chi - \chi_0)^{-1}$ for χ_0 = 0 and -0.000228 emu.mol^{-1}Oe^{-1} in left and right-*y* scale, respectively. The solid black lines signify the linear fits to MCW, Eq. (7.2), in the paramagnetic region yielding the magnitude of *C* and Θ listed in the figure. The plot of χ vs. *1/T* is shown in the inset for the estimation of χ_0 thought linear extrapolation of χ in the limit $1/T \rightarrow 0$ from high temperature data points.

0. Previous studies by Pena *et al.* [162] and Sarvezuk *et al.* [83], respectively, reported μ_{eff} = 3.29 μ_B and μ_{eff} = 3.3 μ_B per Ni^{2+} ion, which are in excellent agreement with our result μ_{eff} = 3.30(2) μ_B /Ni^{2+} for $\chi_0 \neq 0$. Thus, the subtraction of χ from χ_0 leads to the accurate determination of μ_{eff}, *C* and θ values. The lande *g*-factor is determined from the equation $\mu^2 = g^2\mu_B^2 S(S+1)$ and by using μ_{eff} = 3.30(2) μ_B /Ni^{2+} (obtained from MCW law) with *S* = 1 yields *g* = 2.3334, which is in very good agreement with *g* (average of g^{xx}, g^{yy}, and g^{zz}) = 2.34 reported by Heid *et al.* [19]. Since the *g*-factor is greater than 2 (arises only for spin without the contribution of orbital angular momentum), it signifies the contribution of spin-orbital coupling effect to the magnetic ground state of Ni^{2+}. The *z*-component of effective magnetic moment $\mu_z = gS\ \mu_B$ is estimated from *g* = 2.3334 (for $\chi_0 \neq 0$) and *S* = 1, which yields μ_z = 2.33 μ_B, results in good concordance with μ_z = 2.4 μ_B reported by neutron diffraction analysis of Heid *et al.* [19].

7.4.3. Magnetic field-induced Spin-flip transitions and saturation magnetization

The magnetic field dependence of magnetization *M*(*H*) was measured at 1.8 K from 0 to 90 kOe for a polycrystalline $NiNb_2O_6$ sample, which shows a noticeable slope change near 10.8 kOe as displayed in the Fig. 7.9. Similar *M* vs. *H* measurements have been carried out up to 90 kOe for the temperatures below T_N, and the slope change at various temperatures is clearly shown in the inset of Fig. 7.10 up to 14 kOe. Further, the field corresponds to slope change can be accurately determined by $\partial M/\partial H$ vs. *H* plot, which yields a peak

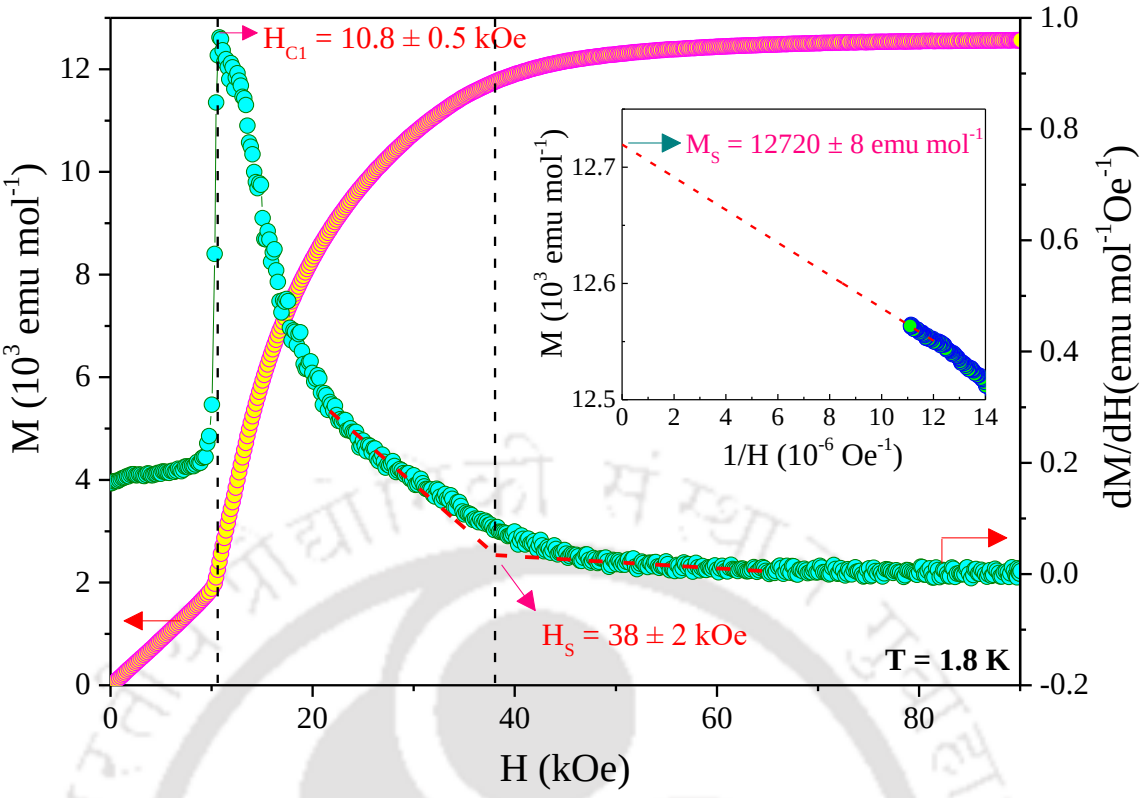

Fig. 7.9. The field dependence of Magnetization (M) at 1.8 K and the corresponding plot of computed dM/dH vs. H in the right-y scale peaks at H_{C1} = 10.8 ± 0.5 kOe. The dashed red lines show the linear extrapolation of dM/dH for the determination of H_S = 38 ± 2 kOe. The plot of M vs. $1/H$ at T = 1.8 K is shown in the inset for the estimation of M_S in the limit of $1/H \rightarrow 0$ at H > 40 kOe.

at H_{C1} = 10.8 kOe for T = 1.8 K as shown in the right y-scale of Fig. 7.9. This value is in excellent agreement with H_c = 10.5 kOe for $H||c$ at T = 2 K reported by Heid *et al.* [19] and also in concordance with our estimated value of H_{C1} = 10.6 kOe at T = 1.7 K from the digitalised data of Pena *et al.* [162]. Similarly, for different $T < T_N$, the $\partial M/\partial H$ vs. H plots are shown in Fig. 7.10, indicates the decrease of H_{C1} with rise in temperature. In $NiNb_2O_6$, the Ni^{2+} ferromagnetic chains align antiferromagnetically with neighbouring chains along the c-axis resulting over all antiferromagnetic behaviour. Since our system is polycrystalline, all the grains are oriented randomly. As a result, the M vs. H plot contains information for the $H||a$, b and c-axis. For $H > H_{C1}$, fraction of the grains whose local easy axis (c-axis) coincides with the direction of applied field flip the spins of oppositely oriented neighbouring ferromagnetic chains to align along its direction. This leads to a transition from AFM to spin-flip phase as shown in the latter HT-phase diagram. Usually spin-flip transitions are first order with a finite jump in magnetization and possess hysteresis loop, which are observed in $NiNb_2O_6$ single crystal [19]. However, the current system is polycrystalline, we witness a continuous change in magnetization, but Sarvezuk *et al.* [83] reported a weak hysteresis loop even in a powder sample. Since the a-axis is an intermediate hard axis, as H exceeds H_{C2} for fraction of the grains have their a-axis coincides with the field direction, there would be another spin-flip phase transition. The critical field H_{C2} could not be detected for the current polycrystalline sample because of less fraction of grains oriented along field direction, but $H_{C2} = H_a$ = 27.8 kOe for $H||a$ is reported in single crystal studies [19]. Further increase in H at a specific field H_S (= $M_S/\chi_\perp$) leads to the IFM state where all the spins are forcefully brought to align parallel

to the applied field by overcoming the exchange coupling field, H_E (=H_S). The magnetic field H_S = 38 ± 2 kOe at T = 1.8 K is determined from the linear extrapolation of $\partial M/\partial H$ vs. H curve which is shown as dotted lines in the Fig. 7.9. [75]. This experimental value is in close agreement with our estimated value H_b = 37 ± 2 kOe for $H||b$-axis at T = 2 K from the digitalized data of Heid *et al.* [19]. Similar estimation of H_S has been done for different temperatures up to 5 K, above which the system enters into paramagnetic region as shown in the latter *HT*-phase diagram.

The Saturation magnetization is determined from M vs. $1/H$ plot at 1.8 K as shown in the inset of Fig. 7.9, the linear extrapolation of M in the limit of $1/H \rightarrow 0$ yields M_S = 12720(8) emu mol^{-1}. Further using the relation $M_S = N_A.g.\mu_B.S$ at absolute zero and g = 2.3334 (obtained from MCW law) with S = 1 yields the calculated M_S = 13032 emu mol^{-1}. This calculated value is just 2.4 % larger than the experimental value, and this negligible difference is attributed to the decreasing nature of M_S with a rise in temperature, as we estimated M_S experimentally at 1.8 K compared to the calculated value at 0 K. This good agreement confirms the spin S = 1 and g = 2.3334 for the magnetic ground state of Ni^{+2} in $NiNb_2O_6$ sample. Next, from $H_E = H_S$ = 38 kOe and M_S = 12720 emu mol^{-1}, the equation $M_S = \chi_\perp H_E$ [79] yields $\chi_\perp$ = 0.34 emu.mol^{-1}Oe^{-1}, which is in excellent agreement with the peak value of χ = 0.36 emu.mol^{-1}Oe^{-1} at T_P = 6.5 K measured for H = 500 Oe as shown in the Fig. 7.6(a). Here $\chi_\perp$ is the susceptibility measured perpendicular to the easy axis in single crystals, which is nearly independent of temperature below T_N and it is equal to the peak value of χ in AFM

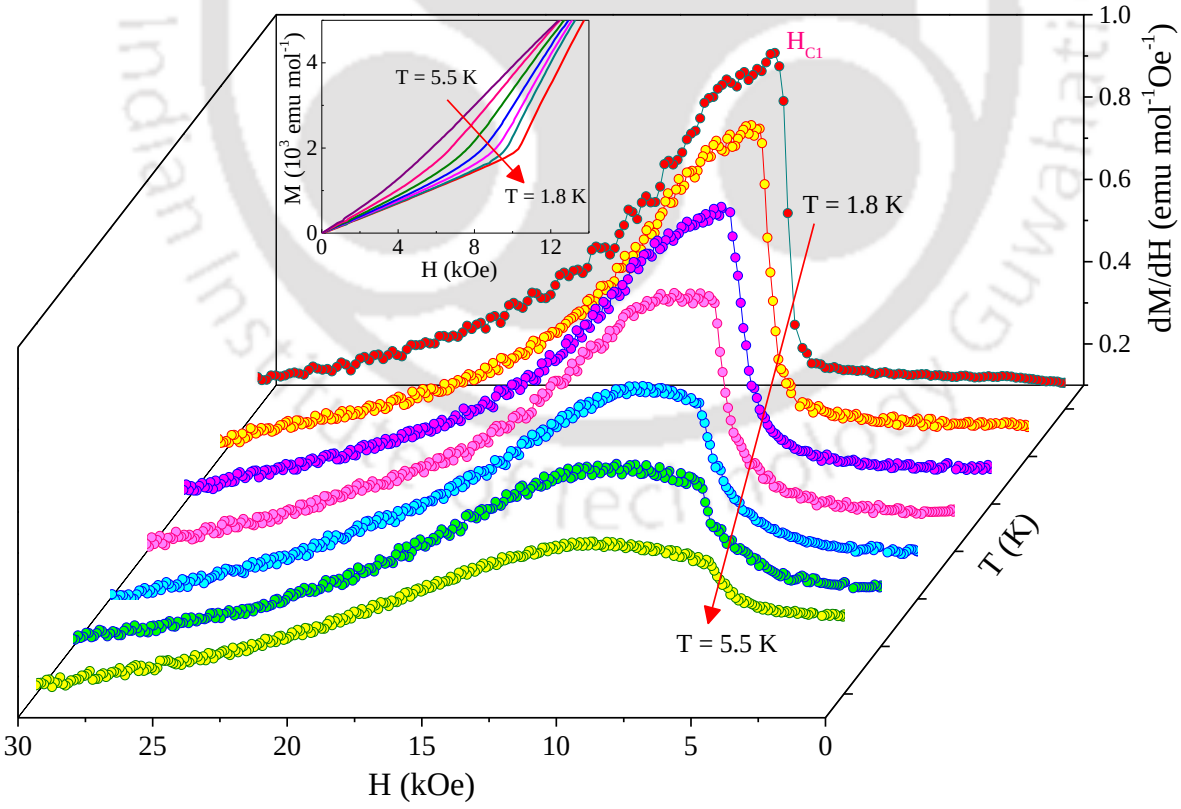

Fig. 7.10. The plots of computed *dM/dH* vs. *H* using the data of the isothermal *M* vs. *H* curves for various temperatures in the range 1.8 - 5.5 K and the peaks correspond to the spin-flip field, H_{C1}. Inset shows the clear change of slops near H_{C1} for distinct temperatures in *M* vs. *H* plots.

systems, further it is evidenced in strong antiferromagnets like MnF_2 [171] and $RbMnF_3$ [172]. This good consistency between experimental and calculated $\chi_\perp$ provides the confirmation of H_S in this columbite.

7.4.4. Field-Temperature (H-T) phase diagram

The field-temperature (*H*-*T*) phase diagram is separated for *H*||*a* and *H*||*b*-axis as shown in Figs. 7.11(a) and (b), respectively. For *H*||*a*-axis, we utilized the field dependence of specific heat data on single crystal from ref [10] where the T_N reduces almost to zero as the field approaches to the critical field H_{QCP} ~ 35 kOe at QCP. Further increase of field (> 35 kOe) leads to quantum fluctuations and quantum disorder

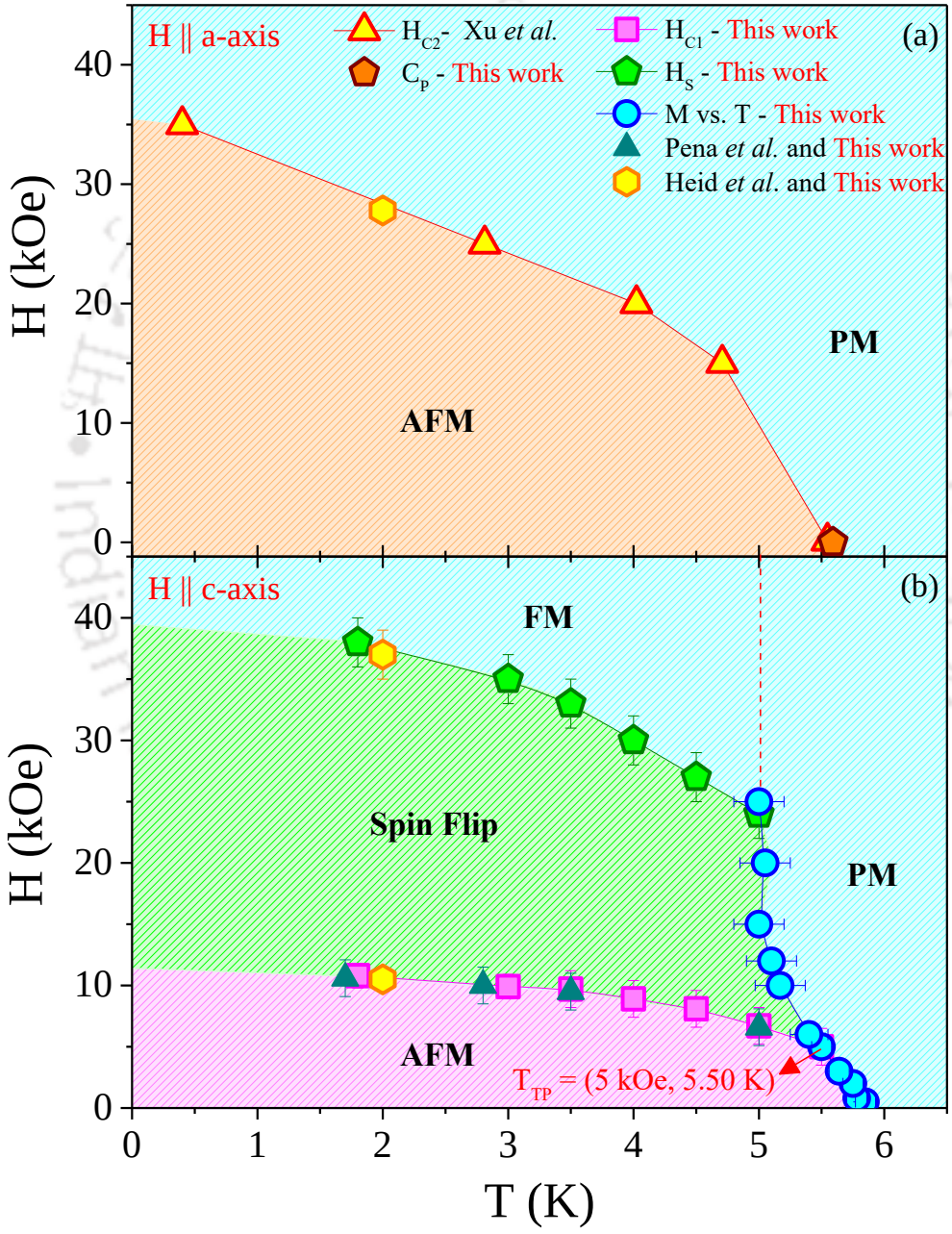

Fig. 7.11. *H*-*T* phase diagram of $NiNb_2O_6$ sample for *H* parallel to the *a*-axis in (a) and *H* parallel to the *c*-axis yielding a triple point, $T_{TP}(H,T)$ = (5 kOe, 5.50 K) in (b). Lines connecting the data points are visual guides, and references to sources of the data points are listed in the figure. The acronyms used for the magnetic phases are as follows: PM, paramagnetic; AFM, antiferromagnetic; and IFM, induced ferromagnetic.

even at 0 K. Next, we included the spin-flip field H_a for $H||a$-axis from ref [19] and T_N = 5.59 ± 0.02 K from the current C_P data at H = 0 in the Fig. 7.11(a).

Since H_{C1} falls in the range of H_c for $H||c$ on single crystal (from ref [19]), so we used the temperature variation of H_{C1} and H_S determined from $\partial M/\partial H$ vs. H plots for the mapping of H-T phase diagram along the $H||c$-axis (Fig. 7.11(b)). Further we included T_N vs. H and T_C vs. H from the peaks and inflection points in $\partial(\chi T)/\partial T$ vs. T and $\partial M/\partial T$ vs. T plots respectively, at different H. Furthermore, we added the magnetic field H_b determined from the digitalized data of ref [19] at 2 K which lies in the range of H_S. Our estimation of H_{C1} vs. T from the digitalized M vs. H data of Pena *et al.* [162] at different temperatures follows the same trend as the H_{C1} vs. T reported for the current sample as shown in the Fig. 7.11(b). Summarizing all the data points leads to four distinct magnetic phases that include AFM, Spin-flip, IFM and PM phase with a triple point at T_{TP} (H, T) = (5 kOe, 5.50 K) where AFM, Spin-flip and PM phases coexist in the H-T phase diagram mapped along the $H||c$-axis (Fig. 7.11(b)). This determination of H-T phase diagram for $NiNb_2O_6$ system is new and a significant result of this work.

7.4.5. Exchange interaction terms

Since the $NiNb_2O_6$ sample possesses a similar crystal structure and the same magnetic moment alignment with tilt angle 31° to c-axis as the $CoNb_2O_6$ system, it exhibits intrachain ferromagnetic exchange interactions (J_0) along the c-axis and the interchain antiferromagnetic exchange interactions with constants J_1 and J_2 along the b-axis and in ab-plane, respectively, as shown in Fig. 7.1(b). To evaluate the exchange constants for the present system we used the same method as in $CoNb_2O_6$ system reported in ref [146]. For this we solved the equations of energy eigenvalues from the proposed Hamiltonian in ref [146] and the obtained equations for J_1 and J_2 as follows,

$$J_1 = -\, g\,\mu_B \cos\alpha\, (2H_{C1} + H_S)/(6S) \tag{7.3}$$

$$J_2 = -\, g\,\mu_B \cos\alpha\, (H_S - H_{C1})/(6S \cos 2\alpha) \tag{7.4}$$

Using the experimental values H_{C1} = 10.8 kOe and H_S = 38 kOe for $H||c$-xais with S = 1, α = 31° and g = 2.3334 (obtained from MCW law), the equations 7.3 and 7.4 yields J_1/K_B = -1.335 K and J_2/K_B = -1.298 K, respectively. The slightly higher negativity of J_1 compared to J_2 indicates relatively strong AFM interactions

Table 7.1. The intrachain ferromagnetic exchange constant, J_0 and the interchain antiferromagnetic exchange constants J_1 and J_2 are listed from this work and literature.

J_0	J_1	J_2	References
4.20 K	-1.335 K	-1.298 K	This work
9.86 K	-1.07 K	-0.43 K	[19]
6.0 K	-0.35 K ($J_\perp$)	-0.35 K ($J_\perp$)	[83]
7.12 K	-0.29 K ($J_\perp$)	-0.29 K ($J_\perp$)	[162]

along the *b*-axis, which is due to less spacing between Ni atoms along the *b*-axis (5.68 Å) compared to spacing along the diagonal (7.57 Å) in ab-plane. Next, by using the standard equation $J_0/K_B = 3T_C/(Z\,S(S+1))$ from MFT with S =1, T_C = 5.60 K (near the triple point, T_{TP} above which the spin-flip to PM transition occurs) and Z = 2 (nearest neighbours along the ferromagnetic chain i.e. *c*-axis) yields J_0/K_B = 4.20 K. The above estimated results are listed in Table 7.1 along with the exchange constants from previous research groups.

The temperature variation of magnetic susceptibility from the Heisenberg linear chain (HLC) as follows [39],

$$\chi = \chi_0 + \frac{C}{T}\left(\frac{1+\Gamma}{1-\Gamma}\right) \tag{7.5}$$

In equation 7.5, $\Gamma = coth(y) - (1/y)$ with $y = 2JS^2/k_BT$ and we use $S = 1$, χ_0 = -2.28 × 10^{-4} emu.$mol^{-1}Oe^{-1}$ and C = 1.36 ± 0.02 emu K $mol^{-1}Oe^{-1}$ obtained from MCW. Fig. 7.12 shows the best fit of equation 7.5 above 15 K to the χ vs. T data in the paramagnetic region, which yields the total magnetic exchange strength, J/K_B = 7.00 K. Since $J/K_B = J_0/K_B + |J_1/K_B| + |J_2/K_B| = 6.833$ K, which is in decent agreement with J/K_B = 7.00 K from the HLC model. This establishes the accurate determination of exchange constants J_0, J_1 and J_2 in $NiNb_2O_6$ system.

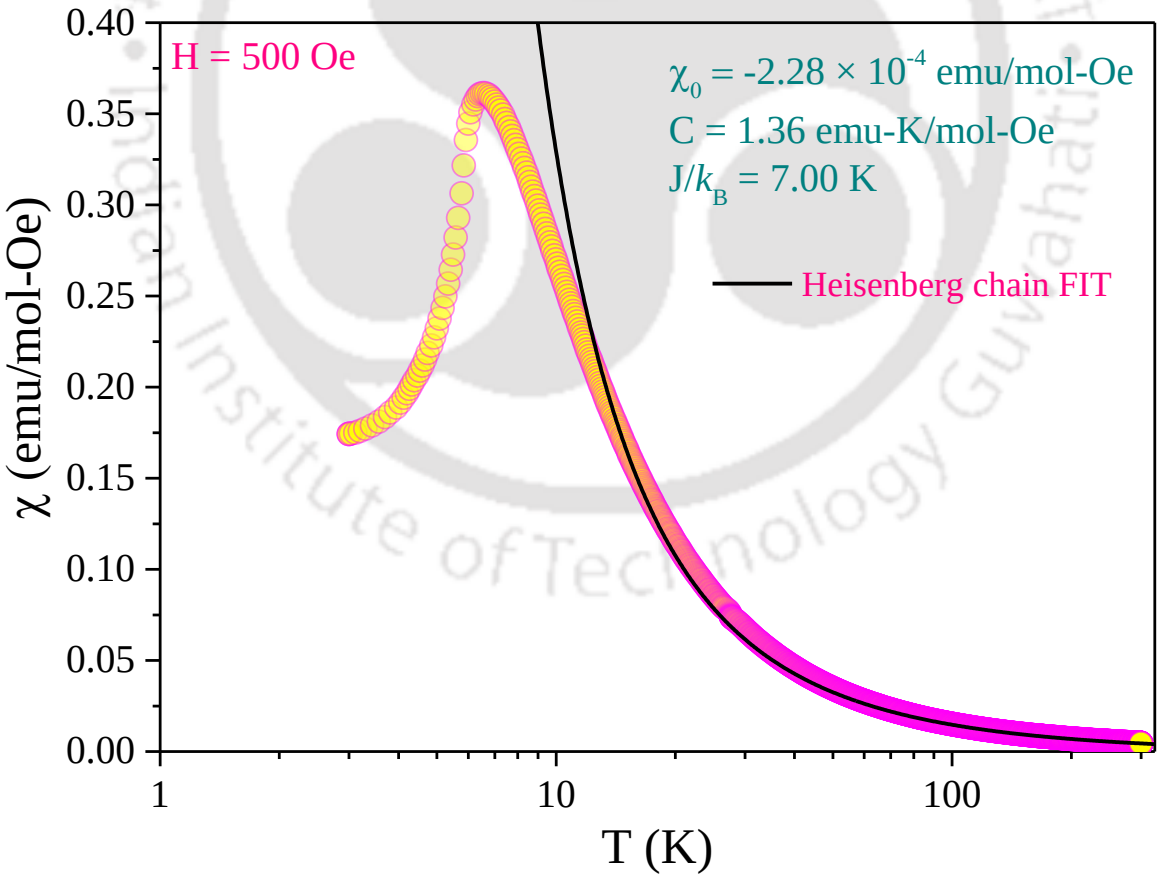

Fig. 7.12. Temperature variation of magnetic susceptibility $\chi(T)$ measured under ZFC condition for H = 500 Oe in the temperature range 3 - 300 K. The solid black line represents the fits to Heisenberg linear chain model provided in Eq. (7.5).

7.5. Summary and conclusions

In this section we sum-up all the key results analysed on the basis of magnetization and specific heat (C_P-T) data of $NiNb_2O_6$ polycrystals. Magnetic susceptibility (χ) studies reveal overall antiferromagnetic character of the investigated system below the Néel temperature, T_N = 5.85 ± 0.07 K determined from the $\partial(\chi T)/\partial T$ vs T plots which is in agreement with the C_P-T data. The C_P vs T near T_N is fitted to power-law expression $C_P = A|T - T_N|^{-\alpha}$ yielding the critical exponent α = 0.349(2) (0.349(1)) for $T > T_N$ ($T < T_N$), respectively. Molecular field theory has been successfully employed to estimate the strength of intrachain exchange interaction J_0/k_B (= 4.20 K) for Ni^{2+} ions in which the spins (S = 1) align along the c-axis. While, the interchain exchange interactions J_1/K_B = -1.335 K and J_2/K_B = -1.298 K have been evaluated from the experimentally obtained magnitudes of H_{C1} = 10.8 kOe, H_{C2} = 27.8 kOe and spin-saturated field H_S = 38 kOe. These magnitudes are consistent with the strength of total magnetic exchange interaction J/K_B = 7.00 K obtained from χ-T data fitted with the Heisenberg linear chain model. Further, the H–T phase diagram mapped using various order parameters acquired from the χ(T,H) including the field-induced transitions (H_{C1}(T) and H_S(T)) yields a Triple-point, T_{TP} (H, T) = (5 kOe, 5.50 K) that separates multiple spin-configuration in this interesting system. For T > 25 K, the best fits of χ(T) data to the modified Curie-=Weiss law ($\chi = \chi_0 + C/(T - \theta)$) with $\chi_0 = -2.28 \times 10^{-4}$ emu $mol^{-1}Oe^{-1}$ yields Weiss temperature θ = 10.5 K, and Curie constant C = 1.36 ± 0.02 emu K $mol^{-1}Oe^{-1}$, the latter giving effective magnetic moment μ_{eff} = 3.30(2) μ_B per Ni^{2+} ion and further yields g = 2.3334.

Chapter 8
Conclusions and Scope for Future Research

In this chapter we recapitulate some of key results achieved in the current research work and describes rough layout for the possibility of future research. Below we provide chapter wise important findings of all the results presented in the previous chapters and sum-up this section by discussing the likely prospect for further research in the field of columbites.

8.1. Conclusions

As we outlined in Chapter 3, we present salient features of the results obtained on $MnNb_2O_6$ system. Specifically, the significance of magnetic field-temperature (H–T) phase diagram, specific heat (C_P) exponents, exchange constants and magnetic ground state of the antiferromagnetic (AFM) polycrystalline $MnNb_2O_6$ are summarized below. The thermal variation of magnetic susceptibility χ (= M/H) shows the Néel temperature at T_N = 4.33 K, which is accurately determined from the peak in $\partial(\chi T)/\partial T$ vs T plot, further it is consistent with the transition temperature T_N = 4.36 K obtained from the C_P vs T data. Additionally, the specific heat data in the vicinity T_N is fitted to the equation $C_P = A|T - T_N|^{-\alpha}$ yielding the critical exponent α = 0.15 (0.12) for $T < T_N$ ($T > T_N$). Mathematical fit of $\chi = \chi_0 + C/(T - \theta)$ to the experimental χ vs T data for T > 50 K with $\chi_0 = -1.85 \times 10^{-4}$ emu mol^{-1}Oe^{-1} yields C = 4.385 emu K mol^{-1}Oe^{-1} and $\theta = -17$ K which results in effective magnetic moment μ_{eff} = 5.92 μ_B per Mn^{2+} ion. This supports Mn^{2+} having an effective ground state spin of S = 5/2 and g = 2.001 as well as an AFM dominating exchange interaction. Next from the implication of molecular field theory (MFT) and using the values of T_N and θ, the exchange constants $J_0/k_B = -1.08$ K and $J_\perp/k_B = -0.61$ K were determined for Mn^{2+} ions. The intrachain coupling along the chain c-axis is represented as J_0 and the $J_\perp$ denotes interchain coupling perpendicular to the c-axis, respectively. These exchange constants agree with the anticipated χ vs T variation for the Heisenberg linear chain. By means of the M-H isotherms, M-T data at various fields, and by making use of the literature data, the H-T phase diagram has been mapped which yields a triple-point T_{TP} (H, T) at (18 kOe, 4.06 K). Additionally, the anisotropy energy $H_A \approx$ 0.8 kOe has been estimated using the spin-flopped transitions obtained from M-H data along with the data corresponding to the forced ferromagnetic transitions measured at high fields H > 192 kOe.

In Chapter 4 we focus our study on the dielectric relaxation and the mechanism of ac-electrical charge transport in the polycrystalline $MnNb_2O_6$ system. At temperatures above 300 K, Arrhenius-like behaviour of ac-conductivity ($\sigma(\omega, T)$) dominates in the frequency range 50 Hz - 5 MHz, with activation energies (E_{ac}) ranging between 0.45 and 0.38 eV. Furthermore, the activation energy has a quadratically decreasing trend, according to the equation $E_{ac}(f) = A + Bf + Cf^2$ with the characteristic coefficients A (0.413 eV), B (0.023 eV/Hz) and C (−0.004 eV/Hz^2). Next to analyse the dispersive nature of the measured electrical conductivity $\sigma(\omega, T)$ data, the Double power law has been employed. These results provide evidence for the correlated-barrier hopping (CBH) conduction mechanism of charge carriers between 173 K and 473 K. Moreover, the temperature variation of the frequency exponent, s(T), exhibits two unique regions,

both are associated with the CBH mechanism with different slopes $\partial s_1/\partial T = -1.9\times10^{-3}$ K^{-1} and $\partial s_2/\partial T = -1.3\times10^{-3}$ K^{-1} in Region-I (173–300 K). The slope $\partial s_1/\partial T = -1.7\times10^{-3}$ K^{-1} with non-linear variation of s_2 apparent in Region-II (300–473 K). Nevertheless, thermally activated Arrhenius-like behaviour prevails in the second region. The analysis of dynamical response of complex electric modulus spectra ($M^*(\omega, T)$) (based on the Kohlrausch-Williams-Watts method) reveals non-Debye type relaxation process with the decay exponent β falling between 0.794 and 0.840. Yet, the depressed semicircles in Nyquist plots as well as the greater magnitude of the full width half maximum (FWHM ≈ 1.44 decades) of the normalized master plots (M''/M''_{max} vs ω/ω_{max}) are compared to the FWHM (= 1.14 decades) for ideal Debye situation which supports the conclusion of the non-Debye type relaxation process in the investigated system. We obtained a noticeable dispersion in relaxation times ($\tau \approx 935.8-0.36$ μs) with temperature corresponding to both short-range and long-range conductivity regions in the $M^*(\omega, T)$ data. Finally, this research yields an estimate of the charge carrier activation energy, E_M = 0.44 eV obtained from Modulus spectroscopy are in-line with the activation energies $E_{ac}(f, T)$ obtained from the Arrhenius expression.

Next, we extended the summary of results pertaining to the *H*–*T* phase diagram, tricritical point, critical exponents, and exchange constants of the tantalite columbite $MnTa_2O_6$ (MTO) in Chapter 5 by means of high field (~250 kOe) and low-*T* measurements (from 1.5 K to 400 K). The results of magnetic susceptibility χ (= *M*/*H*) measurements reveals that MTO exhibits robust AFM ordering below the T_N = 5.97 K. The C_P vs *T* data is consistent with the χ –*T* data. For $T \sim T_N$, the C_P -*T* data is analysed using the equation $C_P = A|T - T_N|^{-\alpha}$ yielding the critical exponent α = 0.13 (0.10) for $T < T_N$ ($T > T_N$). On the other hand, the modified Curie-Weiss fit ($\chi = \chi_0 + C/(T - \theta)$) to the experimental data of χ-*T* for *T* > 25 K yield $\chi_0 = -2.12 \times 10^{-4}$ emu mol^{-1}Oe^{-1} , *C* = 4.44 emu K mol^{-1}Oe^{-1} and Weiss temperature θ = −24 K. Using these magnitudes, we estimated the effective magnetic moment μ_{eff} = 5.96 μ_B per Mn^{2+} ion of MTO which supports Mn^{2+} having an effective ground state spin of *S* = 5/2 and Landé g-factor *g* = 2.015. This magnitude of '*g*' is consistent with the *g* = 2.0155 obtained from the electron spin resonance spectroscopy. Using the molecular field theory (MFT) and the values of T_N and θ, exchange constants $J_0/k_B = -1.5 \pm 0.2$ K and $J_\perp/k_B = -0.85 \pm 0.05$ K are estimated for Mn^{2+} ions in MTO. Here J_0 represents the intrachain coupling along the chain of *c*-axis and the interchain coupling $J_\perp$ perpendicular to the *c*-axis. Our results demonstrate that prediction of a Heisenberg linear chain model provides semiquantitative agreement with the observed variation of χ-*T* in MTO system. Using the *M*-*H* isotherms and *M*-*T* data at various *H*, a complete *H*-*T* phase diagram has been mapped for MTO. Such *H*-*T* phase diagram provides a clear and vivid existence of a triple-point T_{TP} (*H*, *T*) at (17.0 kOe, 5.69 K) which separates all the three magnetic phases: AFM phase, spin-flop and paramagnetic phases. Moreover, we estimated the magnetic anisotropy field $H_A \approx 1.34$ kOe using the experimental values of spin-flop field H_{SF} = 23.5 kOe and the exchange field H_E = 206.4 kOe for MTO system which are in close consonance with the findings of its isostructural system $MnNb_2O_6$.

Further we have extended our studies on Ising chain ferromagnet $CoNb_2O_6$ (CNO) in Chapter 6 which is a unique system among the columbite family of compounds having T_C = 2.9 K. Detailed magnetic

measurements in this system results in the effective ground state spin of Co^{2+} in CNO is S = 1/2 rather than the S = 3/2 predicted by Hund's criteria which is resulting from the collective effects of spin-orbit coupling and a noncubic crystalline field. Our results based on the Ising linear chain expression $\chi = \chi_0 + (C/T)\exp(J_0/2k_BT)$ with S = ½ in paramagnetic region demonstrate that the intrachain ferromagnetic exchange interaction J_0/k_B in CNO is ~ 6.2 K. Additionally, from the experimentally obtained critical fields of spin-flip transitions with S = ½, we have evaluated the interchain AFM exchange strengths $J_1/k_B = -0.42$ K and $J_2/k_B = -0.67$ K for CNO bulk polycrystals.

Lastly, we have explored the magnetic properties of $NiNb_2O_6$ (NNO) polycrystals in Chapter 7 which also exhibits robust AFM behaviour below the $T_N = 5.85 \pm 0.07$ K with a tri-critical point in the H–T plane at T_{TP} (H, T) = (5 kOe, 5.50 K). The heat-capacity data C_P vs T yields sharp λ-type anomaly at T_N = 5.59 ± 0.02 K consistent with the long-range AFM behaviour noticed in the magnetization data. Further, the critical behaviour near T_N has been studied in NNO system using the equation $C_P = A|T - T_N|^{-\alpha}$ which provides the critical exponents α = 0.349(2) (0.349(1)) for $T > T_N$ ($T < T_N$). The best fit of χ vs T data for T > 25 K to modified Curie-Weiss law: $\chi = \chi_0 + C/(T - \theta)$ with $\chi_0 = -2.28 \times 10^{-4}$ emu $mol^{-1}Oe^{-1}$ yielding θ = 10.5 K, and C = 1.36 ± 0.02 emu K $mol^{-1}Oe^{-1}$, the latter giving magnetic moment μ = 3.30(2) μ_B per Ni^{2+} ion and further yields Landé g-factor = 2.3334. Also, by means of the molecular field theory (MFT), we determined the intrachain exchange constant J_0/k_B = 4.20 K for Ni^{2+} ions along the chain c-axis. Next, from the experimental values of cirtical fields H_{C1} = 10.8 kOe and H_S = 38 kOe we have determined the interchain exchange constants J_1/K_B = -1.335 K and J_2/K_B = -1.298 K perpendicular to c-axis. These exchange constants are consistent with the total magnetic exchange strength, J/K_B = 7.00 K obtained from χ vs T variation of the Heisenberg linear chain model.

8.2. Prospective for Future Work

Although we have explored a wide range of intriguing structural, dielectric, magnetic, specific heat, and entropy studies of several transition metal columbite systems in this thesis, still there is plenty of study that can be explored on the columbite. Considering from the fundamental physics point of view and commercial applications, there is a need to explore the physical properties of these systems with site specific substation at Nb or Ta sites for robust applications. Below we provide a brief overview of possibility for the future research work on these systems:

One can explore the methods to synthesize the nanostructures of columbites and try to investigate their magnetic behaviour, such work will be a completely new proposal which is missing in the literature till now. Magnetic properties of $NiTa_2O_6$ and (Mn/Ni/Co)$[(Nb/Ta)_{1-x}A_x]_2O_6$ (where A = Mo, W and Cr) are also not initiated till now which will be a open to study. On the other hand, exploring the magneto-dielectric properties in $CoNb_2O_6$, $MnTa_2O_6$ and $NiNb_2O_6$ systems is a new idea which is not initiated in the literature till now. Hence there is a scope for a detailed study of dielectric spectroscopy over a wide window of temperatures (4 K to 600 K) at various magnitude of *ac*-driving frequencies and external magnetic fields.

The optical energy band gap (E_g) and temperature dependent Electron Spin Resonance spectroscopy studies are completely lacking in the literature. Such study will bring completeness to the research in the field of Columbites which will shed light on their local atomic environment. Last but not least a detailed Phonon dynamic studies in the columbites will be completely new work to be explored in future in consonance with the temperature dependence of the Raman spectroscopy.

References

[1] Y. Zhang, C. You, B. Fu and J. Cao, *Ferroelectrics.* **451**, 54 (2013).
[2] M. L. Blanco, U. Amador and F. G. Alvarado, *J. Solid State Chem.* **182,** 1944 (2009).
[3] Y. Zhang, Y. C. Zhang and M. Xiang, *Mater. Lett.* **178,** 175 (2016).
[4] C. Y. You and Y. C. Zhang, *J. Mater. Sci.: Mater. Electron.* **27,** 6606 (2016).
[5] Y. C. Liou, Y. T. Chen and W. C. Tsai, *J. Alloy. Comp.* **477,** 537 (2009).
[6] V. Shanker and A. K .Ganguli, *Bull. Mater. Sci.* **26**, 741 (2003).
[7] Y. C. Liou, C.Y. Shiue and M. H. Weng, *J. Eur. Ceram. Soc.* **29,** 1165 (2009).
[8] T. Liang, S. M. Koohpayeh, J. W. Krizan, T. M. McQueen, R. J. Cava and N. P. Ong, *Nat. Commun.* **6**, 7611 (2015).
[9] A. W. Kinross, M. Fu, T. J. Munsie, H. A. Dabkowska, G. M. Luke, S. Sachdev, and T. Imai, *Phys. Rev. X* **4**, 031008 (2014).
[10] Y. Xu, L. S. Wang, Y. Y. Huang, J. M. Ni, C. C. Zhao, Y. F. Dai, B. Y. Pan, X. C. Hong, P. Chauhan, S. M. Koohpayeh, N. P. Armitage, and S. Y. Li, *Phys. Rev. X* **12**, 021020 (2022).
[11] Y. Shapira, S. Foner, and A. Misetich, *Phys. Rev. Lett.* **23**, 98 (1969).
[12] Y. Shapira and S. Foner, *Phys. Rev. B* **1**, 3083 (1970).
[13] K. Amelin, J. Engelmayer, J. Viirok, U. Nagel, T. Lorenz and Z. Wang, *Phys. Rev. B* **102**, 104431 (2020).
[14] R. Coldea, D. A. Tennant, E. M. Wheeler, E. Wawrzynska, D. Prabhakaran, M. Telling, K. Habicht, P. Smeibidl, And K. Kiefer, *Science* **327**, 177 (2010).
[15] H. J. Lee, I. T. Kim and K. S. Hong, *Jpn. J. Appl. Phy.* **36**, 1318 (1997).
[16] R. C. Pullar, *J. Am. Ceram. Soc.* **92,** 563 (2009).
[17] A. Orera, F. G. Alvarado and J. T. S. Irvine, *Chem. Mater.* **19**, 2310 (2007).
[18] F. G. Alvarado, A. Orera, J. C. Va´zquez and J. T. S. Irvine, *Chem. Mater.* **18**, 3827 (2006).
[19] C. Heid, H. Weitzel, F. Bourdarot, R. Calemczuk, T. Vogt and H. Fuess, *J. Phys. Condens. Matter* **8**, 10609 (1996).
[20] S. Karmakar, A. B. Garg, M. Sahu, A. Tripathi, G. D. Mukherjee, R. Thapa, and D. Behera, *J. Appl. Phys.* **128**, 215902 (2020).
[21] T. J. S. Munsie, M. N. Wilson, A. Millington, C. M. Thompson, R. Flacau, C. Ding, S. Guo, Z. Gong, A. A. Aczel, H. B. Cao, T. J. Williams, H. A. Dabkowska, F. Ning, J. E. Greedan and G. M. Luke, *Phys. Rev. B* **96**, 144417 (2017).
[22] S. Lei, C. Wang, D. Guo, X. Gao, D. Cheng, J. Zhou, B. Chenga and Y. Xiaoa, *RSC Adv.* **4**, 52740 (2014)
[23] I. Yaeger, A. H. Morrish, C. Boumford, C. P. Wong, B. M. Wanklyn and B. J. Garrard, *Solid State Commun.* **28**, 651 (1978).
[24] R. I. Gulyaeva, S. A. Petrova, V. M. Chumarev and E.N. Selivanov, *J. Alloy. Comp.* **834,** 155153 (2020).
[25] M. A. White and G. Neshvad, *J. Chem. Thermodynamics* **23**, 455 (1991).
[26] S. R. de Oliveira Neto, E. J. Kinast, M. A. Gusmao, C A dos Santos, O. Isnard and J. B. M. da Cunha, *J. Phys. Condens. Matter* **19**, 356210 (2007).
[27] T. Wang, T. Ma, T. Ge, S. Shi, H. Ji, W. Li and G. Yang, *J. Alloy. Comp.* **750,** 428 (2018).
[28] E. Husson, Y. Repelin, Nguyen Quy Dao and H. Brusset, *J. Chem. Phys.* **67**, 1157 (1977).
[29] B. D. Cullity and C. D. Graham. "Introduction to magnetic materials", John Wiley & Sons (2011).
[30] A. H. Morrish, "The Physical Principles of Magnetism", Wiley-IEEE Press; 1 edition (2001).
[31] S. Blundell, "Magnetism in Condensed Matter", Oxford University Press, Oxford (2001).
[32] R. C. O' Handley, "Modern Magnetic Materials: Principles and Applications", New York: John Wiley, (2000).
[33] M. Getzlaff, "Fundamentals of Magnetism", Springer Science & Business Media (2007).
[34] J. M. D. Coey, "Magnetism and magnetic materials", Cambridge university press (2010).

[35] N. Prasai, "Spin-Phonon Coupling and Magnetic Heat Transport in Low-Dimensional Quantum Antiferromagnets, PhD. Thesis, University of Miami (2015).
[36] M. E. Fisher, *Am. J. Phys.* **32**, 343 (1964).
[37] Heisenberg, W. Zur Theorie des Ferromagnetismus, *Z. Physik* **49**, 619 (1928).
[38] R. Skomski, "Simple models of magnetism", Oxford University Press (2008).
[39] C. Coulon, H. Miyasaka, and R. Clerac, *Struct. Bond* **122**, 163 (2006).
[40] E. Ising, *Zeitschrift für Physik* **31**, 253 (1925).
[41] C. Kittel, Introduction to Solid State Physics (Publication, New York, NY: Wiley, 1953).
[42] J. Rodríguez-Carvajal, Lab. Léon Brillouin (CEA-CNRS), CEA/Saclay, 91191 Gif Sur Yvette Cedex, France (2015).
[43] W. Kraus and G. Nolze, *J. Appl. Crystallogr.* **29**, 301 (1996).
[44] J. F. Moulder, Handbook of X-Ray Photoelectron Spectroscopy: A Reference Book of Standard Spectra for Identification and Interpretation of XPS Data (1992).
[45] J. J. Shea, *IEEE Electr. Insul. Mag.* **19**, 73 (2003).
[46] P. S. Bagus, E. S. Ilton, and C. J. Nelin, *Surf. Sci. Rep.* **68**, 273 (2013).
[47] Philip H. Rieger, Electron Spin Resonance (The Royal Society of Chemistry, Thomas Graham House, Science Park, Milton Road, Cambridge CB4 0WF, UK, 2007).
[48] H. H. Woodbury and G. W. Ludwig, *Phys. Rev.* **117**, 102 (1960).
[49] N. J. Kidner, B. J. Ingram, Z. J. Homrighaus, T. O. Mason, and E. J. Garboczi, *MRS Online Proc. Libr. Arch.* **756**, (2003).
[50] B. Fe and O. Nb, *Phys. B Phys. Condens. Matter* **406**, 3470 (2011).
[51] O. S. Doroshkevych, A. V Shylo, O. V Saprukina, I. A. Danilenko, T. E. Konstantinova, and L. A. Ahkozov, *World J. Condens. Matter Phys.* **2**, 1 (2012).
[52] P. Electrochemistry, C. Elements, C. Equivalent, and C. Models, *Appl. Note AC* **286**, R491 (2010).
[53] J. R. Macdonald and W. B. Johnson, in Impedance Spectrosc. Theory, Exp. Appl. Second Ed. (2005), pp. 1–26.
[54] PPMS DynaCool User's Manual, 1307-110, Rev. D1 (2017).
[55] Physical Property Measurement System, Heat Capacity Option User's Manual (Quantum Design, 2010).
[56] J. S. Hwang, K. J. Lin, C. Tien, *Rev. Sci. Instrum.* **68**, 94 (1997).
[57] O. V. Nielsen, T. Johansson, L. M. Holmes, G. J. Cock, L. W. Roeland, and A. A. Ballman, *J. Magn. Magn. Mater.* **1**, 320 (1976).
[58] O. V. Nielsen, B. Lebech, F. K. Larsen, L. M. Holmes, and A. A. Ballman, *J. Phys. C: Solid State Phys.* **9**, 2401 (1976).
[59] L. M. Holmes, A. A. Bailman, and R. R. Hecker, *Solid State Commun.* **11**, 409 (1972).
[60] I. Yaeger, A. H. Morrish, and B. M. Wanklyn, *Phys. Rev. B* **15**, 1465 (1977).
[61] I. Yaeger, A. H. Morrish, B. M. Wanklyn, and B. J. Garrard, *Phys. Rev. B* **16**, 2289 (1977).
[62] D. Prabhakaran, F. R. Wondre and A. T. Boothroyd, *J. Cryst. Growth* **250**, 72 (2003).
[63] H. Weitzel and S. Klein, *Solid State Commun.* **12**, 113 (1973).
[64] I. Maartense, I. Yaeger and B. M. Wanklyn, *Solid State Commun.* **21**, 93 (1977).
[65] W. Scharf, H. Weitzel, I. Yaeger, I. Maartense and B. M. Wanklyn, *J. Magn. Magn. Mater.* **13**, 121 (1979).
[66] C. Heid, H. Weitzel, P. Burlet, M. Bonnet, W. Gonschorek, T. Vogt, J. Norwig and H. Fuess, *J. Magn. Magn. Mater.* **151**, 123 (1995).
[67] S. Kobayashi, H. Okano, T. Jogetsu, J. Miyamoto, and S. Mitsuda, *Phys. Rev. B* **69**, 144430 (2004).
[68] S. Thota, S. Ghosh, Maruthi R, D. C. Joshi, R. Medwal, R. S. Rawat, and M. S. Seehra, *Phys. Rev. B* **103**, 064415 (2021).
[69] C. M. Morris, R. V. Aguilar, A. Ghosh, S. M. Koohpayeh, J. Krizan, R. J. Cava, O. Tchernyshyov, T. M. McQueen, and N. P. Armitage, *Phys. Rev. Lett.* **112**, 137403 (2014).

[70] J. Geyer-Lippmann, A. Simon, and F. Z. Stollmaier, *Anorg. Allg. Chem.* **516**, 55 (1984).
[71] H. Nesbitt and D. Banerjee, *Am. Mineral.* **83**, 305 (1998).
[72] P. Pramanik, S. Ghosh, P. Yanda, D. C. Joshi, S. Pittala, A. Sundaresan, P. K. Mishra, S. Thota, and M. S. Seehra, *Phys.Rev. B* **99**, 134422 (2019).
[73] M. E. Fisher, *Philos. Magn.* **7**, 1731 (1962).
[74] E. E. Bragg and M. S. Seehra, *Phys. Rev. B.* **7**, 4197 (1973).
[75] V. Narang, D. Korakakis and M. S. Seehra, *J. Magn. Magn. Mater.* **368**, 353 (2014).
[76] A. R. King and H. Rohrer, *Phys. Rev. B.* **19**, 5864 (1979).
[77] S. Riegel and G. Weber, *J. Phys. E.* **19**, 790 (1986).
[78] L. P. Kadanoff, W. Gotze, D. Hamblen, R. Hecht, E. A. S. Lewis, V. V. P. Ciauskas, M. Rayl and J. Swift, *Rev. Mod. Phys.* **39**, 395 (1967).
[79] J.D. Rall, M. S. Seehra and E.S. Choi, *Phys. Rev. B* **82**, 184403 (2010).
[80] L. B. Mendelsohn, F. Biggs, and J. B. Mann, *Phys. Rev. A* **2**, 1130 (1970).
[81] P. Dutta, M. S. Seehra, S. Thota and J. Kumar, *J. Phys. Condens. Matter.* **20**, 8 (2008).
[82] M. S. Seehra, and T. M. Giebultowicz, *Phys. Rev. B* **38**, 11898 (1988).
[83] P. W. C. Sarvezuk, M. A. Gusmão, J. B. M. da Cunha, and O. Isnard, *Phys. Rev. B* **86**, 054435 (2012).
[84] H. Weitzel, *Z. Kristallogr. Cryst. Mater.* **144**, 238 (1976).
[85] Maruthi R, M. S. Seehra, S. Ghosh, R. Medwal, R. S. Rawat, B. Weise, E. S. Choi, and S. Thota, *J. Phys. Condens. Matter* **34**, 155801 (2022).
[86] Maruthi R, S. Ghosh, M. S. Seehra, D. C. Joshi, M. R. Chowdhury, R. Medwal, R. S. Rawat, B. Weise and S. Thota, *J. Phys. Condens. Matter* **33**, 345801 (2021).
[87] X. Mi, J. Cuiran and W. Xin, *J. Wuhan Univ. Technol. Mater. Sci. Ed.* **27,** 50 (2011).
[88] H. J. Lee, K. S. Hong and S. J. Kim, *Mater. Res. Bull.* **32**, 847 (1997).
[89] R. C. Pullar, K. Okeneme and N. M. Alford, *J. Eur. Ceram. Soc.* **23,** 2479 (2003).
[90] H. J. Lee and K. S. Hong, *J. Mater. Res.* **12**, 1437 (1997).
[91] J. Hazarika and A. Kumar, *Synth. Met.* **198**, 239 (2014).
[92] N. Sivakumar, A. Narayanasamy and N. Ponpandian, *J. Appl. Phys.* **101**, 084116 (2007).
[93] A. P. Barranco and J. D. L. S. Guerra, *Dielectric Relaxation Phenomenon in Ferroelectric Perovskite-related Structures*, ISBN: 978-953-307-4399, 166 (2010).
[94] N. E. Rajeevana, R. Kumarb, D. K. Shuklac, P. P. Pradyumnana, S. K. Arorad and I. V. Shvets, *Mater. Sci. Eng. B* **163,** 48 (2009).
[95] S. K. Jena, D. C. Joshi, S. Ghosh, K. Dasari and S. Thota, *J. Phys. D: Appl. Phys.* **54,** 425303 (2021).
[96] H. M. Zeyada, F. M. E. Taweel, M. M. E. Nahass and M. M. E. Shabaan, *Chin. Phys. B* **25,** 077701 (2016).
[97] H. Bouaamlat, N. Hadi, N. Belghiti, H. Sadki, M. N. Bennani, F. Abdi, T. Lamcharfi, M. Bouachrine and M. Abarkan, *Adv. Mater. Sci. Eng.*, 8689150 (2020).
[98] M. A. M. Seyam, *Appl. Surf. Sci.* **181**, 128 (2001).
[99] N. Ortega, A. Kumar, P. Bhattacharya, S. B. Majumder and R. S. Katiyar, *Phys. Rev. B* **77,** 014111 (2008).
[100] R. T. George, D. C. Joshi, S. Nayak, N. Tiwari, R. N. Chauhan, P. Pramanik, T. A. Dar, S. Ghosh, and S. Thota, *J. Appl. Phys.* **123**, 054101 (2018)
[101] S. Sumi, P. P. Rao, M. Deepa and P. Koshy, *J. Appl. Phys.* **108**, 063718 (2010).
[102] S. Mahboob, G. Prasad and G. S. Kumar, *Bull. Mater. Sci.* **29**, 35 (2006).
[103] A. M. A. Karim, A. H. Salama and F. A. El-Samahy, *Nanoarchitectonics* **14,** 1 (2020).
[104] S. Nasrin, M. Megdiche and M. Gargouri, *Ceram. Int.* **42,** 943 (2016).
[105] A. Sharma, A. Kumar and N. Mehta, *Measurement* **75,** 69 (2015).
[106] W. Hizi, H. Rahmouni, M. Gassoumi, K. Khirouni and S. Dhahri, Eur. *Phys. J. Plus* **135,** 456 (2020).
[107] T. Mondal, S. Das, T.P. Sinha, P.M. Sarun, *Mater. Sci. Pol.* **36**, 112 (2018).

[108] M. Javed, A. A. Khan, M. S. Ahmed, S. N. Khisro, J. Kazmi, M. S, R. Bilkees, M. N. Khan and M. A. Mohamed, *Physica B: Condensed Matter* **599**, 412377 (2020).
[109] N. A. El-Ghamaz, A. Z. El-Sonbati, M. A. Diab, A. A. El-Bindary and S. M. Morgan, *Mater. Res. Bull.* **65,** 293 (2015).
[110] M. M. Costa, G. F. M. Pires, A. J. Terezo, M. P. F. Graca and A. S. B. Sombra, *J. Appl. Phys.* **110,** 034107 (2011).
[111] A. M. Nawar, H. M. A. El-Khalek and M. M. El-Nahass, *Org. Opto-Elect.* **1**, 25 (2015).
[112] M. A. L. Nobre, S. Lanfredi, *J. Phys. Chem. Solids* **64,** 2457 (2003).
[113] D. P. Almond, A. R. West, *Solid State Ion.* **11,** 57 (1983).
[114] A. K. Pradhan, T. K. Nath and S. Saha, *Mater. Res. Express* **4,** 076107 (2017).
[115] K. P. Padmasree, D. K. Kanchan and A. R. Kulkarni, *Solid State Ion.* **177,** 475 (2006).
[116] A. Bagum, M. B. Hossen, and F. U. Z. Chowdhury, *Ferroelectrics* **494**, 19 (2016).
[117] J. Liu, C. G. Duan, W. G. Yin, W. N. Mei, R. W. Smith and J. R. Hardy, *J. Chem. Phys.* **119,** 2812 (2003).
[118] M. A. L. Nobre and S. Lanfredi, *J. Appl. Phys.* **93,** 5557 (2003).
[119] B. V. R Chowdari and R. Gopalakrishnan, *Solid State Ion.* **23,** 225 (1987).
[120] R. Bergman, *J. Appl. Phys.* **88**, 1356 (2000).
[121] S. Gupta, G. Sharma, S. K. Deshpande, V. G. Sathe, and V. Siruguri, *J Mater Sci: Mater. Electron.* **33**, 4072 (2022).
[122] M. A. L. Nobre and S. Lanfredi, *J. Appl. Phys.* **93,** 5576 (2003).
[123] S. Lanfredi, G. Palacio, F. S. Bellucci, C. V. Colin and M. A. L. Nobre, *J. Phys. D: Appl. Phys.* **45,** 435302 (2012).
[124] E. Kolonelou, A. N. Papathanassiou and E. Sakellis, *Mat. Chem. Phys.* **232**, 319 (2019).
[125] E. Kolonelou, E. Loupou, P. A. Klonos, E. Sakellis, D. Valadorou, A. Kyritsis and A. N. Papathanassiou, *Polymer* **224**, 123731 (2021).
[126] E. V. Hauff, *J. Phys. Chem. C* **123**, 11329 (2019).
[127] L. He and Z. Ling, *Appl. Phys. Lett.* **98,** 242112 (2011).
[128] T. L. Rao, M. K. Pradhan, S. Singh and S. Dash, *J. Mater. Sci. Mater. Electron.* **31**, 4542 (2020).
[129] Y. Lian, Y. Zheng, D. Wang, Y. bai, H. Yan, Z. Wang, J. Zhao, H. Zhang, *J. Colloid Interface Sci.* **606,** 77 (2022).
[130] Q. J. Li, S. Q. Xia, X. Y. Wang, W. Xia, Y. Yu, Y. M. Cui, J. Zhang, J. Zheng, C. Cheng, Y. D. Li, H. Wang, S. G. Huang and C. C. Wang, *J. Alloy. Comp.* **616,** 577 (2014).
[131] Z. Imran, M. A. Rafiq, M. Ahmad, K. Rasool, S. S. Batool and M. M. Hasan, *AIP Adv.* **3,** 032146 (2013).
[132] J. T. S. Irvine, D. C. Sinclair and A. R. West, *Adv. Muter.* **2**, (1990).
[133] A. N. Mansurova, R. I. Gulyaeva, V. M. Chumarev and S. A. Petrova, *J. Alloy. Comp.* **695,** 2483 (2017).
[134] C. Tealdi, M. C. Mozzati, L. Malavasi, T. Ciabattoni, R. Amanteaa and C. B. Azzonib, *Phys. Chem. Chem. Phys.* **6**, 4056 (2004).
[135] Y. Liu, S. Huang, X. Li, H. Song, J. Xu, D. Zhang and X. Wu, *Inorg. Chem.* **59**, 18122 (2020).
[136] F. Liu, X. Yang, B. Wang, Y. Guan, X. Liang, P. Sun and G. Lu, Sens. *Actuators B Chem.* **229,** 200 (2016).
[137] W. Scharf and H. Weitzel, *Solid State Commun.* **18**, 249 (1976).
[138] G. R. Reddy, S. Balasubramanian and K. Chennakesavulu, *RSC Adv.* **5**, 81013 (2015).
[139] J. R. Pilbrow, *J. Magn. Reson.* **58**, 186 (1984).
[140] S. K. Jena, D. C. Joshi, Z. Yan, Yajun Qi, S. Ghosh and S. Thota, *J. Appl. Phys.* **128**, 073908 (2020).
[141] S. Ghosh, D. C. Joshi, P. Pramanik, S. K. Jena, S. Pittala, T. Sarkar, M. S. Seehra and S. Thota, *J. Phys. Condens. Matter* **32**, 485806 (2020).
[142] T. Kataoka, Y. Sakamoto, Y. Yamazaki, V. R. Singh, A. Fujimori, Y.Takeda, T. Ohkochi, S. I. Fujimori, T. Okane, Y. Saitoh, H. Yamagami and A. Tanaka, *Solid State Commun.* **152**, 806 (2012).

[143] S. Sachdev, *Quantum Phase Transition* (Cambridge University Press, 1999).
[144] T. Hanawa, K. Shinkawa, M. Ishikawa, K. Miyatani, K. Saito and K. Kohn, *J. Phys. Soc. Jpn.* **63**, 2706 (1994).
[145] S. Mitsuda, K. Hosoya, T. Wada, H. Yoshizawa, T. Hanawa, M. Ishikawa, K. Miyatani, K. Saito, and K. Kohn, *J. Phys. Soc. Jpn.* **63**, 3568 (1994)
[146] S. Kobayashi, S. Mitsuda, M. Ishikawa, K. Miyatani, and K. Kohn, *Phys. Rev. B* **60**, 3331 (1999).
[147] S. Kobayashi, S. Mitsuda, and K. Prokes, *Phys. Rev. B* **63**, 024415 (2000).
[148] S. Kobayashi, S. Mitsuda, S. Hosaka, H. Tamatsukuri, T. Nakajima, H. Koorikawa, K. Prokeš, and K. Kiefer, *Phys.Rev. B* **94**, 134427(2016).
[149] P. W. C. Sarvezuk, E. J. Kinast, C. V. Colin, M. A. Gusmao, J. B. M. da Cunha and O. Isnard, *Phys. Rev. B* **83**, 174412 (2011).
[150] P. W. C. Sarvezuk, E. J. Kinast, C. V. Colin, M. A. Gusmão, J. B. M. da Cunha, and O. Isnard, *J. Appl. Phys.* **109**, 07E160(2011).
[151] Z. Wang and M. S. Seehra, J. Phys.: Condens. Matter. **29**, 225803, (2017).
[152] M. E. Lines, *Phys. Rev.* **131**, 546 (1963).
[153] N. McIntyre and D. Zetaruk, *Anal. Chem.* **49**, 1521 (1977).
[154] T. H. Ko, K. Devarayan, M.-K. Seo, H.-Y. Kim, and B.-S. Kim, *Sci. Rep.* **6**, 20313 (2016).
[155] N. Mottaghi, M.S. Seehra, J. Shi, M. Jain and M. B. Holcomb, J. Appl. Phys. **128,** 073903 (2020).
[156] N. D. Mermin and N. W. Ashcroft, *Solid State Physics* (Holt, Rinehart and Winston, New York, 1976), pp 644–653.
[157] P. Burgardt and M. S. Seehra, *Solid State Commun.* **22**,153 (1977).
[158] M. Nandi, D. Prabhakaran, and P. Mandal, *J. Phys.: Condens. Matter* **31**, 195802 (2019).
[159] P. W. C. Sarvezuk, J. B. M. da Cunha, and O. Isnard, *AIP Advances* **10**, 035016 (2020).
[160] Maruthi R, S. K. Deshpande, V. Deshmukh, K. Singh and S. Thota, *J. Phys. D: Appl. Phys.* **56,** 025501 (2022).
[161] M. E. A. de Dompablo, Y L Lee and D. Morgan, *Chem. Mater.* **22**, 906 (2010).
[162] J. Peña, M. A. Gusmão and O. Isnard, *Phys. Rev. B* **103**, 094409 (2021).
[163] L. Chen, J. Zhang, X. Ren,b R. Ge, W. Teng, X. Sun and X. Li, *Nanoscale* **9**, 16632 (2017).
[164] M. Yang and R. Rao, *J Mater Sci* **53**, 15487 (2018).
[165] W. He, X. Li, S. An, T. Li, Y. Zhang and J. Cui, *Sci. Rep.* **9**, 10838 (2019).
[166] L. Li, E. Han, L. Zhu, S. Qiao and C. Du, *Ionics* **26**, 2655 (2020).
[167] R. Jana, A. Gupta, R. Choudhary and O. P. Pandey, *J. Sol-Gel Sci. Technol.* **96**, 405 (2020).
[168] T. E. Jones, T. C. R. Rocha, A. K. Gericke, C. Stampfl, R. Schlogl and Simone Piccinin, *Phys. Chem. Chem. Phys.* **17**, 9288 (2015).
[169] T. Hanawa, M. Ishikawa, and K. Miyatani, *J. Phys. Soc. Jpn.* **61**, 4287 (1992).
[170] C. M. N. Kumar, Y. Xiao, H. S. Nair, J. Voigt, B. Schmitz, T. Chatterji, N. H. Jalarvo and Th Brückel, *J. Phys.: Condens. Matter* **28**, 476001 (2016).
[171] D. T. Teaney, *Phys. Rev. Lett.* **14**, 898 (1965).
[172] D. T. Teaney, V. L. Moruzzi, and B. E. Argyle, *J. Appl. phys.* **37**, 1122 {1966).
[173] A. R. Miedema, R. F. Wielinga, and W. J. Huiskamp, *Phys. Letters* **17**, 87 (1965).
[174] P. Nordblad, L. Lundgren, E. Figueroa, U. Gafvert and O. Beckman, *Physica Scripta.* **20**, 105 (1979).